DOCTORAL THESIS

EXPERIMENTAL VELOCITY PROFILE DISTRIBUTION CHARACTERIZATION OF MOUNTAIN RIVERS

Author:

Blanca MARIN-ESTEVE

Supervisor:

Prof. Dr Allen BATEMAN PINZON

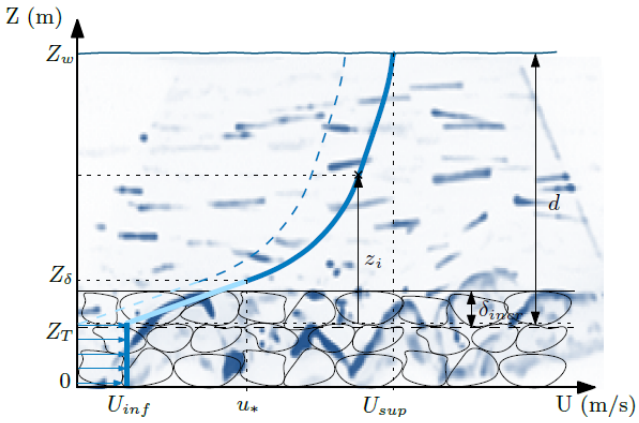

A thesis submitted in fulfilment of the requirement

for the degree of Doctor of Philosophy in the

Doctorat en Enginyeria Civil

UNIVERSITAT POLITÈCNICA DE CATALUNYA
BARCELONATECH

Escola Tècnica Superior d'Enginyeria
de Camins, Canals i Ports de Barcelona

Barcelona, April 2023

Founded by:

GITS

GOBIERNO DE ESPAÑA
MINISTERIO DE ECONOMÍA, INDUSTRIA Y COMPETITIVIDAD

Per a la Cristina

Abstract

The aim of this thesis is to improve our understanding of the behaviour of mountain rivers and to predict their morphological functioning under conditions of low relative submergence. Mountain rivers have received less attention in the field of river hydraulics, which has generally relied on information that is more relevant to rivers with a lower gradient, leading to inconsistencies in the analysis of steep streams. This thesis aims to address this gap by investigating to what extent and in what ways the log-law equation can describe the velocity profile distribution across steep channels with porous beds. Specifically, we seek to determine which parameters of the velocity profile distribution are influenced by channel slope, relative submergence and interstitial discharge.

To conduct this study, experiments were performed in a rectangular flume using a 14.5 mm median diameter gravel bed under a threshold of movement conditions. Several flow discharges were performed for each of the flume slopes considered, which ranged from 2%–10%, with relative submergences between 0.7–3.7. Velocity measurements were taken with an Acoustic Doppler Velocimeter and complemented with the Particle Tracking Velocimetry technique to measure velocities in the near-bed region. Using the general normalised least squares regression approach, we analysed several parameters in the construction of a velocity profile.

The results of our study demonstrated that the experimental dimensionless velocity profiles collapsed to the log-law formulation once the optimization procedures were applied to the proposed objective functions. We found that the reference datum definition is an essential variable to consider and should be located below the crests of the roughness elements and then moved deeper as the channel slope increases. The Von Karman parameter remained constant at 0.4 regardless of the channel slope, discharge and relative submergence. We found that the minimum velocity of the profile, which is nonzero at the bed structure given interstitial discharge, depends on the channel slope but not on relative submergence.

The Karman–Prandtl logarithmic velocity profile is validated for velocity profiles in hydraulically rough flows under low relative submergence conditions, given a well-defined reference level.

The significance of our study lies in its contribution to the theoretical understanding of the prediction of flow resistance by focusing on velocity distribution across steep channels, thereby reducing uncertainties in flood hazard mapping in mountainous regions and contributing to the development of a baseline for the analysis of mountain rivers. Our findings have important implications for the analysis and management of mountain rivers, which are essential for improving the conservation of these critical ecosystems.

Resum

Tot i que fa més d'un segle que s'investiga la morfologia dels rius, l'estudi ha estat centrat principalment en el curs baix d'aquests. De manera que la majoria de les teories en el camp de la hidràulica fluvial s'han desenvolupat en rius amb pendent baixa. Aquesta tesi tracta sobre les formulacions utilitzades en la gestió del risc d'inundacions en rius de muntanya i busca millorar la comprensió del comportament d'aquest tipus de rius, per poder predir el seu funcionament morfològic. Més concretament, aquesta tesi té com a objectiu abordar el buit existent en hidràulica fluvial en rius de muntanya investigant si es pot aplicar, i de quina manera, l'equació de la llei logarítmica per descriure la distribució del perfil de velocitat en rius d'alta pendent amb llits porosos. Concretament, busca determinar quins paràmetres de la distribució del perfil de velocitat estan influenciats pel pendent del riu, la submersió relativa i el cabal intersticial.

Per dur a terme aquest estudi, es va dur a terme una campanya experimental en un canal rectangular utilitzant un llit de grava de 14,5 mm de diàmetre mitjà, amb pendents d'entre un 2% i un 10%, submersions relatives d'entre 0.7 i 3.7, i sempre mantenint les condicions del flux per sota de l'inici de moviment. Les mesures de velocitat es van prendre amb un Acoustic Doppler Velocimeter i es van complementar amb la tècnica de Particle Tracking Velocimetry. S'han analitzat diversos paràmetres per a la construcció del perfil de velocitat utilitzant una regressió normalitzada de mínims quadrats.

Els resultats demostren que els perfils experimentals de velocitat adimensionals col·lapsen a la formulació de la llei logarítmica una vegada aplicats els procediments d'optimització. S'ha vist que la definició del nivell de referència és una variable a tenir en compte, que s'ha de situar per sota de les crestes dels elements del llit, i que s'ha de desplaçar endins del llit a mesura que augmenta el pendent del canal. El paràmetre de Von Karman s'ha mantingut constant a 0.4, independentment del pendent del canal, el cabal i la submersió relativa. També s'ha vist que la velocitat mínima del perfil, que és diferent de zero a la superfície del llit degut al cabal intersticial, depèn del pendent del canal però no de la submersió relativa. D'aquesta manera, el perfil de velocitat logarítmic de Karman–Prandtl està validat per a perfils de velocitat en fluxos hidràulicament rugosos en condicions de submersió relativa baixa.

La importància del nostre estudi rau en la seva contribució a la comprensió teòrica de la predicció de la resistència al flux, centrant-se en la distribució de velocitats sobre llits porosos amb pendent pronunciat, reduint les incerteses en la creació de mapes de risc d'inundació a les regions de muntanya i contribuint a l'extensió de la base de dades per a l'anàlisi dels rius de muntanya. D'aquesta manera, les nostres troballes tenen implicacions importants per a l'anàlisi i la gestió dels rius de muntanya.

Table of Contents

List of Tables

List of Figures

List of Symbols

Variable	Description
$\{i, j\}$	Experiment i and profile j
A	Coefficient of the log-law equation (-)
a_r	Parameter of the log-law equation (-)
B	Roughness coefficient of the log-law equation (-)
B_w	Channel width (m)
C_t	Correlation threshold (-)
d	Water depth (m)
d^+	Experimental water depth (m)
D_a	Aperture diameter (m)
d_{diff}	Diffraction point source diameter (px)
d_p	Particle diameter in the object space (px)
d_τ	Particle image diameter (px)
D_{50}	Median diameter of bed particle (m)
e	Void ratio (-)
Fr	Froude number (-)
f	Focal length (m)
$f_\#$	Number of f-lens (-)
I_t	Intensity threshold (-)
k	Von Karman constant (-)
K	Average projection of the roughness (m)
k_s	Height of relative roughness (m)
l	Height of the image plane (m)
L	Height of the source plane (m)

Variable	Description
l_w	Interrogation window length (px)
L	Height of the source plane (m)
M	Magnification factor (-)
N_s	Source density (-)
N_I	Image density (-)
Q_{inf}	Interstitial discharge (l/s)
Q^+_{inf}	Experimental interstitial discharge (l/s)
Q_{sup}	Superficial discharge (l/s)
Q^+_{sup}	Experimental superficial discharge (l/s)
Q_{tot}	Total discharge (l/s)
Q^+_{tot}	Experimental total discharge (l/s)
Re	Reynolds number (-)
Re^*	Particle or roughness Reynolds number (-)
R_h	Hydraulic radius (m)
R_h / D_{50}	Relative submergence (-)
r_n	Neighbourhood radius (px)
$r_{particle}$	Representative radius (px)
S_f	Energy slope (m/m)
S_s	Specific gravity (Tn/m^3)
U	Depth-averaged mean flow velocity (m/s)
$\vec{u}$	Velocity vector of a tracked particle (m/s)
u_i'	Instantaneous streamwise velocity measured at a certain depth (m/s)
$\overline{u_i}$	Mean local streamwise velocity at a certain depth (m/s)
$\overline{u_i^+}$	Experimental mean local streamwise velocity at a certain depth (m/s)

Variable	Description
$U_{\inf}$	Mean interstitial flow velocity (m/s)
$U_{\inf}^{+}$	Experimental mean interstitial flow velocity (m/s)
u_*	Shear velocity (m/s)
u_*^{+}	Experimental shear velocity (m/s)
v	Vertical velocity (m/s)
$vel_{\%}$	Percentage of minimum velocity similarity with neighbour particles (%)
V_s	Solid volume (m^3)
V_T	Total volume (m^3)
V_V	Void volume (m^3)
W_S	Material´s solid weight (kg)
z	Height over reference level (m)
z^{+}	Experimental height from the reference level (m)
z_o	Height of the origin of the velocity profile (m)
Z	Water level (m)
Z_c	Level of top of the crests (m)
Z_c^{+}	Experimental level of top of the crests (m)
Z_o	Level of origin of velocity profile (m)
Z_L	Level of 'L' plates (m)
Z_L^{+}	Experimental level of 'L' plates (m)
Z_T	Level of reference bed (m)
Z_w	Level of water surface (m)
Z_w^{+}	Experimental level of water surface (m)
$Z_{w\delta}$	Level of corrected water surface (m)
Z_δ	Level of water surface at velocity equal to u_* (m)

Variable	Description
α	Flume slope (%)
α_t	Texture factor (-)
β	Coefficient of proportionality between δ_{incr} and D_{50} (-)
γ	Water specific weight (N/m^3)
δ_{incr}	Shifting distance of the reference level from the bed crests (m)
δ_o	Shifting distance of the profile origin from the bed crests (m)
$\delta_{\sup}$	Shifting distance for vibration of water surface (m)
δ_z	Depth of field (m)
Δ	Vertical distance from the area of PTV measurements to $Z_{w\delta}$ (m)
Δt	Time incremental (s)
$\Delta\vec{x}$	Position vector incremental (m)
Δz_o	Thickness of the light sheet (m)
ε	Energy dissipation (m^2/s^3)
λ	Wavelength of the laser light (nm)
ν	Kinematic viscosity of water (m^2/s)
ρ_W	Water density (kg/m^3)
σ_i	Standard deviation of the i variable
ϕ	Bed porosity (-)
φ	Coefficient of proportionality between K and D_{50} (-)

List of Abbreviations

Abbr.	Description
ADV	Acoustic Doppler Velocimetry
AOI	Area Of Interest
BCC	Binary Cross-Correlation method
CC	Cross-Correlation method
CCD	Charge-Coupled Devices
CMOS	Complementary Metal-Oxide-Semiconductor
DPSSL	Diode-Pumped Solid-State Laser
GITS	Sediment Transport Research Group
ICCRM	Integrated Cross-Correlation and Relaxation Method
LD	Laser Diode
LDV	Laser Doppler Velocimeter
LSV	Laser Speckle Velocimetry
PIV	Particle Image Velocimetry
PTV	Particle Tracking Velocimetry
PTVlab	Particle Tracking Velocimetry laboratory software (Pantalano, 2020)
RM	Relaxation Method
ROI	Region Of Interest
UPC	Universitat Politècnica de Catalunya

Chapter 1: Introduction

This chapter explains the motivation for this thesis and outlines the research objectives presented in each subsequent chapter.

1.1. Motivation

Despite over a century of work done on river hydraulics, a significant portion has been dedicated to rivers with moderate to low gradients. The importance of understanding river hydraulics lies in its application to flood mitigation, habitat, restoration, scour and erosion assessment, and it is vital to both engineering and geomorphology (Buffington and Montgomery 1999; Lamb et al. 2017a; Rickenmann and Recking 2011; Yager et al. 2007). However, the hydraulics of mountain streams remain poorly understood due to their substantial differences from alluvial rivers. Mountain streams typically feature steep, coarse-bedded channels and shallow, rough flows with subsurface flow, channel bed forms, immobile boulders and seasonally variable floods (Fernández 2019; Lamb et al. 2017a).

Nevertheless, the absence of a widely recognized baseline for the hydraulics of steep streams has resulted in the application of parameters designed for rivers with a lower gradient, causing inconsistencies in the analysis of steep streams. For instance, many studies compare the measurement of hydraulic and sediment transport in natural steep streams, which includes the challenges posed by immobile boulders and bed forms, to empirical relations designed for low gradient rivers with planar beds. Such comparisons often reveal substantial differences due to effects attributed to the presence of form drag by immobile boulders or step-pool bed configurations (Ferguson 2012; Nitsche et al. 2012; Rickenmann 2001; Yager et al. 2012), although some authors still question the extent to which the hydraulics of steep streams differ from those of lower gradient rivers, despite the rough beds (Lamb et al. 2017a).

An accurate estimation of discharge during a flow requires knowledge of water velocity, as velocity is often used to estimate the discharge associated with a particular flow depth. Therefore, flow velocity plays a critical role in determining many fluvial processes and flow characteristics, such as river engineering, risk and environmental assessment, the understanding of channel morphodynamics, the validation of numerical modelling, the computation of flow discharge and bed load sediment and the estimation of the transport of pollutants and nutrients and the assessment of aquatic habitat quality (Adams and Zampiron 2020; Rickenmann and Recking 2011; Schneider et al. 2015b).

In certain situations, flow velocity can be determined directly using instruments such as a current metre or calculated from the continuity equation (Q/A), provided the discharge and the wetted area are known. However, in many cases, direct measurement is not possible. In these instances, it is necessary to predict water velocities through other means. One effective approach is to use flow resistance equations, which, given some channel properties (such as

slope, grain size and roughness), are able to establish the relationship between the water depth and velocity of flow. These equations can provide an estimation of water velocities in the absence of direct measurements.

Despite its importance, predicting accurate flow resistance in mountain streams can be a complex task, particularly in relation to determining the roughness coefficient (Nezu and Nakagawa 1993; Powell 2014). Theoretically, it should be feasible to predict flow velocities based on the boundary conditions and on some understanding of the flow magnitude (Zimmermann 2010). However, the difficulties arise from the complexity and uncertainties associated with the definition of channel roughness, especially in mountain streams with large boulders, particle clusters and diverse channel forms (Jarrett 1987; Powell 2014). In fact, there is ongoing discussion among researchers on the velocity profile distribution in mountain streams, with some supporting the use of log-law (Aberle and Smart 2003; Einstein and El-Samni 1949; Fernández 2019; Grass 1971; Nezu and Nakagawa 1993; Rouzes et al. 2018; Smart 1999), and others suggesting alternative approaches, such as the “S-shaped” profile (Bathurst 1985; Ferro 2003a; Ferro and Baiamonte 1994; Jarrett 1990; Katul et al. 2002).

Although flow resistance relationships have been widely researched and analysed over time and across different geographical locations (Bathurst et al. 1979; Comiti et al. 2007; Ferguson 2021; Henderson 1966; Keulegan 1938; Millar 1999; Recking et al. 2008a; Smart et al. 2002; Zimmermann 2010), there is still no well-tested, consistently accurate equation for calculating the resistance coefficients of mountain rivers. There is still significant uncertainty around the velocity profile of mountain rivers (Wohl 2010) due to the lack of a standard measure by which to characterize the roughness of a bed in this environment (Adams 2022; Millar 1999; Nezu and Nakagawa 1993). The large bed grains in mountain rivers pose a challenge, as they are often above the water surface at low flows and can be as high as the flow depth during high-flow events (Bathurst 1993; Smart et al. 2002; Zimmermann 2010). Furthermore, steep gradient streams often contain coarse bed material, leading to significant subsurface flow through the bed (Lamb et al. 2017a; Packman et al. 2004). Finally, different resistance equations may apply to different ranges of relative submergence, further complicating the determination of an accurate coefficient (Smart et al. 2002). These phenomena may result in the misrepresentation of hydraulic variables, such as water depth and roughness height, consequently impacting local average velocity and flow resistance.

The accurate prediction of variations in velocity with depth is critical in various fields in which high- and low-flow conditions are of special significance. The estimation of bankfull discharge is also crucial for flood risk assessment with ungauged streams, and it can be determined using

high water marks or other stage indicators (Ferguson 2021). On the other hand, low velocities and small water depths are important when prescribing the minimum flows needed for aquatic habitat protection.

The Manning equation is widely used in hydrology to predict the flow velocity of a river or stream based on its roughness coefficient. However, the accuracy of these predictions is limited by the fact that the invariant roughness coefficient is often calibrated from flow measurements taken at a single point in time (Ferguson 2010). Additionally, researchers frequently only have access to data collected before or after an event rather than during the event itself, which further complicates the application of the Manning equation and the determination of the roughness coefficient for a certain study event (Adams 2022). Evidence suggests that Manning's coefficient usually decreases significantly with increasing discharge, even in the same stream (Chow 1959; Ferguson 2010; Fernández 2019; Rickenmann and Recking 2011; Zimmermann 2010). This can result in an underestimation of flow resistance by the Manning–Strickler formula, even in high flows (Ferguson 2010, 2021). Therefore, it is necessary to take into account temporal variations in the roughness coefficient in any flow resistance prediction (Wohl 2010). Thus, any predictive model of flow resistance should account for both spatial and temporal variations in roughness coefficients to ensure accuracy and reliability in its discharge estimates (Powell 2014; Trieste and Jarrett 1987).

This thesis aims to increase our understanding of the vertical distribution of flow velocity in steep, shallow channels that have rough, planar beds under steady flow and non-motion conditions. This study employs a combination of experimental and numerical methods to investigate the factors that affect flow velocity in these channels. Its objective is to provide a comprehensive examination of the subject, to present a thorough analysis of the key factors that affect flow velocity in such channels, and to expand the existing data collected under conditions of low relative submergence and steep, planar, rough beds.

To this end, experiments were conducted in the Morphodynamics Laboratory I of the Sediment Transport Research Group (GITS) at the Civil and Environmental Department of Universitat Politècnica de Catalunya using an Acoustic Doppler Velocimeter (ADV) complemented with the Particle Tracking Velocimetry (PTV) technique to collect data on instantaneous velocities. These data were then analysed to gain insight into the complex interactions that occur between flow velocity, subsurface discharge, bed roughness and relative submergence in steep, shallow channels.

The following sections provide a brief overview of the topics addressed in the thesis, with further detail and analysis presented throughout the dissertation.

1. 1. 1. Differences between moderate and low gradient rivers

Evidence suggests that the hydraulics of steep streams differ significantly from their better studied counterparts with lower gradients. For instance:

- Friction factors (i.e. coefficients that relate bed shear stress to average flow velocity) are greater in steep rivers than predicted by the empirical models developed for lower gradient rivers (Aberle and Smart 2003; Bathurst 1985; Ferguson 2007; Ferro 2003b; Rickenmann and Recking 2011; Wilcox and Wohl 2007), particularly at low relative submergence (Lamb et al. 2017a; b; Recking et al. 2008a), as flow resistance increases strongly with decreasing relative submergence (Bathurst 1985; Lee and Ferguson 2002; Limerinos 1970; Reid and Hickin 2008; Schneider et al. 2015b; Wilcox et al. 2006).
- The flow velocity profile of steep streams can deviate from the well-known classic logarithmic profile developed for lower gradient rivers (Byrd et al. 2000; Nikora et al. 2004; Wiberg and Smith 1991; Wohl and Thompson 2000).
- The intensity of near-bed velocity fluctuations due to turbulence is weaker in shallow, rough flows (Lamb et al. 2008). Additionally, near-bed turbulence intensities have been proven to be a function of relative roughness (Lamb et al. 2017a).
- Semi-empirical models developed to estimate initial sediment motion and bed load flux in lower gradient rivers tend to overestimate sediment transport when applied to steep rivers (Mueller et al. 2005; Rickenmann 2001; Yager et al. 2012).

There are several reasons why the empirical relationships developed for low-gradient planar-bed rivers may not be applicable to steep streams:

- The presence of large boulders (rarely mobile), particle clusters and bed forms, such as pool-riffle or step-pool sequences (Buffington and Montgomery 1999; Ferguson 2012; Millar 1999; Nitsche et al. 2012; Schneider et al. 2015a; Yager et al. 2007).
- Interlocking boulders in steps and other bed structures can stabilize sediment and reduce transport rates (Church et al. 1998; Zimmermann 2010).
- These bed forms can also create a series of overspills and pools that affect the development of a logarithmic boundary layer and may limit the scale and intensity of turbulence (Fernández 2019; Wohl and Thompson 2000; Zimmermann 2010).
- The bed form drag on immobile boulders and boulder steps is often considered the primary mechanism that slows the flow, increasing the friction factor (Aberle and Smart

2003; Buffington and Montgomery 1999; Ferguson 2012). Additionally, it is assumed that this reduces the bed stress available to drive sediment transport, which may explain the increased Shields numbers for initial sediment motion (Ferguson 2012; Mueller et al. 2005; Recking 2009) and the reduced sediment transport rates in steep streams (Rickenmann 2001; Schneider et al. 2015a; Yager et al. 2007). However, recent studies on steep river hydrodynamics in the absence of complex bed geometries have shown that reduced sediment transport rates may be due to the reduced turbulence intensities that occur in flows with low relative submergence rather than to changes in the local-mean flow resulting from macro-scale form drag (Lamb et al. 2017a).

Additionally, the empirical relationships of low gradient planar-bed rivers may not be applicable to steep streams even when the latter lack bed forms, channel forms, grain interlocking or large immobile boulders (Lamb et al. 2017a). Steep streams tend to have a flow depth of the same order of magnitude as the size of their boulders or cobbles (Bayazit 1976). Moreover, shallow flows on steep slopes with planar, rough beds can reach or surpass unity Froude numbers, resulting in highly three-dimensional flow patterns with spills over the grain tops (Zimmermann 2010), standing and breaking waves (Lawrence 2000) and significant aeration (Vallé and Pasternack 2006). Additionally, the combination of steep bed gradients and coarse bed material can result in significant subsurface flow through the bed (Lamb et al. 2017a).

1. 1. 2. Planar beds

To empirically assess the impact of boulders and bed forms on flow and sediment transport, researchers typically compare observations from rivers or flumes that have these features with “base cases” that do not have bed forms while controlling for other variables. This approach is based on the classic linear stress partitioning theory for rivers, which assumes that the total frictional stress is the sum of drag on bed sediment, banks, and the form drag caused by bed forms and other macroscale roughness (Einstein and Barbarossa 1952). This partitioning of friction factors has also been adopted by other approaches (Ancey and Pascal 2020; Millar 1999; Rickenmann and Recking 2011).

Building on the foundations established by Nikuradse (1933), decades of measurement of flow hydraulics for planar, rough beds in low-gradient rivers have created a bed form-free base case (Lamb et al. 2017a). This makes it possible to quantify the impact of bed forms on momentum conservation, flow resistance, velocity profile structure and sediment transport (Meyer-Peter and Müller 1948). Specifically, Parker (1991) was able to effectively use the Manning–Strickler formula to determine the resistance coefficients in a low gradient gravel bed river with a planar bed. However, similar, well-established theories for base-case flow resistance (i.e. for rough,

planar beds without larger-scale morphological form drag) are not yet available for steep streams (Lamb et al. 2017a). This gap in knowledge stems from the lack of natural high-gradient streams without bed forms and immobile boulders (Rickenmann 2012; Yager et al. 2012), and the fact that most flume experiments have focused on lower gradient rivers, or they have complicated effects related to bed forms or channel geometries such as step-pools (Zimmermann 2010) and sediment transport (Recking et al. 2008a, 2008b).

There is a need to develop and test theories for the hydraulics of steep streams with simple, rough and planar beds that lack bed forms and large boulders (Lamb et al. 2017a). This would establish a baseline, similar to that obtained from studies performed on low-gradient rivers and pipe flow, and provide a point of reference for comparison with the more complex geometries and bed structures typically found in natural steep rivers. By gaining a deeper understanding of the basic hydraulic principles of steep streams with simple bed geometries, it will be possible to better comprehend and predict the flow dynamics in more complicated systems, such as mountain streams.

According to Lamb et al. (2017a), a surprising similarity was discovered between the local averaged flow velocity in steep streams with planar beds and that in low-gradient gravel bed rivers. These researchers found that the flow resistance in their flume experiments was similar to that in natural mountain streams, despite the fact that the experiments lacked bed forms, immobile boulders, and other sources of macro-scale form drag that are thought to dominate flow resistance in natural channels. These findings raise questions about the accuracy of applying stress-partitioning techniques to mountain streams and suggest that macro-scale form drag in mountain streams may be less significant than is typically assumed (Lamb et al. 2017a).

1. 1. 3. Velocity profile and flow resistance

The Chezy, Darcy–Weisbach and Manning constants are the most widely used classical methods for predicting flow resistance in channels. These methods are based on empirical observations of channel flow and have their origin in the "law of the wall," as first proposed by Von Karman. The law of the wall describes the relationship between the velocity of the flow and the roughness of the channel boundary, which determines the flow resistance in the channel. Building upon Karman's law, Keulegan (1938) developed flow resistance equations for hydraulically rough channels. Keulegan integrated the Karman–Prandtl log-law velocity profile distribution over a channel cross-section and obtained an expression for the average velocity of a section for turbulent flow over a rough boundary.

The study of flow resistance prediction in channels has been a topic of ongoing research for many years, leading to various modifications of the classical methods to better suit channels with relatively rougher beds (Aberle and Smart 2003; Bathurst et al. 1979; Comiti et al. 2007; Ferguson 2007, 2010, 2021; Lamb et al. 2017a; Millar 1999; Recking et al. 2008a; Rickenmann and Recking 2011; Smart et al. 2002; Zimmermann 2010).

To meet this objective, some authors have suggested the utilization of logarithmic resistance relationships, which integrate the logarithmic profile for turbulent flow over a rough boundary. These equations, based on the wall's law, work over a wide range of conditions provided the roughness height is accurately defined (Bray 1980; Ferguson 2007, 2021; Hey 1979; Lamb et al. 2017a; López and Barragán 2008). This is despite the known limitations of the wall law in describing velocity profiles in low relative submergence flows (Ferguson 2007).

However, the velocity profile distribution in mountain streams continues to be a subject of debate among researchers. While some laboratory studies over gravel beds with low relative submergence have found that the velocity profile could be described with the log-law if certain parameters (e.g. roughness height or reference datum) are adjusted (Aberle and Smart 2003; Einstein and El-Samni 1949; Fernández 2019; Grass 1971; Nezu and Nakagawa 1993; Rouzes et al. 2018; Smart 1999), others have observed that the velocity profiles of low relative submergence flows are 'S-shaped', with the point of inflection lying just above the crests of the roughness elements, defining the transition between the slower motion within the roughness space and the faster moving flow above it (Bathurst 1985; Ferro 2003a; Ferro and Baiamonte 1994; Jarrett 1990; Katul et al. 2002).

To this end, numerous experimental studies have explored the statistical description of turbulent characteristics in open channel flows (Fernández 2019; Nakagawa and Nezu 1977; Nikora and Goring 2000; Niño and Garcia 1996), with a specific emphasis on the near-bed region (Antonia and Krogstad 2001; Jiménez 2004; Raupach et al. 1991). Nezu and Nakagawa (1993) noted that two critical questions must be addressed to accurately describe turbulent structures over rough beds: (1) What parameter should be used to represent the size of roughness elements? and (2) Where should the reference datum for water depth be located? Moreover, in permeable beds, significant subsurface flow occurs through the bed on steep slopes, resulting in a nonzero velocity at the bed structure. This velocity has been found to impact both the magnitude and shape of the velocity profile in the near-bed region and also higher, in the surface flow (Lamb et al. 2017a).

Another approach to predicting flow resistance involves an examination of the Strickler–Manning empirical formula for steep channels. Some authors have examined how best to characterize the roughness coefficient (Bathurst 2002; Canovaro and Solari 2007; Comiti et al. 2009; Smart et al. 2002), while others have noted that the classical definition may not hold for relatively small channels with cobble or boulder beds, as Manning's coefficient varies with the stage, and sometimes by more than a factor of two (Ferguson 2010, 2021; Jarrett 1984).

Other researchers, rather than modifying traditional approaches, have proposed alternative approaches, such as non-dimensional hydraulic geometry relationships (Aberle and Smart 2003; Comiti et al. 2007; Ferguson 2007; Rickenmann 1991, 1994; Rickenmann and Recking 2011) or roughness-layer models, based on mixing-layer analogies (Lamb et al. 2017a). Others have studied how flow resistance can be described in relation to step-pool structures (Canovaro and Solari 2007; Comiti et al. 2009; Lee and Ferguson 2002; Maxwell and Papanicolaou 2001), or specifically, in shallow flows (Bathurst 1985, 2002; Ferguson 2007; Jarrett 1984; Katul et al. 2002; Rickenmann 1991; Smart et al. 2002).

To avoid the difficulties of estimating the resistance coefficient, various researchers have proposed alternative approaches to avoid the explicit estimation of this coefficient (Jarrett 1984; López et al. 2007). However, there is no theoretical basis for these approaches, and the coefficients are highly dependent on the data used to fit them (Rupp and Smart 2007).

Almost all of the proposed and studied methods for analysing flow in steep streams require a prior definition of the roughness coefficient. Traditional methods for defining the roughness coefficient use the grain size as a reference (e.g. D_{50} or D_{84}) (Ferguson 2007; Millar 1999; Wong and Parker 2006; Yen 2002), but in such complex environments, selecting a unique grain diameter may be difficult, or even an unreliable variable (Ferguson 2021). Some researchers have proposed using the standard deviation of bed elevations about the mean log profile as a roughness length, but there is still ongoing debate over the most appropriate method for characterizing roughness (Aberle and Smart 2003; Ferguson 2021; Smart et al. 2002).

1. 1. 4. Extreme events in mountain streams

The Nicola River valley in British Columbia was affected by a series of severe events in 2021: the heatwave and the Lytton Creek Fire in June and an atmospheric river with an associated flood event in November (BGC Engineering Inc. 2022; Gillett et al. 2022; White et al. 2023). The heatwave and wildfire resulted in the burning of the mountainous slopes that drain into the Nicola River, and the atmospheric river brought high-intensity rainfall to the region, leading to extreme flooding and changes in the river course through bank erosion and sediment deposition

(BGC Engineering Inc. 2022). This combination of events resulted in landslides, debris flows, debris floods and extreme flooding, with an estimated return period of between 100 and 500 years (Gillett et al. 2022).

In mid-July 2021, a persistent low-pressure system brought extreme rainfall to central Europe, causing record-breaking water levels and severe flooding in the Ahr River valley in Germany and in the Vesdre, Meuse and Gete River valleys in Belgium (Mohr et al. 2022). Reconnaissance observations in August 2021 documented the severe and often irreparable damage caused by the floodwaters to bridges in the Ahr and Erft rivers, with modern bridges, designed and constructed in the last two decades, suffering severe damage, and historic bridges being completely destroyed (Lemnitzer et al. 2021).

In October 2019, Catalonia was impacted by a devastating storm that struck the Francolí River. The most significant damage was caused by the loss of riverside vegetation, including hundred-year-old trees and pine forests, with an estimated return period of over 200 years (UPC 2020). This loss not only led to the loss of an important ecological element, but also exposed the bridges along the river to increased risk. Without the protective cover of the vegetation, the abutments of some of the bridges were washed out, and large quantities of woody debris clogged two of the bridges, leading to increased flow through the abutment and over the deck and then a wave caused by the collapse of the debris jam (Martín-Vide et al. 2023). This resulted in several bridge failures, including the collapse of two bridges.

In June 2013, Vall d'Aran (Catalonia) was impacted by a flash flood and torrential flood event that caused significant geomorphological damage, including bank erosion and vertical incision. Here, the return period is estimated to be between 30 and 50 years (Victoriano et al. 2016). During this event, the Garona River underwent significant changes, including channel modification and avulsion. The river experienced severe bank erosion and widening along its entire length as well as deepening in certain sections. Additionally, the event triggered debris flows in some tributary catchments, which increased the sediment load of the stream, leading to fan reactivation and deposition. Some bridges were unable to handle the flood discharge, resulting in clogging and overflow sedimentation in adjacent areas (Victoriano et al. 2016).

These events highlight the need for further research and understanding of the behaviour of mountain rivers during extreme flood events. Despite our current understanding and technology, there is still much to be learned about how these channels react and the impact that these floods can have on surrounding areas. For example, during major floods, bank erosion on steep gravel-bed rivers can result in even more devastating consequences than overland

flooding, affecting both infrastructure and communities that fall outside of traditional floodplain boundaries, as evidenced during the November 2021 atmospheric river event in the Nicola River valley (Davidson et al. 2022). Despite its significant impact, bank erosion is not currently accounted for in hydraulic models used to simulate and map flood inundation, which may lead to an underestimation of flood risk.

Similarly, with the damage to bridges on the Ahr and Erft rivers, it became evident that both the intensity of the rainfall and the local topography were decisive factors in explaining the degree of destruction, where the high discharge and streamflow caused high-flow velocities that led to failures such as bridge scour, road embankment instability and the erosion of aggregate foundations (Lemnitzer et al. 2021).

Finally, the devastating impact of the Francoli River storm highlights the importance of vegetation management along river banks to protect critical infrastructure and also the crucial role that vegetation plays in managing the flow of water and reducing erosion (Davidson 2016; Martín-Vide et al. 2023). This event emphasized the need for improved planning and design strategies for infrastructure in areas prone to extreme weather events and flash floods.

Despite standard discharge designs being based on 100–200 year return period events, recent events, such as the one that took place in Vall d'Aran, Catalonia in June 2013, demonstrate that these standards may be inadequate for mountain streams. This event, with an estimated return period of only 50 years, caused significant damage to infrastructure and highlighted the need for further research and the adaptation of discharge designs to mountain streams.

Additionally, it is important to consider the potential effects of climate change on these mountain streams. Climate change is expected to increase the frequency and intensity of these types of floods, making it crucial that we continue to study and understand the interactions between mountain rivers and extreme weather events. With a better understanding of these processes, we can ensure that communities and the environment are better prepared and protected against the consequences of future floods in a changing climate.

1.2. Thesis Objectives

The main objective of this thesis is to comprehensively understand the behaviour of high mountain rivers and to predict the morphological functioning of flows over a steep channel under low relative submergence conditions. This better understanding of mountain rivers will allow future research to develop more accurate methods to predict flow resistance and thereby reduce the uncertainties in flood hazard mapping in mountainous regions.

The thesis can be broken down into two specific research questions, used to address the main objective:

- **Question 1:** Is the well-known logarithmic profile still valid for steep channels under low relative submergence conditions?

One of the main issues to be addressed in fulfilling the primary objective is whether the velocity profile distribution of a highly energetic flow (steep slope) in a coarse bed at low relative submergence flows still follows the well-known logarithmic profile. Therefore, a secondary but no less critical objective is to define the velocity profile distribution and all its parameters for steep channels with low relative submergence over a permeable bed.

- **Question 2:** Which parameters of the velocity profile distribution are affected by slope, relative submergence, and interstitial discharge? How can we predict them?

In answering this question, the main emphasis is placed on how the interstitial discharge, the roughness of the bed material, the relative submergence and the flume slope affect the datum definition, Von Karman's constant value and the roughness parameter of the velocity profile distribution.

To answer each research question and fulfil the main objective, experiments were conducted in a flume with a flatbed under non-motion conditions, in which discharge and flume slope varied from one experiment to the other. The same sediment was used as the bed layer throughout all experiments. Velocity measurements were collected with an ADV and a PTV methodology, which has been defined, calibrated and validated under low relative submergence conditions in the present thesis.

1.3. Document Structure

In the first chapter of this thesis, we introduce and motivate the object of our research and describe the goals of the thesis. Chapters 2–6 contain the main contributions of the study.

Chapter 2 is devoted to formally defining the experimental device that supported the experiments, the experimental campaign, the methodology of execution and the materials used in each experiment in the laboratory. This chapter contains only a summary of the works mentioned, which are extensively developed in the thesis appendices.

Chapter 3 encompasses a set of checks conducted on the data series measured by the ADV and PTV techniques to verify their quality and correct execution.

Chapter 4 corresponds to one of the publications listed in the next section. This chapter is self-contained, preserves the associated paper's structure and can be read independently. Nevertheless, we have tried to keep the notation as homogenous as possible. This chapter describes and characterises the velocity profile distribution on steep creeks under low relative submergence through the log-law equation. An addendum has been added at the end of this chapter to provide a sensitivity analysis on the reference datum definition. This addendum was not included as part of the research article submitted to the peer-review journal.

Chapter 5 focuses on the roughness parameters obtained in *Chapter 4*, and assesses how they are affected by steep flumes under low relative submergences conditions.

To conclude this document, global conclusions and the main contributions of the thesis are summarized in *Chapter 6*. Furthermore, we list future lines of research to be pursued based on the development of this thesis.

Two appendices are included with this thesis: *Appendix A: Experimental Setup Calibration Procedures* and *Appendix B: Supplemental Figures and Tables*. Whereas the first focuses on the calibrations needed to conduct the experiments (e.g. slope measurement, discharge measurement), the second shows the results from the analysis conducted in each chapter.

Finally, all of the experiment's raw data can be found in an open-source repository (Marin-Esteve et al. 2021).

1.4. Research Publications

Chapter 4 corresponds to the following paper sent to the Journal of Hydraulic Research which is now under revision.

> Marín-Esteve, B., Bateman, A., Sosa-Pérez, R. (under review). "*Log-Law Velocity Profile in Steep Rough Channels.*" Journal of Hydraulic Research.

Additionally, some of the knowledge of mountain regions as developed in this research has already been applied to hydraulic modelling in a case study of a flash flood with extensive woody debris that occurred in the upper Francoli River valley after the rainstorm on October 22, 2019. This publication is as follows:

> Martín-Vide, J. P., Bateman, A., Berenguer, M., Ferrer-Boix, C., Amengual, A., Campillo, M., Corral, C., Llasat, C., Llasat-Botija, M., Gómez, S., Marín-Esteve, B., Núñez-González, F., Prats-Puntí, A., Ruiz-Carulla, R., Sosa-Pérez, R. (2023). "*Large Wood Debris that Clogged*

Bridges in a Flash Flood, Followed by a Sudden Release. A Case Study." Journal of Hydrology: Regional Studies.

1.5. Conference Talks

In addition, the author has presented the contents of this thesis as *presenting speaker* at the following international conferences:

- Marín-Esteve, B., Bateman, A., Sosa, R. (2021). "Medidas de velocidades con PTV en cauces de alta pendiente." LAHDI 2021 – Congreso Latinoamericano de Hidráulica. Online.
- Marín-Esteve, B., Bateman, A., Fernández, C., Lin, C. (2019). "Sediment threshold of motion on rivers with steep slopes: impulse criterion." RCEM 2019 – River, Coastal and Estuarine Morphodynamics Symposium. Auckland, New Zealand.
- Marin-Esteve, B., Fernández, C., Bateman, A. (2019). "Theoretic-experimental study on the morphological behaviour of rivers with steep slopes." EGU 2019 – European Geosciences Union General Assembly. Wien, Austria.

Chapter 2: Experimental Setup

This chapter describes the experimental work carried out to investigate the velocity profile distributions and resistance of steep creeks under low relative submergence conditions.

2.1. Introduction

This chapter presents a detailed description of the laboratory flume used to conduct the experiments in this study. It includes the dimensions of the flume, the instrumentation and materials used to measure flow variables.

The chapter begins by describing the flume dimensions and configuration, followed by a detailed description of the physical characteristics of the material used in the experiments. The chapter then proceeds to explain the experimental procedure, which is essential for ensuring the validity and reproducibility of the results.

2.2. Laboratory Facilities

The experiments were carried out in the hydraulic flume of the Morphodynamics Laboratory I of the Sediment Transport Research Group (GITS). The facility is situated in Campus Nord in the Civil and Environmental Department of the Universitat Politècnica de Catalunya and comprises a straight rectangular flume with glass walls, measuring 9 m long, 0.4 m wide, and 0.6 m high (Figure 2.1 and Figure 2.2). The flume's slope is variable, ranging from 0 to 30 degrees and pivoting from the bottom end.

Depth measurements were taken at equally spaced intervals along the channel (Figure 2.2-b).

The recirculation system was composed of four tanks connected by pipes, with water flowing over the channel by gravity from the constant head tank (named "black tank" below for simplicity) upstream of the channel (Figure 2.1). The water then flushed over the 9-meter channel to a receiving tank (reception tank), which overflowed into another receiving tank (spillway tank). Lamination of the water was achieved before it flushed over the rectangular weir located at the end of the spillway tank, where a piezometer was installed to control water discharges. The downstream tank is a water collection tank. A pumping system propels the water from the downstream tank to the black tank.

The discharge was measured using two magnetic flowmeters in the pipe connecting the black tank at the channel's entrance. In some experiments, discharge was added to the system after the magnetic valves, and the discharge measurements had to be conducted through the piezometer located in the rectangular weir in the spillway tank.

The test zone was located in the center of the flume section, 5.65 m from the inlet, where a fully developed turbulent flow was achieved (Figure 2.1).

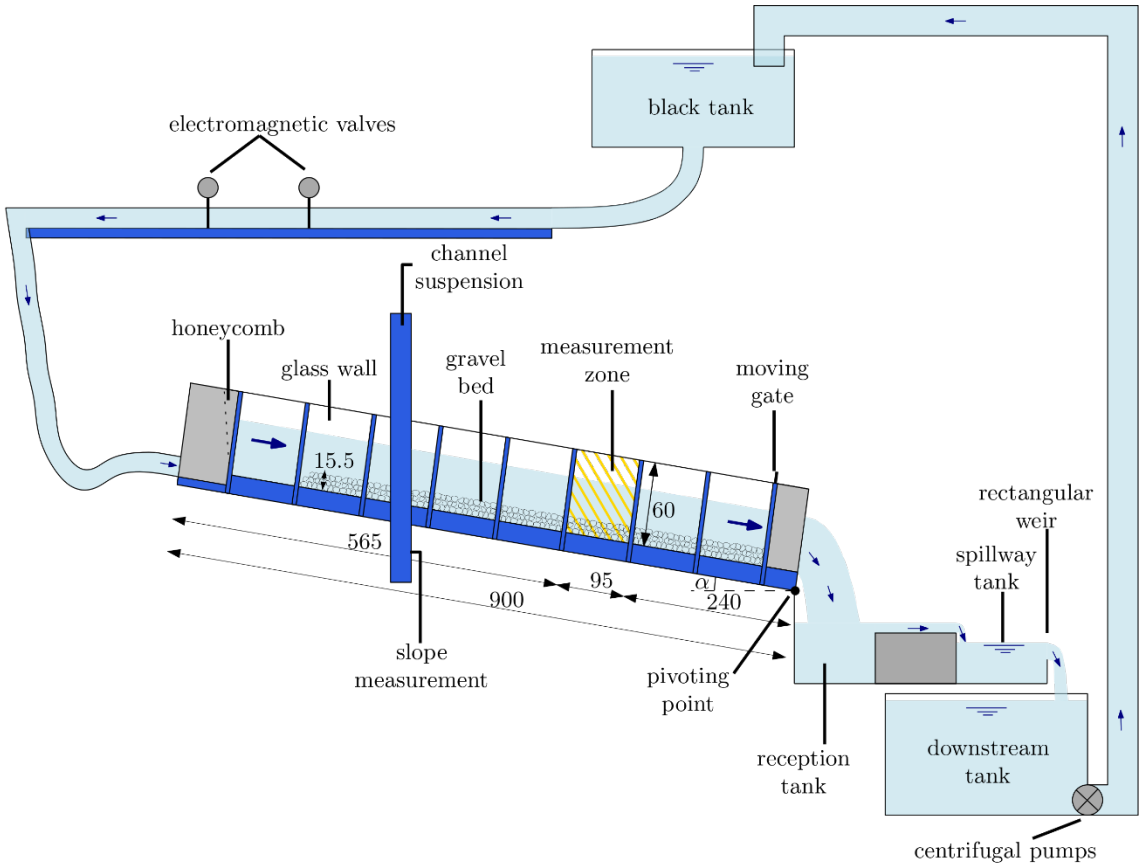

Figure 2.1. Schematic illustration of the experimental apparatus (all measurements are in cm).

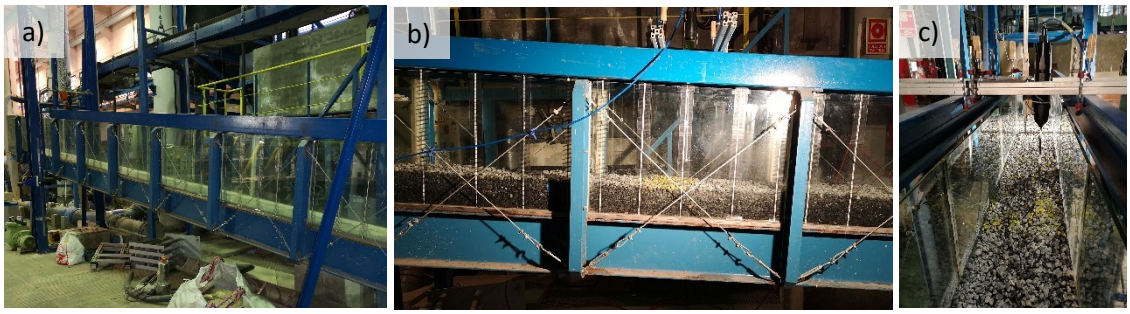

Figure 2.2. (a) Looking upstream to the flume, (b) test zone, and (c) cross-section downstream looking.

The sections below describe the essential components that constituted the laboratory facilities used in the present thesis.

2. 2. 1. Pumping system

The experimental setup involves the gravity-driven flow of water from the black tank through the flume into the reception tank, which subsequently overflows to the spillway tank, and then to the downstream tank via a rectangular weir. To maintain the continuous flow of water, a pump system in the downstream tank propels the water back to the black tank (Figure 2.1).

The pumping system is comprised of two pumps in parallel (Figure 2.3-a). The system pumps the water from the downstream tank through a pipe to the black tank upstream of the channel

(Figure 2.1). The pumps work with direct starting and can work simultaneously, with a maximum discharge of 55 l/s per pump, resulting in a total discharge of 110 l/s when both pumps are active.

However, the maximum discharge in the flume is only achieved when the flume slope is around 0%, as the water is gravity-driven from the black tank to the flume, and the difference in the water column between the black tank and the channel's entrance depends on the flume's slope. As the slope increases, the difference becomes smaller, resulting in a lower maximum discharge. For instance, at a 2% flume slope, the maximum discharge achievable in the gravity-driven channel is about 40 l/s.

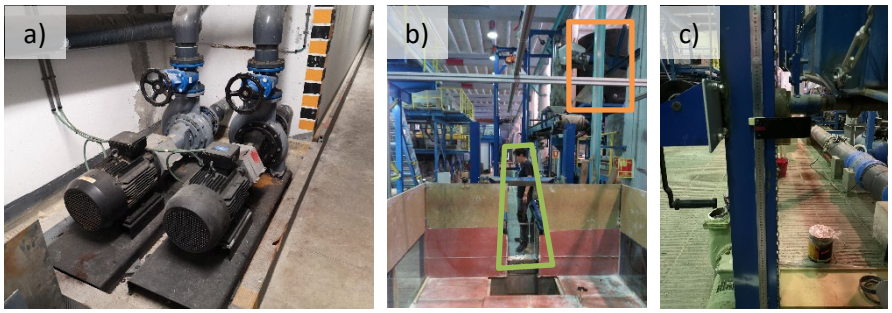

Figure 2.3. (a) Pumping system in the downstream deposit, (b) experimental device looking upstream from the bottom of the spillway tank (black tank in orange and flume in green), and (c) flume's slope measuring tape.

To control the discharge introduced to the flume, two electro-pneumatic valves (Figure 2.4-a) were installed in parallel, one in a 150 mm pipe and the other in a 40 mm pipe. Both valves are SAMSO global valves (model 3277) with an electro-pneumatic positioner (model 3767) and a pneumatic actuator (model 3277), which are independently controlled by a computer. The difference between the actual discharge provided by the pumps and the one flowing throughout the flume overflows into the tank downstream from the black tank, before flowing through the valves.

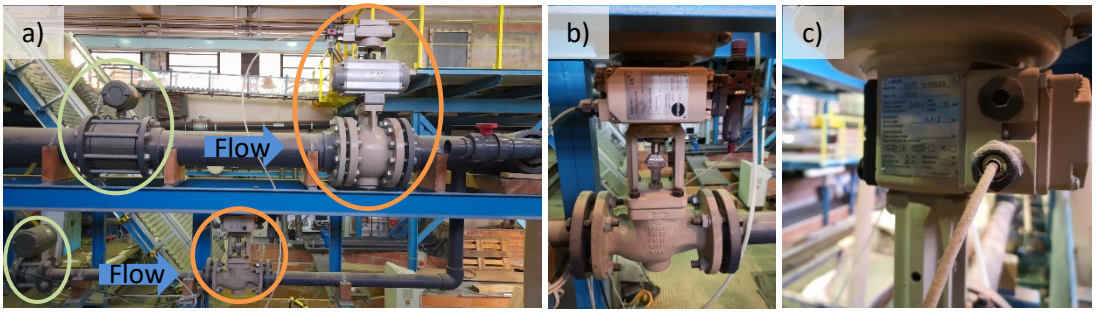

Figure 2.4. (a) Electro-pneumatic valves (in orange) and magnetic flowmeters (in green) (b) electro-pneumatic small valve and (c) detail of its pneumatic actuator.

To almost achieve incipient motion in some experiments, higher discharges were required, and therefore an additional flow rate system was employed. Apart from the pumps mentioned earlier, a submersible electric pump of model RANGER MC 15/50 was utilized in such cases. The pump's flow rate ranges between 0.85 and 12.5 l/s, depending on the water column difference. The pump was installed in an intermediate tank, which received water that overflows from the black tank to the downstream tank. This discharge was introduced to the flume at its entrance, just before the honeycomb as shown in Figure 2.1. The intermediate tank was only functional when the additional pump was required.

2. 2. 2. Discharge measurement

The experimental setup included two different methodologies for measuring the discharge on the flume depending on the pumping system used. In most cases, the flow discharge was measured using two YAKOHAWA magnetic flowmeters, model SE215ME-150 mm (50 l/s) and SE204ME-40 mm (5 l/s), positioned before each electro-pneumatic valve (Figure 2.4-a).

The computer not only enabled the researcher to adjust the opening of each valve but also recorded the valve opening and the flow rate every 0.5 seconds. These magnetic flowmeters functioned by applying a magnetic field to the pipe and measuring the voltage across it with a total flow measurement accuracy of ± 0.2%.

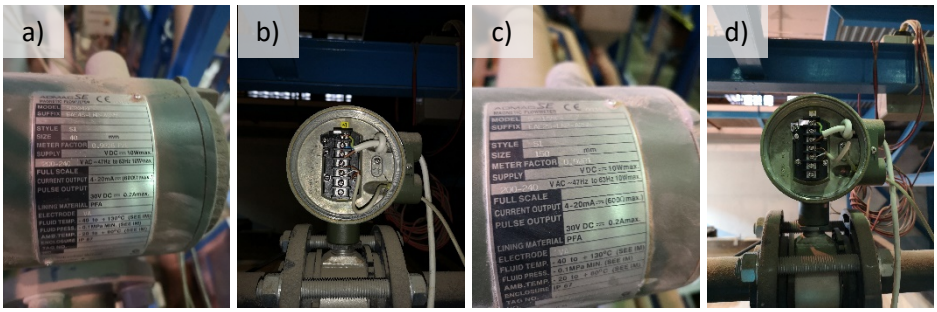

Figure 2.5. YAKOHAWA magnetic flowmeters (a) - (b) for the 150 mm pipe and (c) - (d) for the 50 mm pipe.

When the additional pump was used, the magnetic flowmeters located upstream of the additional discharge entrance could not measure the total discharge. Therefore, in these cases, the discharge was measured using the rectangular weir in the spillway tank (Figure 2.1 and Figure 2.6-a), while a water gauge in the downstream tank was used to determine its water height (Figure 2.6-b and c). To calculate the flow discharge, the water height at the rectangular weir was used, along with its geometrical characteristics and a calibration curve (Figure 2.6-d). The calibration process is described in *Appendix A: Calibrations for the Experimental Setup*.

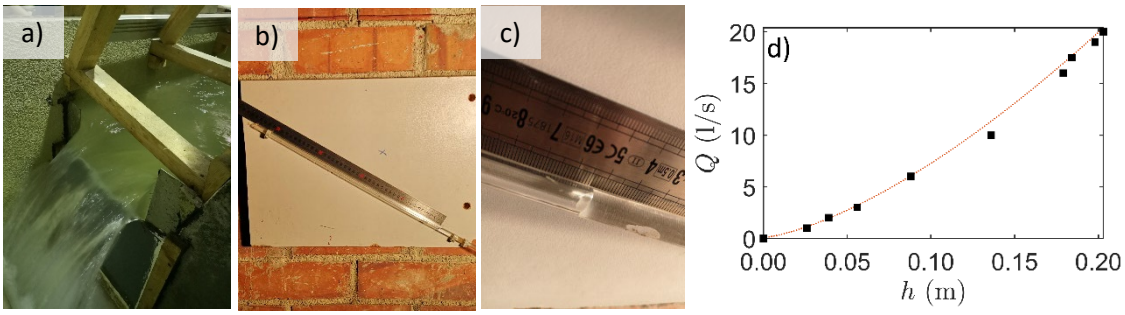

Figure 2.6. (a) Water flowing through the rectangular weir, (b) water gauge installed to measure the water height at the rectangular weir, (c) detail of the gauge, and (d) calibration curve of the rectangular weir.

2.2.2.a. Interstitial flow

Considering the porosity of the bed, it was anticipated that a portion of the flow would pass beneath the test zone. Therefore, direct flow rates obtained from magnetic valves, or the rectangular weir could not be used without accounting for the subsurface flow. This led to the differentiation of total discharge (Q_{tot}), interstitial discharge or infiltrated discharge ($Q_{\inf}$), and surface discharge ($Q_{\sup}$).

The total discharge (Q_{tot}) was measured through direct flow rates obtained from magnetic valves. On the other hand, an ink tracer consisting of a dilution of 2% milk was employed in each experiment to measure interstitial discharge. This involved injecting the tracer into the bed layer about half its thickness (Figure 2.7) and recording its movement (at 60 frames per second) through the glass wall of the channel.

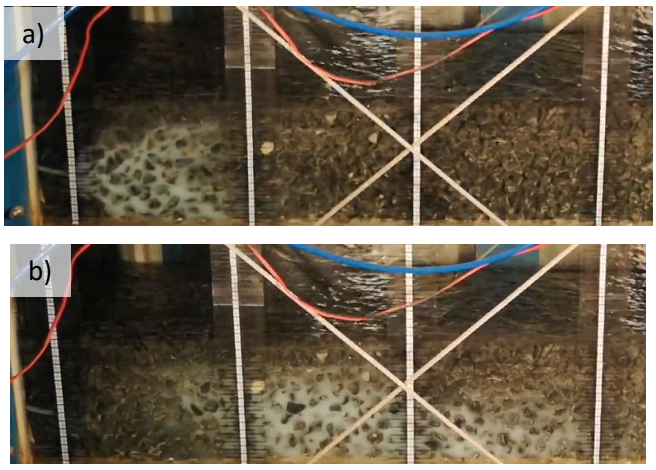

Figure 2.7. Interstitial flow measurement (with 3 % flume slope). (a) first time step, (b) last time step.

The interstitial flow can then be calculated using equation (2.1), where $U_{\inf}$ is the measured interstitial velocity using the tracer, ϕ is the bed porosity, B_w is the channel width, and Z_o is the bed layer height. Subtracting the interstitial discharge from the total discharge yields the surface flow ($Q_{\sup}$).

$$Q_{\text{int}} = U_{\text{inf}} \phi B_w Z_o 1000 \tag{2.1}$$

2. 2. 3. Channel slope

The experimental setup includes a flume that is capable of variable slope adjustment, ranging from 0 to 30 degrees. The flume is suspended by a metallic structure and pivots around the downstream point (Figure 2.2-a). The channel's inclination is controlled by an electric motor and a hook, which is suspended to a bridge crane.

To measure the channel slope, a calibrated measuring tape (±0.25 mm) was placed on the bridge crane pillar (Figure 2.3-c). Details of its calibration can be found in *Appendix A: Experimental Setup Calibration Procedures.*

2. 2. 4. Water depth measurement

Water depths (d) in the flume were measured using two methods. Firstly, transparent gauge levels were attached to the wall every 20 cm along the flume (Figure 2.8-a) with an accuracy of ± 0.5 mm. Each of these meters started at the bottom of the channel (Figure 2.8-b) and gave the water height (Z_w), which includes the height of both water and bed layer. Average values of all the heights along the flume could be obtained since the meters were distributed uniformly along the flume.

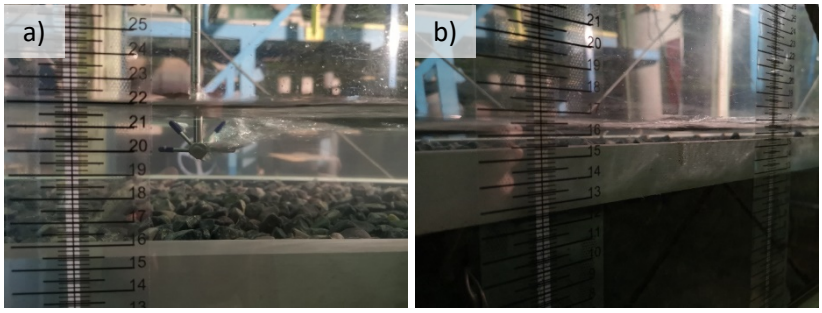

Figure 2.8. Meters placed along the channel for bed and water heights assessments.

In addition, a local measurement of water height was performed using a limnimeter placed in the test zone. This method provided the local water height at the point where ADV measurements were taken, with an accuracy of ± 0.001 m.

2. 2. 5. Sediment control

To prevent sediment from flowing to the downstream tanks, plates were installed at the upstream and downstream ends of the channel (Figure 2.10). The downstream plate also served as a support for the material when the motion threshold was reached.

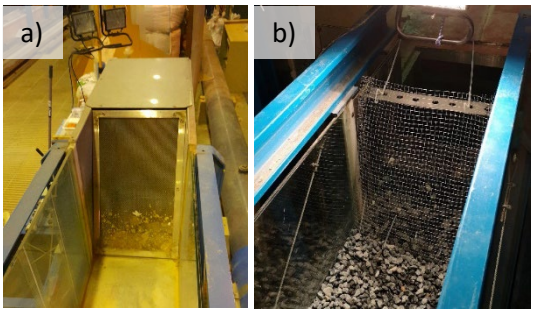

Figure 2.9. Plate (a) upstream and (b) downstream of the flume.

2. 2. 6. Velocities measurement

Three different techniques were used to measure velocities: two to measure velocity within the flow and one to measure water surface velocity. The first two techniques involved an ADV and PTV to register velocity profiles. The third technique obtained the water surface velocity by tracking a floating particle between two cross-sections marked by red laser sheets. A more detailed description of each technique is provided in the following subsections.

2.2.6.a. Acoustic Doppler Velocimeter (ADV)

Velocity measurements were conducted using a 3D SONTEK 10 MHz ADV with a cable mount probe in a side-looking physical arrangement. The position accuracy of the ADV was ± 0.01 mm, with a nominal range velocity set at 1.00 m/s, a transmission length of 1.8 mm, a sampling rate of 25 Hz, and a measurement accuracy of ± 1 mm/s. The ADV measurements were extended until the standard deviation of the time series achieved a constant value to eliminate the eddies associated with local turbulence.

Although the manufacturer NORTEK (2018) states that a side-looking ADV can be utilized as a 2D velocimeter in shallow waters, calibrations were performed to ensure that streamwise velocity direction was not affected if the upper legs of the ADV were not introduced into the water. Only the streamwise velocity (u) was measured, because not all the legs of the ADV were continuously introduced into the water (Figure 2.10-c).

Another important consideration in the methodology used in this thesis to measure velocities is the potential for measurement errors when using ADV to measure velocities below 1 cm from the bed (Finelli et al. 1999), as the near-bed region is of interest. Additionally, in highly turbulent flows or when the bed surface is rough, measurement errors can become more significant (Fernández 2019; Martin et al. 2002). Therefore, to ensure the accuracy of the results, it was necessary to verify the measured velocities using other methods, such as PTV.

Chapter 3 provides a more detailed description of the methodology used to measure velocities using an ADV.

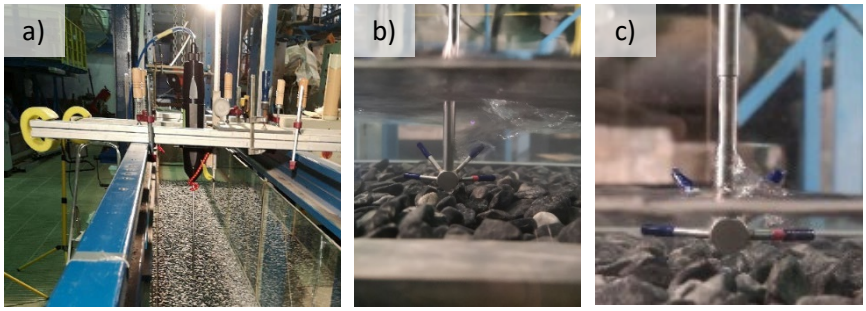

Figure 2.10. (a) ADV placement into the channel, (b) ADV collecting data, and (c) ADV collecting data in shallow water depths.

2.2.6.b. Particle Tracking Velocimetry (PTV)

PTV was used as a velocity measurement technique to overcome the limitations of ADV with small water depths. The PTV setup consisted of a high-speed Complementary Metal-Oxide-Semiconductor (CMOS) monochrome camera (model Basler A504k) with an AF Nikkon 50 mm f/1.4D lens and an extension tube of 20 mm. A green diode laser (LD) of a wavelength of 532 nm was used to illuminate the tracking particles. The laser power was set at 2 Hz for all experiments, achieving an accuracy of ± 1 mm/s. The tracking particles had a diameter of 0.2 mm (Figure 2.11-a and Figure 2.12-a). The software XCAPTM of EPIX© was used for image recording, with a recording frame of 2 ms and an exposure of 0.2 ms.

To avoid laser reflection, the laser sheet was introduced directly into the water without any air between the laser and the water. The laser was introduced into a small transparent cylinder, and the system was placed in the first few millimeters of water (Figure 2.11-b).

More information about the PTV function, configuration, and pre-processing can be found in *Chapter 3*.

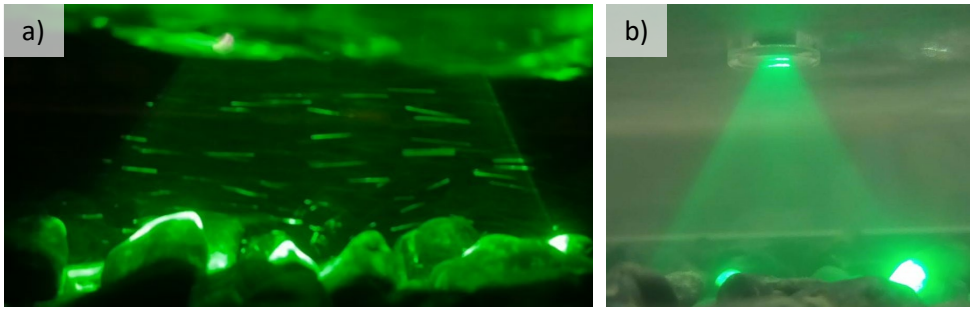

Figure 2.11. Laser sheet used in PVT, (a) with tracking particles, and (b) detail of the transparent cylinder introduced into the flow.

2.2.6.c. Superficial velocities

As mentioned earlier, while the ADV and PTV techniques provided velocity information along the profile from the bed to a certain depth below the water surface, they were unable to measure the water surface velocity. To address this limitation, a third method was used that involved tracking a floating particle to estimate the flow velocity at the surface.

A 1 cm^2 tracer particle of expanded polystyrene was added to the flow, and its movement was recorded at 60 frames per second between two cross-sections marked by two laser sheets separated by a specific distance. The surface velocity was calculated as the average of three measurements obtained by tracking the particle between the cross-sections. The accuracy of the velocity measurements was ± 0.2%.

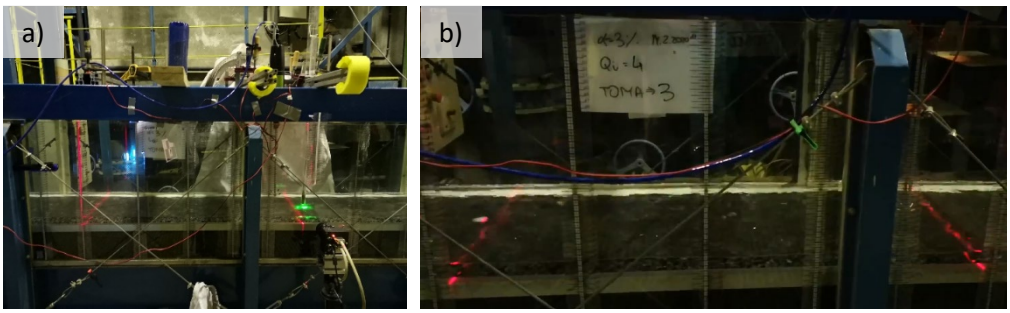

Figure 2.12. (a) Velocity measurement: superficial, ADV and PVT, and (b) superficial velocity measurement.

2.3. Characteristics of the Materials

The experiments were conducted using the same bed material, a basaltic gravel (Figure 2.13-a). This section provides an overview of the sediment characteristics and the methodology followed to obtain them.

2. 3. 1. Void ratio

The void ratio (e) and porosity (ϕ) of the basaltic gravel were determined through immersion and weighing techniques (Figure 2.13). The void volume (V_V) was calculated as the difference between the total volume (V_T) and the solid volume (V_S). The total volume was obtained by directly filling the container with water (Figure 2.13-b), while the solid volume was determined using equation (2.2).

$$V_S = \frac{W_S}{\rho_w S_s} \tag{2.2}$$

Where W_S is the solid weight of the material, S_s its specific gravity, and ρ_W the water density (assumed to be 1000 kg/m³ between 10 — 20 degrees Celsius). The solid weight was obtained

by weighting the same container filled with the material instead of water. The value of S_s for the basaltic gravel was found to be 2.961 Tn/m³, based on a previous experiment conducted by Bateman et al. (2010) using the same material.

By applying the equation (2.3) and equation (2.4), the basaltic gravel was found to have a void ratio (e) of 0.698 and a porosity (ϕ) of 0.41.

$$e = \frac{V_V}{V_S} \tag{2.3}$$

$$\phi = \frac{V_V}{V_T} \tag{2.4}$$

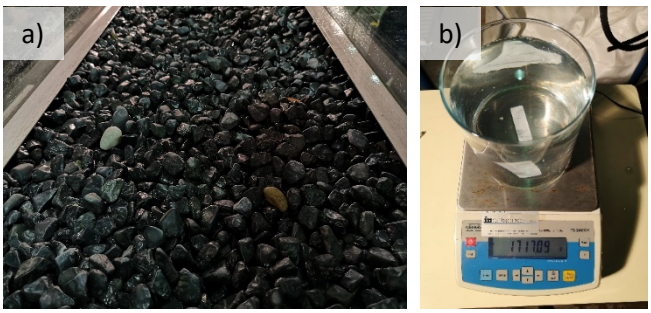

Figure 2.13. (a) Basaltic gravel placed in the flume, and (b) weighing scale with the container filled with water.

2. 3. 2. Sieve analysis

To determine the particle size of the material used in the experiments, a combined sieve analysis was conducted. The material passed through a series of sieves with gradually decreasing mesh sizes of 25, 21, 19, 16, and 13 mm. Each sieve was attached to the structure depicted in Figure 2.14. The material used in the experiments was the portion that passed through the 16 mm sieve and was retained at the 13 mm sieve.

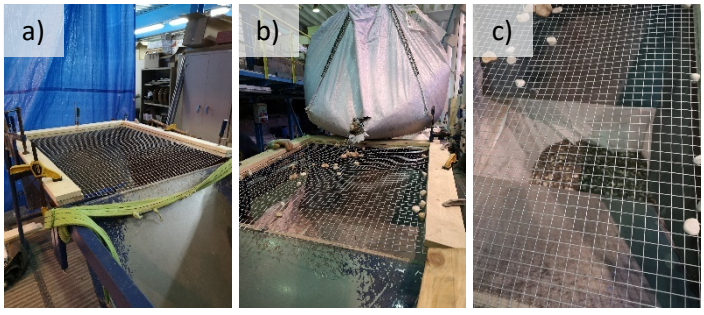

Figure 2.14. Experimental device used to sieve the material.

Additionally, using this combined sieve analysis, the material used in the experiments was determined to be uniformly graded, with a narrow particle size distribution range between 13–16 mm. This ensures that the particles meet the exact size specifications for the experiment

and that armouring processes will not occur. The particle size is assumed to be D_{50} = 14.5 mm with a standard deviation of 1.5 mm.

2.4. Experimental Procedure

This section provides detailed information on the procedures followed in the laboratory to ensure the validity and reliability of the results obtained, as the experimental procedure is a critical component of the experimental setup chapter because it outlines the specific steps taken to conduct the experiments accurately. This section includes information about the specific steps taken to prepare the experimental setup, and the procedure used to collect and analyze data.

To ensure reliable results, all experiments were conducted using the same bed material with a $D_{50} = 14.5 \pm 1.5$ mm and mean density of 2.961 Tn/m^3, and measurements were taken at the same location, which was 5.65 m from the inlet. This approach minimizes the influence of external factors and allows for the experiments to be conducted under the same conditions, reducing the effects of external factors and ensuring the validity of the results.

2. 4. 1. Description of the experiments

The objective of the experiments is to examine the velocity profile distribution in steep slope channels with low relative submergence and under non-motion flow conditions. An experiment is defined as a series of profiles measured on the same day with identical bed slope and sediment placement, but varying discharges (ranging chronologically from low to high). The profiles are identified by the notation $\{i, j\}$, where i denotes the experiment number and j is the profile number within the i experiment.

A total of 30 experiments were conducted, 155 profiles were measured in this study. The flume slopes varied between 2 and 10%, with Reynolds numbers ($\mathrm{Re} = 4R_h U/\nu$) ranging from $1.15 \cdot 10^4$ to $1.86 \cdot 10^5$, relative submergence varying between 0.7–3.7, superficial flow discharges from 1–29 l/s. All the experiments were under the threshold of motion of the bed material. Although a detailed summary of the characteristics of the experiments is presented in *Appendix B: Supplemental Figures and Tables*, Table 2.1 provides a concise overview of the main hydraulic characteristics of the experiments.

Table 2.1. Summary of the hydraulic and physical conditions of the experiments.

α (%)	Num	D_{50} (m)	Q_{sup} (l/s)		d (m)		R_h/D_{50} (-)		Re (-)		Fr (-)	
			min	max	min	max	min	max	min	max	min	max
2	24	0.0145	1.39	29.05	0.012	0.074	0.79	3.71	11521	186307	0.84	1.24
3	10	0.0145	5.50	19.51	0.022	0.048	1.36	2.69	43377	138502	1.30	1.52
4	20	0.0145	3.29	15.86	0.016	0.039	1.00	2.27	26796	116207	1.33	1.71
6	18	0.0145	2.33	10.41	0.014	0.029	0.88	1.75	19100	79784	1.14	2.01
7	13	0.0145	1.96	6.22	0.012	0.024	0.76	1.47	16277	48725	1.20	1.71
8	15	0.0145	2.90	5.37	0.013	0.021	0.83	1.29	23632	43175	1.23	2.13
10	19	0.0145	1.66	4.22	0.011	0.016	0.71	1.02	13778	34245	1.07	2.25

Kamphuis (1974) proposed a Moody-type diagram to describe the friction factor for oscillatory flows, where the friction factor is defined as $f_f = 8\left(u_*/U\right)^2$, with u_* the shear velocity and U the depth-averaged velocity. The experiments are clearly on the fully rough regime regardless the flume slope or the relative roughness (Figure 2.15).

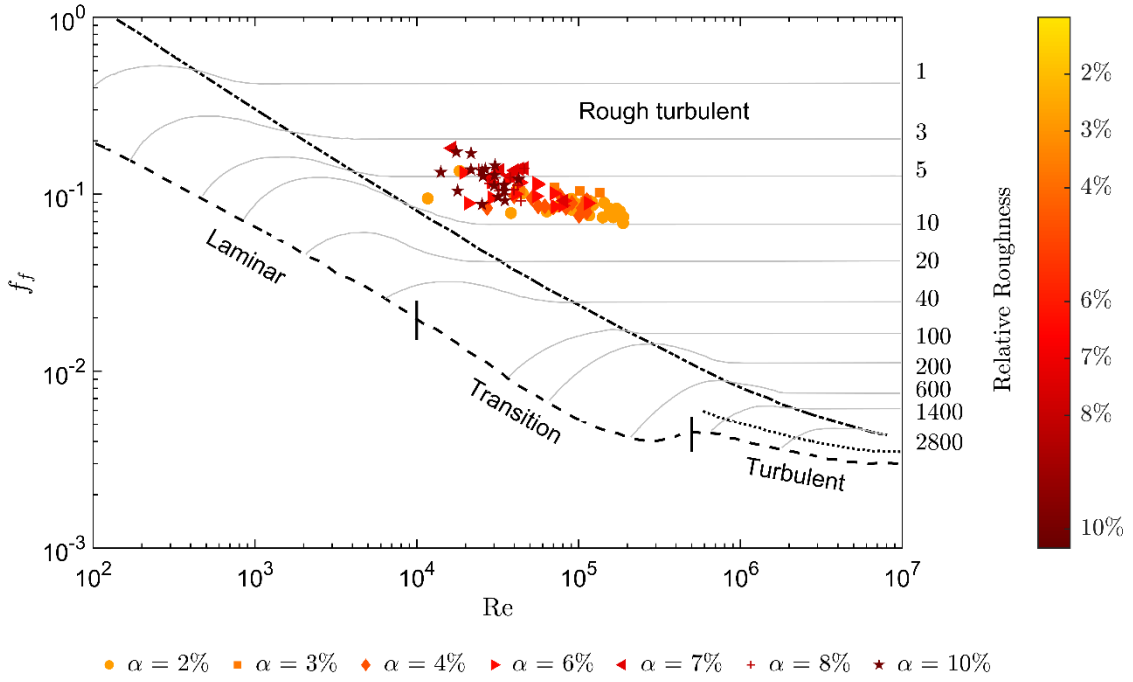

Figure 2.15. Friction factor defined within the Kamphuis (1974) diagram.

Although the non-motion conditions were verified visually in the lab, as no bed particle was moving while conducting the experiments, the dimensionless Shields stress ($\tau^* = \tau_o / g\left(\rho_s - \rho_w\right)D_{50}$) has shown to be below the well-known 0.056 value (Figure 2.16).

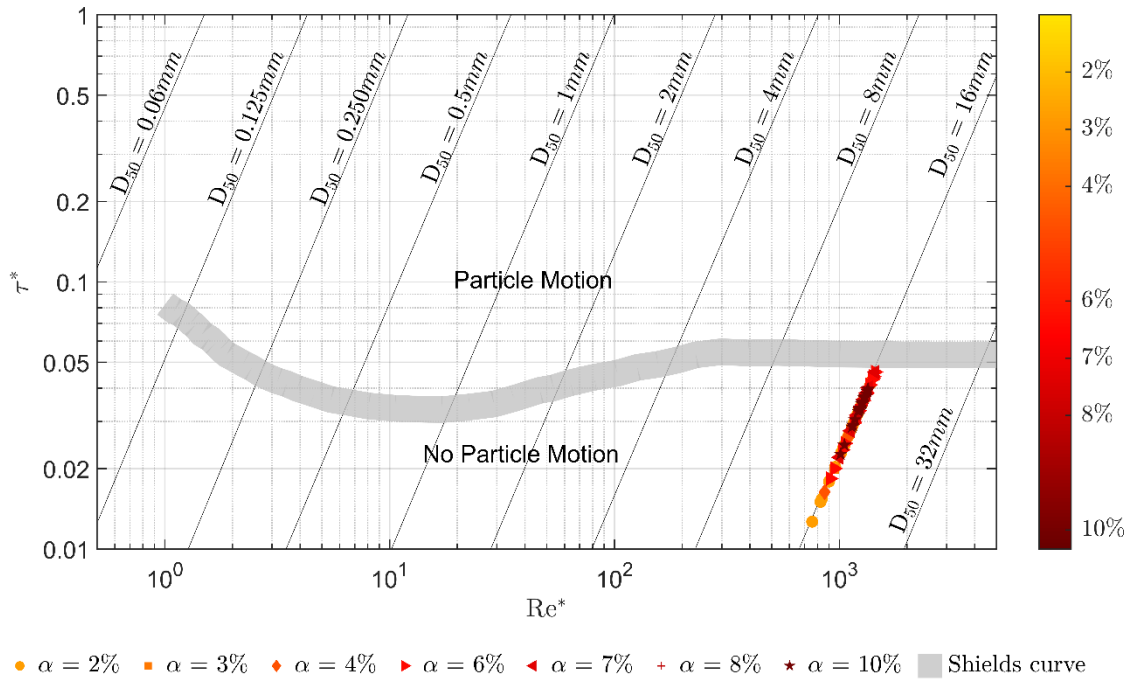

Figure 2.16. Representation of the experiments on the Shields graph.

2. 4. 2. Experimental execution methodology

In this study, a well-defined experimental execution methodology was followed to investigate the velocity profile distribution under non-motion and low relative submergence flow conditions for steep slopes.

The experimental procedure involved several steps. Generally speaking, firstly, the bed material was placed in the flume, and then the flume slope was adjusted to the desired angle. Once the slope was set, the experiments began by gradually increasing the discharge until the desired discharge was reached. Measurements were taken once the flow conditions were uniform (approximately 10 min after the discharge increased). The process was repeated for each discharge until the maximum discharge was reached. This last discharge was defined experimentally as the higher discharge at which the bed material was still motionless. The experiment was terminated when the motion-discharge was reached. Then, a new experiment was started, and the procedure was repeated from the beginning, including placing the bed material in the flume.

The subsequent subsections provide a comprehensive and chronological description of each of these steps.

2.4.2.a. *Placement of the bed material*

To start a new experiment, the initial step involved preparing the bed by covering the flume with a sediment layer that was approximately 15.5 cm deep (Figure 2.17). Two "L" aluminum plates of 3 cm wide and 2.5 m long (Figure 2.13-a) were introduced at a certain height from the bottom of the flume, levelled as a trail for the correct levelling of the bed's material surface. To avoid the flattening of the bed surface, these "L" plates supported the rake used to comb the bed surface. They ensured that the top crests of the bed particles did not surpass the plates (Figure 2.175-c), and that the bed material layer depth was kept constant along the channel, so the bottom of the flume and the surface layer of the bed were parallel. It is important to highlight that the flume slope was not achieved using the bed material but with the tilting system of the flume. Using the "L" plates, both the level of the bed and the top of the particles are correctly defined. Moreover, it ensures that the relative slope between the flume and the bed is negligible.

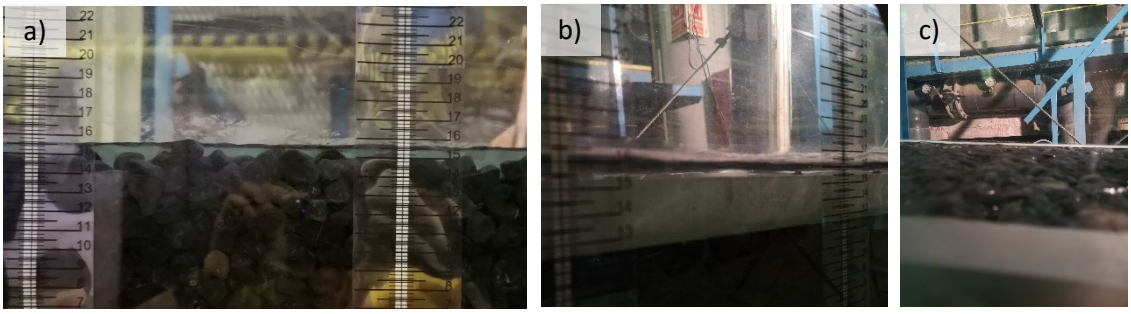

Figure 2.17. (a) Bed irregularity observed without the aluminum plates, (b) aluminum plates, and (c) bed regularity with the plates.

2.4.2.b. *Flume slope positioning*

After the bed material was properly placed, the flume slope was gradually elevated using the electric motor until the desired slope for the experiment was achieved. The flume slope was obtained through the calibrated curve of the measuring tape on the bridge crane pillar (Figure 2.3-c). Details of its calibration can be found in *Appendix A: Experimental Setup Calibration Procedures*. The slopes examined in this study include 2%, 3%, 4%, 6%, 7%, 8%, and 10%.

2.4.2.c. *Non-motion experiments*

Once the sediment and slope were arranged, the experiment's flow discharge was initiated gradually to avoid the sudden motion of particles caused by the wavefront. Specifically, a small discharge was initially introduced and gradually increased until the desired discharge for the experiment was reached.

The flow was increased every minute by approximately 0.5 l/s to avoid any issues related to wavefronts. The water level was normalized using a vertical-moving gate situated at the downstream end of the channel (Figure 2.1).

Data collection began ten minutes after the depth was normalized. The flow discharge was measured using two YAKOHAWA magnetic flowmeters, and water heights were assessed using transparent gauge levels spaced at 20 cm intervals along the flume. Ink tracers were used to measure the infiltrated flow, and an ADV reinforced by PTV registered the velocity profiles. Additionally, the surface velocity was calculated by tracking a floating particle between two cross-sections marked by red laser sheets. *Appendix B: Supplemental Figures and Tables* provides a comprehensive summary of the experimental measurements conducted in each experiment and profile.

After completing all the measurements, the discharge was increased following the same procedure to move to the next discharge. This process was repeated until the experiment's final discharge was achieved.

Chapter 3: Velocity Measurements

This chapter establishes the definition, calibration and validation of the PTV technique employed in this thesis to study flows over steep creeks under low relative submergence conditions. Furthermore, the suitability of PTV as a measurement technique for rough macro flows where the use of ADV is not feasible is demonstrated.

3.1. Introduction

The acquisition of experimental data in fluid mechanics is a challenge faced by both scientists and engineers. Therefore, it is necessary to continue to develop precise and pragmatic techniques. A fluid has several properties that can be measured: temperature, pressure, viscosity and velocity. This chapter focuses on the practical measurement of velocity profiles in a shallow flow in a laboratory flume.

There are different techniques for measuring the velocity of a fluid; *indirect methods* can achieve velocity measurement by using the relationship between flow velocity and other flow properties or, conversely, by using the *direct measurement* of flow particle velocity (Tavoularis 2005). Within this second group are *i*) *frequency shift* methods, based on the Doppler effect, and *ii*) *marker tracking* methods, which follow the movement of tracers incorporated into the flow.

The Doppler effect consists of a change within the wave frequency relative to an observer moving towards the wave source. Therefore, methods based on this effect measure the displacement of the frequency of the waves scattered by the particles of the moving flow. The best-known instruments for this category of measurement are the Laser Doppler Velocimeter (LDV) and the ADV, which use light and sound waves, respectively (Tavoularis 2005). On the other hand, marker-tracking methods are based on the acquisition of the tracer position as a function of the timing of tracer particles that faithfully follow the movement of the flow without disturbing the flow or its properties (Raffel et al. 2018). In general, these techniques are quite complex, and the costs of the necessary equipment are high (Mujal-Colilles 2013).

Optical measurement methods fall within marker-tracking techniques. These records, through a high-quality lens, the light scattered by the tracking particles added to the flow (Figure 3.1). The flow velocity is assumed to be the same as the velocity of the particles added to the flow. Depending on the particle density in the recorded image, three different optical measurement methodologies are distinguished (Westerweel 1993): Particle Tracking Velocimetry (PTV), Particle Image Velocimetry (PIV), and Laser Speckle Velocimetry (LSV). PTV is the method with the lowest source and image density and LSV that with the highest (Westerweel 1993). This research focuses on defining, calibrating and applying the PTV methodology to measure velocities in flows with steep slopes and very low relative submergences. On the basis of the work carried out by Fernández (2019), it is assumed that the ADV methodology is calibrated for macro-rough flows, and it is therefore used as the starting methodology in the present investigation.

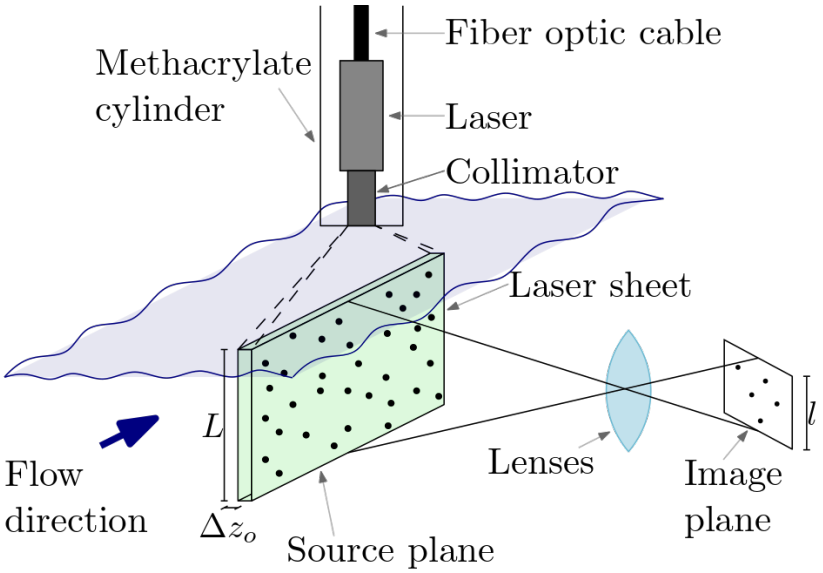

Figure 3.1. Schematic representation of the operation of the optical measurement.

3. 1. 1. Acoustic Doppler Velocimeter (ADV)

As already mentioned, the ADV is one instrument among a group that measures frequency displacement within the direct measurement of flow velocity. It has been widely used in both the field and laboratory for more than 50 years.

ADV measures flow velocity by transmitting a pair of short pulses of a specific frequency into a control volume. This signal travels through the water and is reflected by suspended particles within this control volume (Figure 3.2). The receivers (or beams) of the ADV detect this echo again. The data processing module measures the phase change between the signal emitted and the one received by each receiver. The ADV can have from two to four beams, depending on the number of velocity components to be measured. ADVs are therefore able to accurately measure the mean values for flow velocity and direction. However, the ADV uses a control volume within the fluid where the signal is reflected by the receptors, so the result is only representative of the volume of fluid studied.

The ADV has been one of the most widely used velocity measurement instruments. However, its ability to accurately resolve flow turbulence is still uncertain (Barkdoll 2002). In addition, it has shown some limitations when taking measurements under certain flow conditions, such as high-energy turbulent flows (Fernández 2019) and flows with small depths. In this sense, one of the main limitations of the ADV is the minimum depth necessary for data collection, since the transmitters must be completely submerged for the Doppler effect to operate correctly. When measuring at distances less than 1 cm from the bed, potential measurement errors may appear (Finelli et al. 1999). As the bed surface roughness increases, or in aerated flows such as highly turbulent flows, these measurement errors become increasingly significant (Fernández 2019;

Martin et al. 2002). The instrument's technical specifications indicate that the correct operation is from 1 cm in depth but will depend on the hardness of the bed (NORTEK 2018).

Figure 3.2. Details of a three-beam downward-looking ADV (Source: www.sontek.com).

3. 1. 2. Optical measurements – Particle Tracking Velocimetry (PTV)

As noted above, *optical measurement* methods correspond to *tracing techniques* in velocimetry measurement. This section will focus only on techniques that use particle displacement methods. Optical measurements, such as PIV or PTV, are based on the direct determination of the two fundamental dimensions of velocity: length and time (Raffel et al. 2018). Both techniques seek to locate the same tracer particle in two consecutive frames and thus obtain the displacement of the particle between the pairs of frames. The velocity of the flow is assumed to be the same as the particle velocities. Hence, between two instants, the velocity of the particle is defined by:

$$\vec{u} = \frac{\Delta \vec{x}}{\Delta t} \tag{3.1}$$

These techniques use the imaging of small particles, as represented in Figure 3.1. Small tracer particles are added to the flow, and the plane of interest within the flow is illuminated using a laser sheet. The light scattered by the tracer particles is then recorded via a high-quality lens.

The light sheet is created by laser light; thus, optics to transform the initial circular section into a planar sheet are needed. Although using these optics, the light sheet has a finite thickness (Δz_0). It is optimal to have the focal length of the spherical lens located at the centre of the source plane, since it concentrates the higher intensity of light, thus creating less noise on the PIV results (Mujal-Colilles 2013). The camera optics will define the resolution of pixels per millimetre through the magnification factor M.

$$M = \frac{image}{real} = \frac{L}{l} \tag{3.2}$$

Where L is the image size (size of the image on the sensor) and l is the actual size, as shown in Figure 3.1. Magnification is a lens property (subject to distance) and does not change regardless of the lens. In order to ensure that the highest number of particles within the light sheet are in focus, the depth of field (δ_z), as defined by Adrian (1991) in equation (3.3), has to be higher than the thickness of the source plane (Mujal-Colilles 2013), as defined in equation (3.4).

$$\delta_z = 4\left(1 + M^{-1}\right)^2 f_{\#}^2 \lambda \tag{3.3}$$

$$\delta_z > \Delta z_o \tag{3.4}$$

Where $f_{\#}$ is the f-number of the lens, defined as the ratio between the focal length (f) and the aperture diameter (D_a), and λ is the wavelength of the laser light.

Particles in the source space are not represented as a single point in the image space; their representation depends on geometrical factors and light-scattering behaviour. Thus, the error in velocity measurements depends on the particle image diameter (d_τ) in the image space. Optimizing this particle image diameter (d_τ) and the uncertainty in locating the image centroid is essential to minimize this error (Raffel et al. 2018).

From the magnification factor, the diffraction point source diameter in the image space (d_{diff}) can be obtained as

$$d_{diff} = 2.44\left(1 + M\right) f_{\#} \lambda \tag{3.5}$$

Thus, particle image diameter should follow:

$$d_\tau = \sqrt{\left(M d_p\right)^2 + \left(d_{diff}\right)^2} \tag{3.6}$$

Where d_p is the particle diameter. Thus, the effective diameter of a particle in the image space (d_τ) has to be between 2 and 3 px (Mujal-Colilles 2013).

Two dimensionless numbers describe the information content of the recorded image: the source density (N_s) and the image density (N_I) (Westerweel 1993). The source density is the density of particles inside an interrogation area in the source plane, whereas the image density corresponds to particles inside an interrogation area in the image. The first, source density, is given by Adrian (1984) and defined as the mean number of particles in a cylindrical volume formed by the intersection of the illuminating light sheet (with width Δz_o) with a circle whose diameter is that of the particle image projected back into the fluid, thus d_τ / M .

$$N_s = C \Delta z_o \frac{\pi d_\tau^2}{4 M^2} \tag{3.7}$$

That is why a small N_s implies a low probability of more than one particle inside this cylinder; hence, this implies solitary images. On the other hand, the image interrogation spot is defined as the intersection of the light sheet with a circle whose diameter (d_i/M) is equal to the diameter of an interrogation spot projected back into the fluid (Adrian 1991). If no interrogation spot is used, the diameter can be replaced by the maximum two-dimensional displacement of the particles; thus, the modulus of both displacements ($|\Delta x|$). The image density is given by Adrian and Westerweel (2011) as equation (3.8).

$$N_I = C\Delta z_o \frac{\pi d_i^2}{4M^2} \tag{3.8}$$

If small values of N_i are obtained, the probability of finding more than one particle in an interrogation cell is small (Figure 3.3-a). Depending on the values of N_S and N_I, according to Westerweel (1993), we are able to distinguish between three different modes of the recorded image: Particle Tracking Velocimetry (PTV), Particle Image Velocimetry (PIV) and Laser Speckle Velocimetry (LSV).

PTV is the method with the lowest source and image density N_I <<1. Therefore, the particles are very separate from each other, and for this reason, it is easy to identify the image of the same particle in both frames and thus obtain the local flow velocity (Westerweel 1993). On the other hand, since the image density is low, the velocity cannot be determined at any arbitrary position, but only at the positions where a tracer particle is present. Therefore, the PTV determines the velocity field in a Lagrangian reference frame (Brevis et al. 2011).

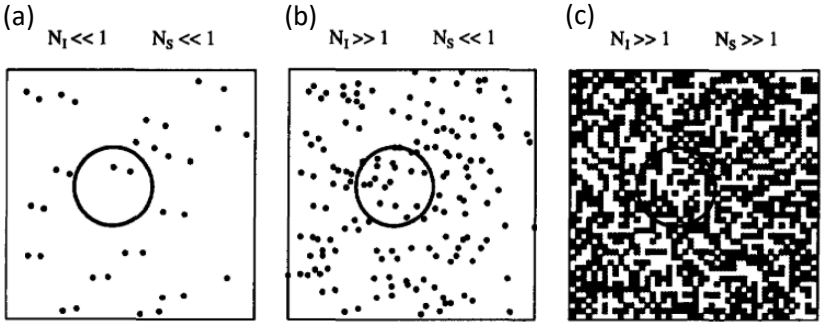

Figure 3.3. Image types in (a) Particle Tracking Velocimetry (PTV), (b) Particle Image Velocimetry (PIV), and (c) Laser Speckle Velocimetry (LSV). The circle indicates the interrogation area (Westerweel 1993).

In contrast, Particle Image Velocimetry (PIV) is a method that gives a greater density of information on the flow field by increasing the density of tracer particles (N_S <<1 and N_I >>1), which determines the velocity field within an Eulerian frame of reference (Brevis et al. 2011). Individual particle images are still distinguishable (Figure 3.3-b), but it is no longer possible to

identify individual particle pairs unambiguously. Thus, a statistical method is needed to determine the most probable displacement. Nevertheless, in this case, the interrogation area always contains a sufficient number of particle images to determine the (local average) flow velocity in any position (Westerweel 1993).

Usually, tracing methods are well suited to flow field measurements with accuracy at any magnification (Adrian and Westerweel 2011; Raffel et al. 2018). Optical measurements of flow velocity that use tracing particles are non-intrusive methods, in contrast to other techniques that require the use of pressure tubs or hot wires and may produce disturbances in the flow. However, because tracer particles are employed to measure flow velocity, every experiment must be checked to ensure that particles faithfully follow the motion of the fluid. At low seeding concentrations (PTV), the seeding concentration may be sufficient for reliable particle image matching between subsequent frames (Raffel et al. 2018). However, at high seeding concentrations (PIV), two sources of error can occur due to the increasing density of the particles. First, the likelihood of identifying non-corresponding particle images increases. Second, overlapping particle images may increase random error (Raffel et al. 2018). These problems can be solved by using sophisticated particle-tracking approaches.

PTV is well suited to analysing flows with a strong velocity gradient, such as turbulent boundary layers (Raffel et al. 2018): since the velocity vector pertains to a single particle image, the velocity information is obtained with high spatial localization within the limits of the traceability of particles (Ohmi and Li 2000). Unlike PIV, where the target is the mean velocity of a group of particles, the velocity information in PTV is smaller due to the interrogation window used by the approaches needed for particle tracking (Raffel et al. 2018).

In addition, PTV is an appropriate method for the measurement of near-wall flow, as the seeding concentration drops towards the wall due to the Saffman effect and because the PTV is less sensitive to errors in the case of an inhomogeneous seeding distribution (Raffel et al. 2018). PTV allows for complete 3D measurement using volumetric lighting and stereoscopic analysis (Ohmi and Li 2000).

On the other hand, an essential aspect of PTV analysis is that identifying the particle and the matching algorithm strongly influences the quality and quantity of the recovered spatiotemporal information (Brevis et al. 2011). When the particle displacements are of the same order as the particle image size, errors related to the identification of the centroid of those particles can become particularly significant (Brevis et al. 2011; Raffel et al. 2018). This research will focus on the PTV technique, since it is one of the techniques used in many experiments.

The methodology followed for PTV consists of *i*) detection of particle images from the recordings (usually done by eliminating background intensity and analyzing the images, searching for a local maximum), *ii*) calculation of the particle position vector of each pair of frames and *iii*) pairing particle images corresponding to the same physical tracer (Raffel et al. 2018).

3.1.2.a. Image recording

a.1). Particles

Since the velocity of the tracers is assumed to equal the flow velocity, the optical properties of the particles used as tracers play an essential role in selecting suitable tracers (Raffel et al. 2018). Ideally, the tracer particles should follow the fluid's movement strictly; they should neither disturb the flow nor interact with it. In addition to considering the dynamic response of the particles, their light-scattering characteristics must also be taken into account. This is why the flow must be seeded with particles that are small enough to follow the motion of the fluid, yet large enough to scatter sufficient light to form bright images (Adrian and Westerweel 2011).

a.2). Light sources

Optical measurements require an intense light source (Figure 3.1), with lasers being the most widely used (Adrian and Westerweel 2011) due to their ability to emit monochromatic light with high energy density and collimate into a thin sheet of light without chromatic aberration (Raffel et al. 2018).

a.3). Recording strategies

Once the image is formed on the image plane, the images are recorded by briefly exposing a video chip or photographic film. However, the most widely used electronic image sensors are solid-state, such as Charge-Coupled Devices (CCD) and CMOS arrays. In both cases, electronic imaging chips consist of rectangular or square arrays of sensors that convert light energy in the image plane into electrical signals (Adrian and Westerweel 2011). Each sensor and its associated storage or electronics is called a pixel.

Recording modes can be classified into two main categories: *i)* methods that record two or more overlapping exposures in a single frame and *ii)* methods that record each exposure in a single frame (Figure 3.4). These are commonly known as single frame—multiple exposures and multiple frames—single exposure techniques. Today, thanks to affordable pulsed laser and electronic camera technologies, multi-frame–single exposure recording is the preferred method for recording optical measurements, such as PTV and PIV. Today's commercially available high-

speed CMOS cameras exceed thousands of frames per second at full megapixel resolution at readout speeds of up to 25 Gigapixels per second (Raffel et al. 2018).

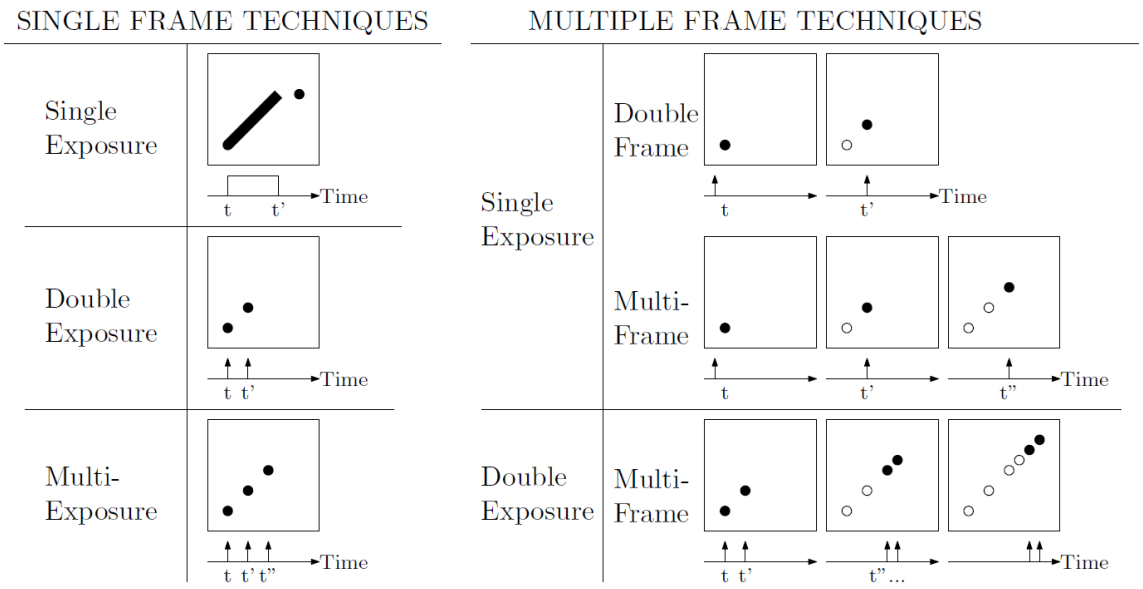

Figure 3.4. Single frame and multiple frame technique schemes following Raffel et al. (2018).

Legend markers: **● particle position in the current frame and ○ particle position in previous frames.**

3.1.2.b. Particle detection

Once the images have been recorded, the next step is to locate the centroid of each particle for all frames and so reconstruct the trajectory of the particle, frame by frame, and finally, get the velocity estimate. However, due to noise, light reflections and other interferences, the detection of particles requires pre-processing of the images. This step is usually done by removing the background intensity and analysing the images for a local intensity maximum.

The precision of the displacement measurement depends on the precision of the definition of the position of the images of the detected particles, since the displacement of these is obtained from the difference between two of their locations. Consequently, any systematic error that affects both position measurements will cancel both out in the same way. However, the systematic errors are small relative to the spacing between particle images. Therefore, the primary sources of error in the PTV technique are random events (noise) and image pixelization (Adrian and Westerweel 2011).

Particle detection is based on an appearance method that detects objects using their luminance so that all pixels whose luminance is greater than a specific threshold value are considered to belong to a potential particle (Tauro et al. 2019). The problem is finding and defining the optimal threshold value. The standard method used for a long time to detect individual particles has

been the simple single-threshold methodology. However, this method is only applicable if the display image comprises a small number of particles of the same brightness and size. Therefore, when these conditions are not met, this threshold leads to severe data loss. To avoid this, some authors propose using multiple thresholds (Ohmi and Li 2000; Takehara and Etoh 1999), where the main concept is to scan the image piece-by-piece with variable and locally better suited threshold levels.

Typically, in multi-threshold methods, the centre of the particle image is denoted as the local maximum of the discrete distribution approximated by a continuous Gaussian fit function (Raffel et al. 2018). Since the brightness pattern of a particle image has a peak near the centre of the image, the brightness decreases concentrically with increasing distance from the peak (Takehara and Etoh 1999). Takehara and Etoh (1999) proposed a particle mask correlation method following a Gaussian peak-fitting scheme. One of the main advantages of this method is that it captures only particle-like objects, regardless of size or average brightness. This makes the separation of two or more particle images automatic and exact.

3.1.2.c. Particle tracking

Once particles have been detected in all frames, the next step is to identify a pair of particle images that correspond to the same particle in two consecutive frames. The centroids of these two images are used to calculate the displacement between the frames. This process is commonly known as *interrogation*. Different interrogation methods and vector field characteristics depend on image density (PTV or PIV) and image recording (single-frame or multi-frame). This section discusses the most commonly used interrogation methods in low image density (PTV) with multi-frame single-exposure image recording.

Generally, particle tracking proceeds by segmenting the image plane into a set of isolated images corresponding to bright spots assumed to be particle images (Adrian and Westerweel 2011). Also, if a superposition of two or more particle images appears, they are either discarded, or an effort is made to separate the images and find their centroids. The simplest method by which to relate particle images between frames is the nearest particle algorithm (Raffel et al. 2018). However, this algorithm cannot correctly assign which particle image of a second frame corresponds to a particle image of the first frame when the particle images are very close together (their displacement is less than the separation between the particle images). For this reason, in cases where the particles are very close together, the algorithm matches each particle image in the first frame with its nearest neighbour particle in the next frame. The main problem with this algorithm is that each particle image must match another particle image in the next

frame; thus, if a particle image does not have a matching image available, the algorithm will force it to relate incorrectly to another.

More elaborate approaches can be found in the literature that allow for increasing the density of particle images. These methods include relaxation methods (Ohmi and Li 2000), spring force models (Okamoto and Hassan 1995), models based on cross-correlations (Brevis et al. 2011; Hassan et al. 1992; Uemura et al. 1989) and hybrid models (Brevis et al. 2011), among others.

c.1). Cross-correlation based methods (CC)

These methods are based on a space-temporal cross-correlation of the images of particles lying within small regions called *interrogation spots*. The entire field of view of the flow is divided into a grid of interrogation windows (Adrian and Westerweel 2011). The image intensity of each interrogation window centred on the target particle position is arranged on a matrix to obtain the highest cross-correlation coefficient after comparing the intensity matrix of the first frame with a set of sub-matrices in the second frame. This set of second matrices is obtained after extracting the intensities of the second frame located inside the interrogation windows centred on each of the candidate positions (Adrian and Westerweel 2011).

The algorithm generally uses binary intensity matrices and is known as the binary cross-correlation (BCC) method (Brevis et al. 2011; Hassan et al. 1992; Uemura et al. 1989). The method calculates the correlation coefficient by comparing the image patterns of the first frame with a possible candidate pattern in the second frame. Therefore, BCC tracks individual particles based on the most significant similarity of particle distribution patterns. A single or multiple intensity threshold level can be used (Ohmi and Li 2000). BCC is characterized by a low computation time and an acceptable speed data retrieval rate. However, the additional complexity of the algorithm and the difficulty of applying it to strongly rotating and shearing flows are disadvantages.

c.2). Relaxation methods (RM)

Relaxation methods (RM) minimize a local or global cost function (Raffel et al. 2018). The separation between two-particle images gives the cost of a match. In this way, the search begins with random matches, and new matches are made. The search algorithm is expressed as a linear array operation. This algorithm is similar to the nearest neighbour search, but all matches are done simultaneously, so there is a unique solution.

Ohmi and Li (2000) present a modified RM in which a quasi-rigid search radius is used in the second frame to identify possible matching particles. This is carried out for all particles detected

in the first frame. The particle matching probability between the first and second frames is defined for each possible pair of particles for each particle in the first frame. In addition, the probability of non-coincidence is also considered (Ohmi and Li 2000). Therefore, since it is an iterative process, the probability of correctly matching the particles between the first and second frames gradually increases towards 1, while the other probabilities tend towards 0. The success of the RM algorithm depends on neighbouring particles having a similar motion, so they can fail in the case of solitary particles (Brevis et al. 2011).

c.3). Hybrid methods

A recent goal of PTV systems has been to define suitable algorithms for higher-density particle imaging. New models combine some previously mentioned algorithms to solve the temporal coincidence problem and provide good performance with high particle densities (Brevis et al. 2011).

The method proposed by Brevis et al. (2011) consists of a hybrid method that integrates the CC method with the RM (ICCRM). Initially, a CC step is used to determine a preliminary solution in the velocity field; the matching particles accepted in this step are assumed to be valid and do not participate in the next step, which consists of an RM analysis. When a particle reaches the convergence criteria in the RM iteration method, it is assumed to be valid and does not enter the next RM iteration step. This ensures a continuous decrease in the number of particles analyzed by RM. As Brevis et al. (2011) proposed, using a two-step hybrid system can improve the algorithm's performance compared to implementing each one alone. In this integrated method, the CC and RM methods complement each other since, under circumstances in which one works perfectly, the other has limitations, and vice versa: CC can match particles with little neighbour information, whereas it is precisely in this situation that RM has problems.

3.2. Materials and Methods

3. 2. 1. Laboratory definition and experimental procedures

The experiments were conducted in the hydraulic flume of the Morphodynamics Laboratory I of the GITS group described in *Chapter 2*. This section focuses on two different velocity measurement techniques: ADV and PTV.

3.2.1.a. Acoustic Doppler Velocimeter (ADV)

Following the thorough study of ADV configurations carried out by Fernández (2019) in order to perform the calculations correctly, the device requires, in general, five different input variables

before starting to use it. These input variables are, *i*) the temperature of the water, *ii*) the salinity of the fluid, *iii*) the control volume size, *iv*) the nominal velocity range and *v*) the frequency of data collection. Among these configuration parameters, the last three values are more subjective and depend on the user's criteria.

Transmit length is the length of the acoustic pulses transmitted by the instrument. The sampling volume size was optimized for a given transmit length by the manufacturer to give the best performance. Theoretically, a shorter transmit length is better because it has a higher signal bandwidth (Fernández 2019). However, the received echoes are low and hence increase measurement error. For this reason, the control volume at the experiments was established at a height of 7 mm and located 5 cm from the transmitter (Figure 3.5).

The user can set the nominal velocity range from 3–250 cm/s. Setting the velocity range to an appropriate value for the measured flow is an essential instrument parameter for good data quality (NORTEK 2018). Too large a velocity range will result in noisy data because the detected phase shift will be smaller than the ambiguity velocity. On the contrary, a range that is too low will result in the decorrelation of the return signals or phase wrapping. The nominal velocity range was set at 1.00 m/s.

The frequency of data collection defines the amount of data acquired per second. The sample rate introduced as an input represents the absolute upper limit of the resolvable waves. The upper limit is half the sample rate, also known as the Nyquist limit. The user can set a maximum frequency of 200 Hz. This value corresponds to the maximum data storage capacity of the sensor. If the sample rate is less than 200 Hz, the device averages the data. According to Lohrmann (1994), Doppler noise appears in the signal at around 10 Hz. Thus, considering the Nyquist criteria, a sample rate over 20 Hz may have significant Doppler noise. Fernández (2019) analysed a range of sampling rates, and concluded that 25 Hz was the correct frequency for data collection. Thus, the velocity data were sampled at a rate of 25 Hz.

The ADV consists of a 3D Sontek 10 MHz ADV side-looking physical arrangement, with a position accuracy of ± 0.01 mm, configured at a nominal range velocity of ± 1.00 m/s, with a transmission length of 1.8 mm, a sampling rate of 25 Hz, and a ± 1.00 mm/s of measurement accuracy (Figure 2.8-a, Figure 2.10 and Figure 3.5).

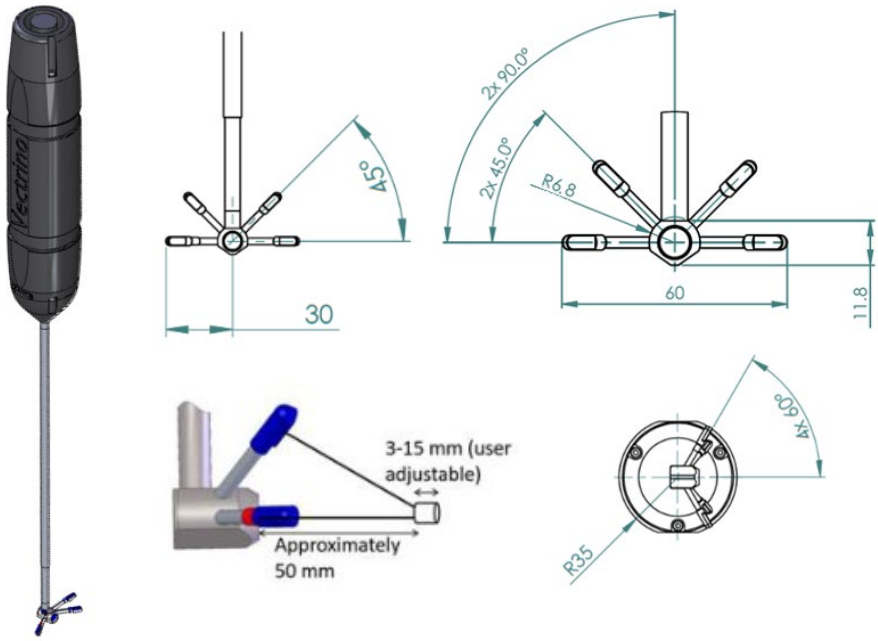

Figure 3.5. Details of side-looking ADV with its dimensions and volume control definition (NORTEK 2018)

The ADV was introduced through the water surface of the flow until it reached the target zone of measurement. When the water depth (d) was lower than 2 cm, velocities were still measured, although not all legs of the ADV were introduced into the water (Figure 2.10-b). Because all legs of the ADV were not introduced into the water, it was only possible to measure streamwise velocity (u). Although the manufacturer stated that the side-looking ADV could be used as a 2D velocimeter in shallow waters (NORTEK 2018), calibrations were made to verify that the streamwise velocity direction was not affected if the upper legs of the ADV were not introduced into the water.

The stability of the data collected by ADV was evaluated to ensure that sufficient data were recorded for each sampled point of the velocity profile, following the procedure proposed by Fernández (2019), since it is known that measurement errors occur with highly turbulent flows and high bed roughness (Fernández 2019; Martin et al. 2002). This procedure creates a moving average for each statistical parameter until the calculated values do not change. Accordingly, the velocity data series was sampled at a frequency of 25 Hz for a minimum of 4 min (240 s), resulting in 6000 velocity measurements for each measured point of each profile tested. In this investigation, the statistical parameter that controlled the sampling time was defined as the average velocity ($\overline{u}$). Therefore, given a point in the velocity profile, $\overline{u}$ was calculated for each time step. The sampling time was defined as the time elapsed until $\overline{u}$ remained constant.

3.2.1.b. Particle Tracking Velocimetry (PTV)

The PTV system used consisted of the elements shown in Figure 3.1. These included: *i*) A high-speed CMOS (PV-MV13); *ii*) a monochrome camera (model Basler A504k) with an active pixel digital sensor of 1280 H x 1024 V pixels, a pixel size of 12 µm, and a pixel depth of 8 bits with a sensor image area of 15.36 mm wide, 12.29 mm high and 19.67 mm diagonal; *iii*) an AF Nikkon 50 mm f/1.4D lens with an extension tube of 20 mm (Neewer Auto Focus Macro Extension tube metal model); *iv*) a green (LD) with 532 nm wavelength pumped by a diode solid-state laser (DPSSL), model MGL-H-532, with a PSU-H-LED power supply, rated at a variable output between 4 and 2000 mW; *v*) a fibre optic cable that transmitted the laser to a *vi*) collimator (model TL100-A25-SMA from Monocrom, Figure 3.6-b), and since the collimator and the fibre optic cable were non-water-resistant, *vii*) a transparent methacrylate cylinder was used (Figure 3.1, Figure 2.11-b and Figure 3.6). Finally, tracking particles with a grain diameter of 0.2 mm and a relative density of 2.65 were used (Figure 2.11-a).

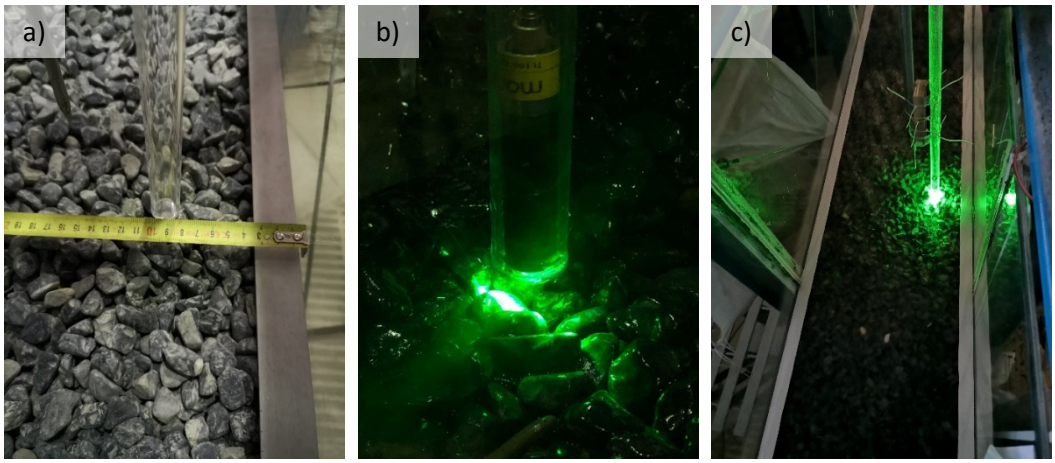

Figure 3.6. (a) PTV laser placement from the right glass flume wall, (b) collimator and laser switched on and introduced inside the flowing water, and (c) placement with the laser switched on.

Laser power was set at 2 Hz for all tests; XCAP^{TM} of EPIX© was used as the software for image recording. The recording frame was set at 2 ms with an exposure of 0.2 ms with at least 500 frames per second recorded for each profile. Variable focal length and magnification settings were used, depending on the lens and the camera's distance from the test area in each experiment.

A calibration photograph was taken for each test, photographing a graduated ruler (Figure 3.7).

Once the recording was finished, it was exported as a video using the XCAP^{TM} program. All the exported videos were transformed into a TIFF sequence (Figure 3.8-a) to be analysed later using PTVlab (Pantalano 2020), software that complements Matlab ©, which transformed the

recordings (Figure 3.8-a) into vectors of position and velocity (Figure 3.8-c) within the area of interest (AOI).

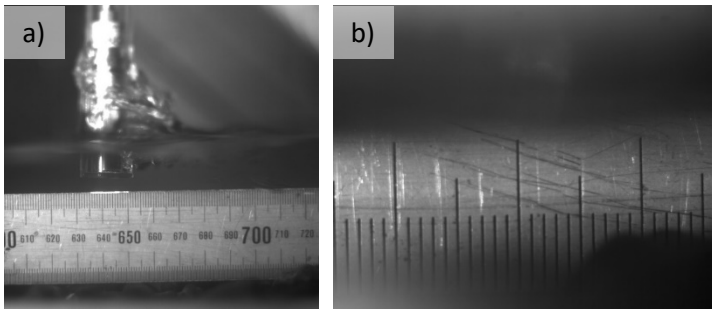

Figure 3.7. Calibration photographs under the water for (a) 2% and (b) 10% flume slopes.

To verify the correct operation of the proposed PTV methodology, velocity measurements were made with both techniques in two profiles simultaneously (2% and 3% slopes). It was not possible to carry out tests with steeper slopes due to the limitations of the ADV in relation to small depths. However, velocity profile measurements with slopes of 6%, 8% and 10% were conducted with the PTV technique.

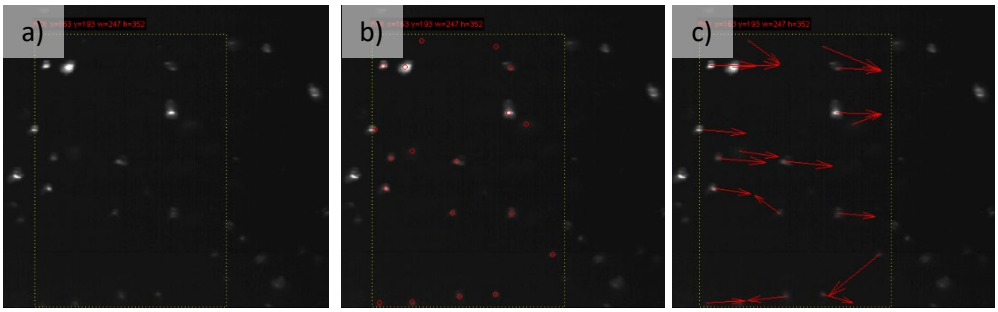

Figure 3.8. Screenshots of PTVlab software for (a) AOI definition, (b) particle detection, and (c) vector velocity for an 8% slope fume test.

3. 2. 2. Experimental data treatment

All data were obtained by experimentation; therefore, it was necessary to manage and cleanse the data. ADV data were obtained by averaging all ADV measurements for each point in which the instrument was located. No ADV data treatment (clean or spike suppression) was needed, since average values were considered and prolonged measurement periods were carried out in the lab.

In contrast, the PTV data was obtained through the PTVlab (Pantalano 2020), an add-on of Matlab © that transforms the recordings into position and velocity vectors. PTVlab software is based on three steps: particle detection, tracking algorithm and data calibration. Specifically, a Gaussian mask algorithm is used to detect the particles, a CC method is used to track the

particles (Brevis et al. 2011), and the vectors are calibrated using photography. The variables and settings specific to each step are defined below.

3.2.2.a. PTV: Particle detection

The Gaussian mask algorithm (Gaussian Mask) was used as the particle detection algorithm, and it followed the same procedure as explained previously and proposed by Takehara and Etoh (1999). The PTVlab software (Pantalano 2020) applies the Gaussian mask algorithm using a Gaussian kernel matrix, obtained from a representative radius of the particle, input as $r_{particle}$ with its position. In addition, a correlation threshold (C_t) is used to define the correlation filter between peaks (it is also used to filter intensity peaks that are close to each other). Finally, an intensity threshold (I_t) defines the minimum intensity when binarizing the image.

In this investigation, the correlation threshold was set at 0.5 for all experiments, but the representative radius and intensity threshold changed throughout the experiments. All the settings applied in this investigation are listed in Table 3.1. If no extension tube was used, $r_{particle}$ had a value of 3 px. However, if an extension tube was used, it was 10 or 15 px. The intensity threshold (I_t) depends on the contrast between the brightness of the particles and the darkness of the image background. Therefore, this entirely depended on the recording of each profile, with values falling within the range of 5–30 (Table 3.1). Eventually, the detected particles were selected in the manner exemplified in Figure 3.8-b.

3.2.2.b. PTV: Particle tracking

This investigation used the CC method as a tracking algorithm; input values considered are commented on below.

The length of the interrogation window (l_w) has been estimated as the maximum displacement of a particle. This displacement is defined as the displacement of a particle at the superficial velocity of each profile plus a 50% margin (Table 3.1). The CC algorithm centres this interrogation window on the position of the target particle image in the first frame to find the reference matrix for the target particle. This matrix is obtained by extracting the image intensities within this interrogation window. For the second frame, the interrogation window is not focused on every particle detected in the second frame but on the target particle's exact location in the first frame. In this way, only the images of particles within the interrogation area centred on the target particle of the first frame are considered. All particles that are candidates for being the target particle of the first frame are located in the second frame. A new interrogation window is placed for each of these second frame candidates, and a reference matrix is obtained.

Therefore, there can be more than one candidate particle in the first frame and more than one reference matrix for the same target particle in the first frame. A CC coefficient is calculated between the reference matrix obtained from the first frame and each of the matrices found in the second frame, and then the particles with the highest CC coefficient are matched.

Table 3.1. PTV variables for particle detection and particle tracking used in PTVlab calculations for channel bed experiment (i), profile (j) and slope (α). Variables for particle detection: correlation coefficient threshold for detection (C_t), representative particle radius ($r_{particle}$) and threshold intensity (I_t). Variables for particle tracking: interrogation area length (l_w), minimum correlation coefficient (C_{min}), percentage of minimum velocity similarity with neighbour particles ($vel_{\%}$) and radius of the region containing particles with similar motion (r_n).

Profile			Particle detection			Particle tracking			
α (%)	i	j	C_t	$r_{particle}$ (px)	I_t	l_w (px)	$C_{\min}$	$vel_{\%}$ (%)	r_n (px)
2.00	4	1	0.5	3	24	30	0.01	80	5
3.00	8	1	0.5	3	24	30	0.01	80	5
3.99	13	1	0.5	3	23	40	0.01	80	5
6.00	16	1	0.5	10	25	70	0.01	80	15
6.00	16	2	0.5	10	25	85	0.01	80	15
6.00	16	3	0.5	10	25	95	0.01	80	15
6.00	16	4	0.5	10	40	105	0.01	80	15
6.00	16	5	0.5	10	40	125	0.01	80	15
6.00	16	6	0.5	10	30	135	0.01	80	15
8.00	24	1	0.5	10	35	80	0.01	80	15
8.00	24	2	0.5	10	35	90	0.01	80	15
8.00	24	3	0.5	10	28	95	0.01	80	15
8.00	24	4	0.5	10	30	100	0.01	80	15
8.00	24	5	0.5	10	30	110	0.01	80	15
10.00	27	1	0.5	15	22	100	0.01	80	23
10.00	27	2	0.5	15	22	110	0.01	80	23
10.00	27	3	0.5	15	25	120	0.01	80	23
10.00	28	1	0.5	10	22	100	0.01	80	15
10.00	28	2	0.5	10	22	120	0.01	80	15
10.00	29	1	0.5	15	22	60	0.01	80	23
10.00	29	2	0.5	15	22	75	0.01	80	23
10.00	29	3	0.5	15	30	110	0.01	80	23
10.00	30	1	0.5	10	16	70	0.01	80	15
10.00	30	2	0.5	15	16	60	0.01	80	23
10.00	30	3	0.5	10	16	90	0.01	80	15
10.00	30	4	0.5	10	16	100	0.01	80	15
10.00	30	5	0.5	10	16	110	0.01	80	15
10.00	30	6	0.5	10	16	120	0.01	80	15

After the CC analysis, several filters were applied to increase the confidence of this method (Brevis et al. 2011). First, a CC threshold filter was applied that compares the CC coefficient with the threshold value. All CC coefficient values above this threshold ($C_{\min}$) are accepted. In this

research, a minimum correlation coefficient of 0.1 was used. Second, a double match filter is applied; this filter checks that a particle in the first frame has a unique match in the next frame. However, if a particle in the first frame has more than two matches in the second frame, this filter compares the offsets to neighbouring particles in terms of direction and magnitude. The most similar offset is then kept as a good match. The main problem here is how to define which particles are neighbour particles and which are not. In this case, a neighbourhood radius (r_n) is used. This has been defined as the region containing particles with similar motion and obtained as the representative radius of the particle ($r_{particle}$) increased by 50%. Therefore, it ranged between 5 and 23 px (Table 3.1).

Once the neighbouring particles are defined, the next problem is to define the similar displacement of those particles. To do so, PTVlab calculates the maximum displacement difference between these neighbouring particles with reference to the number of neighbouring particles. PTVlab then compares this last value with another input variable, defined as the minimum velocity similarity percentage with neighbouring particles ($vel_{\%}$). Those particles where the input value is greater than the calculated value are then filtered out. A minimum of 80% similarity was used (Table 3.1).

3.2.2.c. PTV: Position and velocity vector calibration

Once the particle detection and tracking algorithms have been run, calibration of the calculated data is performed using a calibration photo. This calibration image consists of taking an image of a ruler under the water with the camera and recording the settings of each experiment (Figure 3.7). Thus, the position and velocity vectors could be calibrated knowing that the actual distance and the lapse between frames was 2 ms (Figure 3.8-c).

3.2.2.d. Data filtering

A relative frequency analysis was conducted to filtrate the output data from the PTVlab software. This filter is based on an analysis of the frequency distribution of the flow velocity.

For this, a study of frequencies by depth intervals (every 0.4 mm) was carried out: Velocity measurements were grouped at every 0.4 mm of water depth throughout the total water depth. Then, each of these groups was filtered according to a frequency distribution. This filter uses a frequency distribution to find the velocity at which the frequency is smaller or greater than the threshold values of 8% and 4%, respectively. These two different threshold values in the frequency distribution are derived from the unbalanced data obtained from PTV, in which lower velocities appear more frequently than higher ones. This fact comes directly from the PTV

calculations, where higher velocities are limited by the length of the interrogation area (l_w), since the highest velocity obtained from PTVlab is directly related to the size of the interrogation area. However, the interrogation area should be kept as small as possible to avoid detecting too many particles in each interrogation area.

Once the data has been filtered, the mean values of each group's velocity and water depths can be calculated.

3.2.2.e. Methodology validation

The exact velocity profiles were measured simultaneously with the two different methodologies: ADV and PTV. The ADV methodology is assumed to be calibrated and validated, provided the measurements are made within the application limits of the ADV itself, given that Fernández (2019) studied ADV measurements under highly turbulent flows.

These simultaneous velocity profile measurements were carried out with moderate slopes (2% and 3%) and significant water depths due to the limitations of ADV in measuring small water depths and near-bed measurements. Moreover, the discharge was set far from the particle's threshold of motion to ensure the stability of the flow and the bed throughout the test. ADV and PTV measurements were performed in the same experiment without stopping or changing any test parameters (channel slope, bed surface, discharge rate). This meant that once the average velocities had been calculated using both measurement techniques, the profiles obtained with the two techniques could be compared.

3.3. Results and Discussion

The results from the experiments and approximations are gathered in this section: 119 profiles were analysed in this research, 94 were measured with ADV and 25 with PTV, with flume slopes that varied between 2% and 10%, with extremely low relative submergences ranging from 0.7 to 3.7, superficial flow discharges between 1–29 l/s, with Reynolds number ($\mathrm{Re} = 4R_h U/\nu$) values in the range from $1.15 \cdot 10^4$ to $1.86 \cdot 10^5$, and grain Reynolds numbers (Re^*) from 520 to 1440. Therefore, the flow throughout all of the experiments was under rough-turbulent conditions since $\mathrm{Re} > 2000$ and $\mathrm{Re}^* > 68$ (Powell, 2014).

3. 3. 1. ADV stability

Following the procedure proposed by Fernández (2019) for highly turbulent flows over a macro-roughness bed, the ADV's stability was evaluated to ensure that enough data were recorded for each sampled point. In this investigation, the statistical parameter that controls the sampling

time was defined as the average velocity ($\bar{u}$). Therefore, at a given point in the velocity profile, $\overline{u_i}$ is calculated for each time step. The sampling time is defined as the time elapsed until $\overline{u_i}$ remains constant.

Figure 3.9-a and Figure 3.9-c show the instantaneous velocities (u_i') measured with ADV in profiles with 2% and 10% slopes, respectively. As the slope steepens, the turbulence increases significantly; hence, the sampling time is increased. The turbulence also increases when the relative submergence decreases, so the sampling time also increased in those profiles.

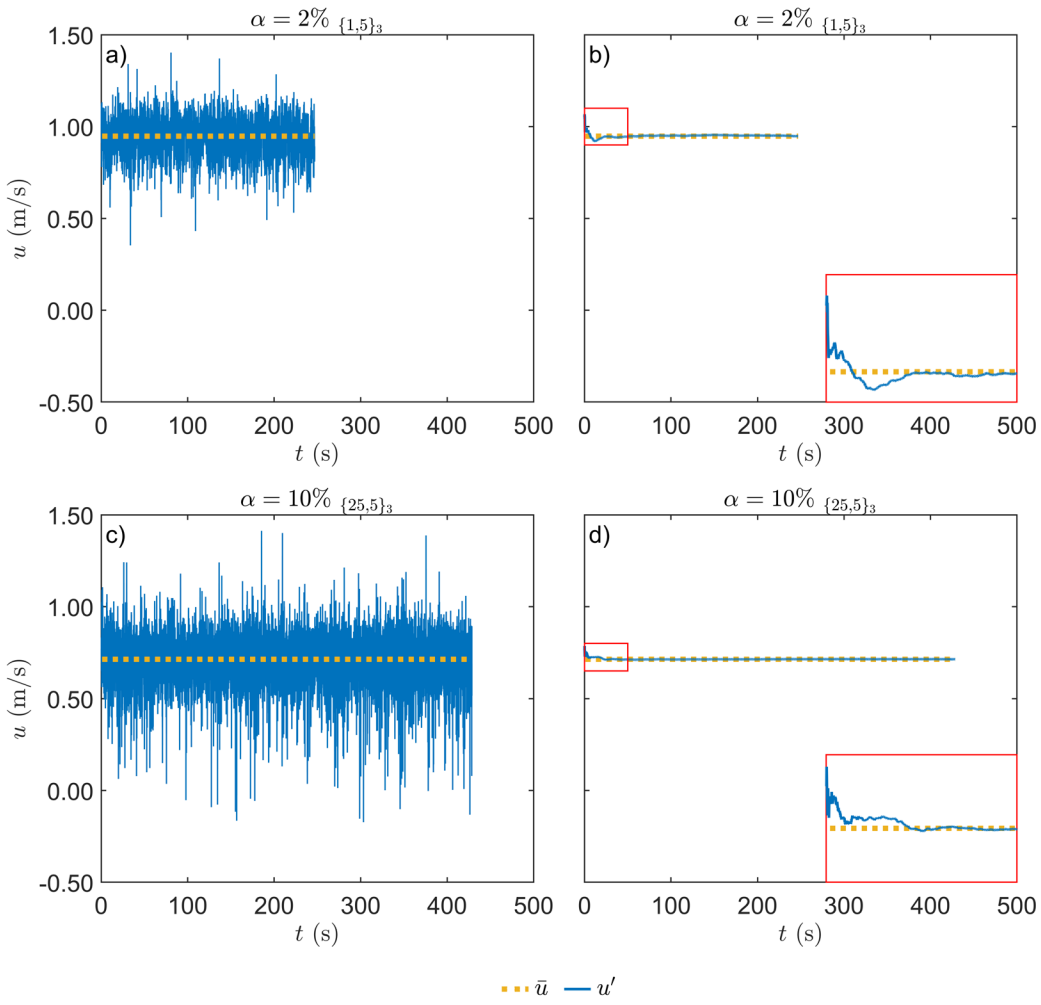

Figure 3.9. (a) Instantaneous velocity (u'), (b) average velocity ($\bar{u}$) for a slope of 2%, (c) instantaneous velocity (u'), and (d) average velocity ($\bar{u}$) for a slope of 10%.

Another phenomenon that was also considered when establishing the sampling time was the proximity of particles on the bottom to the study area; as the ADV approached the bed, the sampling time increased within the same velocity profile. However, the stability of the average velocity was achieved within the first 50 seconds of measurement (Figure 3.9-b and Figure 3.9-d) in all the sampling points carried out. Nevertheless, all sampling points were measured for more than 250 s (4 minutes) each.

Regarding the velocity profiles measured at small depths (less than 1.5 cm) with ADV, potential measurement errors may appear when measuring at distances of less than 1 cm from the bed (Finelli et al. 1999). Furthermore, as bed surface roughness increases, or in aerated flows, such as highly turbulent flows, these measurement errors become more significant (Fernández 2019; Martin et al. 2002). Together with the difficulty of keeping the bed stable when approaching the bed with the ADV for more than 4 minutes, this fact produced serious measurement difficulties near the bed and throughout the entire velocity profile while measuring those profiles with the ADV in the lab.

3. 3. 2. PTV data filtering

The output data from the PTVlab software were filtered using the relative frequency distribution for the flow velocity of each profile. Figure 3.10 shows the frequency analysis for some of the depths for a 6% channel slope velocity profile. The frequency of the data is not well balanced (Figure 3.10), since the peak is not located in the centre of the distribution. Hence, the importance of considering two different threshold limits.

At the end of the process, the cloud of data considered for further calculations was focused on the high-frequency velocities (the blue bars of Figure 3.10, which correspond to the blue cloud of Figure 3.11-a).

Another analysis relating to the filtering of PTV data consisted of locating the filtered data in the image plane. Therefore, each velocity vector (u,v) could be located at the position (x,z) at which PTVlab detected the particle (Figure 3.11-b). Here, most of the filtered data is located on the right side of Figure 3.11-b. This fact is derived from the limitations of both the interrogation area and the area of interest in the PTVlab configuration.

In Figure 3.11-b, the flow moves from left to right; therefore, a particle moving towards the end of the region of interest may disappear from one frame and also from the next one because it flowed outside of the calculation zone. In this situation, either the “missing” particle is filtered out by matching algorithms or, on the contrary, mismatches appear. The latter is the case on the right side of Figure 3.11-b since negative velocities are detected. These negative velocities are explained because the particles detected near the right side of the calculation zone in the first frame are not detected in the second frame (since they are outside the calculation zone), so they “disappear” in the second frame.

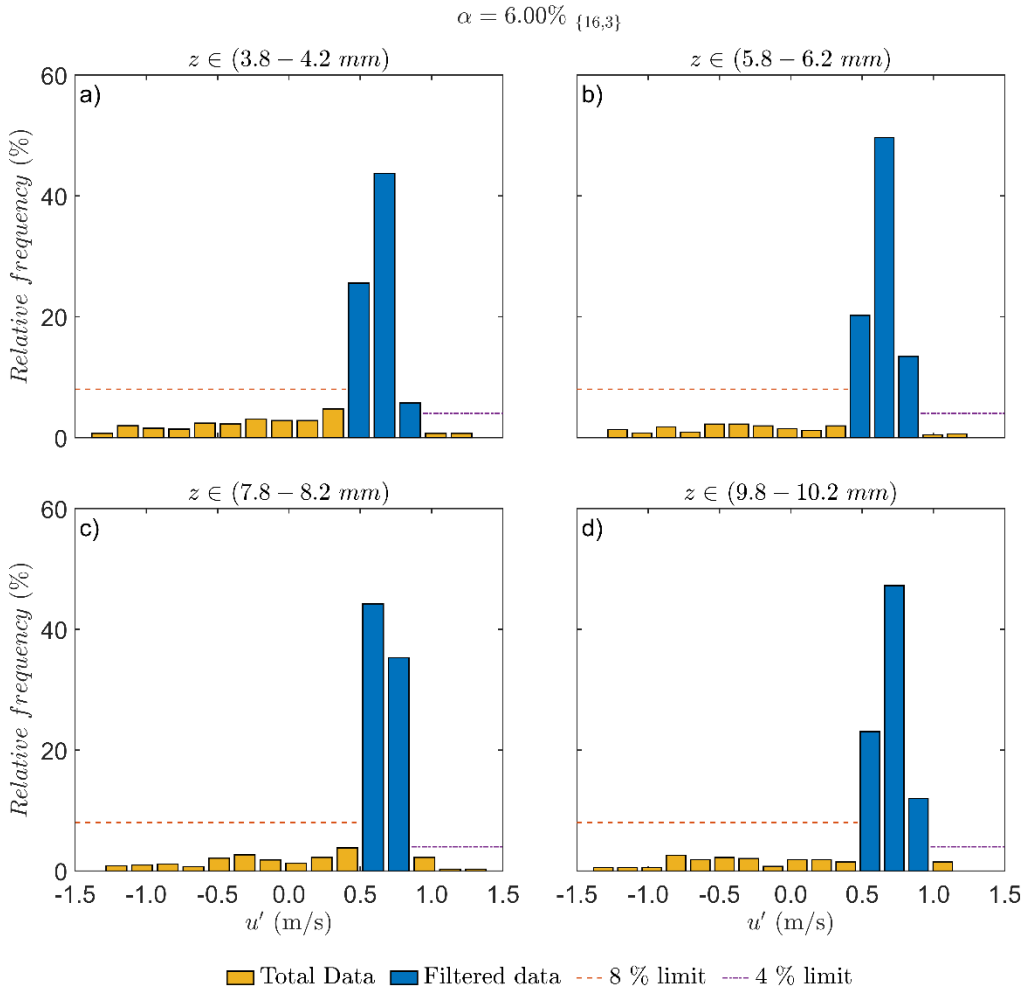

Figure 3.10. Relative frequency histogram of streamwise velocity of the profile {16,3}, 6% channel slope, for water depths between (a) 3.8–4.2 mm, (b) 5.8–6.2 mm, (c) 7.8–8.2 mm and (d) 9.8–10.2 mm.

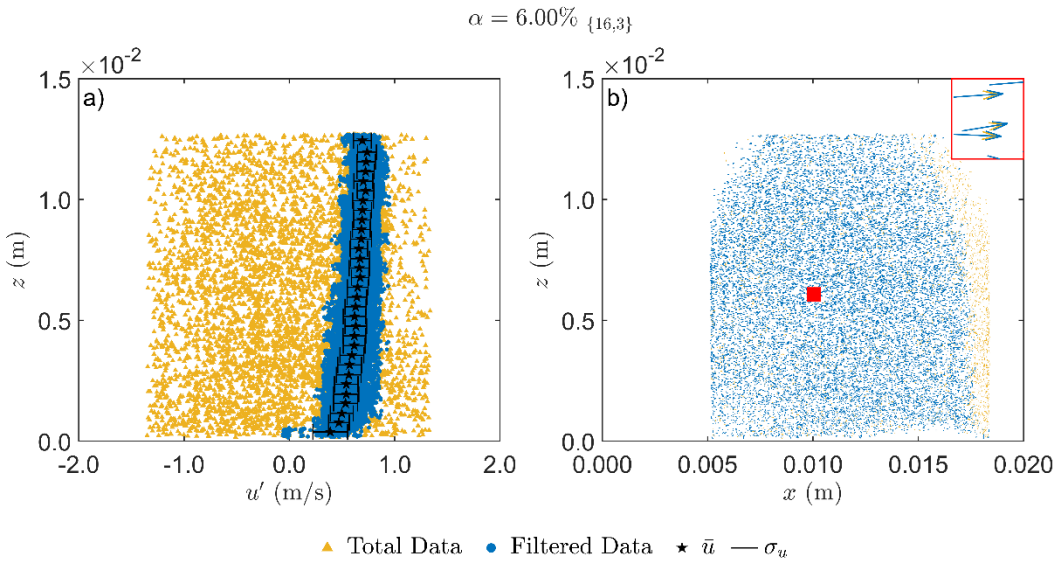

Figure 3.11. (a) Streamwise velocity data as a function of water depth and (b) velocity vectors located in their coordinates (x,z) for a 6% channel slope, profile {16,3}.

Therefore, PTVlab software matches these particles with particles located behind their initial position. Therefore, these particles appear to have travelled backwards, and thus, the velocity is negative. This is why it is necessary to filter and handle the PTV data.

3. 3. 3. Methodology validation

This section aims not to evaluate the measured velocity profiles per se, but to study whether the proposed PTV technique works correctly when measuring the velocity profile under steep slope flume and low relative submergence conditions. In this context, the validation of the proposed PTV methodology was carried out on slopes of 2% and 3%.

The hydraulic variables for each test are detailed in *Appendix B: Supplemental Figures and Tables*. The validation in the experiment with a 2% slope was carried out with a total flow of 16.15 l/s and a water depth of 5 cm (Table 3.2). In contrast, the validation with a 3% slope was carried out with a total flow of 16.27 l/s and a water depth of 4.2 cm. Figure 3.12 shows the extent to which the profiles measured with both techniques (PTV and ADV) coincide.

Table 3.2. Summary of hydraulic and physical conditions of the experiments for the PTV validation for the experiment (i) and profile (j).

α (%)	i	j	Q_{sup} (l/s)	Q_{inf} (l/s)	Type	d (m)	R_h/D_{50} (-)	k_s (m)	u_* (m/s)
2	4	1	15.45	0.69	PTV	0.048	2.7	0.014	0.088
2	5	1	15.45	0.69	ADV	0.049	2.7	0.014	0.087
3	8	1	15.47	0.79	PTV	0.042	2.4	0.011	0.101
3	9	1	15.47	0.80	ADV	0.042	2.4	0.012	0.100

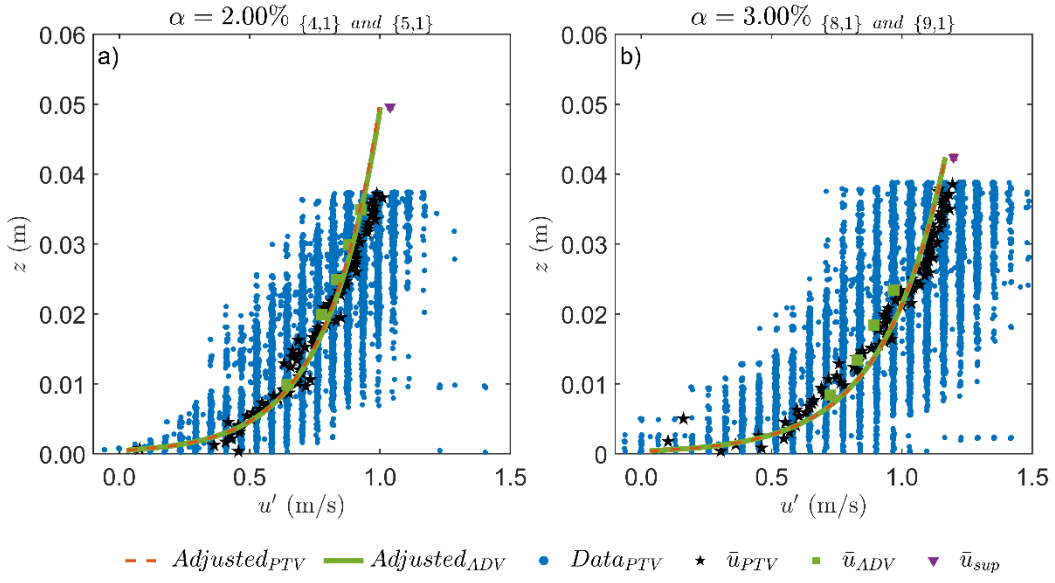

Figure 3.12. Velocity profiles as a function of water depths for (a) 2% channel slope and (b) 3% channel slope with both techniques.

However, the PTV measurements (Figure 3.12) extended from near the bed to almost the free water surface of the profile, while the ADV (Figure 3.13) was measured at close water heights, and measurements near the bed were not possible. Despite these differences, both techniques resulted in very similar velocity profiles. In addition to giving equivalent shear velocities (u_*) and roughness heights (k_s) after the optimization process (explained in detail in *Chapter 4*), this was true of the data obtained with both ADV and PTV.

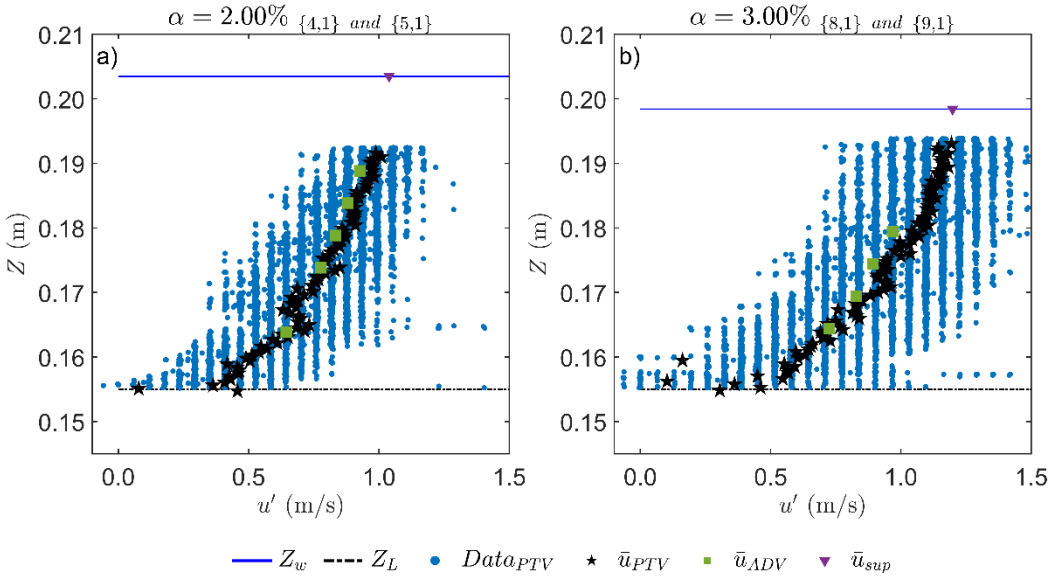

Figure 3.13. Velocity profiles as a function of water heights for (a) 2% channel slope and (b) 3% channel slope with both techniques.

3. 3. 4. Velocity profile measurements in steep flows under low relative submergences

Figure 3.14 shows six profiles measured and analyzed in the steepest channel slopes considered in this research as a function of water depth. All profiles in Figure 3.14 were measured following the PTV methodology described in this chapter.

Two different profiles are presented for slopes of 6%, 8% and 10 %. Figure 3.14 shows how the PTV made it possible to measure velocity profiles with extremely small depths (less than 2 cm). The spatial distribution of PTV measurements can also be observed, with particular interest, in the area near the bed, which the ADV method could not measure. It is evident how the PVT can measure near the bed, but it can also measure a few millimetres below (around 2–3 mm) the particle crests, marked as a dotted line in Figure 3.14. It is also evident how the frequency study filters noise from the images (in yellow) until it leaves a cloud of points (in blue).

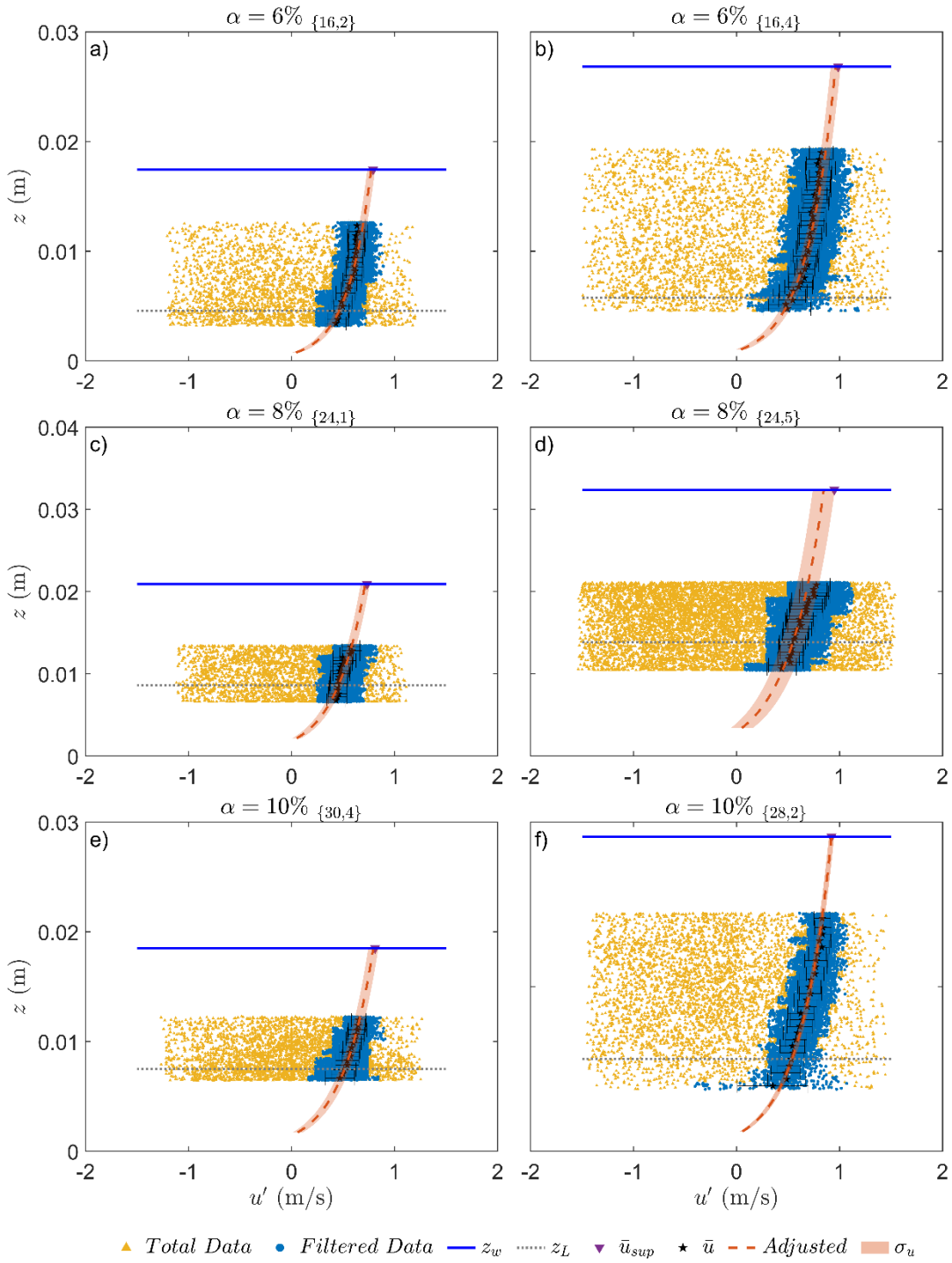

Figure 3.14. Velocity profile measured using PTV as a function of water depths for (a, b) 6%, (c, d) 8%, and (d, e) 10% flume slopes.

Similarly, Figure 3.15 shows the velocity profiles measured on the same slopes as Figure 3.14, but using ADV.

Many problems were encountered in the laboratory when measuring profiles with steep slopes and small depths using the ADV methodology. To the extent that some of the bed particles were displaced or moved due to the presence of the ADV. When the ADV was brought closer to the bottom of the bed, it increased the bottom tension, causing particle movement and therefore changing the original hydraulic conditions. Moreover, since it takes more than 30 minutes to measure a complete velocity profile, the probability that this instability will occur in the course of the measurement was very high. Specifically, erroneous profiles were obtained in which the first measurements corresponded to the initial hydraulic variables and the last points measured corresponded to the new ADV-modified conditions.

Nevertheless, Figure 3.15 also shows that some of the profiles were measured using the ADV without significant problems or errors. Comparing Figure 3.15 with Figure 3.14 and the PTV calibration figures (Figure 3.12 and Figure 3.13), it can be observed that the measurement points in the case of ADV are limited and localized, with higher deviations than those from profiles measured with PTV. Furthermore, ADV could not be measured near the bed (or the water surface). An exception to this is shown in Figure 3.15-e and Figure 3.15-f; where, with a 10% slope, it was possible to measure near the bed since a gap was generated in the bed, although different velocities were obtained.

Similarly, if we focus on the upper part of the profile, an area without measurements is observed around the water surface elevation with both techniques (Figure 3.14 and Figure 3.15). In the case of ADV, both the emitters and the control volume must always be submerged. Furthermore, a safety distance between the water surface and the first measured point of the profile must be considered due to the entrance of air and fluctuations in the water surface (Figure 2.10-b and Figure 2.10-c). In the case of the PTV, this distance is determined by the distance at which the laser penetrates the water (of the order of 1–2 mm) and by the area of the profile stopped by the introduction of the laser itself.

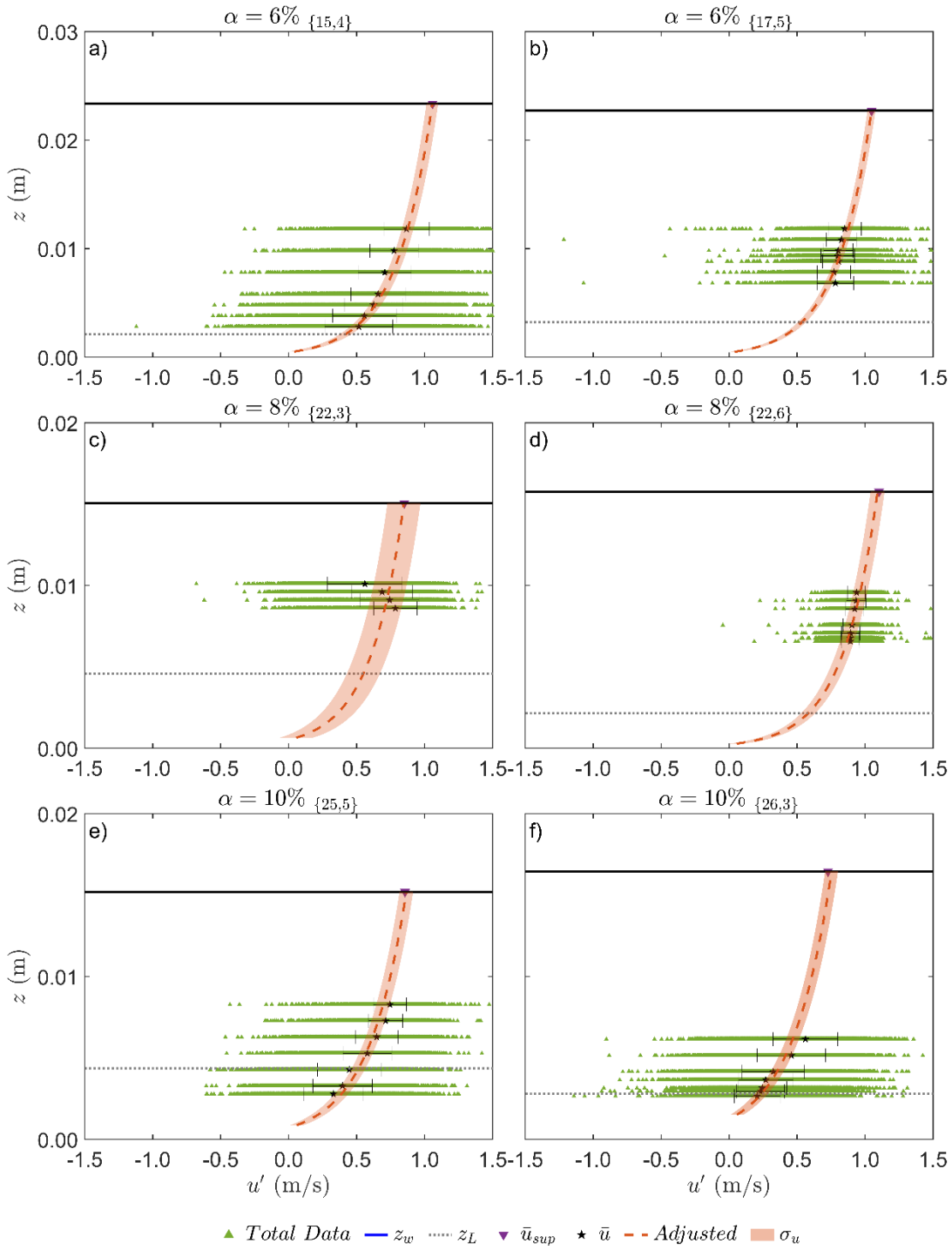

Figure 3.15. Velocity profile measured using ADV as a function of water depths for (a, b) 6%, (c, d) 8%, and (d, e) 10% flume slopes.

Chapter 4: Velocity Profile Distribution

In this chapter, the log-law equation has been applied to the experimental data sets. The variables required for defining the velocity profile distribution are studied by comparing various formulations proposed by previous studies.

This chapter corresponds to a manuscript submitted to an international peer-review journal.

4.1. Introduction

Although the hydrodynamics of mountain rivers has been studied for the last three decades, there are still many unsolved problems, such as calculating the local average velocity, especially in the near-bed region, and its related properties that act as resistance to the flow (Ferro 2003b; Nikora et al. 2004).

Flow in mountain rivers is typically shallow, with the ratio of the mean hydraulic radius to the mean grain diameter (relative submergence) often less than five in low-flow conditions and ten in flood conditions (Bathurst 1985; Lee and Ferguson 2002). Moreover, the beds are formed by sand, gravel, and boulders, which constitute a rough surface and could have complicated bed configurations (i.e. step-pools, bars, or flat beds). Consequently, steep bed gradients and coarse bed materials produce significant subsurface flow throughout the permeable beds (Lamb et al. 2017a). These phenomena may misrepresent hydraulic variables, namely depth, roughness height, and velocity.

Numerous experimental studies have shed light on the structure of the statistical description of the turbulent characteristics of open channel flows (Nakagawa and Nezu 1977; Nikora and Goring 2000; Niño and Garcia 1996), especially in the near-bed region (Antonia and Krogstad 2001; Jiménez 2004; Raupach et al. 1991). Nezu and Nakagawa (1993) commented that the following two questions must be answered before turbulent structures over rough beds can be accurately described: (1) which parameter should be used to represent the size of the roughness elements? and (2) where should the level from which the water depths are computed be located? (i.e. where is the reference datum?). This research focuses on the latter.

4. 1. 1. Logarithmic velocity profile

Keulegan (1938) extended Nikuradse's studies to channels and continued Prandtl's (1926) previous work, developing the relationship between the local mean velocity at a certain distance to the bed ($\overline{u(z)}$) and shear velocity (u_*) in a an hydraulically rough flow over an impermeable bed, which can be approximated by equation (4.1)

$$\frac{\overline{u(z)}}{u_*} = \frac{1}{k}\ln\left(\frac{z_o}{K}\right) + B\left(\mathrm{Re}^*\right) \tag{4.1}$$

where z_o is the profile origin water depth; K is the average projection of the roughness; k is the Von Karman constant, although there is some debate as to whether or not it is a constant (Powell 2014), and B is a function of the boundary or grain Reynolds number ($\mathrm{Re}^* = u_* k_s / \nu$).

More in detail, Keulegan (1938) assumed that the logarithmic profile starts at the water depth at which the velocity is 0 (i.e. $z_o = k_s/30$), developing the well-known Von Karman–Prandtl velocity-distribution (log-law equation) as defined in equation (4.2):

$$\frac{\overline{u(z)}}{u_*} = \frac{1}{k}\ln\left(\frac{30z}{k_s}\right) \tag{4.2}$$

where z is the water depth and k_s is Nikuradse's roughness sand height, known as the relative roughness height.

Schlichting (1968) studied the coefficient B in channel flows with different hydraulic conditions and stated that it is a constant of 8.5 for a rough wall. Thus, equation (4.1) and equation (4.2) are equivalent under hydraulically rough conditions.

The analysis of pipe flow described above forms the basis for flow resistance. Keulegan (1938) developed flow resistance equations for hydraulically smooth and rough channels derived from the Von Karman–Prandtl velocity-distribution law. Keulegan integrated the Von Karman law for a channel cross-section to obtain an expression for the average velocity of the section U, described in equation (4.3), in which d is the total water depth and is known as the resistance relationship after Keulegan for turbulent flow.

$$\frac{U}{u_*} = \frac{1}{k}\ln\left(\frac{11d}{k_s}\right) \tag{4.3}$$

4. 1. 2. Velocity profile in low relative submergence flows

It is well accepted that open channel flows can be divided into three layers, namely laminar, transition, and turbulent layers. In the laminar layer, the flow is purely laminar, as there is non-existent turbulence, and the laminar viscosity is responsible for the shear stress. As flow distances from the boundary, it is capable of oscillating until it can create vorticity, and hence turbulence. The turbulent layer is formed by the roughness, the logarithmic, and the outer layers (Nikora et al. 2001). Nevertheless, in flows with relative submergence below 4, only the roughness and subsurface layers are present (Ferguson 2007; Nikora et al. 2001). Gravel beds are hydraulically rough, so the viscous sublayer is assumed to be insignificant, and the water depth is not high enough to correctly develop a turbulent layer. Therefore, no logarithmic layer is developed to apply directly the log-law of the wall. Nevertheless, laboratory studies over gravel beds with low and large relative submergence have shown that the velocity profile could be described with the log-law if some parameters were modified (Aberle and Smart 2003; Einstein and El-Samni 1949; Fernández 2019; Grass 1971; Nezu and Nakagawa 1993; Rouzes et al. 2018; Smart 1999). Moreover, Amir and Castro (2011) and Eiff et al. (2014) showed that the log-law can penetrate the roughness sublayer rather than exist above it, as the classical view

states (Jiménez 2004; Nikora et al. 2001). More recently, Ferguson (2021) demonstrated that the logarithmic law estimates flow resistance correctly if the calibration of relative submergence is applied by optimizing the k_s/D_{84} factor to give the minimum root mean square error. For permeable rough beds, Nikora et al. (2001) added a subsurface layer at the bottom to account for the flow occurring through the pores between the granular particles that conform the bed material. In addition, the flow through rough beds may be compared to the well-known driven cavity flow, since a tangential velocity is applied at the cavity top boundary to drive the fluid at the cavity; corner and primary eddies may then appear at the cavity, depending on the depth-to-width ratio (Shankar and Deshpande 2000). Considering movable beds, Song et al. (1994) stated that the log-law could express the mean velocity profile in open channels even with a moving gravel bed.

On the other hand, several researchers have noted that velocity profiles in low relative submergence flows are 'S-shaped', where the point of inflection lies just above the crests of the roughness elements and defines the transition between the slow motion that occupies the roughness space and the faster-moving flow above it (Bathurst 1985; Ferro 2003a; Ferro and Baiamonte 1994; Jarrett 1990; Katul et al. 2002).

4. 1. 3. Reference level definition in a rough flow

When applying the log-law to a gravel bed, the first problem one must solve is where to locate the reference level Z_T, from which all water heights z_i and water depths d are measured (Figure 4.1). For a smooth boundary and fully turbulent flow, the origin of the velocity profile is taken on the boundary. However, if the wall is composed of loose grains, a generally accepted and standard definition of Z_T is not available (Nezu and Nakagawa 1993). The reference datum determination becomes more difficult as the bed becomes permeable (Figure 2.17-a) and mobile, and the origin of the profile may be entrained in the flow below the crests of the sediment bed (Amir and Castro 2011). Furthermore, the assumption than the profile starts with zero velocity cannot be applied under permeable beds. Therefore, the position of the reference bed or bed surface datum (Z_T) for the profile is unknown and must be specified beforehand, since it is neither the bed surface level nor the top (or the mean) level of the bed grains with permeable and rough beds.

Many authors have suggested shifting the reference level in permeable gravel-bed rivers (Amir and Castro 2011; Chen et al. 2020b; Eiff et al. 2014; Fernández 2019; Koll 2006; Nikora et al. 2001; Yu and Tan 2006). Several definitions of the location of the reference datum (Z_T) and the profile origin height (z_o) are present in the literature. Shlichting (1968) suggested that a

geometrical bed level should be defined as the level obtained if all the roughness elements were laid down uniformly. Ferro and Baiamonte (1994) located Z_T as the level obtained by replacing the bed roughness elements with an equivalent bed layer of the same volume and with a constant thickness. They considered Z_T a constant, although different concentrations of coarser elements were used in the experiments. Grass (1971) proposed shifting z_o to yield the straightest line on a series of semilogarithmic plots of mean velocity data. Years later, Grass et al. (1991) used a combination of the progressive method that shifts the origin adapted by Perry and Joubert (1963) and they introduced a linear regression to obtain the straightest line in the logarithmic zone.

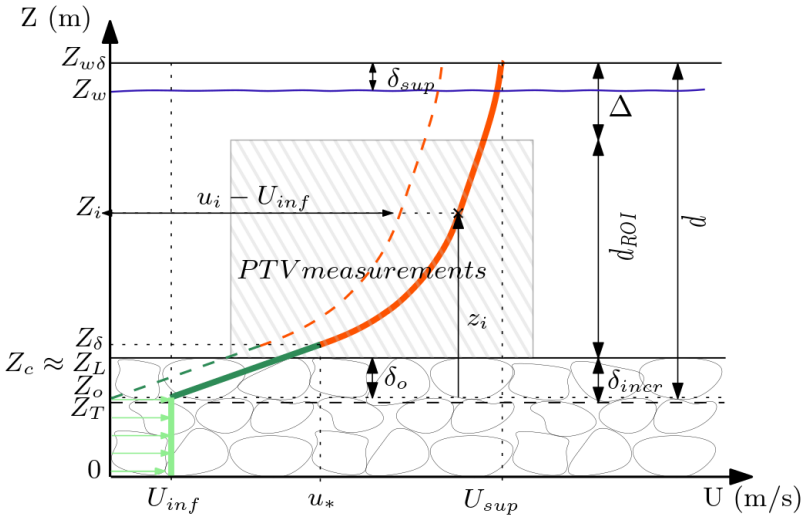

Figure 4.1. Schematic illustration of all variables related to velocity profile adjustment and optimization procedures conducted.

Einstein and El-Samni (1949) suggested that the logarithmic profile only fits the velocity data if Z_T is displaced at a distance $\delta_o = 0.2D_{50}$ below the top of the roughness elements, in which δ_o is the shifting distance from the top crests of the roughness elements to the origin of the velocity profile. On the same path, many researchers (Fernández 2019; Grass 1971; Nezu and Nakagawa 1993; Nikora et al. 2001; Smart 1999; Yu and Tan 2006) have suggested that Z_T lies at a distance below the top of the elements. Experimental data have brought about slightly different results, depending on the researchers. Many authors have used the shifting distance of the reference level from the crests of bed particles as δ_{incr}, defining δ_{incr} as proportional to the diameter of the roughness elements, as in equation (4.4):

$$\delta_{incr} = \beta D_{50} \tag{4.4}$$

In this manner, β is identified from empirical works to be 0.2 at impermeable beds (Einstein & El-Samni, 1949), 0.25 (Yu & Tan, 2006), and 0.35 (Ferro & Baiamonte, 1994).

On the other hand, some authors have proposed a relationship between δ_o and D_{50} as $\delta_o = 0.21D_{50}$ (Grass et al. 1991) or $\delta_o = 0.4D_{50}$ (Ferro 2003a), and others a relationship between δ_o and a roughness parameter such as k_s. Bayazit (1983) reported δ_o as varying from 0.15 to 0.35 times k_s. Experimental works have obtained 0.18 and 0.25 (Van Rijn 1987) as a proportionality constant between δ_o and k_s.

This shifted position of the reference level enables agreement between measured velocity distribution and the logarithmic law (Einstein and El-Samni 1949; Nezu and Nakagawa 1993). Nevertheless, the effect of a poor selection of Z_T becomes markedly significant if the level of the measurement point is in the near-bed region (Yu and Tan 2006). Furthermore, overestimating Z_T has a more significant effect on friction velocity and roughness size assessment than underestimating it (Yu and Tan 2006).

4.2. Materials and Methods in the Laboratory

4. 2. 1. Laboratory definition and experimental procedure

The experiments were carried out in the flume of Morphodynamics Laboratory I of the GITS-UPC group (Figure 4.2 and Figure 2.1). A straight rectangular flume measuring 9 m in length, 0.4 m in width, and 0.6 m in height with glass walls was used, and its slope (α) varied from 0 to 30 degrees pivoting from an axis situated at the bottom end. The test zone was defined as the center of the flume section situated 5.65 m from the inlet; hence, a fully developed turbulent flow was achieved in the test zone (Coscarella et al. 2020; Yalin and Da Silva 2001). The flume was covered with a 15.5 cm deep sediment layer, a black basaltic gravel with a D_{50} of 14.5 mm (±1.5 mm), a mean density of 2.97 Tn/m^3, and a porosity of 0.411. Two L aluminium plates of 3 cm width and 2.5 m length were introduced at a certain height from the bottom of the flume (Z_L). These were used as a trail for correctly leveling the bed's material surface, since they supported the rake while combing the bed surface.

The experiment was defined as a set of profiles measured on the same day with the same bed slope. The flow rate was gradually increased until the desired discharge was reached. All profiles worked under non-motion conditions; maximum flow discharge was defined as the larger discharge without reaching the threshold of motion of the bed particles. The water level was normalized through a vertical-moving gate at the downstream end of the channel.

The data collection started ten minutes after the flow rate had been reached and the depth normalized. Flow discharge was measured using two YAKOHAWA magnetic flowmeters of 50 l/s and 5 l/s (± 0.2%) located after the water discharge's electromagnetic valves. Water

depths (± 0.5 mm) were assessed using transparent gauge levels attached to the wall and spaced 20 cm along the flume. Ink tracer was recorded at 60 frames per second three times per experiment to measure the mean infiltrated velocity at the bottom of the channel. An ADV and PTV registered the velocity profiles. The surface velocity was calculated as the average value of tracking a floating particle between two cross-sections marked by red laser sheets three times per run. The tracking particle consisted of 0.01 m long and 0.01 m wide expanded polystyrene and was recorded at 60 frames per second with an accuracy of ± 0.2%.

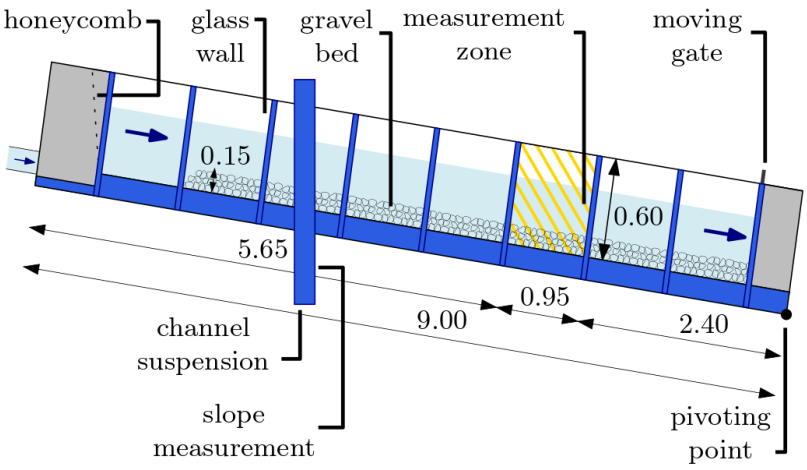

Figure 4.2. Schematic illustration of the experimental apparatus.

Velocity measurements were taken with a 3D SONTEK 10 MHz ADV with a cable mount probe in a side-looking physical arrangement with a position accuracy of ± 0.01 mm. The nominal range velocity was set at 1.00 m/s with a transmission length of 1.8 mm, a sampling rate of 25 Hz, and ± 1 mm/s of measurement accuracy. The ADV measurements were prolonged until the standard deviation of the time series achieved a constant value to eliminate the eddies associated with the local turbulence.

PTV was also used as a velocity measurement technique due to the physical limitations of ADV at small water depths. A high-speed complementary metal–oxide–semiconductor (CMOS) monochrome camera (Basler A504k), an AF Nikkon 50 mm f/1.4D lens with an extension tube of 20 mm, a green LD with a wavelength of 532 nm and tracking particles with a D_{50} of 0.2 mm were used. XCAPTM by EPIX© was used as the software for the image recording. The recording frame was set at 2 ms with an exposure of 0.2 ms, and the laser power was 2 Hz for all the experiments, achieving an accuracy of ± 1 mm/s.

The profiles were indexed as $\{i, j\}$, where i is the experiment and j is the profile number of the i experiment.

4. 2. 2. Experimental data treatment

Experimental or measured variables are denoted with superscript $^+$, water heights computed from the reference datum are denoted with lowercase letters (z_i), and water levels measured from the flume bottom are denoted with uppercase letters (Z_i). Data collected in the laboratory consist of the following direct experimental variables: water and bed levels (Z_w^+ and Z_L^+, respectively), flume bed slope (α), flow discharges (Q_{tot}^+), bed grain diameter (D_{50}), interstitial velocity ($U_{\inf}^+$), superficial velocity ($U_{\sup}^+$), and mean flow velocity at a certain height ($\overline{u_i^+}$). Derived experimental variables, such as interstitial discharge ($Q_{\inf}^+$), superficial discharge ($Q_{\sup}^+$), water height (z^+), and shear velocity (u_*^+), were obtained from these experimental variables.

Water depths d^+ were calculated according to equation (4.5):

$$d^+ = Z_w^+ - Z_L^+ \tag{4.5}$$

Total discharge Q_{tot}^+ was obtained by averaging the data from the magnetic flow meters, and the experimental shear velocity (u_*^+) was derived from the bed shear stress (τ_o), as shown in equation (4.6):

$$u_*^+ = \sqrt{\frac{\tau_o^+}{\rho}} = \sqrt{gR_h^+ \sin\alpha} \tag{4.6}$$

where R_h^+ is the experimental hydraulic radius. *Appendix B: Supplemental Figures and Tables* provides the experimental measurements conducted in the experiments.

On the other hand, water velocities at a certain level were obtained using ADV or PTV. ADV data were obtained by averaging all the ADV measurements for each point at which the instrument was located. No ADV data treatment (clean or spike suppression) was needed; since no spikes were detected during the measurements, prolonged measurement periods were carried out in the lab, and average values were considered.

PTV data were obtained through PTVlab (Pantalano 2020), an add-on of Matlab©, which transforms recordings into position and velocity vectors. PTVlab software is based on three steps: particle detection, tracking algorithm, and data calibration. In this manner, a Gaussian mask algorithm was used to detect the particles. The correlation coefficient threshold for detection was fixed at 0.5 for all experiments, but the representative radius ($r_{particle}$) and intensity threshold (I_t) changed along with the experiments (Table 4.1). After particle detection, a cross-correlation method (Brevis et al. 2011) was applied as the tracking algorithm, in which the interrogation window length (l_w) was estimated as the maximum displacement of a particle,

assumed as the displacement of a particle under the superficial velocity of each profile plus a 50% margin. Thus, as discharge increased, velocity increased too, and so the interrogation area was higher. A constant minimum correlation coefficient of 0.1 and a minimum similarity between neighboring particles of 80% were used. However, the neighborhood radius (r_n) was obtained as the $r_{particle}$ incremented by 50%. A relative frequency analysis was carried out to filter the output data from the PTVlab before adjusting it to a velocity profile distribution. *Chapter 3* provides a detailed description of the velocimetry measurements and methodology used in the research study.

Table 4.1. Parameters used for particle detecting and particle tracking for the PTV technique.

	Particle Detection		Particle Tracking	
α (%)	$r_{particle}$ (px)	I_t (-)	l_w (px)	r_n (px)
2	3	24	30	5
3	3	24	30	15
4	3	23	40	15
6	10	25-40	70-135	15
8	10	28-35	80-110	15
7	-	-	-	-
10	15	16-30	60-120	15/23

4.3. Experimental Results

A summary of the results from the experiments is provided in this section, the complete set of results can be found in *Appendix B: Supplemental Figures and Tables*. The research analyzed 119 profiles with flume slopes that varied between 2% and 10%, extremely low relative submergence ranging from 0.7 to 3.7, and superficial flow discharge of 1–29 l/s, with Reynolds number ($\mathrm{Re} = 4R_h U/\nu$) values in the range from $1.15 \cdot 10^4$ to $1.86 \cdot 10^5$, roughness Reynolds numbers (Re^*) from 520 to 1440, and Froude numbers between 0.84 and 2.25. Therefore, the flow throughout all experiments was under rough turbulent conditions because $\mathrm{Re} > 2000$ and $\mathrm{Re}^* > 68$ (Powell 2014) and threshold motion conditions ($\bar{\tau} < 0.053$). The laminar boundary layer could be ignored, as the transition from laminar to the turbulent boundary layer occurred upstream from the measuring zone.

4. 3. 1. Interstitial velocity

Interstitial velocity was one of the essential variables measured in 120 profiles. Figure 4.3-a shows the flume slope's effect on interstitial velocity; as the slope gets steeper,

the $U_{\inf}^{+}$ becomes greater. Moreover, given a flume slope $U_{\inf}^{+}$ is constant, no matter the relative submergence (Figure 4.3-b). In this way, it is possible to define a linear regression between $U_{\inf}$ and α. Furthermore, $U_{\inf}$ is proven to be constant throughout the vertical within the bed material at each of the profiles, as the tension gradients are zero. Therefore, the interstitial flow follows a piston flow that moves at $U_{\inf}^{+}$. Lastly, $U_{\inf}^{+}$ is always smaller than u_* (approximately 44% smaller on average).

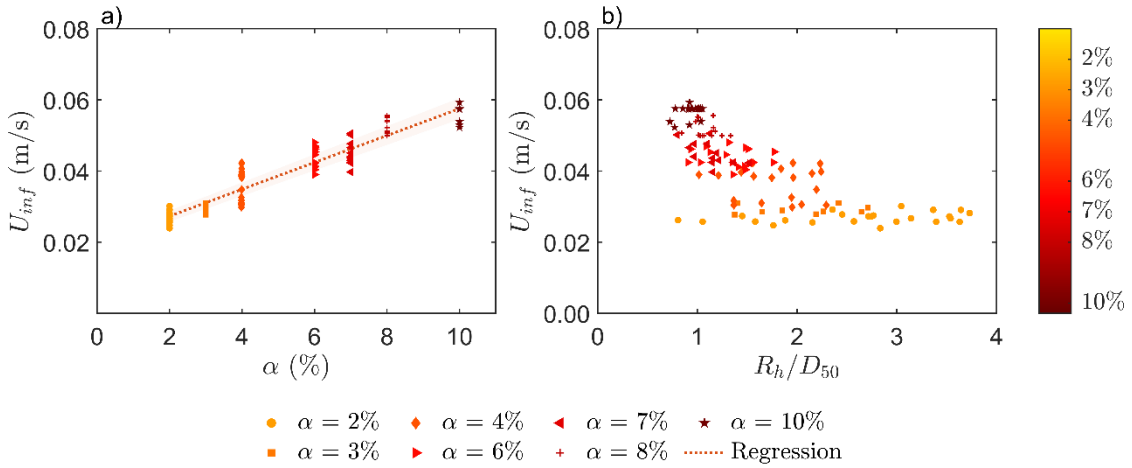

Figure 4.3. (a) Interstitial velocity as a function of flume slope and (b) interstitial velocity as a function of relative submergence.

4. 3. 2. Velocity profiles

Although this section focuses only on the experimental data, a reference level had to be defined to obtain the water depths of each profile. Therefore, two different definitions for the reference level were applied to the experimental data, namely a constant reference datum fixed at the level of the crests of the bed particles (Method *a*) and a datum displaced at $0.2D_{50}$ below the crests (Method *b*).

Method *a* followed the definition often used for alluvial flows; that is, the reference level was the level at which bed particles' crests tops were located; thus, the shifting distance is zero ($\delta_{incr} = 0$). Method *b* followed Einstein and El-Samni (1949), in that the reference level was located $0.2D_{50}$ below the crests ($\delta_{incr} = 0.2D_{50}$).

Dimensionless log profiles are shown in Figure 4.4 for each method considered in this section, together with the theoretical log-law equation in equation (4.2). The different definitions of Z_T change how the experimental data are plotted (Figure 4.4-a and Figure 4.4-b). Nevertheless, straight lines are observed in both methods. Further analysis will be developed in sections coming sections.

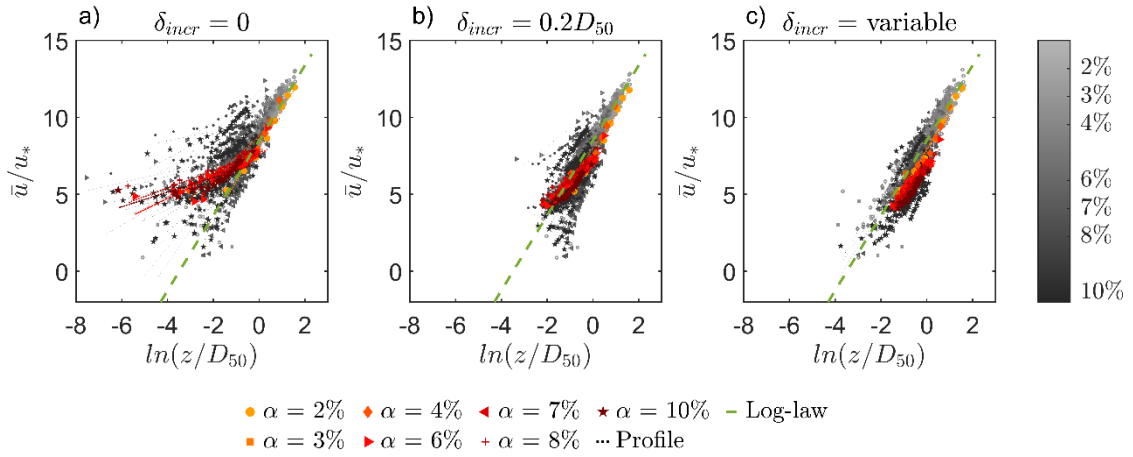

Figure 4.4. Dimensionless log profiles in the horizontal semi-log scale of all the profiles for (a) Method a: zero shifting distance, Method b: fixed shifting distance at $0.2D_{50}$, and (b) Method c: optimized shifting distance.

4.4. Analytical Methodology

4. 4. 1. Velocity profile distribution adjustment

The approaches presented in this research followed the three-layer model proposed by Nicola et al. (2001) on a permeable and hydraulic rough bed, at which the velocity profile is divided into three different flow sections, the logarithmic, roughness, and subsurface layers (Figure 4.1, from top to bottom), since some authors assume that the laminar, or viscous, layer does not develop at low relative submergence flows (Ferguson 2007; Nikora et al. 2001).

The logarithmic layer has been defined as between the water surface level ($Z_{w\delta}$) and the water surface level (Z_δ) (at which u_* is obtained). The roughness layer occupies the flow region between the bed particles' roughness crests and troughs, and is defined between Z_δ and Z_o (water level at which the flow velocity is $U_{\inf}$). Lastly, the subsurface layer occupies the pores between granular particles and is defined as within the water level Z_o and the bottom of the channel.

In this research, it was assumed that the bottom layer (subsurface layer) is a piston flow with $U^+_{\inf}$. To parameterize the velocity distribution in the second layer (roughness layer), an analogy with the viscous layer was applied (Nikora et al. 2001); it was assumed to have a linear velocity relationship. The top layer (logarithmic layer) had the velocity distribution defined by the logarithmic profile (equation (4.2)), since the experimental profiles suggested a log-dependency (Figure 4.4). 'Velocity profile' or 'profile' is used for both the linear and logarithmic sections of the profile depicted in Figure 4.1.

The approaches presented in this section are based on a general normalized least squares regression. The solution uses nonlinear function optimization methods of the sum of squares. The aim of this section is to construct an objective function capable of harmonizing all the parameters to minimize the error between the calculated and measured variables. Variables with different magnitudes construct the objective function (i.e. velocities, flow discharges, water levels); thus, it is necessary to normalize each addend with its respective standard deviation σ_{i^+} to achieve dimensionless errors. The process in both approaches consists of adjusting the parameters that minimize the objective function, and therefore minimizing the addition of all the normalized squared differences considered in each approach (Bateman 1993). These differences are between the measured variables and their respective variable derived from the optimization.

Two approaches are used, the first (equation (4.7)) applies to ADV data, and the second (equation (4.8)) to the PTV data. Both approaches follow similar procedures, but because different measurements were conducted in each velocity measurement technique, diverse arrangements are needed in each approach. The variable to adjust in both approaches relative to their experimental values is the shear velocity (u_*), and the parameters to be optimized are the Von Karman's constant (k), the relative roughness height (k_s), and the reference bed's shifting distance from the height of the crests of the bed particles (δ_{incr}). Furthermore, in PTV, the reference level Z_T is defined as a parameter to be optimized. Each profile is treated independently in both objective functions except for the term inside brackets.

Due to the presence of the piston flow at the bottom of the velocity profile, the minimum velocity at the profile is $U_{\inf}$; therefore, no null velocity is achieved at any point of the profile, and the origin of the velocity profile has a non-zero velocity equal to $U_{\inf}$. However, to better control this origin of the velocity profile, the fitting of the profile has been displaced on a relative coordinate system, so the velocity at the origin of the profile is 0 (i.e. $u_i = u_i^+ - U_{\inf}^+$). In the end, the resulting profile corresponds to the profile measured in the flume, and the origin of the velocity profile height has been obtained from the height at which the profile flows at $U_{\inf}$.

Moreover, as the water surface was vibrating during the experiments due to the high turbulence flow, an error on the water surface level measurement was added to both approaches, although it was accounted in different ways. This error was considered to be $\delta_{\sup}$ in the case of the ADV optimization function and was included in a broader variable (Δ) in the case of the PTV optimization (Figure 4.1). That is why the first four terms of both approaches are the same, but the final term of the ADV data objective function changes into two terms in the PTV data function. These terms correspond to the water surface level ($Z_{w\delta}$) and the crests of the bed

surface level (Z_c). Z_c is assumed to be the value measured as the level of the L plates ($Z_c^+ = Z_L$) (Figure 4.1).

k is evaluated independently for each trial in each calculation approximation. However, k should be the same for all profiles. That is why the mean value of k is entered as the value to be optimized. Therefore, all the profiles tend to the average value of k in each approximation. This is achieved with the term introduced in the brackets.

$$F_{obj}\left(k,u_*,\delta_{incr},\delta_{\sup},k_s\right) = \sum \frac{\left(\overline{u_i^+(z)} - u_i(z) - U_{\inf}^+\right)^2}{\sigma_{u_i^+}^2} + \frac{\left(u_*^+ - u_* - U_{\inf}^+\right)^2}{\sigma_{u_*^+}^2} + \frac{\left(Q_{tot}^+ - Q_{tot}\right)^2}{\sigma_{Q_{tot}^+}^2} + \left[\frac{\left(\overline{k} - k_i\right)^2}{\sigma_{\overline{k}}^2}\right] + \frac{\left(d^+ - d\right)^2}{\sigma_{d^+}^2} \tag{4.7}$$

$$F_{obj}\left(k,u_*,\delta_{incr},\Delta,k_s,Z_T\right) = \sum \frac{\left(\overline{u_i^+(z)} - u_i(z) - U_{\inf}^+\right)^2}{\sigma_{u_i^+}^2} + \frac{\left(u_*^+ - u_* - U_{\inf}^+\right)^2}{\sigma_{u_*^+}^2} + \frac{\left(Q_{tot}^+ - Q_{tot}\right)^2}{\sigma_{Q_{tot}^+}^2} + \left[\frac{\left(\overline{k} - k_i\right)^2}{\sigma_{\overline{k}}^2}\right] + \frac{\left(Z_w^+ - Z_{w\delta}\right)^2}{\sigma_{Z_w^+}^2} + \frac{\left(Z_c^+ - Z_c\right)^2}{\sigma_{Z_c^+}^2} \tag{4.8}$$

On the other hand, the other variables in the objective functions are derived from the parameters that optimize the functions (i.e. $k,u_*,\delta_{incr},\delta_{\sup},\Delta,k_s,Z_T$). That is the case for velocities at a given water height ($u_i(z)$), water depth (d), total discharge (Q_{tot}), level of the roughness crests (Z_c), and level of the water surface ($Z_{w\delta}$). $u_i(z)$ are calculated by applying a log-law profile using the equation (4.2), d as in equation (4.9), and Q_{tot} as computed by equation (4.10).

$$d = Z_{w\delta} - Z_o \tag{4.9}$$

$$Q_{tot} = Q_{\sup} + Q_{\inf} \tag{4.10}$$

As all the experiments had interstitial discharge, the total discharge needed to be divided into interstitial and superficial discharge at a given water level (i.e. superficial discharge was flowing above this level, and interstitial discharge below it). The problem with calculating discharges is that doing so relies on defining the water level at which the superficial discharge starts, although this level physically corresponds to the height from the bottom of the channel to the crests of the bed surface, and applying the assumption that the reference level has shifted a distance below the top crests implies that the height of the bed layer may be smaller than initially

considered. Z_o is assumed as the level at which the origin of the profile starts (Figure 4.1) in both approaches and is calculated as the water level at which the velocity is equal to $U_{\inf}^{+}$ ($\overline{u_{z_o}} = U_{\inf}^{+}$). Furthermore, the interstitial discharge is assumed as a piston flow with constant velocity ($U_{\inf}^{+}$). Therefore, interstitial discharge is computed as in equation (4.11):

$$Q_{\inf}\left(m^3/s\right) = \phi B_w U_{\inf}^{+} Z_0 \tag{4.11}$$

where B_w is the width of the channel and ϕ is the bed porosity formed from interlocking particles.

On the other hand, the superficial discharge depends on velocity, with a linear distribution at the bottom and a logarithmic distribution above it (Figure 4.1). Therefore, the superficial discharge is obtained from the integration of the linear and logarithmic profile, as defined in equation (4.12):

$$Q_{\sup}\left(m^3/s\right) = UB_w(Z_{w\delta} - Z_{\delta}) + (u_* - U_{\inf}^{+})B_w(Z_{\delta} - Z_o)/2 \tag{4.12}$$

where the mean velocity (U) is obtained from the velocity profile integration following equation (4.3) and Z_{δ} is the water level at which the velocity is equal to u_* and it is obtained through the equation (4.2).

Z_c is obtained through equation (4.13):

$$Z_c = Z_T + \delta_{incr} \tag{4.13}$$

The corrected water level ($Z_{w\delta}$) is computed as defined by equation (4.14) in the case of the ADV data and by equation (4.15) for PTV:

$$Z_{w\delta} = Z_w^{+} + \delta_{\sup} \tag{4.14}$$

$$Z_{w\delta} = Z_T + \delta_{incr} + d_{ROI} + \Delta \tag{4.15}$$

where d_{ROI} is the PTV measurement area's height (Figure 4.1).

Finally, two shifting distances have been used; δ_{incr} is defined from the crests to the reference level, and δ_o is defined as the distance from the crests to the origin of the velocity profile. Whereas δ_{incr} is obtained from the optimization, δ_o is derived from the optimization and computed as the shifting distance of the height at which the velocity of the profile is equal to the $U_{\inf}$.

4.5. Analytical Results

This section gathers the results obtained from the analytical methodology proposed in the previous section and applies them to the experimental data described in section *4.3. Experimental Results* For a more detailed examination of the results, please refer to *Appendix B: Supplemental Figures and Tables*.

4. 5. 1. Reference level determination

As seen previously in the experimental results (*4. 3. 2 Velocity profiles*), a reference level had to be defined beforehand, although the definition of this datum could not be done experimentally. A third method was added to assess the sensitivity of the data to the reference level definition to the initial study (Figure 4.4).

This last method (Method *c*) is based on the idea that the stress over the top of the particles can penetrate into the spaces left by the grains until they connect to the infiltration discharge. Hence, it considers the reference level obtained per profile from the objective function defined in equations (4.7) and (4.8) for ADV and PTV data, respectively.

Dimensionless log profiles are shown in Figure 4.4 for each method considered, together with the theoretical log-law equation defined in equation (4.2). The definition of Z_T changes how the experimental data behaves; the slopes are significantly different (Figure 4.4) because the dimensionless parameters change. Further analysis will be developed in section *4. 5. 2. Von Karman constant*.

Although two different shifting distances (δ_{incr} and δ_o) were defined in the velocity adjustment (i.e. direct from the optimization and by computing the shifting distance at which the velocity profile achieves the interstitial velocity, respectively), both shifting distances show the same trends and similar values (Figure 4.5 and Table 4.2). In general, a steeper flume achieves greater δ_{incr} . Furthermore, δ_{incr} is more likely to increase as relative submergence decreases; that is, at a constant flume slope (for example a 6%), δ_{incr} increases as relative submergence decreases. The average δ_{incr} -value is 0.003 m, with a standard deviation of 0.002 m. On the other side, δ_o is systematically smaller than δ_{incr} , with $\overline{\delta_o} = 0.002 \pm 0.002$.

Another concept found in the literature regarding the shifting distance of the reference level is the relation between δ_{incr} and D_{50} , defined in equation (4.4) as the coefficient β . Because D_{50} is unchanged through the experiments, the same trends of δ_{incr} (Figure 4.5 and Table 4.2) are observed for β . The average β -value is 0.17 with a standard deviation of 0.15.

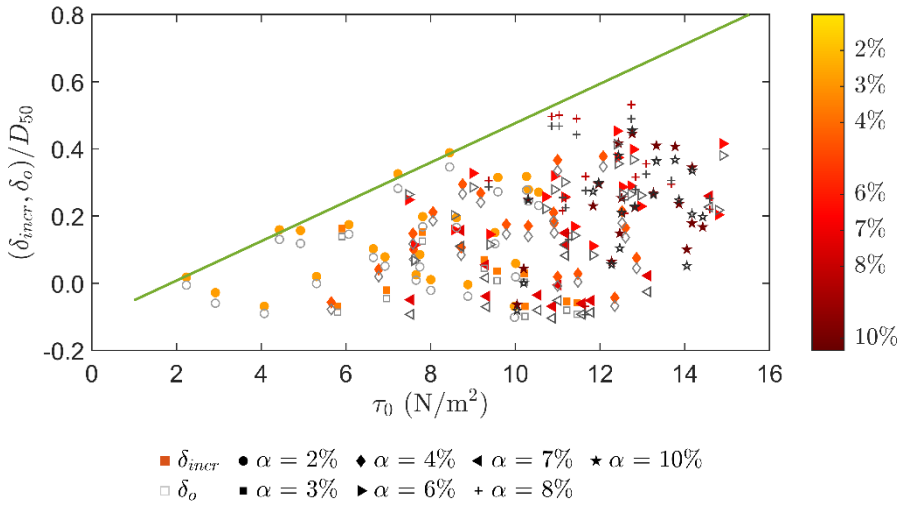

Figure 4.5. Optimized shifting distance as a function of bed shear stress.

Table 4.2. Statistical values of shifting distances of the reference level resulting from the approaches defined in equations (4.7) and (4.8) as a flume slope function.

α (%)	$\overline{\delta_{incr}}$ (mm)	$\sigma_{\delta_{incr}}$ (mm)	$\overline{\beta}$ (-)	σ_β (-)
2	1.9	1.9	0.13	0.13
3	0.3	1.3	0.02	0.09
4	2.2	1.8	0.15	0.12
6	3.8	1.5	0.26	0.10
8	0.5	1.5	0.03	0.10
7	4.4	2.3	0.31	0.16
10	3.4	2.0	0.23	0.14

4. 5. 2. Von Karman constant

The inverse slopes of the profiles shown in Figure 4.4 are the Von Karman k values. Because each method considers a different reference level definition, the behaviour of the profiles changes drastically between each method, whereas fixing the reference datum at the crests (Method *a*) causes the dispersion of slopes, and hence of k; defining the level at the fixed distance of Method *b* causes a gathering of the profiles with similar slopes. This behaviour is also observed in Method *c*, but with better fitting. However, this gathering was expected, since a constant k for all the profiles is applied as an assumption in this last method.

Depending on the reference level definition method, the Von Karman k-values are obtained in two different ways; if the reference level is fixed at a certain distance, k is obtained as the inverse slope of the profiles shown in Figure 4.4 (Methods *a* and *b*), but if it is obtained as a

parameter of the objective functions (Method *c*), k is directly obtained from the optimization. Although mild slopes tend to the theoretical constant of 0.4 for all methods (Figure 4.6-a), a high dispersion is observed with the steeper ones, given the datum definition in the first method ($\delta_{incr} = 0$) and the second ($\delta_{incr} = 0.2D_{50}$).

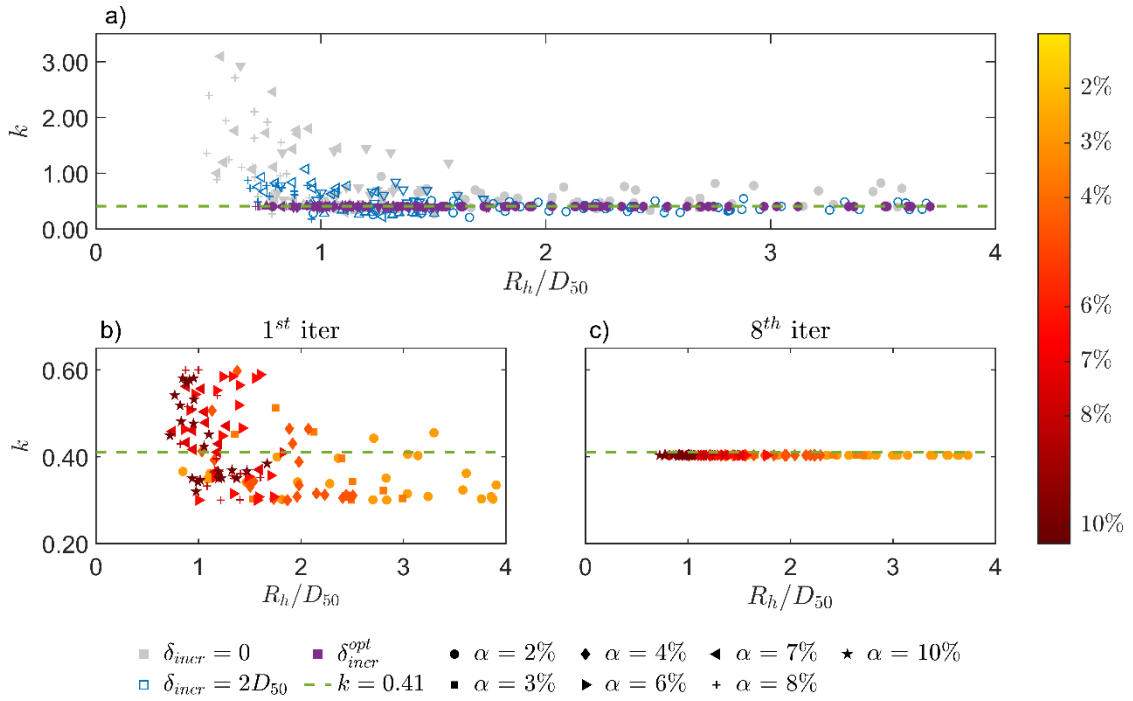

Figure 4.6. Von Karman's constant k as a function of relative submergence for all methods for the definition of the reference level and values of k obtained in the iterations 1, and 8 (last one) of the general normalized least square regression in (b), and (c), respectively.

Furthermore, another relevant aspect to consider is the effect of relative submergence over k. Thus, two data sets can be defined as a function of relative submergence (Figure 4.6-a): the ones with extremely low relative submergence ($R_h/D_{50} < 2$) and the rest ($R_h/D_{50} \geq 2$). In this way, low relative submergence profiles have a dispersion of k -values more than three times higher than the other profiles. This high dispersion of the k -values is obtained in the two first methods considered, although it is highly pronounced in the first.

It is assumed that the Von Karman constant k is indeed constant along all channel slopes and relative submergences in the objective functions of the present research. Hence, eight iterations were carried out to achieve a constant standard deviation of $\overline{k}$ between two consecutive iterations. Figure 4.6-b and Figure 4.6-c show the results for the first and last iteration, respectively. It can be seen how k values tend to gather around a constant value of 0.4 with almost no dispersion at the last iteration. A mean value of 0.403 ± 0.002% was found as a constant value for Von Karman's constant.

4. 5. 3. Velocity profile adjustment

This section summarizes the mean velocity profiles and log profile of the approaches. In this way, Z_T was located below the crests of the roughness elements of the bed surface, Z_L was shown to be above the actual level of the crests (Z_c), and minor corrections over the water surface were observed. Another relevant aspect was that the PTV technique allowed the measurement of the velocities inside the bed region below (<3 mm) and above the cobble crests, showing that the velocity profile followed the distribution proposed at the near-bed region. This measurement was possible due to the roughness of the bed surface (due to its porosity) and the camera's perspective.

Furthermore, zero velocity was not observed at any point of the profiles; the minimum velocity of each profile corresponded to the interstitial velocity, which increased as the slope steepened (Figure 4.3-a and Table 4.3).

Table 4.3. Measured and optimized variables of the profiles shown in Figure 4.6.

			Measured				Optimized				
i	j	α (%)	$U^+_{\inf}$ (m/s)	Z^+_w (m)	Z^+_c (m)	$Q_{\sup}$ (l/s)	$Z_{w\delta}$ (m)	Z_T (m)	d (m)	k_s (m)	u_* (m/s)
16	3	6	0.04	0.170	0.155	5.0	0.172	0.151	0.021	0.017	0.091
16	4	6	0.04	0.175	0.155	6.9	0.176	0.152	0.025	0.018	0.103
24	4	8	0.05	0.169	0.155	4.8	0.170	0.151	0.019	0.017	0.101
28	1	10	0.06	0.165	0.155	3.1	0.166	0.151	0.015	0.018	0.096

Figure 4.7 shows four velocity profiles as a function of water levels, and Table 4.3 shows the relevant values of each of these profiles. For a more detailed examination of the results, please refer to *Appendix B: Supplemental Figures and Tables*.

4.6. Discussion of the Results

4. 6. 1. Interstitial Discharge through a Steep Channel

Lamb et al. (2017) stated that the flow through a channel bed is, on average, proportional to the bed slope, since a hydraulic head gradient drives the groundwater layer (i.e. interstitial discharge increases as the slope steepens). In this research, interstitial discharge was obtained through interstitial velocity, and it increased as the channel slope increased (Figure 4.3-a). On the other hand, different values of $U_{\inf}$ were obtained for the same α (Figure 4.3-b). It can be assumed that these differences are measurement errors because no trend was observed between relative submergence and $U_{\inf}$ (Fig. Figure 4.3-b). Consequently, $U_{\inf}$ was assumed to be constant for

a given channel slope, and therefore $U_{\inf}$ was independent of the relative submergence, and hence independent from the flow discharge. The same conclusion was stated by Lamb et al. (2017a).

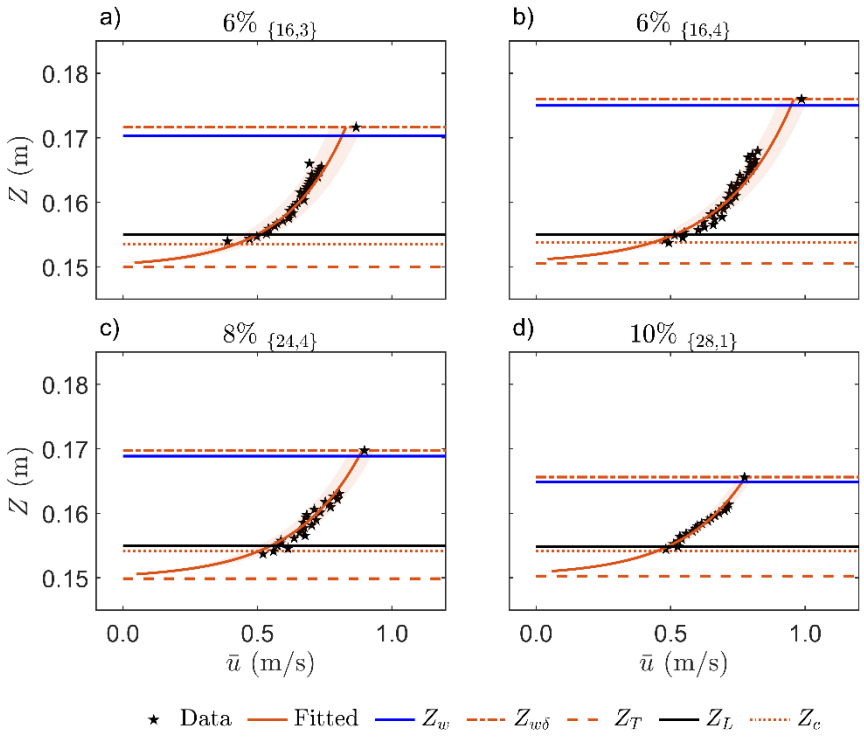

Figure 4.7. Velocity profiles from PTV data for (a) 6%, (b) 6%, (c) 8% and (b) 10% slope flume as a function of water levels.

4. 6. 2. Reference level determination

The datum values changed the plotting of the data ($\delta_{incr} = 0$ in Figure 4.4-a, $\delta_{incr} = 0.2D_{50}$ in Figure 4.4-b, and the δ_{incr} obtained from the optimization procedure in Figure 4.4-c).

The datum was defined with two independent shifting distances, δ_{incr} and δ_o. Although same trends were observed in both values, δ_o was systematically smaller than δ_{incr} (by 0.0003 m). This difference was within the standard deviations of both shifting distances, therefore, δ_{incr} was assumed equal to δ_o.

Due to the high dispersion of the data obtained from the objective functions (Method *c* for the datum definition), no clear trend between the shifting distances and the relative submergence was observed. However, the shifting distance increased as the flume slope increased (Figure 4.5 and Table 4.2). This phenomenon was provoked by the transversal momentum flux induced by the longitudinal momentum flux acting just at the top of the grains. Therefore, as more longitudinal momentum flux ($\rho u_* u_*$), and therefore, more shear stress ($\tau_o = \gamma R_h \sin\alpha$), acted at the top of the grains, the transversal momentum flux could penetrate deeper (Figure 4.5), as

shown in the well-known cavity-driven flows (Shankar and Deshpande 2000). Furthermore, a clear upper limit of δ_{incr} was observed (Figure 4.5). This envelope limit increased as the slope flume increased.

For a more detailed examination of the effect of the reference level on the velocity profile, please refer to *4.7. Addendum – Sensitivity analysis of datum localization on velocity distribution*.

As mentioned above, some authors have related δ_{incr} and/or δ_o with a characteristic size, some have used bed particle diameter (D_{50}), and others have used the relative roughness height (k_s). The mean value of β obtained in this research was 0.17, which was on the lower side compared with the ones found in the literature; that is, Einstein and El-Samni (1949) proposed a value of $\delta_{incr} = 0.2D_{50}$, Yu and Tan (2006) proposed $\delta_{incr} = 0.25D_{50}$, and Ferro and Baiamonte (1994) proposed $\delta_{incr} = 0.35D_{50}$. In fact, Einstein and El-Samni's (1949) proposal (Method *b,* Figure 4.4-b) shows a better gathering of the data than the standard alluvial definition of the datum (Method *a*), although some dispersion on low relative submergences was still observed.

However, all those values in the literature consider neither the relative submergence nor the flume slope as a variable. Moreover, δ_{incr}, and hence the coefficient β, tends to have a higher value for low relative submergence ($\overline{\beta} \approx 0.19$) and a smaller value for greater relative submergence ($\overline{\beta} \approx 0.12$). That is why relative submergence and not particle diameter should be considered to obtain the shifting distance, since the dependency of the coefficient β to relative submergence and channel slope has been observed ($\delta_{\inf} = f\left(R_h / D_{50}, \alpha\right)$).

On the other hand, some authors proposed the relation between the shifting distance (usually z_o) and the height of the relative roughness (k_s) as 0.25 (Van Rijn 1987). Many empirical attempts have been made to relate k_s to grain size, known as texture coefficient ($\alpha_t = k_s / D_{50}$); for example, this was 6.8 by Bray and Davar (1987), 8.5 by Limerinos (1970), 7.1 by López and Barragán (2003), 5.9 by Millar (Millar 1999) and 3.3 by Strickler (1923).

4. 6. 3. Von Karman as a universal constant

The assumption that the Von Karman constant k keeps a constant value for all channel slopes and relative submergences was made in this research. Because k is a parameter controlled by the proper water nature, and in some way it defines the growing free vortices as they flow away from the turbulent boundary layer, since the experiments were carried out in clear water, this assumption indicates that all the profiles have to have the same k value. Nevertheless, the well-known $k \approx 0.4$ value was not assumed but validated. Furthermore, the reference level definition proved to be a decisive factor for the k-values for extremely low relative submergences

($R_h/D_{50} < 2$) (Figure 4.6-a). Thus, a correct definition of the reference level is crucial in low relative submergence flows over permeable and rough beds.

With the optimized datum, all 119 log-fitted velocity profiles were parallel and tended to a slope of 0.403 (Figure 4.4-c and Figure 4.6-c), which is the Von Karman constant. Similar results were obtained following the definition of the reference level at a shifting distance of $\delta_{incr} = 0.2D_{50}$ (Einstein and El-Samni 1949) in Method *b* (Figure 4.4-b). Although some dispersion of k -values in low relative submergence profiles was present (Figure 4.6-a), the k -values showed no dependency on the channel slope or relative submergence.

On the other hand, several scientific articles have aimed to explain the physical meaning of the reference level over rough mobile beds defining an equivalent Von Karman constant (Ferreira 2015; Franca et al. 2008; Rouzes et al. 2018). However, Rouzes et al. (2018) stated that a free-k approach better fits the experimental data in the upper part of the flow, whereas the constant k gives a better match near the top of the roughness elements. Furthermore, they did not consider the bed to be a porous layer, as the bed material was fine and the slopes milder. Therefore, they did not take into account interstitial discharge, and hence the velocity under the crests of the bed particles was assumed to be zero. That is why, together with the results presented in this research, the Von Karman parameter can be assumed to be a constant value of 0.4 in hydraulically rough flows under low relative submergence and over permeable beds, as stated by Tominaga and Nezu (1992).

4. 6. 4. Logarithmic law velocity profile distribution throughout the water depth in low relative submergence flows

Now that the Von Karman constant value for low relative submergence and hydraulically rough flows has been confirmed to be the theoretical 0.4, it is time to study the assumption that the velocity profile follows a logarithmic distribution, as defined by equation (4.2), throughout the water depth.

In the classical view (Jiménez 2004; Nikora et al. 2001), the logarithmic law exists above the roughness sublayer. However, in flows with low relative submergence (below 4), the logarithmic layer is not developed; therefore, one cannot apply directly the wall, since only the roughness and subsurface layers are present (Ferguson 2007; Nikora et al. 2001).

Despite the recognized inadequacy of the wall law to describe the velocity profiles in flows with low relative submergence, equations based on the log-law correctly describe the velocity profile over these flow conditions (Ferguson 2007). The velocity distributions measured in the experiments of the present research showed a clear logarithm tendency from the water surface

to Z_δ (Figure 4.4-c and Figure 4.7). Moreover, Rouzes et al. (2018) suggested that the logarithmic layer could be observed for even lower submergence values and still be appropriate for modeling the roughness parameters and flow resistance. The same results can be found in the literature (Aberle and Smart 2003; Einstein and El-Samni 1949; Fernández 2019; Grass 1971; Koll 2006; Nezu and Nakagawa 1993; Rousseau 2019; Smart 1999).

The experiments using PTV as a velocity measurement technique accurately showed the near-bed velocity profile to be logarithmic from the water surface to near the bed particle's crests (Figure 4.7), and we assumed it to be linear below the crests until piston flow was achieved (Figure 4.1). This confirms the findings of Amir and Castro (2011) and Eiff et al. (2014) that logarithmic law can penetrate the roughness sublayer, contrary to the classical view that it exists above the roughness sublayer (Jiménez 2004; Nikora et al. 2001). For a more detailed examination of all the velocity profile adjustments, please refer to *Appendix B: Supplemental Figures and Tables*.

In contrast, some researchers (Bathurst 1985; Ferro 2003a; Ferro and Baiamonte 1994; Jarrett 1990; Katul et al. 2002) have noted that velocity profile distributions under low relative submergence conditions are S-shaped. However, it has been proved that the incorrect reference level definition may produce some deviations from the log-law profile (Figure 4.4-a), due to forcing the log-law to pass over the crests.

4.6.4.a. Velocity profile adjustment to the logarithmic law

As the results, shown on semi-log paper, demonstrate that the dimensionless variables of the theoretical equation fit a straight line (Figure 4.4), a log-law was applied to describe the velocity profile throughout the complete water depth of the turbulent layer on data obtained in this research under low relative submergence with a porous bed over a steep channel. The methodology proposed in this research optimizes different variables (roughness height, reference level, the Von Karman constant, and shear velocity, among others) to obtain the minimum root mean square error of the proposed functions, which is similar to what Ferguson (2021) proposed recently, which is to calibrate k_s/D_{84}. The reference level was defined at a shifting distance below the bed particle crests (Aberle and Smart 2003; Einstein and El-Samni 1949; Fernández 2019; Grass 1971; Koll 2006; Nezu and Nakagawa 1993; Rousseau 2019; Smart 1999). That is why three different zones can be identified in the velocity profile, namely a subsurface zone, a roughness region, and the top part of the profile. It is assumed that the flow has a constant velocity in the first zone, a piston flow (Rousseau 2019), a very thin layer

with a linear distribution approximation on the second, and a log-law velocity profile distribution in the rest.

The height at which the reference level will be located is in the zone where the transition from a constant to a linear velocity distribution happens. This zone is complex to characterize, since the Reynolds number in the interstitial flow ranges from 7300 to 17900 ($\mathrm{Re} = 4R_h^{\inf} U_{\inf} / \nu$). However, the Reynolds number in the free flow is above 11500 for all the profiles. In this way, the flow over the particle bed transfers momentum to the water under the crests of the stones from a certain depth inside the bed layer (equivalent to the shifting distance).

Although Rousseau (2019) studied this transition zone in detail, a more straightforward assumption was made in this research; that is, the log-law was extended until Z_δ (the water level at which the velocity equals to u_*); from this point until the interstitial velocity was reached, a linear distribution was assumed; and, from this last point until the bottom of the flume, a piston flow was assumed.

As previously mentioned, the interstitial velocity increased as α increased (Figure 4.3-a), and consequently, the minimum velocity of the velocity profiles increased as the slope increased. However, due to the low values of $U_{\inf}$, these changes in the infiltrated velocities cannot be observed in the graphics (Figure 4.7). Furthermore, as the slope increased, the longitudinal momentum increased too, and hence also u_*.

4.7. Addendum – Sensitivity analysis of datum localization on velocity distribution

The reference datum is a critical aspect of the measurements taken in this study, as it provides a fixed point from which all other measurements are referenced. As such, any changes in the reference datum could potentially impact the results of the study. The sensitivity analysis conducted in this addendum explores the effect of different reference datum definitions on the measurements taken in the study. The analysis includes a range of scenarios that simulate variations in the location and elevation of the reference datum, and the results are presented in a way that enables the reader to compare and contrast the impact of each scenario on the study findings.

Four profiles with flume slopes of 2, 3, 6, and 10% and three datum locations for each slope were considered (Figure 4.8): the adjusted shifting distance (δ_{incr}^{opt}), a datum above the top crests (δ_{incr}^{-}), and a datum below the precise datum (δ_{incr}^{+}). It is worth noting that a positive shifting distance (δ_{incr}^{+}) positions the datum below the crests, while a negative one(δ_{incr}^{-}) positions it above the crests. The adjusted shifting distance has been obtained through the optimization equations (4.7) and (4.8).

Deviations from the precise datum level can significantly affect the velocity profile (Figure 4.8), particularly in the near-bed region (left-bottom side of Figure 4.8), as previously noted by Yu an Tan (2006). The impact of datum localization is more pronounced for steeper channels (Figure 4.8-c and Figure 4.8-d), even though the shifting distances assessed on the 6 and 10% flume slope are smaller those on the 2 and 3%. This increased sensitivity to the datum location is because as water depths become smaller, the velocity profile is centred only on the bottom part of the plot, which corresponds to the near-bed region.

Regardless of the flume slope, a datum located above (δ_{incr}^{-}) the theoretical-adjusted datum produces smaller water depths, while a datum below (δ_{incr}^{+}) it produces greater water depths (Figure 4.8). Therefore, given a certain water high (z_i), the dimensionless velocity on the δ_{incr}^{-} will be higher that the velocity on the adjusted. On the contrary, the dimensionless velocity on the δ_{incr}^{+} will produce smaller velocities (Figure 4.8).

The common practise to define the reference level at the top of the crests corresponds to a shifting distance δ_{incr}^{-}. In these cases, the velocity profile may exhibits an “S-shaped” pattern. The S-shaped profile is characterized in the literature (Bathurst 1985; Ferro 2003a; Ferro and Baiamonte 1994; Jarrett 1990; Katul et al. 2002) as a two-layer flow, with a slow layer that occupies the roughness space and a faster flow layer moving above it. This faster flow moves

with greater velocities than predicted by the log-law, and between both layers, there is an inflection point that lies above the crests of the roughness elements. However, our sensitivity analysis suggests that these increased velocities can be explained by a datum defined above the adjusted one (Figure 4.8). In conclusion, a displacement towards the "precise" datum can lead to an S-shaped profile with a point of inflection that moves with the shifting distance of the datum.

In conclusion, this addendum highlights the critical role of the reference datum in velocity profile measurements. Our sensitivity analysis shows that variations in the location and elevation of the datum can significantly impact the velocity profile, particularly in the near-bed region. This analysis highlights underscore the importance of careful consideration of the reference datum in future velocity profile measurements to ensure accurate and reliable results.

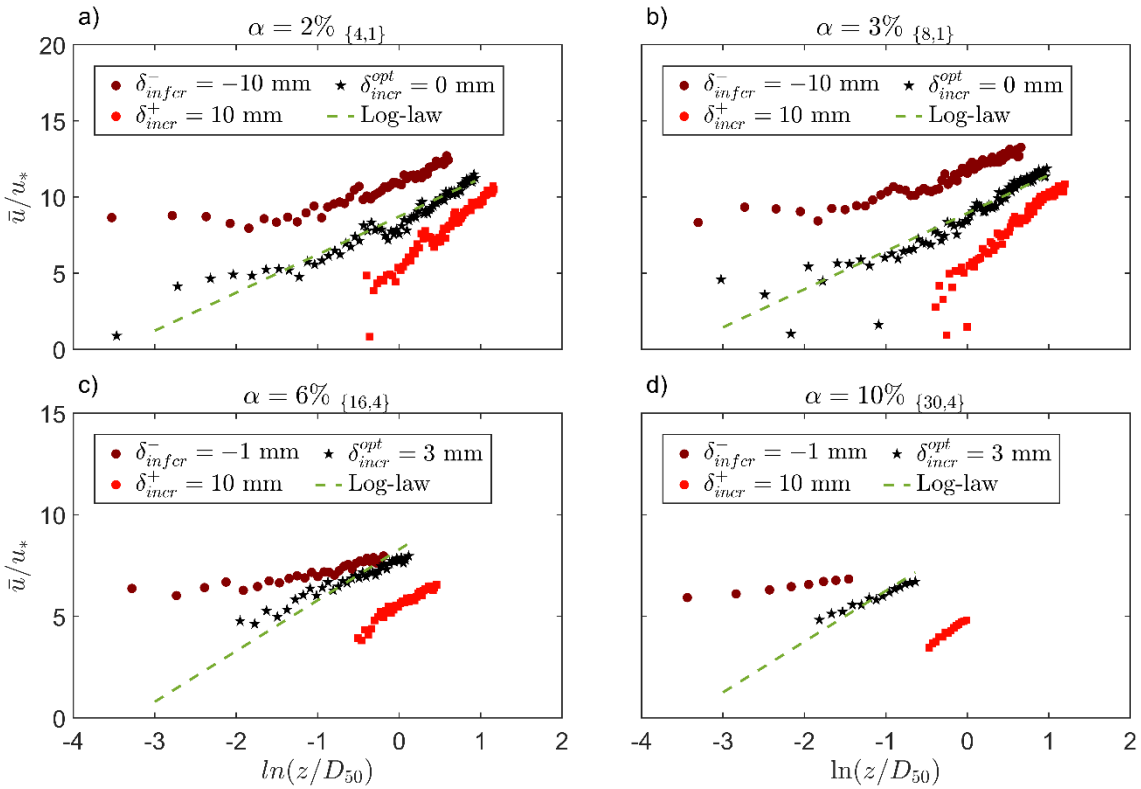

Figure 4.8. Dimensionless log profiles in the horizontal semi-log scale for a 2, 3, 6, and 10% flume slope given different shifting distances of the reference level.

Chapter 5: Roughness Height Parameter

Building upon the variables obtained in Chapter 4, this chapter provides a more detailed analysis of the roughness parameters specified in the log-law equation.

5.1. Introduction

The parameters of the logarithmic law (i.e. k , d , k_s , and B) have been the subject of extensive discussion since its development for rough beds. However, researchers have faced difficulties in determining meaningful values of k_s and water depths as well as Von Karman constants different from the standard 0.4 (Koll 2006). Such challenges have been reported in the literature over the last few decades, mainly due to the ambiguous definition of the water depth origin.

To overcome this issue, Nikora et al. (2002) introduced a redefined zero-plane displacement height, which allowed for determining the parameters of the vertical velocity profile within the wall region without making any fixes assumptions. While *Chapter 4* focused on this plane displacement, this chapter aims to assess the impact of this displacement and low relative submergences effect to the roughness height parameter (K) from the velocity profile distribution.

5. 1. 1. Velocity distribution in rough channels

The relationship between the local mean velocity at a certain distance to the bed ($\overline{u(z)}$) and shear velocity (u_*) in a turbulent flow was obtained by Keulegan (1938) from previous work from Prandtl (1926) and Nikuradse's (1933) experiments. He proposed a general expression of the velocity distribution law as shown in the equation (5.1). Where z is the water depth, K is the average projection of the roughness, and A and B are coefficients.

$$\frac{\overline{u(z)}}{u_*} = B + A \log\left(\frac{z}{K}\right) \tag{5.1}$$

Keulegan (1938) extended Nikuradse's studies to channels, proposing the equation (5.2) for hydraulically rough flow regimes. In which k is the Von Karman constant, u_* is the shear velocity, ν is the kinematic velocity and a_r is a parameter obtained from the linear trend observed from Nikuradse's experiments (Figure 5.1) and defined by equation (5.3). It has a slope equal to $1/k$ and a y-intercept of 8.5.

$$\frac{\overline{u(z)}}{u_*} = a_r + \frac{1}{k}\ln\left(\frac{zu_*}{\nu}\right) \tag{5.2}$$

$$a_r = 8.5 - \frac{1}{k}\ln\left(\frac{k_s u_*}{\nu}\right) \tag{5.3}$$

Nikuradse's experiments and Keulegan investigation identified critical numbers to define a transition region in which kinematic viscosity and relative roughness affect friction (i.e. $3.3 < k_s\, u_*/\nu < 67$). However, the generality of Nikuradse's results has been questioned due to the limited length of the pipes used in the study. That is why these critical numbers were

updated by Schlichting (1968) to $\mathrm{Re}^* \leq 5$ for a hydraulically smooth regime and $\mathrm{Re}^* > 70$ for a hydraulically rough regime.

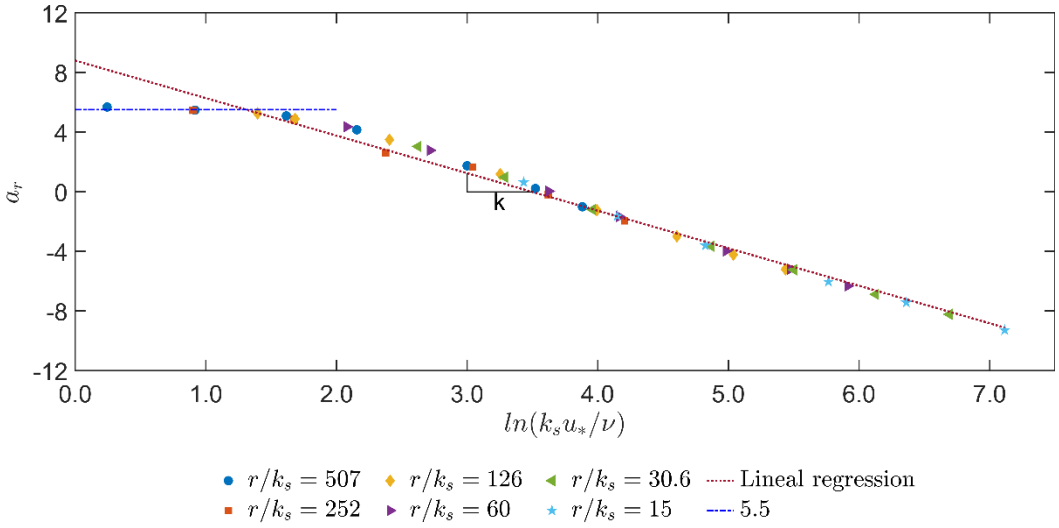

Figure 5.1. Characteristic α_r as a function of roughness Reynolds number (Re^*) for circular pipes with surfaces of closely packed grain sand grains, according to Nikuradse (Keulegan 1938)

Therefore, substituting equation (5.3) into equation (5.2) yields the well-known law of velocity distribution for rough beds (equation (5.4)). Which corresponds to the initial proposal in equation (5.1), with $B = 8.5$, $A = 1/k$, and $K = k_s$. Nikuradse's roughness sand height (k_s) is known as the height of the relative roughness in Keulegan's equation. The constant 8.5 in equation (5.4) is equivalent to the 30 inside the natural logarithm in equation (4.2).

$$\frac{\overline{u(z)}}{u_*} = \frac{1}{k}\ln\left(\frac{z}{k_s}\right) + 8.5 \tag{5.4}$$

5. 1. 2. Relative roughness height definition

Obtaining the roughness height (k_s) or the average projection of the roughness (K) presents a challenge in applying the log-law equation, given the crucial role of relative submergence, packing, granulometry, and particle placement. Flow resistance models in the literature typically rely on Nikuradse's (1933) basic approach to parameterize bed roughness. In his approach, the equivalent sand roughness ($K = k_s$) is estimated as a multiple of the characteristic grain size (equation (5.5)). The texture factor (α_t) accounts for the effects of shape, particle packing, and relative submergence (R_h/D_{50}).

$$k_s = \alpha_t D_x \tag{5.5}$$

The choice of characteristic grain size varies between researchers, but a coarser-average grain size percentile is usually chosen. Several studies suggest that the most appropriate sediment scale is D_{84} (Chen et al. 2020a; Limerinos 1970; MacKenzie et al. 2018; Wiberg and Smith 1991;

Zimmermann and Church 2001), defining $\alpha_t = 1$ for deep flows and $\alpha_t \sim 4$ in the case of gravel beds with low submergence (Ferguson 2021). However, almost all studies use the intermediate grain, D_{50} (Clifford et al. 1992; Jiménez 2004; Keulegan 1938; Monsalve et al. 2017; Schlichting 1968) because it is easier to measure using standard sediment sampling techniques. Nevertheless, there is no consensus regarding the most appropriate measure of bed roughness for use in the flow resistance approach (Powell 2014). This reflects the fact that no single metric describes bed roughness comprehensively.

The texture factor is usually within $2 \leq \alpha_t \leq 5$ (Strickler 1923), assuming D_{50} as the sediment scale. However, its value is not clear in gravel-bed rivers; while Keulegan (1938) assumed a value of α_t =1, other authors found from empirical works other values for α_t in gravel rivers; e.g. 3.3 (Strickler 1923), 3.5 (Ferguson 2021), 5.9 (Millar 1999), 6.8 (Bray and Davar 1987; Clifford et al. 1992), 7.1 (López and Barragán 2003), 8.5 (Limerinos 1970), among others.

Some experimental data suggest that the formulation of Nikuradse can be used for surfaces made up of densely packed and uniformly sized-roughness elements (Powell 2014). However, under conditions of a wide range of particles sizes, packing, protrusions (Hassan and Reid 1990; Monsalve et al. 2017), and bed structure irregularities (Yager et al. 2018), the argument that a grain size can be used to parametrize bed roughness became challenging to sustain. That is why several researchers are developing alternatives to the traditional grain size approach to characterize bed roughness (Aberle and Smart 2003; Chen et al. 2020a; Ferguson 2021; Nitsche et al. 2012; Zimmermann and Church 2001). Some propose to use the standard deviation of bed elevation of the channel thalweg (σ_z) rather than D_{84} (Aberle and Smart 2003; Ferguson 2021). However, there is no consensus on whether σ_z or D_{84} better describes k_s in gravel-bed streams (Chen et al. 2020a). Therefore, until more effective topographic indices of boundary roughness can be identified, most flow resistance models continue to use the basic approach of Nikuradse to parametrize bed roughness.

Other researchers assume that Nikuradse's approach ($k_s \propto D_x$) is too simple to correctly define the flow's roughness, and they propose to obtain k_s from the mean velocity distributions in the region where it coincides with the log-law of the wall region (Nezu and Nakagawa 1993). These two different methods for determining k_s do not necessarily give the same result.

Another aspect to consider is that it may be challenging to determine the equivalent sand roughness k_s for an irregular or rough surface since water depth are unclear with rough surfaces (Clauser 1956; Jiménez 2004). In fact, with increasing geometric roughness heights, measured velocities corresponded less and less than those computed using the equation (5.4), especially

with low relative submergence, which resulted in k_s-values difficult to explain (Koll 2006). Clauser (1956) attributed this problem to the origin of the water depths; he introduced the zero-plane displacement height (as previously seen in *Chapter 4*). Usually, the shift δ_{incr} from some reference location (Jiménez 2004; Nikora et al. 2002) is determined empirically to maximize the quality of the logarithmic fitting shown in the equation (5.4). That is why k_s is no longer assumed as a geometric but rather a hydraulic parameter (Jiménez 2004), and it has become a measure of the hydraulic effect of bed roughness (Koll 2006).

5. 1. 3. Roughness function B

Like the roughness height parameter, some authors have investigated the behaviour of the roughness function B. The roughness function assumes different values depending on the flow regime type, as initially introduced by Keulegan (1938) (Figure 5.1).

B-value ranges between 7.1–9.7 (Figure 5.2) as a function of the roughness Reynolds number Re^* (Nikuradse 1933; Schlichting 1968). Over completely rough regime conditions ($\mathrm{Re}^* > 70$ or $\log(\mathrm{Re}^*) > 1.8$), B is a constant with a value of 8.5 (blue-dotted line in Figure 5.2). However, over hydraulically smooth regime conditions ($\mathrm{Re}^* < 5$ or $\log(\mathrm{Re}^*) < 0.7$) B is a function of the roughness Reynolds number and follows the linear regression shown in Figure 5.2 (in a green-dashed line) and described by the equation (5.6).

$$B = 5.5 + \frac{1}{k}\ln\left(\frac{u_* k_s}{\nu}\right) \tag{5.6}$$

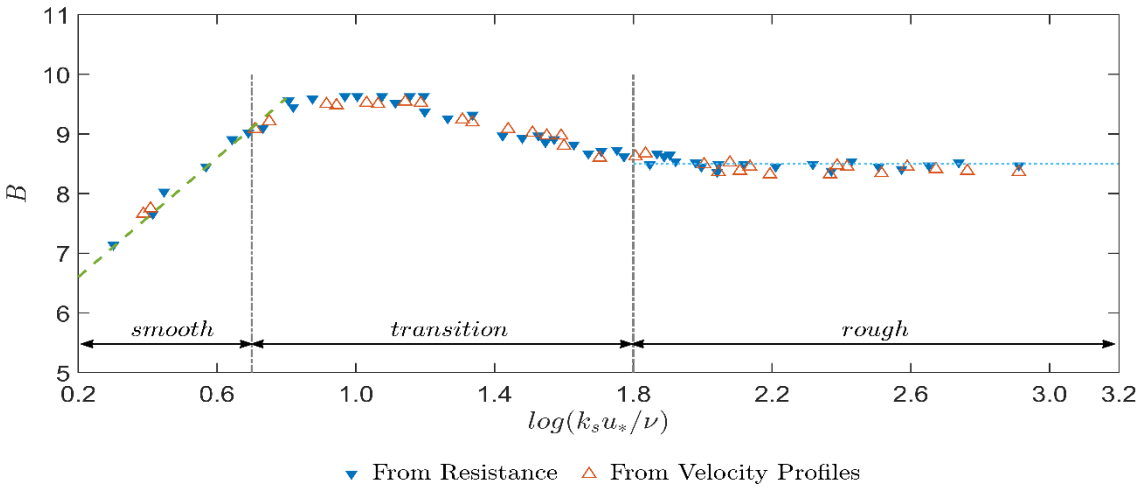

Figure 5.2. Roughness function B in terms of roughness Reynolds number ($Re^* = u_* k_s/\nu$) for Nikuradse's sand roughness curve (Schlichting 1968)

5.2. Materials and Methods

The experiments were conducted in the hydraulic steep flume of the Morphodynamics Laboratory I of the group GITS, described in *Chapter 2*.

This chapter examines how to define the roughness of the log-law equation (5.1) under rough conditions to investigate the influence of relative submergence and flume slope on the log-law equation. The approach assumes that $K = D_{50}/4$ has a fixed value and studies if the parameter B needs to be modified. Assuming K equal to $D_{50}/4$ follows the initial definition of the roughness height proposed by Nikuradse (1933), as $K = D_{50}/4$ is the average projection of the roughening, and it considers all the thoughts and crests of the bed. Moreover, assuming $K = D_{50}/4$ also take into account the results obtained on *Chapter 4*, as $D_{50}/4$ is similar to the average shifting distance of the reference datum.

In this chapter it is studied how the fixed roughness parameter is related to the roughness parameter obtained from the optimization functions (equations (4.7) and (4.8)) as shown in the equation (5.7). Where φ is the roughness coefficient:

$$K \propto \varphi k_s \tag{5.7}$$

Following Keulegan's results, the roughness parameter and the roughness height are related by a $\varphi = 1/30$ which corresponds to $B = 8.5$. Therefore, the coefficient B is also studied. B-values are obtained when $\ln(z/K) = 0$.

5.3. Results

Results from 119 velocity profiles are gathered in this section, with flume slopes that vary from 2% –10%, extremely low relative submergences ranging from 0.7–3.7, superficial flow discharges between 1 and 29 l/s, rough turbulent conditions ($\mathrm{Re} > 2000$ and $\mathrm{Re}^* > 68$) with a main gravel-bed material diameter of $D_{50} = 14.5$ mm. For a more detailed examination of all results, please refer to *Appendix B: Supplemental Figures and Tables*.

Figure 5.3 shows how the coefficient B (obtained when $\ln(z/K) = 0$) behaves differently for each of the roughness parameters plotted; Figure 5.3-a assumes $K = D_{50}$ (as Keulegan), Figure 5.3-b $K = D_{50}/2$ (as the maximum projection of the roughness obtained in *Chapter 4*), and Figure 5.3-c $K = D_{50}/4$ (as the average roughness projection). The B-value is obtained analytically when $\ln(z/K) = 0$ in each profile (shown as a grey dotted line in Figure 5.3).

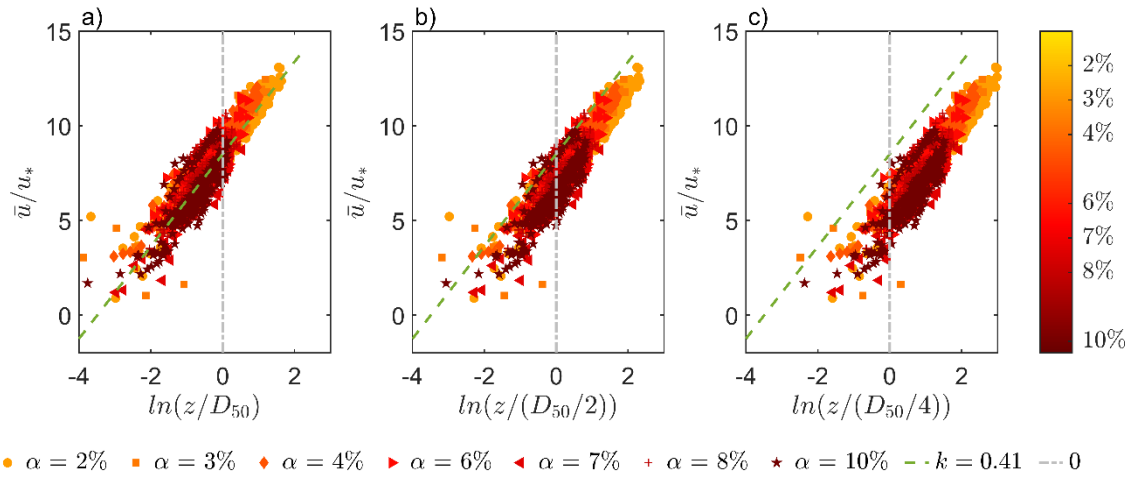

Figure 5.3. Dimensionless log profiles ($\bar{u}/u_*$) as a function of (a) $ln(z/D_{50})$, (b) $ln(z/(D_{50}/2))$, and (c) $ln(z/(D_{50}/4))$ in the horizontal semi-log scale.

Energy dissipation ($\varepsilon = Q_{\text{sup}} S_f \gamma / d\rho$, where Q_{sup} is the superficial discharge, S_f is the energy slope, γ water specific weight, d is the water depth, and ρ the water density (Fernández 2019)) increases as the discharge increased (Figure 5.4). Moreover, given the same superficial discharge, ε was greater for the steeper flumes.

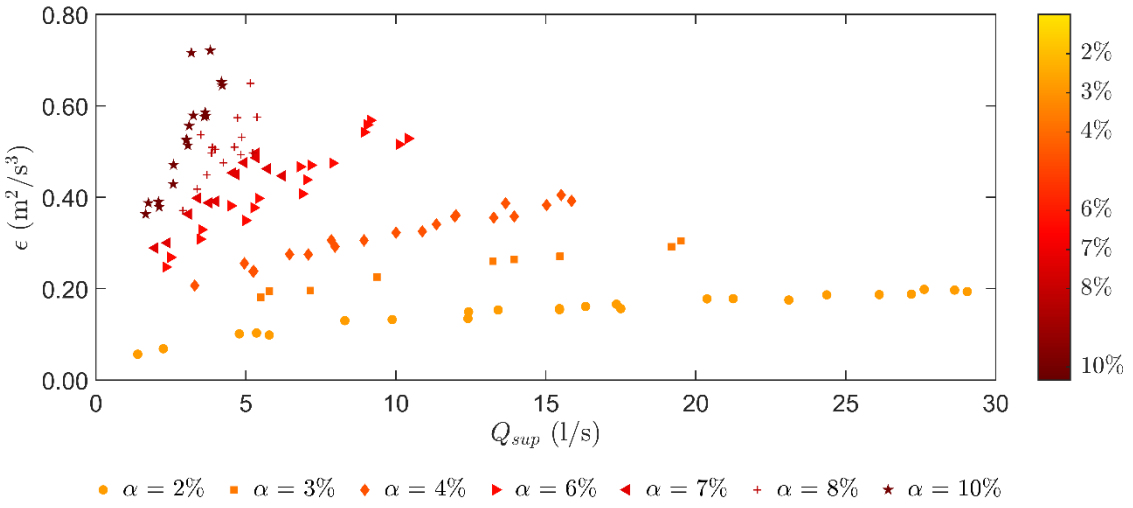

Figure 5.4. Energy dissipation (ε) as a function of superficial discharge.

In this subsection the value of the roughness parameter has been assumed as $K = D_{50}/4$ on the equation (5.1), and proportional to the k_s through the roughness coefficient φ as equation (5.7). Generally speaking, φ tends to slightly decrease as the flume slope steepens (Figure 5.5-a and Table 5.1). No clear trend is observed between φ with relative submergence (Figure 5.7-b), the shifting distance of the reference datum (Figure 5.5-c), and the energy dissipation (Figure 5.5-d). Dimensionless log profiles grouped by flume slopes are provided in *Appendix B: Supplemental Figures and Tables* to offer a comprehensive analysis of the impact of

relative submergence on roughness parameters. Nevertheless, a mean value of $\varphi = 9.26 \pm 2.83$ has been obtained for all the experiments. Therefore, the results are below the well-known 30.

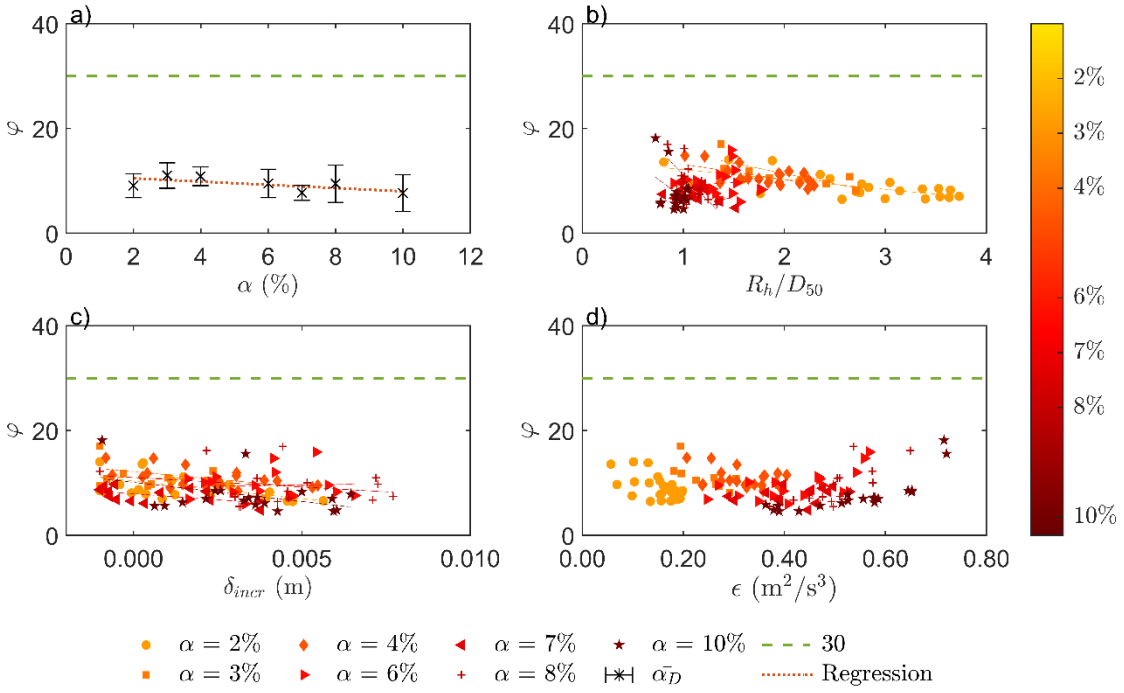

Figure 5.5. α_D as a function of (a) flume slope (α), (b) relative submergence (R_h/D_{50}), (c) shifting distance of datum (δ_{incr}), and (d) energy dissipation (ε).

Table 5.1. Statistical values of the roughness coefficient (φ) and B as a function of the flume slope.

	Roughness coefficient (φ)				B			
α (%)	$\bar{\varphi}$	σ_φ	min φ	max φ	$\bar{B}$	σ_B	min B	max B
2	9.07	2.26	6.46	14.03	5.31	0.54	4.34	6.48
3	11.02	2.43	8.18	17.02	5.75	0.53	4.51	6.30
4	10.84	1.79	8.42	14.81	5.64	0.78	3.85	6.54
6	9.50	2.69	5.97	15.89	5.66	0.82	4.37	7.26
7	7.70	1.43	4.84	9.75	4.54	1.04	1.56	5.88
8	9.42	3.56	5.45	16.96	5.74	0.90	4.14	7.47
10	7.64	3.49	4.58	18.15	4.81	1.01	2.31	6.88

Following Keulegan's (1938) methodology to obtain $B = 8.5$, a linear trend is applied between a_r, as defined in the equation (5.8), and $\ln(Ku_*/\nu)$ with $K = D_{50}/4$ (Figure 5.6). A y-intercept of 5.6 was obtained considering all the experiments (Figure 5.6). However, the y-intercept ranges between 4.9 and 6.1 when each slope is considered independently, it tends to become smaller with steeper slopes.

$$a_r = \frac{\bar{u}}{u_*} - \frac{1}{k}\ln\left(\frac{zu_*}{\nu}\right) \tag{5.8}$$

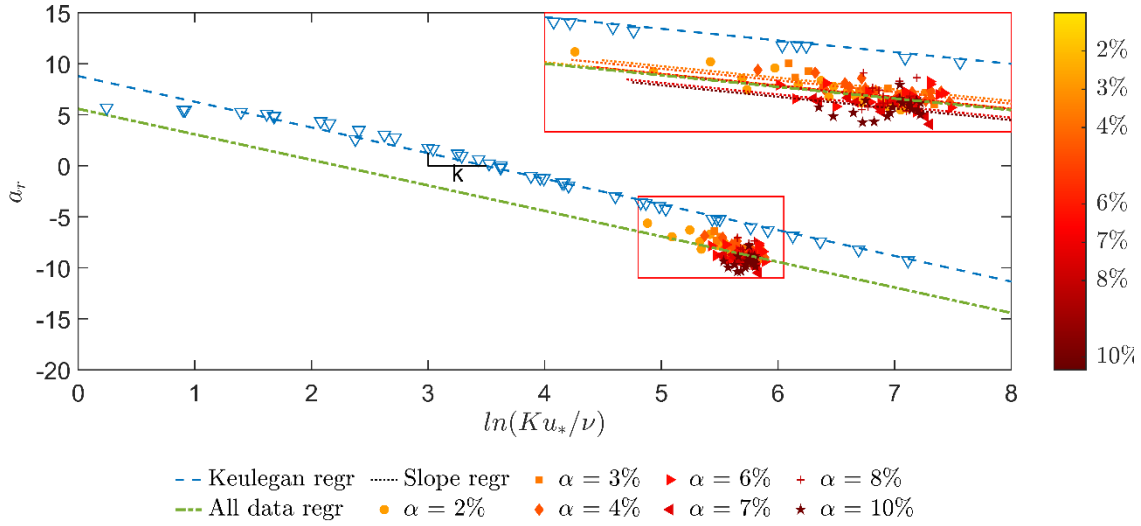

Figure 5.6. Characteristic a_r as a function of roughness Reynolds number (Re^*) for steep flume slopes under low relative submergence conditions and circular pipes with surfaces of closely packed grain sand grains, according to Nikuradse (Keulegan 1938).

Keulegan's (1938) methodology assumes that all profiles share a constant B parameter. In order to assess if this parameter changes as the flume slope or relative submergence vary, the parameter B was also found per each profile as the point at which $\ln(z/K) = 0$ following Schlichting (1968). Results are shown in Figure 5.7 and Table 5.1. Although the B-mean value of all experiments is 5.35 ± 0.91, there is also a trend to decrease the B-value as the flume slope steepens.

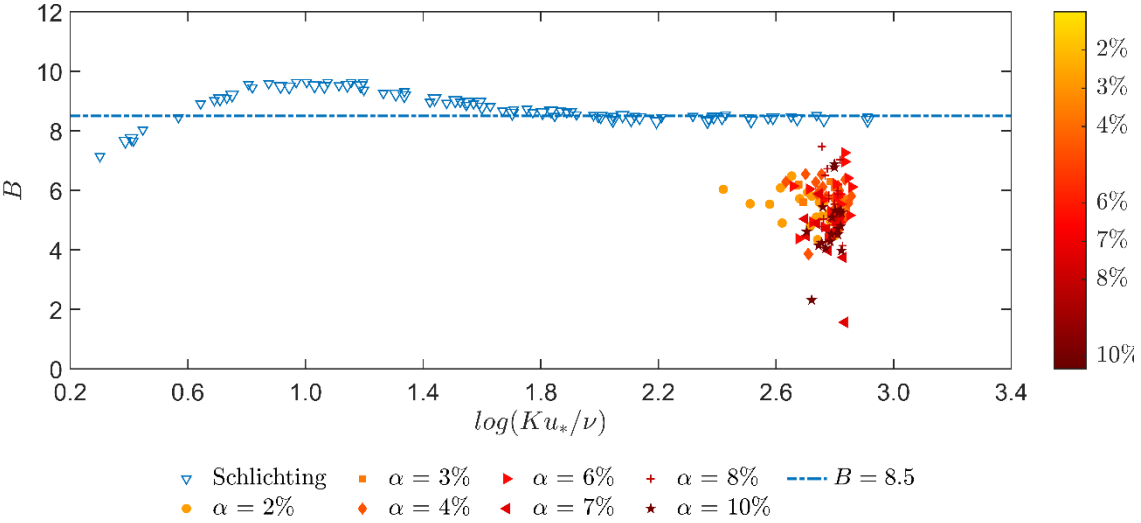

Figure 5.7. Roughness function B in terms of roughness Reynolds number ($Re^* = u_*K/\nu$) with Schlichting's (1968) data and data from experiments.

5.4. Discussion of Results

The adjusted profiles were found to conform to the log-law equation, despite the variations in roughness heights considered (Figure 5.3). However, the left side of each figure exhibited high dispersion of data due to velocity measurements taken in the near-bed region, which were constrained by limitations of the ADV/PTV instrumentation and the influence of the bed interference on the measurements.

If a constant roughness parameter was considered (i.e. $K = D_{50}$, $K = D_{50}/2$, or $K = D_{50}/4$ Figure 5.3-a, -b, -c, respectively) the profiles tended to displace downwards as the flume steepens. Therefore, the roughness function B tended to decrease as the flume slope steepens. Another clear trend was noted between energy dissipation (ε) and flume slope (Figure 5.4). With steeper slopes resulting in greater dissipation and smaller roughness parameters. However, no significant trend was observed between roughness parameters and relative submergence, as indicated in *Appendix B: Supplemental Figures and Tables*, which contains dimensionless log profiles grouped by flume slopes to analyze this impact comprehensively. Notably, energy dissipation (ε) was found to increase with higher discharges (Figure 5.4), which is analogous to the relationship between energy dissipation and relative submergence, where greater submergence resulted in higher dissipation, as expected.

To maintain consistency with Nikuradse's (1933) original definition of roughness height as the average projection of roughness elements, we assume that the roughness parameter is constant and equal to $D_{50}/4$ and proportional to the k_s through the roughness coefficient φ.

The well-known log-law equation (equation (4.2) or (5.4)) assumes that the roughness heigh and the equivalent sand roughness height have a constant relation and equal to 30. However, the results presented in this thesis show that not only this constant varies with changes on the flume slope and relative submergence (Figure 5.5), but it is smaller than the well-known 30 for high relative submergences.

The smaller roughness coefficient (φ) obtained in this study indicates that the roughness of the flow is greater than what is assumed in equation (4.2). This difference between the assumed value of 30 and the values attained in this study increase as the flume slope becomes steeper. As the flume becomes steeper, the energy dissipation (Figure 5.4) and the flux momentum increase, the reference datum becomes deeper (*Chapter 4*), and thus, the roughness increases.

This trend underscores the importance of considering the effect of flume slope when estimating roughness parameters or functions, as the roughness parameter (K) in the log-law equation is

not a geometric parameter but a hydraulic one (Jiménez 2004). It measures the hydraulic effect of bed roughness (Koll 2006) rather than the roughness of the bed itself. Therefore, it is crucial to account for the impact that the roughness has on the flow to accurately predict flow behaviour under different flow conditions.

5. 4. 1. Roughness function

As per Keulegan's (1938) findings, the roughness parameter and roughness height are related through $B = 8.5$, which is analogous to the 30 within the natural logarithm of equation (5.4). Consequently, we also investigate the coefficient B by conducting two separate analyses. The first follows Keulegan's method, which assumes a constant B value for all profiles (Figure 5.6). The second analysis assumes a unique B value for each profile to consider their distinct characteristics (Figure 5.7).

The experiments were conducted under rough conditions ($\mathrm{Re} > 11000$, Figure 2.15), resulting in all data plotted as a narrow cloud on the right-hand side of Figure 5.8. Due to the distance between the data and the point at which B was obtained (y-intercept), the extrapolation of the data may be biased. Nonetheless, all experiments yielded a y-intercept of 5.6 (Figure 5.6). Despite the known limitations of the data being concentrated on the roughness region of the plot, a consistent trend of decreasing B is observed with increasing flume slope, with B ranging from 4.9 — 6.1. This trend is also observed when each B value is obtained independently for each profile (Figure 5.7 and Table 5.1).

In both cases, B-values show a decreasing trend with increasing flume slope, indicating an increase in flow roughness. This trend is consistent with the previously observed trend with the roughness coefficient (φ) and suggests that the flume slope plays a critical role in determining the flow roughness.

5. 4. 2. Roughness height from velocity profile adjustment

This subsection assumes that the roughness coefficient value of 30 within the natural logarithm or the value of 8.5 at the outside, as defined in equation (5.1), are universally valid for all flow conditions. As a result, the variable that absorbs all the roughness effects is the roughness height k_s. This assumption is based on the wide use of the log-law with these constants in the literature.

Experimental data's velocity profile adjustment has followed the normalized least square regressions proposed in the equations (4.7) and (4.8) *Chapter 4*. These approaches are based on

a general normalized least square regression with a nonlinear optimization function, in which the roughness height k_s is one of the parameters.

The results show that k_s generally increases with steeper flume slopes (Figure 5.8-a). k_s tends to change as relative submergence changes (Figure 5.8-b), even using the same bed material throughout all the experiments. The same flume slope and bed particle grain diameter gave different values of k_s as relative submergence and flume slope changed, with more significant changes observed for lower relative submergence and steeper channel slopes.

Nevertheless, there is a high dispersion in k_s-values for steep flume slopes (Figure 5.8-b). This dispersion can be explained by the protuberances observed on the bed surface during the experiments. They were more frequent as the flume steepened. Such protrusions are recognized in the literature as the effective roughness of a given particle size (Hassan and Reid 1990; Monsalve et al. 2017). Additionally, the bed structure, in conjunction with the grain size, can significantly influence flow resistance, particularly in steep channels (Yager et al. 2018). Overall, the mean value of for all experiments is $k_s = 0.013 \pm 0.003$ m.

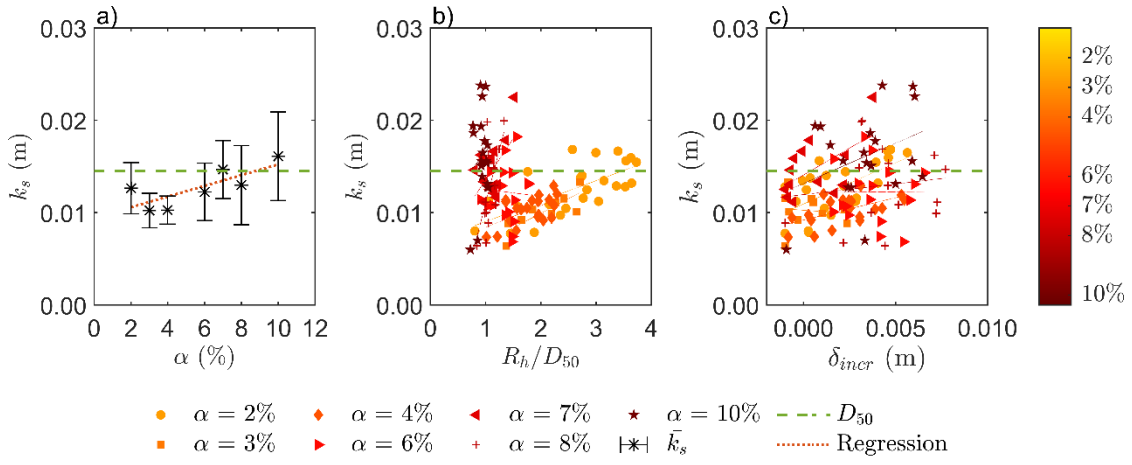

Figure 5.8. k_s as a function of (a) flume slope (α), (b) relative submergence (R_h/D_{50}), and (c) shifting distance of datum (δ_{incr}).

As mentioned earlier, there is typically a correlation between the equivalent roughness height (k_s) and particle grain diameter (D_x) in the literature, through the texture coefficient (α_t). Since the same main grain diameter was utilized in all the experiments, the same patterns seen in k_s are observed for the texture coefficient. Consequently, an average value of $\alpha_t = 0.88$ is obtained for all experiments, even though the values of the texture coefficient varied between 0.41 — 1.64. The values of obtained in this research (i.e. $\overline{\alpha_t} = 0.88$) are significantly lower than those commonly observed in alluvial rivers (i.e. 2) (Kamphuis 1974). Additionally, empirical values for gravel-bed rivers found in the literature range from 3.3 (Strickler 1923) to

8.5 (Limerinos 1970), with values of 6.8 (Bray and Davar 1987), 5.9 (Millar 1999), and 7.1 (López and Barragán 2003) reported as well. The extremely low values of α_t observed in this study are attributed to low values of relative submergence ($R_h/D_{50} < 4$, Figure 5.8-b). This phenomenon was also observed by Fernández (2019), who obtained values of around 1.31 for a relative submergence of approximately 1.5.

The present study's results suggest that the roughness parameter, k_s or α_t , are significantly influenced by relative submergence, a factor that is often overlooked in the literature. As a result, the assumption of a constant 30 value and a roughness height proportional to grain size diameter may no longer hold true for rough conditions over steep flume beds.

It should be noted that the present research only considered uniform sediment. However, the size distribution of the bed material is crucial to consider for non-uniform sediments since some researchers have observed that k_s is significantly greater than that obtained for uniform sediment (Millar 1999).

Chapter 6: Conclusions

This chapter incorporates the conclusions from the experiments (Chapter 2), velocity measurement techniques (Chapter 3), and velocity profile distribution (Chapter 4 and Chapter 5) under steep channels and low relative conditions are included in this chapter. The chapter concludes with a brief overview of future research directions.

6.1. Introduction

This doctoral thesis aimed to investigate the distribution of velocity profiles over permeable, steep, and rough beds under low relative submergence conditions. The research was based on data collected from experiments conducted in the flume of Morphodynamics Laboratory I at the GITS-UPC group. The flume slopes varied between 2% and 10%, with extremely low relative submergence ranging from 0.7 to 3.7, superficial flow discharges ranging from 1 to 29 l/s, and a bed material of $D_{50} = 14.5$ mm. The Reynolds number (Re) ranged from $1.15 \cdot 10^4$ to $1.86 \cdot 10^5$, the roughness Reynolds number (Re^*) ranged from 520 to 1440, and Froude numbers ranged between 0.84 and 2.25. The flow throughout all experiments was under rough turbulent conditions, and under the threshold of bed material movement.

The experiments conducted in this thesis were carried out with great care and attention to detail in order to ensure the validity and reliability of the results. The use of the same bed material with a specific particle size and density, combined with measurements taken at the same location, helped to minimize the effects of external factors and reduce the risk of errors or biases in the data, increasing confidence in the findings of the study.

However, despite these measures, the irregularity of the bed surface due its roughness was a significant source of error in the measurements. While the experimental methodology employed in this thesis attempted to mitigate this source of error using the “L” plates, it was not entirely successful due to their control only over the top of the crests and not the troughs. Consequently, the measurements were taken on different bed surfaces (some on a crest, others in a trough), limiting the accuracy of the results. To overcome this limitation, future research should consider using a high-resolution digital elevation model (DEM) of the bed surface to gain a better understanding of how the crests and troughs change over time and to ensure measurements are taken on the same bed surface.

Moreover, the use of "L" plates to place the bed material in the flume may have affected the roughness of the system, and their removal should be considered in future research to reduce any potential impact on the accuracy of measurements.

The initial velocity profile measurements were conducted using an ADV, but they were plagued by significant challenges. The issues arose mainly due to the ADV’s intrusion into the flow and the high turbulence of the flow. To take accurate measurements, the ADV requires a minimum water depth of 1.5 cm, which was not always achievable during the experiments due to the low relative submergence conditions. Moreover, the ADV’s intrusive nature and the high turbulence

levels introduced air into the control volume, leading to measurement errors. Additionally, measuring the near-bed region required placing the ADV at the bed surface, which caused local tensions and disturbed the experimental conditions by setting some bed particles in motion. A considerable amount of time and effort as expended in attempting to resolve these challenges with the ADV, but ultimately, the team shifted to PTV measurements.

To improve future experiments, the researchers recommend investigating alternative methods for measuring three-dimensional velocities, particularly in the bed-region, to assess the cavity driven flows and their respective vortices. These enhancements will allow for more precise and accurate measurements in future research. Overall, the study demonstrated a rigorous and accurate approach to scientific experimentation, which contributes to the credibility of the results obtained.

In the following sections, we provide a summary of our contributions in light of the objectives proposed in *Chapter 1*. The findings provide new insights into the velocity profile distribution over permeable, steep, and rough beds under low relative submergence conditions. Additionally, the experimental data and analysis methods developed in this thesis can serve as a valuable resource for future studies in this field.

6.2. Velocity Measurements

Velocity measurements were obtained using two different techniques: a side-looking 3D SONTEK ADV and a proposed PTV methodology. Out of the 119 velocity profiles collected in the laboratory, 94 were measured with ADV and 25 with PTV. The PTV methodology was developed in *Chapter 3* in response to the measurement errors and instabilities observed with the ADV during the experiment campaign, particularly when measuring near the bed or under extremely shallow water depths, where measurements with ADV were physically impossible to conduct.

Chapter 3 presents a comprehensive methodology for measuring velocity profiles in steep flows with low relative submergence, using a PTV technique. The proposed methodology consists of four main steps. Firstly, tracer particles, which are illuminated by a green LD sheet, are recorded by a high-speed camera. Secondly, particle detection of each frame is performed through a Gaussian mask. Particle tracking is then conducted by cross-correlation of the detected particles from one frame to the next. Thirdly, the tracked distances between consecutive frames are calibrated, and the velocity is computed using PTVlab software (Pantalano, 2020). Finally, the data cloud is filtered based on frequency intervals determined by water depth.

The PTV measurements proved to be more effective than the ADV measurements in certain conditions. Specifically, ADV measurements were limited to profiles where the tool could be physically placed (i.e. water depths larger than 1.5 cm). Additionally, the ADV was unable to measure near the bed due to the distance between the control volume and the transmitter and the interference from roughness elements on echo. The PTV methodology, on the other hand, was able to measure near the bed and provided more spatially distributed data. Moreover, the ADV measurements had greater deviations compared to the PTV measurements.

Furthermore, the ADV measurements required long sampling times to characterize the full profile (given the discrete measuring), resulting in possible changes to the bed conditions during measurement. Additionally, the ADV's intrusion into the flow caused by its physical introduction into the water caused local bed particle motion, leading to further changes in the bed conditions during measurement. These factors combined make the PTV methodology a more suitable technique for measuring velocity profiles in steep slope flows with low relative submergence, especially in areas near the bed where the ADV cannot provide accurate measurements.

The findings of this study demonstrated that the PTV methodology was effective in measuring velocity profiles near the bed and reduced the flow intrusion caused by the ADV. The PTV methodology was found to be a suitable technique for measuring velocity profiles in steep slope flows with low relative submergence. By providing more accurate and spatially distributed data, this methodology can improve our understanding of flow dynamics in steep and rough channels, which can have significant implications for various applications, such as flood prediction, river management, and ecosystem health.

6.3. Velocity Profile Distribution

Chapter 4 focused on the characterization of velocity profile distributions over steep channels with porous beds under low relative submergence conditions. The study specifically examined the effect of reference level definition on the velocity profiles, and its impact on the validity of the log-law formulation.

The experimental data presented in this study exhibits linear trends on a semilog axes and dimensionless plot, providing evidence that the log-law formulation can accurately define velocity profile distribution for flows under low relative submergence (between 0.8 and 4) with steep slopes (2–10%) over a porous bed, if the reference level is well-defined.

The log-law equation parameters together with the reference level were optimized by minimizing the proposed objective functions, that were based on a general normalized least

squares regression and utilized nonlinear function optimization methods to minimize the sum of squares. The approaches taken in this research followed the three-layer model proposed by Nikora et al. (2001) for permeable and hydraulic rough beds. This model divides the velocity profile into three different flow sections: the subsurface, roughness, and logarithmic layers. The bottom layer (subsurface layer) was assumed to be piston flow with uniform velocity ($U_{\inf}^{+}$). To parameterize the velocity distribution in the mid-layer (roughness layer), an analogy to the viscous layer was applied (Nikora et al. 2001), assuming a linear velocity distribution relationship. The top layer (logarithmic layer) velocity distribution was defined by the logarithmic profile as evidenced by the linear trends observed on a semilog and dimensionless plot.

In this manner, the experimental dimensionless velocity profiles collapsed to the log-law formulation once the optimization procedures were applied to the objective functions proposed, in which the reference datum definition has proven to be an essential variable to consider. This reference datum is located more profoundly in the bed layer as the longitudinal momentum flux ($\rho u_* u_*$) increases (Figure 4.5), incrementing the induced transversal momentum flux. As a result, the reference datum becomes deeper as the channel slope increases with the same bed material. Demonstrating that a fixed shifting distance of the reference datum (e.g. proportional to D_{50}) is not appropriate.

The presence of the interstitial flow through the bed pores, assumed as piston flow, resulted in a non-zero velocity ($U_{\inf}$) at the origin of the velocity profile. This interstitial velocity was found to be dependent on the channel slope (as the flume slope increased, $U_{\inf}$ increased correspondingly), while being $U_{\inf}$ independent of relative submergence ($U_{\inf}$ remained constant for various discharges with the same flume slope).

The optimization of the objective functions included the Von Karman constant k as one of the parameters. It was assumed that k is constant for all channel slopes and relative submergences, as it is controlled by the water nature. The reference level definition was found to be a crucial factor in determining the k-values for extremely low relative submergences ($R_h / D_{50} < 2$). The study found a mean value of 0.403 ± 0.002% for Von Karman's constant, which is equal to the well-known $k = 0.4$.

The findings presented in this study provide strong support for the validity of the Von Karman–Prandtl logarithmic velocity profile in hydraulically rough flows under low relative submergence conditions.

6.4. Roughness Height Parameter

Chapter 5 studies the roughness parameters of the log-law equation, with the focus on the impact of flume slope and relative submergence on roughness. To do so, it is studied how a fixed roughness parameter is related to the roughness parameter obtained from the optimization functions, through a proportional roughness coefficient φ.

The results show that not only φ varies with changes on the flume slope and relative submergence, but it is smaller than the well-known 30 found in high relative submergences. The smaller roughness coefficient (φ) obtained in this study indicates that the roughness is greater than what is assumed in equation (4.2). This difference between the assumed value of 30 and the values attained in this study increase as the flume slope becomes steeper.

The results show that increasing the flume slope leads to greater energy dissipation and flux momentum, resulting in a deeper reference datum (as discussed in *Chapter 4*) and ultimately an increase in roughness. While the results suggest that the mean roughness parameter, $K = D_{50}/4$, aligns with Nikuradse's (1933) original definition as the average projection of roughness, modifications to the constant 30 in equation (4.2) or the constant 8.5 in equation (5.4) are necessary to accurately account for the effect of the bed slope on the roughness.

The present study's results suggest that the roughness parameter, k_s or, the texture factor, α_t, are significantly influenced by relative submergence and flume slope, factors that are often overlooked in the literature. As a result, the assumption of a roughness height proportional to grain size diameter may no longer hold true for rough conditions over steep flume beds under low relative submergences.

These findings emphasize the significance of considering the effect of flume slope when estimating the roughness parameters, particularly in steep streams. Additionally, it is crucial to consider the unique characteristics of each profile to accurately predict flow behaviour under low relative submergence conditions in steep streams.

6.5. Recommendations for the Future

This thesis could be a springboard for understanding the morphological behaviour of mountain rivers to develop accurate methods to predict flow resistance and reduce the uncertainties in flood hazard mapping in mountain regions. However, there are significant knowledge gaps that need to be addressed.

- A better understanding of roughness parameters in low relative submergences and steep bed channels is needed. This can be achieved through experiments using alternative measurement systems such as PIV or LDV to validate the results of velocity distributions in low relative submergence flows with cavity driven flows.
- Additionally, future experiments should be conducted with various bed material grain sizes, to investigate its effect on the reference datum, and other variables of the log-law assessed in this study.
- Future experiments should also investigate the effect of non-uniform particle size distributions on the porosity and permeability of the bed and its influence on the log-law. Future research should consider using a high-resolution digital elevation model (DEM) of the bed surface.
- Accurately predicting flood levels depends on knowledge of the mean flow velocity in a channel, but measuring velocity can be difficult. Typically, velocity is estimated using a flow resistance equation based on a measured depth or discharge. However, traditional approaches from lowland rivers do not work well in mountain regions. To address this limitation, more research is needed to develop theoretical equations that can accurately predict velocity in steep streams with low relative conditions.
- Future experiments should be conducted with suspended sediment to better understand the effect of sediment transport on the velocity distribution and flow resistance under low relative submergences and steep streams.
- To examine the effects of slope and relative submergence under these flow conditions and verify the applicability of the Shields diagram, future experiments should aim to achieve the motion threshold on the bed material.
- Further research is needed to investigate the effects of subsurface flows on particle equilibrium.
- Future research should explore the application of these concepts to the formulation of riprap design, particularly for high mountain rivers.

Addressing these research gaps can improve our ability to predict flow resistance and reduce uncertainties in flood hazard mapping in mountain regions.

References

Aberle, J., and Smart, G. M. (2003). “The influence of roughness structure on flow resistance on steep slopes.” *Journal of Hydraulic Research*, 41(3), 259–269.

Adams, D. L. (2022). “Gravel-bed river behaviour : modelling and analysis of process feedbacks over spatio-temporal scales.” University of British Columbia.

Adams, D. L., and Zampiron, A. (2020). “Short communication: Multiscalar roughness length decomposition in fluvial systems using a transform-roughness correlation (TRC) approach.” *Earth Surface Dynamics*, Copernicus GmbH, 8(4), 1039–1051.

Adrian, R. J. (1984). “Scattering particle characteristics and their effect on pulsed laser measurements of fluid flow: speckle velocimetry vs particle image velocimetry.” *Applied Optics*, 23(11), 1690.

Adrian, R. J. (1991). “Particle-Imaging Techniques For Experimental Fluid-Mechanics.” *Annual Review of Fluid Mechanics*.

Adrian, R. J., and Westerweel, J. (2011). *Particle image velocimetry*. Cambridge university press.

Amir, M., and Castro, I. P. (2011). “Turbulence in rough-wall boundary layers: Universality issues.” *Experiments in Fluids*, Springer, 51(2), 313–326.

Ancey, C., and Pascal, I. (2020). “Estimating Mean Bedload Transport Rates and Their Uncertainty.” *Journal of Geophysical Research: Earth Surface*, Blackwell Publishing Ltd, 125(7).

Antonia, R. A., and Krogstad, P.-Å. (2001). “Turbulence structure in boundary layers over different types of surface roughness.” *Fluid Dynamics Research*, 28(2), 139–157.

Barkdoll, B. D. (2002). “Discussion of ‘Mean Flow and Turbulence Structure of Open-Channel Flow Through Nonemergent Vegetation’ by Fabián Lopez and Marcelo H. Garcia.” *Journal of Hydraulic Engineering*, 128(11), 1032–1032.

Bateman, A. (1993). “Formacion de frentes de onda Un estudio numerico y experimental.” Universitat Politècnica de Catalunya.

Bateman Pinzon, A., Medina Iglesias, V., and Guevara, A. (2010). “Experimental Study of the Influence of Non-Hydrostatic Pressure in Rip Rap Pier Protection.” *Scour and Erosion*, American Society of Civil Engineers, Reston, VA, 639–648.

Bathurst, J. C. (1985). “Flow Resistance Estimation in Mountain Rivers.” *Journal of Hydraulic Engineering*, 111(4), 625–643.

Bathurst, J. C. (1993). “Flow resistance through the channel network.” *Channel network hydrology*, Wiley, 69–98.

Bathurst, J. C. (2002). “At-a-site variation and minimum flow resistance for mountain rivers.” *Journal of Hydrology*, 269(1–2), 11–26.

Bathurst, J. C., Li, R. M., and Simons, D. B. (1979). *Hydraulics of mountain rivers*. Fort Collins, Colorado.

Bayazit, M. (1976). “Free Surface Flow In A Channel Of Large Relative Roughness.” *Journal of Hydraulic Research*, 14(2), 115–126.

BGC Engineering Inc. (2022). *Highway 8 Reinstatement: Geohazard Inventory and Risk Priorization*. Prepared for BC Ministry of Transportation.

Bray, D. I. (1980). “Evaluation of effective boundary roughness for gravel-bed rivers.” *Canadian Journal of Civil Engineering*, 7(2), 392–397.

Bray, D. I., and Davar, K. S. (1987). “Resistance to flow in gravel-bed rivers.” *Canadian Journal of Civil Engineering*, 14(6), 862–862.

Brevis, W., Niño, Y., and Jirka, G. H. (2011). "Integrating cross-correlation and relaxation algorithms for particle tracking velocimetry." *Experiments in Fluids*, 50(1), 135–147.

Buffington, J. M., and Montgomery, D. R. (1999). "Effects of hydraulic roughness on surface textures of gravel-bed rivers." *Water Resources Research*, 35(11), 3507–3521.

Byrd, T. C., Furbish, D. J., and Warburton, J. (2000). "Estimating depth-averaged velocities in rough channels." *Earth Surface Processes and Landforms*.

Canovaro, F., and Solari, L. (2007). "Dissipative analogies between a schematic macro-roughness arrangement and step-pool morphology." *Earth Surface Processes and Landforms*, 1628–1640.

Chen, X., Hassan, M. A., An, C., and Fu, X. (2020a). "Rough Correlations: Meta-Analysis of Roughness Measures in Gravel Bed Rivers." *Water Resources Research*, Blackwell Publishing Ltd, 56(8).

Chen, X., Zhang, M., and Yu, G. (2020b). "Depth-Averaged von Kármán Coefficient in Sediment-Laden Flows Using a Turbulent Kinetic Energy Balance." *Journal of Hydraulic Engineering*, 146(4), 06020003.

Chow, V. Te. (1959). *Open-channel hydraulics*. *McGraw Hill Book Company*, McGraw-Hill Book Company, New York.

Church, M., Hassan, M. A., and Wolcott, J. F. (1998). "Stabilizing self-organized structures in gravel-bed stream channels: Field and experimental observations." *Water Resources Research*, American Geophysical Union, 34(11), 3169–3179.

Clauser, F. H. (1956). "The Turbulent Boundary Layer." *Advances in Applied Mechanics*, 1–51.

Clifford, N. J., Robert, A., and Richards, K. S. (1992). "Estimation of flow resistance in gravel-bedded rivers: A physical explanation of the multiplier of roughness length." *Earth Surface Processes and Landforms*, John Wiley & Sons, Ltd, 17(2), 111–126.

Comiti, F., Cadol, D., and Wohl, E. E. (2009). "Flow regimes, bed morphology, and flow resistance in self-formed step-pool channels." *Water Resources Research*, 45(4), 1–18.

Comiti, F., Mao, L., Wilcox, A. C., Wohl, E. E., and Lenzi, M. A. (2007). "Field-derived relationships for flow velocity and resistance in high-gradient streams." *Journal of Hydrology*, 340(1–2), 48–62.

Coscarella, F., Penna, N., Servidio, S., and Gaudio, R. (2020). "Turbulence anisotropy and intermittency in open-channel flows on rough beds." *Physics of Fluids*, American Institute of Physics Inc., 32(11), 115127.

Davidson, S. (2016). "Modeling disturbance and channel evolution in mountain streams." University of British Columbia.

Davidson, S., Marin-Esteve, B., Schueder, R., Lockwood, K., and Jakob, M. (2022). "Modelling Bank Erosion in Gravel-Bed Rivers to Support Hazard Management." *Canadian Water Resources Association (CWRA 2022)*, Canmore, Alberta.

Eiff, O., Florens, E., and Moulin, F. Y. (2014). "Roughness parameters in shallow open-channel flows." *River Flow 2014*, Taylor & Francis Group.

Einstein, H. A., and Barbarossa, N. L. (1952). "River Channel Roughness." *Transactions of the American Society of Civil Engineers*, American Society of Civil Engineers, 117(1), 1121–1132.

Einstein, H. A., and El-Samni, E. S. A. (1949). "Hydrodynamic forces on a rough wall." *Reviews of Modern Physics*, 21(3), 520–524.

Ferguson, R. I. (2007). "Flow resistance equations for gravel- and boulder-bed streams." *Water Resources Research*, 43(5), 1–12.

Ferguson, R. I. (2010). “Time to abandon the Manning equation?” *Earth Surface Processes and Landforms*, 35(15), 1873–1876.

Ferguson, R. I. (2012). “River channel slope, flow resistance, and gravel entrainment thresholds.” *Water Resources Research*, 48(5), 1–13.

Ferguson, R. I. (2021). “Roughness Calibration to Improve Flow Predictions in Coarse-Bed Streams.” *Water Resources Research*, Blackwell Publishing Ltd, 57(6).

Fernández, C. (2019). “Experimental characterization of turbulence in steep rough streams.” Universitat Politècnica de Catalunya.

Ferreira, R. M. L. (2015). “The von Kármán constant for flows over rough mobile beds. Lessons learned from dimensional analysis and similarity.” *Advances in Water Resources*, 81, 19–32.

Ferro, V. (2003a). “ADV measurements of velocity distributions in a gravel-bed flume.” *Earth Surface Processes and Landforms*, 28, 707–722.

Ferro, V. (2003b). “Flow resistance in gravel-bed channels with large-scale roughness.” *Earth Surface Processes and Landforms*.

Ferro, V., and Baiamonte, G. (1994). “Flow velocity profiles in gravel-bed rivers.” *Journal of Hydraulic Engineering*, 120(1), 60–80.

Finelli, C. M., Hart, D. D., and Fonseca, D. M. (1999). “Evaluating the spatial resolution of an acoustic Doppler velocimeter and the consequences for measuring near-bed flows.” *Limnology and Oceanography*, 44(7), 1793–1801.

Franca, M. J., Ferreira, R. M. L., and Lemmin, U. (2008). “Parameterization of the logarithmic layer of double-averaged streamwise velocity profiles in gravel-bed river flows.” *Advances in Water Resources*, 31(6), 915–925.

Gillett, N. P., Cannon, A. J., Malinina, E., Schnorbus, M., Anslow, F., Sun, Q., Kirchmeier-Young, M., Zwiers, F., Seiler, C., Zhang, X., Flato, G., Wan, H., Li, G., and Castellan, A. (2022). “Human influence on the 2021 British Columbia floods.” *Weather and Climate Extremes*, Elsevier, 36, 100441.

Grass, A. J. (1971). “Structural features of turbulent flow over smooth and rough boundaries.” *Journal of Fluid Mechanics*, 50(2), 233–255.

Grass, A. J., Stuart, R. J., and Mansour-Tehrani, M. (1991). “Vortical structures and coherent motion in turbulent flow over smooth and rough boundaries.” *Philosophical Transactions of the Royal Society of London. Series A: Physical and Engineering Sciences*, 336(1640), 35–65.

Hassan, M. A., and Reid, I. (1990). “The influence of microform bed roughness elements on flow and sediment transport in gravel bed rivers: A reply.” *Earth Surface Processes and Landforms*, 15(5), 739–750.

Hassan, Y. A., Blanchat, T. K., and Seeley, C. H. (1992). “PIV flow visualisation using particle tracking techniques.” *Measurement Science and Technology*, 3(7), 633–642.

Henderson, F. M. (1966). *Open Channel Flow*. Macmillan, New York.

Hey, R. D. (1979). “Flow Resistance in Gravel-Bed Rivers.” *Journal of the Hydraulics Division*, American Society of Civil Engineers, 105(4), 365–379.

Jarrett, R. D. (1984). “Hydraulics of high - gradient streams.” *Journal of Hydraulic Engineering*, 110(11), 1519–1539.

Jarrett, R. D. (1987). “Errors in slope-area computations of peak discharges in mountain streams.” *Journal of Hydrology*, 96(1–4), 53–67.

Jarrett, R. D. (1990). “Hydrologic and hydraulics research in mountain rivers.” *Water Resources*

Bulletin, 26(3), 419–429.

Jiménez, J. (2004). "Turbulent Flows over Rough Walls." *Annual Review of Fluid Mechanics*, 36(1), 173–196.

Kamphuis, J. W. (1974). "Determination of sand roughness for fixed beds." *Journal of Hydraulic Research*, Taylor & Francis Group, 12(2), 193–203.

Katul, G., Wiberg, P., Albertson, J., and Hornberger, G. (2002). "A mixing layer theory for flow resistance in shallow streams." *Water Resources Research*, 38(11), 32-1-32–8.

Keulegan, G. H. (1938). "Laws of turbulent flow in open channels." *Journal of Research of the National Bureau of Standards*, 21(Research Paper 1151), 707–741.

Koll, K. (2006). "Parameterisation of the vertical velocity profile in the wall region over rough surfaces." *River Flow 2006*, Taylor & Francis, 163–172.

Lamb, M. P., Brun, F., and Fuller, B. M. (2017a). "Hydrodynamics of steep streams with planar coarse-grained beds: Turbulence, flow resistance, and implications for sediment transport." *Water Resources Research*, 53(3), 2240–2263.

Lamb, M. P., Brun, F., and Fuller, B. M. (2017b). "Direct measurements of lift and drag on shallowly submerged cobbles in steep streams: Implications for flow resistance and sediment transport." *Water Resources Research*, Blackwell Publishing Ltd, 53(9), 7607–7629.

Lamb, M. P., Dietrich, W. E., and Venditti, J. G. (2008). "Is the critical shields stress for incipient sediment motion dependent on channel-bed slope?" *Journal of Geophysical Research: Earth Surface*, 113(2), 1–20.

Lawrence, D. S. L. (2000). "Hydraulic resistance in overland flow during partial and marginal surface inundation: Experimental observations and modeling." *Water Resources Research*, American Geophysical Union, 36(8), 2381–2393.

Lee, A. J., and Ferguson, R. I. (2002). "Velocity and flow resistance in step-pool streams." *Geomorphology*, 46(1–2), 59–71.

Lemnitzer, A., Stark, N., Anoyatis, G., Doornbos, S., Francois, S., Gardner, M., George, M., van Ginkel, K., Leunge, L., Mavritsakis, A., van Marle, M., Mueller, J., Nichols, E., Rattez, H., Schuettrumpf, H., Stamm, J., and Willems, J. (2021). *Geotechnical Reconnaissance of the 2021 Western European Floods.*

Limerinos, J. T. (1970). *Determination of the Manning Coefficient From Measured Bed Roughness in Natural Channels*. *Geological Survey Water-Supply*.

Lohrmann, A., Cabrera, R., and Kraus, N. C. (1994). "Acoustic-Doppler Velocimeter (ADV) for Laboratory Use." *Fundamentals and Advancements in Hydraulic Measurements and Experimentation*, 351–365.

López, R., and Barragán, J. (2003). "Expresiones para la determinación del factor de fricción en ríos de fuerte pendiente." *Ingeniería Civil*, 130, 43–50.

López, R., and Barragán, J. (2008). "Equivalent Roughness of Gravel-Bed Rivers." *Journal of Hydraulic Engineering*, American Society of Civil Engineers (ASCE), 134(6), 847–851.

López, R., Barragán, J., and Colomer, M. À. (2007). "Flow resistance equations without explicit estimation of the resistance coefficient for coarse-grained rivers." *Journal of Hydrology*, 338(1–2), 113–121.

MacKenzie, L. G., Eaton, B. C., and Church, M. (2018). "Breaking from the average: Why large grains matter in gravel-bed streams." *Earth Surface Processes and Landforms*, John Wiley and Sons Ltd, 43(15), 3190–3196.

Marin-Esteve, B., Bateman Pinzón, A., and Sosa Pérez, R. (2021). "Velocity profile distribution in steep channels with low relative submergence conditions [Dataset]." Universitat

Politècnica de Catalunya.

Martín-Vide, J. P., Bateman, A., Berenguer, M., Ferrer-Boix, C., Amengual, A., Campillo, M., Corral, C., Llasat, M. C., Llasat-Botija, M., Gómez-Dueñas, S., Marín-Esteve, B., Núñez-González, F., Prats-Puntí, A., Ruiz-Carulla, R., and Sosa-Pérez, R. (2023). "Large wood debris that clogged bridges followed by a sudden release. The 2019 flash flood in Catalonia." *Journal of Hydrology: Regional Studies*, 47, 101348.

Martin, V., Fisher, T. S. R., Millar, R. G., and Quick, M. C. (2002). "ADV Data Analysis for Turbulent Flows: Low Correlation Problem." *Hydraulic Measurements and Experimental Methods 2002*, American Society of Civil Engineers, Reston, VA, 1–10.

Maxwell, A. R., and Papanicolaou, A. N. (2001). "Step-pool morphology in high-gradient streams." *International Journal of Sediment Research*, 16(3), 380–390.

Meyer-Peter, E., and Müller, R. (1948). "Formulas for bed-load transport." *Proceedings of 2nd meeting of the International Association for Hydraulic Structures Research*, Stockholm, 39–64.

Millar, R. G. (1999). "Grain and form resistance in gravel-bed rivers." *Journal of Hydraulic Research*, 37(3), 303–312.

Mohr, S., Ehret, U., Kunz, M., Ludwig, P., Caldas-Alvarez, A., Daniell, J. E., Ehmele, F., Feldmann, H., Franca, M. J., Gattke, C., Hundhausen, M., Knippertz, P., Küpfer, K., Mühr, B., Pinto, J. G., Quinting, J., Schäfer, A. M., Scheibel, M., Seidel, F., and Wisotzky, C. (2022). "A multi-disciplinary analysis of the exceptional flood event of July 2021 in central Europe. Part 1: Event description and analysis." *Natural Hazards and Earth System Sciences*.

Monsalve, A., Yager, E. M., and Schmeeckle, M. W. (2017). "Effects of Bed Forms and Large Protruding Grains on Near-Bed Flow Hydraulics in Low Relative Submergence Conditions." *Journal of Geophysical Research: Earth Surface*, Blackwell Publishing Ltd, 122(10), 1845–1866.

Mueller, E. R., Pitlick, J., and Nelson, J. M. (2005). "Variation in the reference Shields stress for bed load transport in gravel-bed streams and rivers." *Water Resources Research*, 41(4), 1–10.

Mujal-Colilles, A. (2013). "PIV applications in vortex rings and oscillatory boundary layers." Universitat Politècnica de Catalunya.

Nakagawa, H., and Nezu, I. (1977). "Prediction of the contributions to the Reynolds stress from bursting events in open-channel flows." *Journal of Fluid Mechanics*, 80(1), 99–128.

Nezu, I., and Nakagawa, H. (1993). *Turbulence in Open-Channel Flows*. (I. Monograph, ed.), A.A. Balkema, Rotterdam.

Nikora, V. I., and Goring, D. (2000). "Flow Turbulence over Fixed and Weakly Mobile Gravel Beds." *Journal of Hydraulic Engineering*, 126(9), 679–690.

Nikora, V. I., Goring, D., McEwan, I., and Griffiths, G. (2001). "Spatially Averaged Open-Channel Flow over Rough Bed." *Journal of Hydraulic Engineering*, 127(2), 123–133.

Nikora, V. I., Koll, K., McEwan, I., McLean, S., and Dittrich, A. (2004). "Velocity distribution in the roughness layer of rough-bed flows." *Journal of Hydraulic Engineering*.

Nikora, V. I., Koll, K., McLean, S., Dittrich, A., and Aberle, J. (2002). "Zero-plane displacement for rough-bed open-channel flows." *Fluvial Hydraulics River Flow 2002*, 83–92.

Nikuradse, J. (1933). *Strömungsgesetze in rauhen Rohren (Laws of flow in rough-pipes)*. *Forschung auf dem Gebiete des Ingenieurwesens*.

Niño, Y., and Garcia, M. H. (1996). "Experiments on particle—turbulence interactions in the near–wall region of an open channel flow: implications for sediment transport." *Journal of Fluid Mechanics*, 326, 285–319.

Nitsche, M., Rickenmann, D., Kirchner, J. W., Turowski, J. M., and Badoux, A. (2012). "Macroroughness and variations in reach-averaged flow resistance in steep mountain streams." *Water Resources Research*.

NORTEK. (2018). "The Comprehensive Manual for Velocimeters." NORTEK.

Ohmi, K., and Li, H.-Y. (2000). "Particle-tracking velocimetry with new algorithms." *Measurement Science and Technology*, 11(6), 603–616.

Okamoto, K., and Hassan, Y. A. (1995). *New tracking algorithm for particle*. *Experiments in Fluids*, Springer-Verlag.

Packman, A. I., Salehin, M., and Zaramella, M. (2004). "Hyporheic Exchange with Gravel Beds: Basic Hydrodynamic Interactions and Bedform-Induced Advective Flows." *Journal of Hydraulic Engineering*, 130(7), 647–656.

Pantalano, A. (2020). "PTVlab (Particle Tracking Velocimetry - lab)." MATLAB Central File Exchange.

Parker, G. (1991). "Selective Sorting and Abrasion of River Gravel. II: Applications." *Journal of Hydraulic Engineering*, 117(2), 150–171.

Perry, A. E., and Joubert, P. N. (1963). "Rough-wall boundary layers in adverse pressure gradients." *Journal of Fluid Mechanics*, 17(2), 193–211.

Powell, D. M. (2014). "Flow resistance in gravel-bed rivers: Progress in research." *Earth-Science Reviews*, Elsevier B.V., 136, 301–338.

Prandtl, L. (1926). "Über die Entstehung der Turbulenz (Turbulent Flows over Rough Walls)." *Verhandlungen des II. Internationalen Kongresses für Technische Mechanik*, Füssli, Zürich, 62–75.

Raffel, M., Willert, C. E., Scarano, F., Kähler, C. J., Wereley, S. T., and Kompenhans, J. (2018). *Particle Image Velocimetry*. *Encyclopedia of Nanotechnology*, Springer International Publishing, Cham.

Raupach, M. R., Antonia, R. A., and Rajagopalan, S. (1991). "Rough-Wall Turbulent Boundary Layers." *Applied Mechanics Reviews*, 44(1), 1–25.

Recking, A. (2009). "Theoretical development on the effects of changing flow hydraulics on incipient bed load motion." *Water Resources Research*, 45(4), 1–16.

Recking, A., Frey, P., Paquier, A., Belleudy, P., and Champagne, J. Y. (2008a). "Feedback between bed load transport and flow resistance in gravel and cobble bed rivers." *Water Resources Research*, 44(5), 1–21.

Recking, A., Frey, P., Paquier, A., Belleudy, P., and Champagne, J. Y. (2008b). "Bed-Load Transport Flume Experiments on Steep Slopes." *Journal of Hydraulic Engineering*, 134(9), 1302–1310.

Reid, D. E., and Hickin, E. J. (2008). "Flow resistance in steep mountain streams." *Earth Surface Processes and Landforms*, 33(14), 2211–2240.

Rickenmann, D. (1991). "Hyperconcentrated flow and sediment transport at steep slopes." *Journal of Hydraulic Engineering*, 117(11), 1419–1439.

Rickenmann, D. (1994). "An alternative equation for the mean velocity in gravel-bed rivers and mountain torrents." *Proceedings ASCE National Conference on Hydraulic Engineering*, 1(1988), 672–676.

Rickenmann, D. (2001). "Comparison of bed load transport in torrents and gravel bed streams." *Water Resources Research*, 37(12), 3295–3305.

Rickenmann, D. (2012). "Alluvial Steep Channels: Flow Resistance, Bedload Transport Prediction, and Transition to Debris Flows." *Gravel-Bed Rivers: Processes, Tools, Environments*, 386–397.

Rickenmann, D., and Recking, A. (2011). “Evaluation of flow resistance in gravel-bed rivers through a large field data set.” *Water Resources Research*.

Van Rijn, L. C. (1987). “Mathematical modelling of morphological processes in the case of suspended sediment transport.” *Delft Hydraulics Communication*.

Rousseau, G. P. D. M. (2019). “Turbulent Flows over Rough Permeable Beds in Mountain Rivers: Experimental Insights and Modeling.” EPFL, Lausanne, 190.

Rouzes, M., Moulin, F. Y., Florens, E., and Eiff, O. (2018). “Low relative-submergence effects in a rough-bed open-channel flow.” *Journal of Hydraulic Research*, Taylor and Francis Ltd., 57(2), 139–166.

Rupp, D. E., and Smart, G. M. (2007). “Comment on ‘Flow resistance equations without explicit estimation of the resistance coefficient for coarse-grained rivers’ by Raúl López, Javier Barragán, and M. Àngels Colomer.” *Journal of Hydrology*, 346(3–4), 174–178.

Schlichting, H. (1968). *Boundary-Layer Theory*. McGraw-Hill, New York.

Schneider, J. M., Rickenmann, D., Turowski, J. M., Bunte, K., and Kirchner, J. W. (2015a). “Applicability of bed load transport models for mixed-size sediments in steep streams considering macro-roughness.” *Water Resources Research*, Blackwell Publishing Ltd, 51(7), 5260–5283.

Schneider, J. M., Rickenmann, D., Turowski, J. M., and Kirchner, J. W. (2015b). “Self-adjustment of stream bed roughness and flow velocity in a steep mountain channel.” *Water Resources Research*, 51(10), 7838–7859.

Shankar, P. N., and Deshpande, M. D. (2000). “Fluid Mechanics in the Driven Cavity.” *Annual Review of Fluid Mechanics*, 32(1), 93–136.

Smart, G. M. (1999). “Turbulent velocity profiles and boundary shear in gravel bed rivers.” *Journal of Hydraulic Engineering*, 125(2), 106–116.

Smart, G. M., Duncan, M. J., and Walsh, J. M. (2002). “Relatively rough flow resistance equations.” *Journal of Hydraulic Engineering*.

Song, T., Graf, W. H., and Lemmin, U. (1994). “Uniform flow in open channels with movable gravel bed.” *Journal of Hydraulic Research*, 32(6), 861–876.

Strickler, A. (1923). “Beiträge zur Frage der Geschwindigkeitsformel in der Rauhigkeit Zahlen für strome, Kanale und Geschlossene Leintungen (Contributions to the Question of a Velocity formula and Roughness Data for Streams, Channels and Closed Pipelines).” *Mitt. des Eidgenössischen Amtes für Wasserwirtschaft*, Bern, Switzerland, 16.

Takehara, K., and Etoh, T. (1999). “A study on particle identification in PTV particle mask correlation method.” *Journal of Visualization*, 1(3), 313–323.

Tauro, F., Piscopia, R., and Grimaldi, S. (2019). “PTV-Stream: A simplified particle tracking velocimetry framework for stream surface flow monitoring.” *CATENA*, 172(May 2018), 378–386.

Tavoularis, S. (2005). *Measurement in fluid mechanics*. *Choice Reviews Online*, Cambridge University Press.

Tominaga, A., and Nezu, I. (1992). “Velocity profiles in steep open-channel flows.” *Journal of Hydraulic Engineering*, 118(1), 73–90.

Trieste, D. J., and Jarrett, R. D. (1987). “Roughness Coefficients of Large Floods.” *Irrigation Systems for the 21st Century. ASCE*, 32–40.

Uemura, T., Yamamoto, F., and Ohmi, K. (1989). “A high speed algorithm of image analysis for real time measurement of two dimensional velocity distribution.” *American Society of Mechanical Engineers*, San Franscisco, 129–133.

UPC. (2020). *Analysis of the flash flood in the Francolí River on October 22, 2019*. Prepared for Agencia Catalana de l'Aigua (ACA).

Vallé, B. L., and Pasternack, G. B. (2006). "Air concentrations of submerged and unsubmerged hydraulic jumps in a bedrock step-pool channel." *Journal of Geophysical Research: Earth Surface*, Blackwell Publishing Ltd, 111(3).

Victoriano, A., García-Silvestre, M., Furdada, G., and Bordonau, J. (2016). "Long-term entrenchment and consequences for present flood hazard in the Garona River (Val d'Aran, Central Pyrenees, Spain)." *Natural Hazards and Earth System Sciences*, Copernicus GmbH, 16(9), 2055–2070.

Westerweel, J. (1993). "Digital particle image velocimetry: Theory and application." TU Delft.

White, R. H., Anderson, S., Booth, J. F., Braich, G., Draeger, C., Fei, C., Harley, C. D. G., Henderson, S. B., Jakob, M., Lau, C.-A., Mareshet Admasu, L., Narinesingh, V., Rodell, C., Roocroft, E., Weinberger, K. R., and West, G. (2023). "The unprecedented Pacific Northwest heatwave of June 2021." *Nature Communications*, Nature Publishing Group, 14(1), 727.

Wiberg, P. L., and Smith, J. D. (1991). "Velocity distribution and bed roughness in high-gradient streams." *Water Resources Research*.

Wilcox, A. C., Nelson, J. M., and Wohl, E. E. (2006). "Flow resistance dynamics in step-pool channels: 2. Partitioning between grain, spill, and woody debris resistance." *Water Resources Research*, 42(5).

Wilcox, A. C., and Wohl, E. E. (2007). "Field measurements of three-dimensional hydraulics in a step-pool channel." *Geomorphology*, 83(3–4), 215–231.

Wohl, E. E. (2010). *Mountain Rivers Revisited*. *AGU Water Resotrces Monograph*, Americam Geophysical Union, Washington, US.

Wohl, E. E., and Thompson, D. M. (2000). "Velocity characteristics along a small step-pool channel." *Earth Surface Processes and Landforms*, 25(4), 353–367.

Wong, M., and Parker, G. (2006). "Reanalysis and Correction of Bed-Load Relation of Meyer-Peter and Müller Using Their Own Database." *Journal of Hydraulic Engineering*, American Society of Civil Engineers (ASCE), 132(11), 1159–1168.

Yager, E. M., Dietrich, W. E., Kirchner, J. W., and McArdell, B. W. (2012). "Prediction of sediment transport in step-pool channels." *Water Resources Research*, 48(1), 1–20.

Yager, E. M., Kirchner, J. W., and Dietrich, W. E. (2007). "Calculating bed load transport in steep boulder bed channels." *Water Resources Research*, 43(7).

Yager, E. M., Schmeeckle, M. W., and Badoux, A. (2018). "Resistance Is Not Futile: Grain Resistance Controls on Observed Critical Shields Stress Variations." *Journal of Geophysical Research: Earth Surface*, Blackwell Publishing Ltd, 123(12), 3308–3322.

Yalin, M. S., and Da Silva, A. F. (2001). *Fluvial processes*. IAHR, Delft, The Netherlands.

Yen, B. C. (2002). "Open Channel Flow Resistance." *Journal of Hydraulic Engineering*, American Society of Civil Engineers (ASCE), 128(1), 20–39.

Yu, G., and Tan, S.-K. (2006). "Errors in the Bed Shear Stress as Estimated from Vertical Velocity Profile." *Journal of Irrigation and Drainage Engineering*, 132(5), 490–497.

Zimmermann, A., and Church, M. (2001). "Channel morphology, gradient profiles and bed stresses during flood in a step–pool channel." *Geomorphology*, 40(3–4), 311–327.

Zimmermann, A. E. (2010). "Flow resistance in steep streams: An experimental study." *Water Resources Research*, 46(9), 1–18.

Appendix A: Experimental Setup Calibration Procedures

Table of Contents

A.1. Introduction

The calibration process is critical to ensure that the experimental setup is operating correctly and producing accurate results. This appendix provides a detailed description of the calibration procedures used for the experimental setup, including the techniques, instruments, and equipment involved in the process. The calibration procedures described in this appendix were conducted to achieve precise measurements and ensure the accuracy of the experimental results.

A.2. Channel Slope Calibration

The experimental flume utilized in the research project had a variable slope, ranging from 0—30 degrees, which could be adjusted by pivoting around the downstream point. The flume was suspended by a sturdy metallic structure, and the system used to raise or lower the channel was powered by an electric motor, which was connected to a bridge crane measuring 7 m in height and 2 m in width.

Accurate measurements of the flume slope were obtained using a calibrated measuring tape with a precision of ±0.25 mm located on the pillar of the bridge crane (Figure A. 1). The measurements of this tape are associated with the flume slope through a calibration curve. This section describes the procedures to obtain the calibration curve.

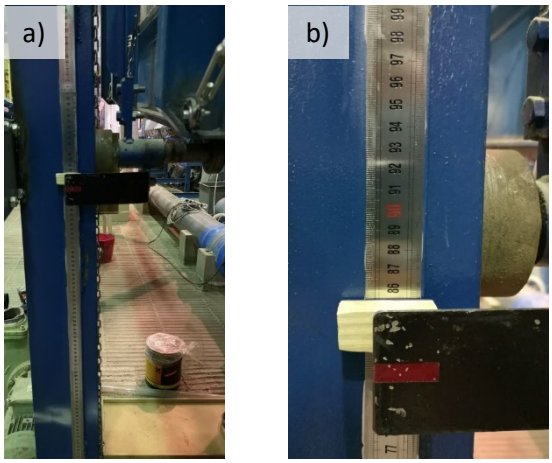

Figure A. 1. Measuring tape used for the slope measurement.

The purpose of this calibration process is to establish a correlation between the readings of the measuring tape (in centimetres) and the corresponding slope of the flume (in percentage). To achieve this, the channel's bottom level was measured using an electronic level (Leica Sprinter 50 model, Figure A. 5) with varying inclinations of the channel.

Two fixed points were identified along the channel: the first being the pivot point of the channel (0_o), and the second (X_1) being the location where the level measurements were conducted (Figure A. 2). Consequently, the distance between these two points remained constant (as a sloping line), while only the elevations changed.

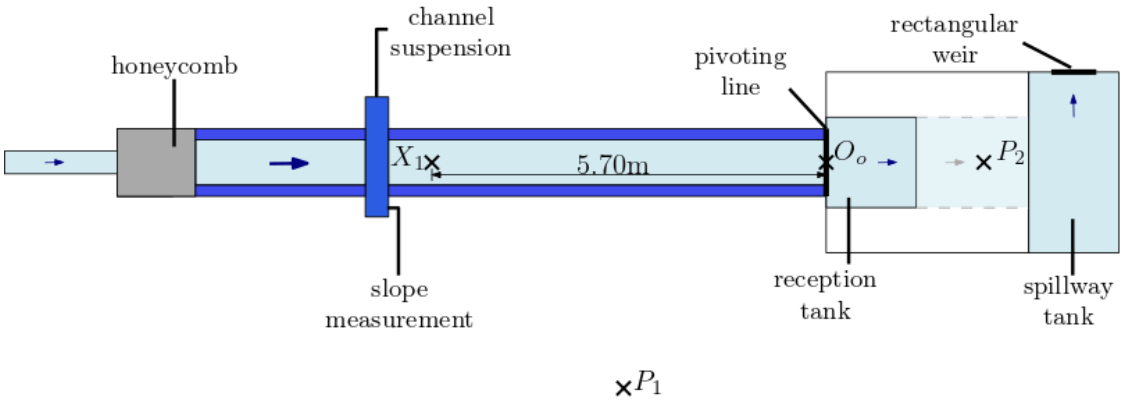

Figure A. 2. Schematic top plan view of the experimental apparatus for calibrating the slope.

The location where the electronic level was placed for all level measurements was at point P_2 (Figure A. 2 and Figure A. 5). The same methodology was employed for each of the flume slopes considered, which involved three steps: first, fixing the channel slope at a specific angle; second, taking level measurements of points 0_o and X_1 from P_2 using the electronic level; and third, recording the value of the measuring tape at the crane. This process was repeated for 15 different flume slopes (Table A. 1).

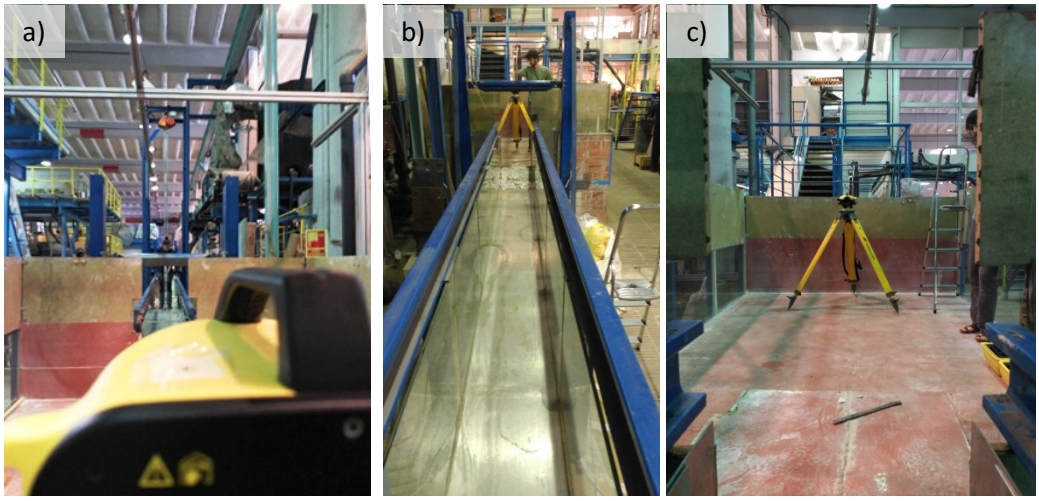

Figure A. 3. Electronic level positioned at the point P_2. (a) looking to X_1, (b) from point X_1 looking to the electronic level at P_2, and (c) from O_o looking to the electronic level at P_2.

A simple trigonometric calculation was used to determine the angle's value, with the hypotenuse of the triangle set at 5.70 meters, and the level differences between X_1 and 0_o (ΔH_{level}) serving as the opposite side. Once the angle for each measurement was calculated, a linear regression was performed between these angles and their corresponding measuring tape

values (Figure A. 4). The resulting calibration curve indicated that the minimum slope was 0.21%, while the maximum was 16.33%.

Table A. 1. Height values from the electronic level, measuring tape values, flume slope (angle and percentage) of each point measured by the electronic level fixed in P2 looking to the point X_1.

Point	H_{level} (m)	ΔH_{level} (m)	α (°)	α (%)	H_{tape} (cm)
O_0	1.071	-	-	-	-
X_1	1.059	0.012	0.121	0.21	13.25
X_1	1.034	0.037	0.372	0.65	16.10
X_1	1.008	0.063	0.633	1.11	19.05
X_1	0.981	0.09	0.905	1.58	22.05
X_1	0.955	0.116	1.166	2.04	24.09
X_1	0.926	0.145	1.458	2.54	28.10
X_1	0.899	0.172	1.729	3.02	31.10
X_1	0.872	0.199	2.001	3.49	34.10
X_1	0.846	0.225	2.262	3.95	36.95
X_1	0.757	0.314	3.158	5.51	46.90
X_1	0.666	0.405	4.074	7.11	57.10
X_1	0.578	0.493	4.962	8.65	67.00
X_1	0.489	0.582	5.860	10.21	77.05
X_1	0.313	0.758	7.642	13.30	97.10
X_1	0.140	0.931	9.400	16.33	116.95

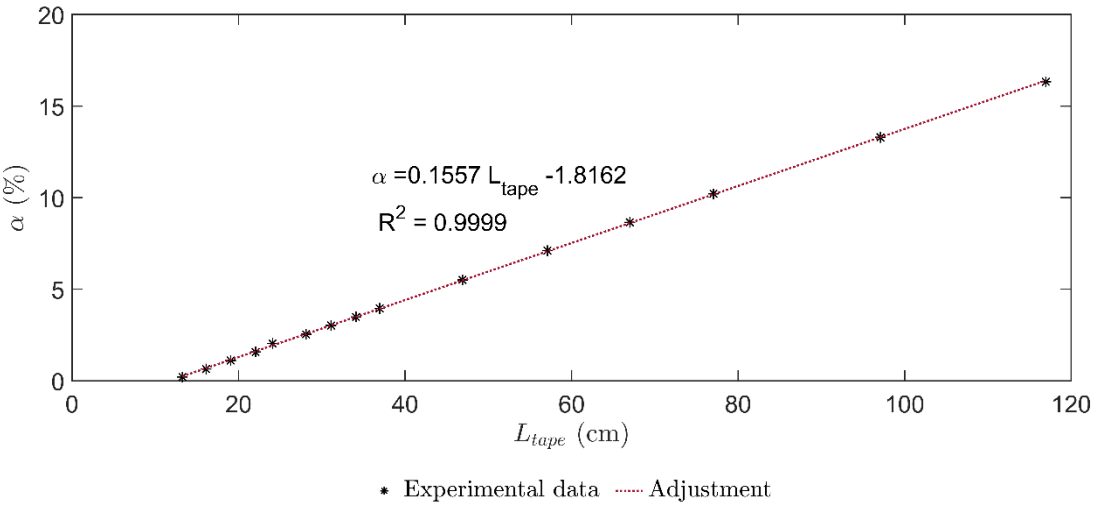

Figure A. 4. Calibration curve of the flume slope.

To measure the minimum flume slope of the channel, the electronic level was positioned equidistantly between both points, at point P_1 (as depicted in both Figure A. 2 and Figure A. 5). The initial level difference between X_1 and 0_o was found to be 0.01 m, which corresponded to 0.1215 m on the measuring tape. Thus, the minimum slope of the flume was calculated to be

0.19%. However, this value was not included in the slope calibration, as the suspension structure did not uniformly support the flume at this slope. Instead, this measurement was taken to establish the flattest possible slope of the flume.

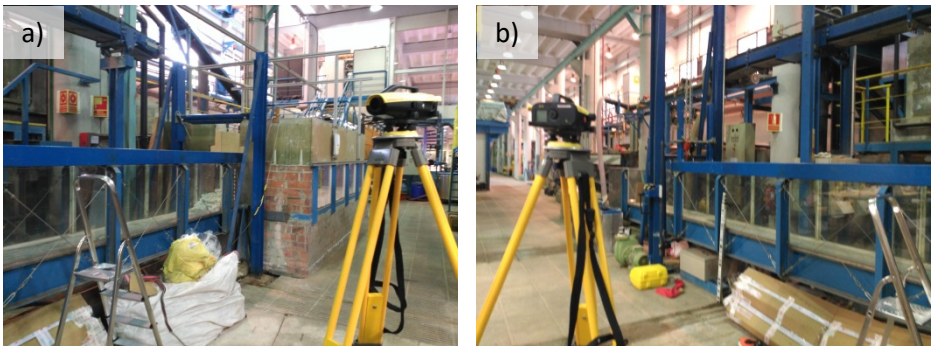

Figure A. 5. Electronic level positioned at the point P_1. (a) looking to X_1, and (b) looking to P_2.

A.3. Weir Calibration

During certain experiments, the use of an additional pump made it impossible for the magnetic flowmeters to measure the total discharge accurately. This was because the flowmeters were positioned upstream of the additional discharge entrance. In those cases, we relied on a rectangular weir located in the spillway tank (Figure 2.1 and Figure A. 2) to measure the discharge. We used a water gauge to measure the water height over the weir. To determine the relationship between the water height and the discharge, a calibration curve was conducted, taking into account the geometric characteristics of the weir.

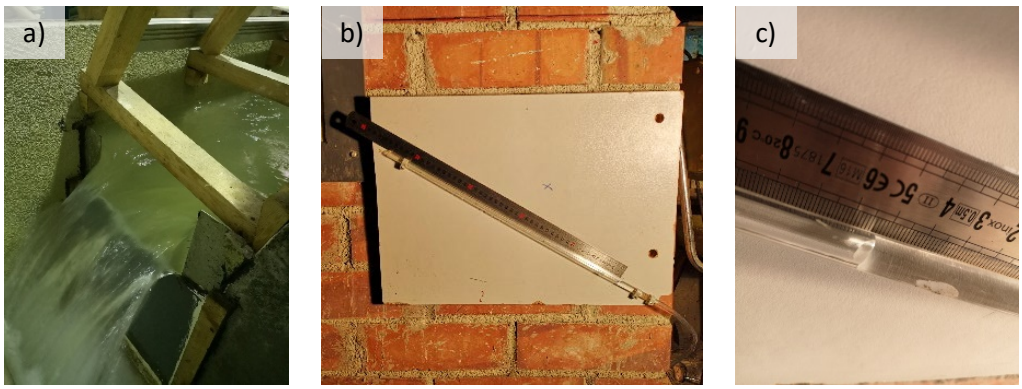

Figure A. 6. (a) Water flowing through the rectangular weir (discharge of 45 l/s on a 2% flume slope), (b) water gauge installed to measure the water height at the rectangular weir, and (c) detail of the gauge.

The rectangular weir is a thin plate located on the downstream wall of the spillway tank, and the water gauge (piezometer) is inclined at a 30-degree angle to improve the measurement

precision. Specifically, a 1-mm increase in water height in the tank corresponds to a 2-mm increase on the piezometer.

A. 3. 1. Introduction

This section will focus on the "partially and fully contracted rectangular weirs" since the experimental flow uses this type of weir. In the literature, we find different types of weirs, but "sharp-crested weirs" are those whose crest length in the flow direction is short enough not to affect the head-discharge relationship. According to (Bos 1978), when the crest width is 0.02 m or less, the nappe is entirely free from the weir body after passing over the weir, and no adhered nappe can occur, even at a minimum head of 0.03 m.

A "rectangular sharp-crested" weir (Figure A. 7) is a rectangular notch symmetrically located in a vertical thin plate (usually metal) perpendicular to the sides and bottom of a straight channel (Bos 1978). If the contractions of the weirs are not fully developed due to the walls or bottom of the approach channel's proximity, these weirs are referred to as "partially contracted weirs." On the other hand, if the bed and walls are far enough from the weir crest and sides that the channel boundaries have no significant impact on the nappe's contraction, these weirs are called "fully contracted weirs."

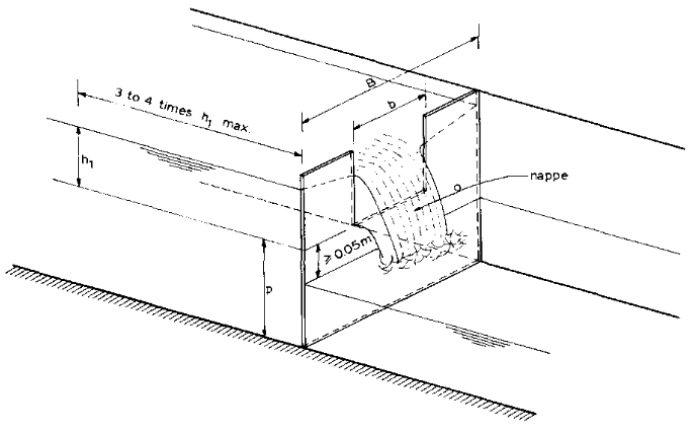

Figure A. 7. Rectangular sharp-crested or thin-plate weir (Bos 1978).

A.3.1.a. Evaluation of discharge through a weir

Kindsvater and Carter (1957) introduced an enhanced method for calibrating rectangular thin-plate weirs that applies to both fully and partially contracted weirs. The ability to rate partially contracted weirs offers design flexibility and can help reduce head drop and side contraction at low crest heights. Additionally, rectangular thin-plate weirs can minimize head loss. The Kindsvater-Carter method is defined by:

$$Q = \frac{2}{3} C_e (2g)^{1/2} b_e h_e^{3/2} \quad \text{(A.1)}$$

Where Q is the discharge (m^3/s), C_e is the effective coefficient of discharge (-), g is the acceleration of gravity (m^2/s), b_e is the effective breadth (m), which equals to $b_e = b + k_b$, where b is the measured length of the weir crest (m), and h_e is the effective head (m), which equals to $h_e = h_1 + k_h$, where h_1 is the head measured above the weir crest (m).

The quantities k_b and k_h represent the combined effects of the several phenomena attributed to viscosity and surface tension. The factor k_b varies as a function of the ratio b / B, as shown in Figure A. 8. On the contrary, the factor k_h is a constant value equal to 0.001 m.

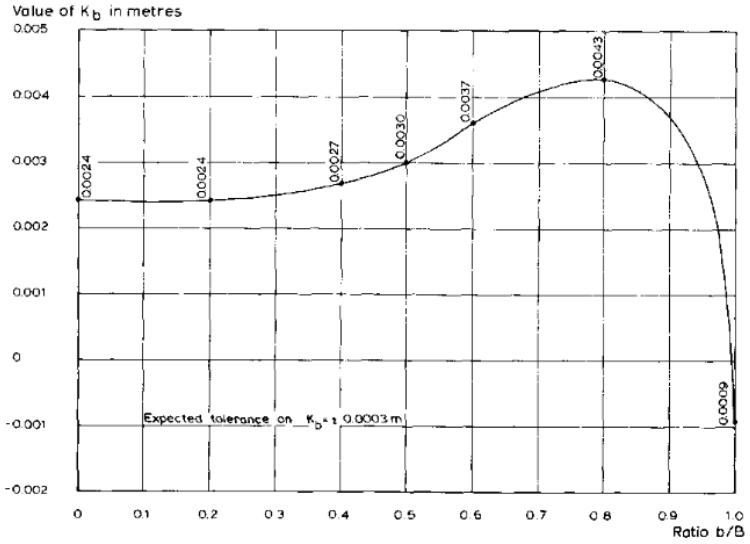

Figure A. 8. Values of k_b as a function of b/B derived from tests at the Georgia Institute of Technology by Kindsvater and Carter (1957).

The effective coefficient of discharge (C_e) considers both the relative depth and the relative width of the approach channel. As a result, C_e is a function of h_1 / P and b / B. The C_e-values can be obtained from the family of curves in Table A. 2 and Figure A. 9. Here, P refers to the vertical distance from the weir crest to the approach pool invert.

Table A. 2. Values for C_e as a function of the ratios h_1/P and b/B (Kindsvater and Carter 1957).

b / B	C_e
1.0	0.075·h$_1$/P +0.602
0.9	0.064·h$_1$/P +0.599
0.8	0.045·h$_1$/P +0.597
0.7	0.03·h$_1$/P +0.595
0.6	0.018·h$_1$/P +0.593
0.5	0.011·h$_1$/P +0.592
0.4	0.0058·h$_1$/P +0.591
0.3	0.002·h$_1$/P +0.59

b/B	C_e
0.2	-0.0018·h_1/P +0.589
0.1	-0.0021·h_1/P +0.588
0.0	-0.0023·h_1/P +0.587

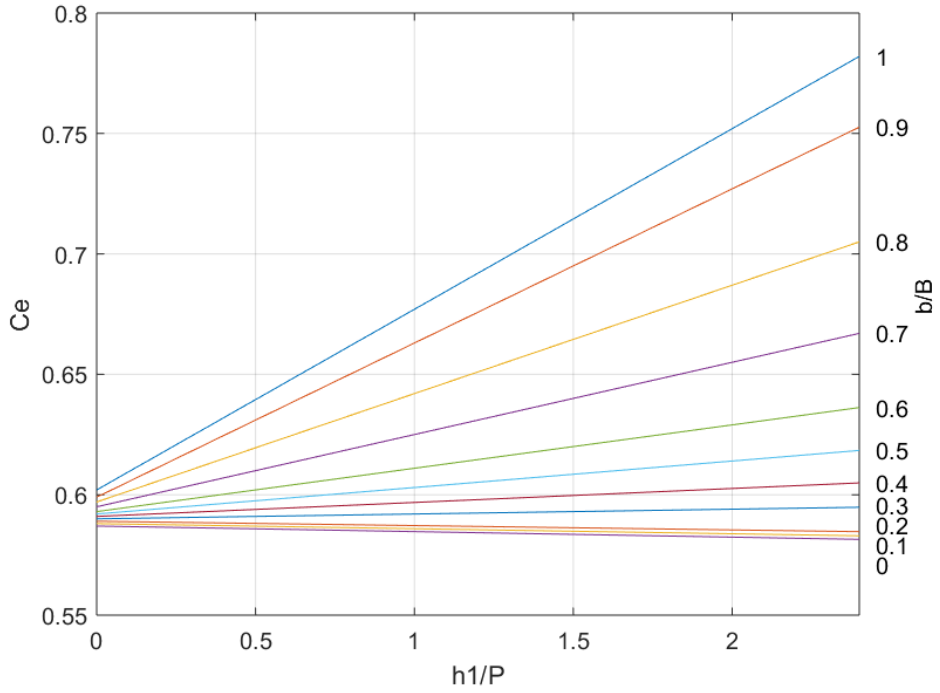

Figure A. 9. C_e as a function of the ratios h_1/P and b/B (Kindsvater and Carter 1957).

A.3.1.b. Limits of application

Equation (A.1) has limitations that vary depending on the type of rectangular sharp-crested weir considered. For a partially contracted weir, the limitations in Table A. 3 apply. The lower limit ($h_1 \leq 0.03m$) ensures the accuracy of measurement, considering the influence of fluid properties. Additionally, h_1 should be measured at a distance of 4 —5 times the maximum head upstream of the weir (Sotelo Avila 1994). An upper limit is recommended for h_1/P to ensure that the critical depth occurs in the approach channel, allowing the weir crest to serve as the control section for applying the equation (A.1). To facilitate aeration of the nappe, the water surface elevation in the downstream channel should be at least 0.05 m below the weir crest level.

Table A. 3. Limitations of a rectangular sharp-crested partially contracted weir (Bos 1978).

h_1	$\leq$	0.03 m
h_1/P	$\geq$	2.0
b	$\geq$	0.15 m
P	$\geq$	0.10 m
Tail water level	$\geq$	0.05 m crest level

In contrast, for a fully contracted weir, the limitations in Table A. 4 apply. These limitations ae more stringent than those for a partially contracted weir (Table A. 3)

Table A. 4. Limitations of a rectangular sharp-crested fully contracted weir (Bos 1978).

$B - p$	$\geq$	$4\ h_1$
h_1/P	$\leq$	0.5
h_1/b	$\leq$	0.5
0.07m	$\leq$	$h_1 <$ 0.60 m
b	$\geq$	0.30 m
P	$\geq$	0.30 m

A. 3. 2. Calibration of the weir system

To measure the discharge using the rectangular weir (which was partially contracted) and the piezometer, a calibration curve was necessary to establish the relationship between water height and discharge. The calibration process involved two stages: first, the calibration of the water gauge (piezometer); and second, the calibration of the entire system. This section details the methodology and presents the results obtained.

A.3.2.a. Calibration of the water gauge meter

To calibrate the water gauge, a limnimeter (Figure A. 10) was used to measure the water height at various levels in the spillway tank. The calibration process involved aligning the 0 measurement of the rectangular thin-plate weir with the 0 measurement of the water gauge. Next, a small and constant discharge was released into the spillway tank until the weir slightly overflowed (Figure A. 10-b). The discharge was then stopped, and the height measurement was taken when the weir ceased overflowing.

Figure A. 10. Details of the spillway tank during weir calibration. (a) Limnimeter over the tank measuring the 0 from the weir, and (b) thin rectangular plate in the 0 of the calibration.

The remaining points on the calibration curve were measured using the same methodology. A total of 11 points were measured (Table A. 5), with each point requiring at least 10 minutes between discharge changes to ensure uniform conditions. At each point, three measurements were taken: the limnimeter height ($h_{\lim}$), the piezometer height (h_{piez}), and the discharge (Q) from the electromagnetic flowmeters. The height of the weir (h_{weir}) was calculated as the difference between the limnimeter height ($h_{\lim}$) and its zero point. Although the electromagnetic flowmeter values provided an approximate discharge for each point, they were not used in the flow calibration. Instead, they provided a general overview of the system.

Table A. 5. Values from the height of the piezometer and the limnimeter during piezometer calibration.

Point	h_{piez} (cm)	$h_{\lim}$ (cm)	h_{weir} (cm)	Q (l/s)
0	0.0	102.81	0.00	0
A	5.6	105.81	3.00	3
B	17.9	111.50	8.69	16
C	19.8	112.29	9.48	19
D	20.3	112.77	9.96	20
E	18.4	111.95	9.14	17
F	13.6	109.06	6.25	10
G	8.8	107.20	4.39	6
H	3.9	104.86	2.05	2
I	2.6	104.15	1.34	1
0	0.0	102.81	0.00	0

The values presented in Table A. 5 were used to perform a linear regression analysis (Figure A. 11). This analysis aimed to determine the height from the weir in relation to the water gauge height.

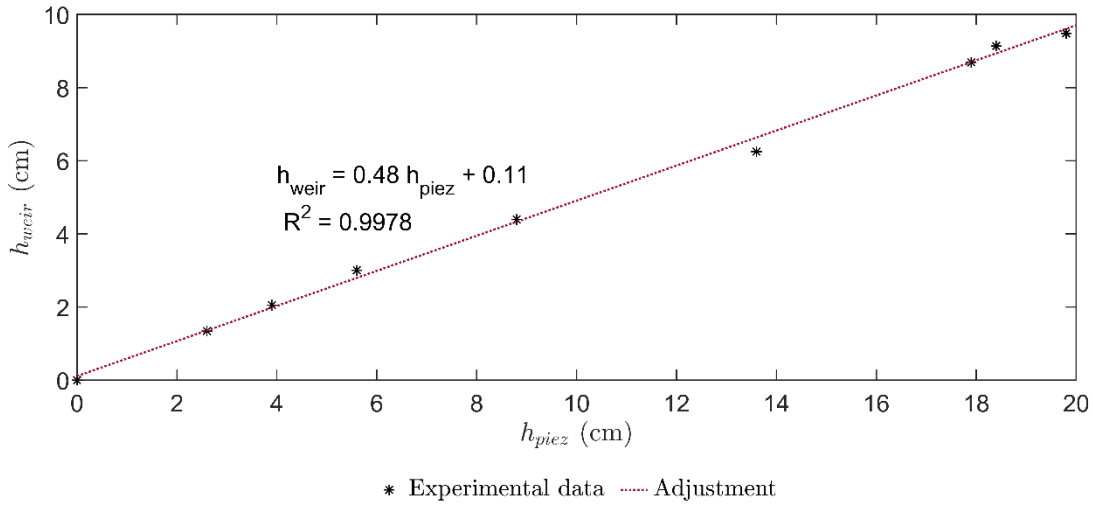

Figure A. 11. Calibration curve between piezometer and spillway tank height.

A.3.2.b. Calibration of the formulation for weir discharge measurement

After calibrating the water gauge, the discharge flowing through the weir was measured by comparing known flow rates obtained from volumetric calculations at the upstream tank (black tank) with discharge values obtained from the rectangular weir formula described earlier (equation (A.1)). This calibration between existent formulas (Kindsvater and Carter 1957) and the discharge values at the lab system was necessary given limitations of the formula's applicability, specifically for water heights over the weir smaller than 0.03 m.

The rectangular weir is considered partially contracted due to the proximity of the approach channel walls to the weir (Figure A. 12), which means that the nappe contraction was not fully developed. The water depth was measured at 1 m from the weir crest, which is 4-5 times the maximum head as recommended by Sotelo Avila (1994).

In the calibration process, six different discharges (1, 3, 5, 10, 15, and 20 l/s) were considered. The two lowest discharges were strictly necessary because the water heights in these cases did not adhere to the limitations given in Table A. 3. For each discharge considered, the following methodology was employed: i) a stabilization time was given to ensure a constant discharge, ii) the recirculation pump was stopped, and iii) a video of the water height reduction on the black tank was taken while noting the value of the water gauge on the rectangular weir.

The following sections describe the volumetric calculation of the discharge, the application of the weir formation to the weir in the flume, and a comparison between the discharges obtained from the volumetric calculation and the formulation.

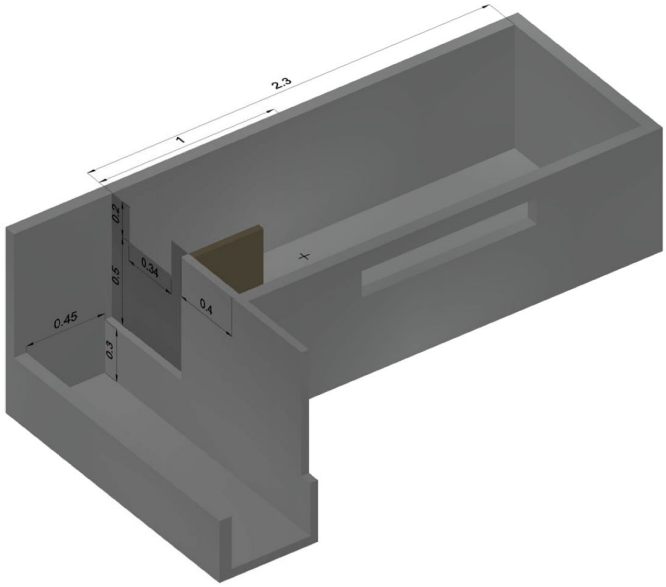

Figure A. 12. Scheme of the spillway tank, the rectangular weir, and the height measuring point (in meters).

b.1). Volumetric discharge measurement

The discharge is driven by gravity and originates from a tank located upstream of the flume, known as the black tank. This tank is replenished by pumps from another tank situated upstream of the weir (Figure 2.1).

To determine the volumetric flow rate of the discharge, the goal was to calculate the amount of water that entered the flume from the black tank per unit of time. This was achieved by calculating the volume of water, which is equal to the difference between the water levels in the black tank, and the black tank's surface area. The discharge is then obtained by dividing this volume by the time elapsed between the two water levels.

The black tank has a cylindrical shape with an internal diameter of 2.46 m and is equipped with a water dump to prevent overflow. The dump has a rectangular shape with a width of 0.32 m and a length of 2 m. The surface area of the black tank was determined using:

$$A_{bt} = \pi\left(\frac{2.46}{2}\right)^2 - 0.32x2 = 4.11m^2 \quad \text{(A.2)}$$

To measure the water heights in the black tank, a second water gauge was installed on the wall outside the tank (Figure A. 13). The black tank is constantly refilled by pumps from the downstream tank, and any excess flow that does not flow through the flume is diverted by the dump to the downstream tank and re-enters the pump system. This behaviour must be considered during the volumetric measurement of the black tank.

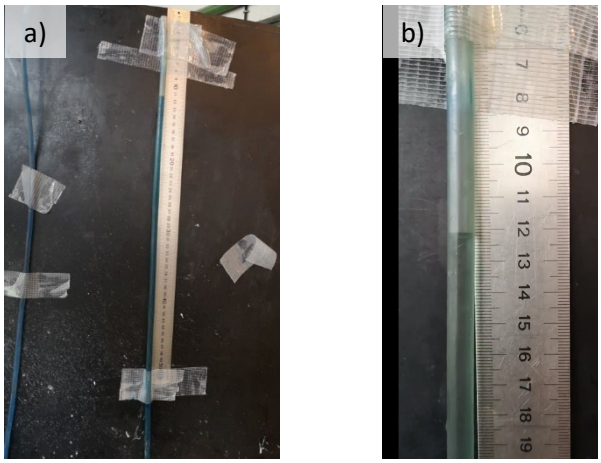

Figure A. 13. Water gauge located on the black tank's wall to measure its water height.

To ensure accurate measurements, the maximum water level of the tank for the volumetric measurement was defined as the water height at which water starts to flow only through the flume, and there is no overtopping of the black tank through the dump to the downstream tank.

This maximum height, measured by the gauge, was found to be 12.15 cm and was used as the starting water height for all the calibration points.

The methodology for the volumetric discharge measurement on the black tank involved firstly switching on the pumping system, with the discharge flowing through the flume and the black tank constantly being refilled. Once the system stabilized, the pumping system was switched off, and the water elevations in the black tank started to descend as the black tank was emptied by overtopping through the dump and the discharge flowing towards the flume. When the water elevation reached 12.15 cm on the black tank's water gauge, the recording of the descent of this water level began.

The recording was stopped when the water level reached the final calibration point. To obtain the next calibration point, the pumps were switched on until the black tank was refilled, and the system stabilized with the new discharge. However, the introduction of air into the black tank whenever the pumps were stopped and switched on back again meant that the column water inside the black tank's gauge had to be emptied before starting the calibration of the next point.

The behaviour of the black tank also depends on a constant load to maintain a steady discharge over the channel. If the water height drops too low, the calibration will not yield conclusive results, thereby affecting the discharge over the channel. Due to this, it was not possible to achieve significant water height differences between the calibration points. The volumetric discharge measurements for all the discharge rates are presented in Table A. 6. The duration of the recording time varies for each discharge rate as it takes longer to achieve conclusive height reductions for lower discharges, such as 1 l/s, compared to higher discharges like 20 l/s.

b.1). Rectangular sharp-crested weir discharges

Once the exact discharge flowing through the flume towards the weir is determined, it can also be calculated using the method defined by Kindsvater and Carter (1957) for a partially contracted weir, taking into account the limitations specified in Table A. 2. This method involves using the water level of the weir to calculate the discharge, as described in equation (A.1).

The geometry of the weir is depicted in Figure A. 10 and Figure A. 12, and all variable definitions follow Figure A. 7 (Bos 1978). The measured length of the weir crest is denoted by b, the total width of the weir is B, the height from the bottom of the spillway tank to the crest of the weir is p, the height of the weir crest is $h_{\max}$, k_b varies as a function of b/B, and according to Figure A. 8, is 0.0035 m, $b_e = b + k_b$ and k_h is both constant values equal to 0.001 m.

Table A. 6. Volumetric discharge measurement data: water height on the black tank (h_{black}), observed time of the measured height (t), corresponding volume (V), and calculated discharge through volumetric measurement (Q_{vol}). On grey, the mean value for each calibration point.

Point	h_{black} (cm)	t (s)	V (m^3)	Q_{vol} (l/s)
A	12.15	26	-	-
	14.85	137	0.11	1.00
	17.6	241	0.22	1.04
	-	-	-	1.02
B	12.15	26	-	-
	15	67	0.12	2.86
	18.4	114	0.26	2.92
	-	-	-	2.89
C	12.15	20	-	-
	15.15	46	0.12	4.75
	20.1	89	0.33	4.74
	-	-	-	4.74
D	12.15	17.2	-	-
	15.1	29.3	0.12	10.03
	19.9	49	0.32	10.02
	24.3	67	0.50	10.03
	-	-	-	10.03
E	12.15	16.8	-	-
	13.8	21	0.07	16.16
	19.4	37	0.30	14.76
	26.1	56	0.57	14.64
	-	-	-	15.19
F	12.15	13.9	-	-
	27	45	0.61	19.64
	30.4	52	0.75	19.70
	-	-	-	19.67

Table A. 7. Characteristics of the rectangular weir.

b (m)	B (m)	p (m)	h_{max} (m)	b_e (m)	k_b (m)	k_h (m)
0.335	0.550	0.500	0.200	0.370	0.035	0.001

Hence, the discharge can be calculated by using equation (A.1) and the water heights measurements obtained from the spillway tank gauge (h_{piez}), which also provide the weir height values (h_{weir}) through its calibration process (Figure A. 11). The weir height value is also used in the formulation. The effective coefficient of discharge (C_e) can be derived from Table A. 2 and

is utilized in conjunction with the value of $C_{e1} = 0.018$ and $C_{e2} = 0.593$ 0.593 for in Table A. 8 to present the obtained results.

Table A. 8. Rectangular-weir discharge data; water height on the piezometer (h_{piez}), water height on the weir (h_{weir}), effective head of the weir ($h_e = h_1 + k_h$), effective coefficient of discharge (C_e), and computed discharge (Q_{weir}).

Point	h_{piez} (m)	h_{weir} (m)	h_e	C_e	Q_{weir} (l/s)
A	0.0245	0.0129	0.014	0.593	1.06
B	0.0520	0.0260	0.027	0.593	2.88
C	0.0745	0.0368	0.038	0.594	4.77
D	0.1270	0.0620	0.063	0.594	10.27
E	0.1665	0.0810	0.082	0.594	15.24
F	0.2017	0.0975	0.099	0.595	20.10

The discharge has been obtained through both the volumetric and weir formulation for each calibration point. This enabled us to verify the accuracy of the Kindsvater and Carter (1957) formulation in predicting the discharge flowing though the rectangular weir in the flume (Figure A. 14).

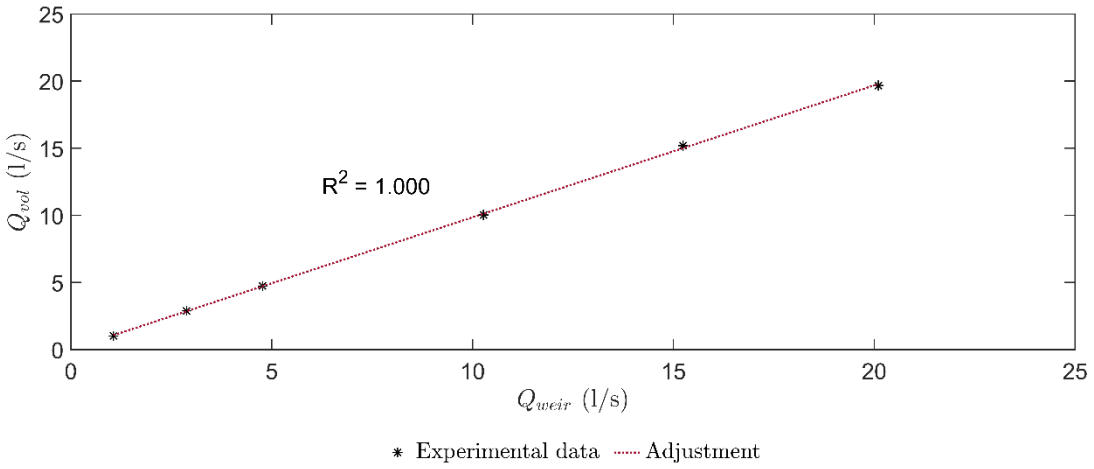

Figure A. 14. Relation between the volumetric discharge and the discharge computed from the rectangular weir formulation.

A.3.2.c. Calibration of the magnetic flowmeters

The validation of the magnetic flowmeters' calibration was performed using the same calibration points used to test the applicability of the equation (A.1) for the rectangular weir in the flume. The magnetic flowmeters were found to reduce the load effect on the discharge measurement, and their recordings were used to determine the duration of each experiment.

Figure A. 15 displays the discharge values recorded by the magnetic flowmeters for each calibration point listed in Table A. 6 and Table A. 8. These recordings showed that the discharge throughout the flume changed as the height of the black tank decreased. This effect was more

pronounced at higher discharges than at lower ones, as illustrated in Figure A. 15-f and Figure A. 15-a, respectively. To minimize this effect during the calibration experiments, a variable duration was considered for each discharge experiment, and a maximum reduction of 0.4 l/s was allowed.

To validate the calibration of the magnetic flowmeters, the averaged values obtained from Figure A. 15 were compared to the results obtained from the volumetric and weir discharge calculation, with both values found to be consistent within the measurement accuracy (Table A. 9).

Hence, the efficacy of the Kindsvater and Carter (1957) formula in accurately determining the discharge flowing through the flume has been established, not only through the volumetric measurements but also with the magnetic flowmeters.

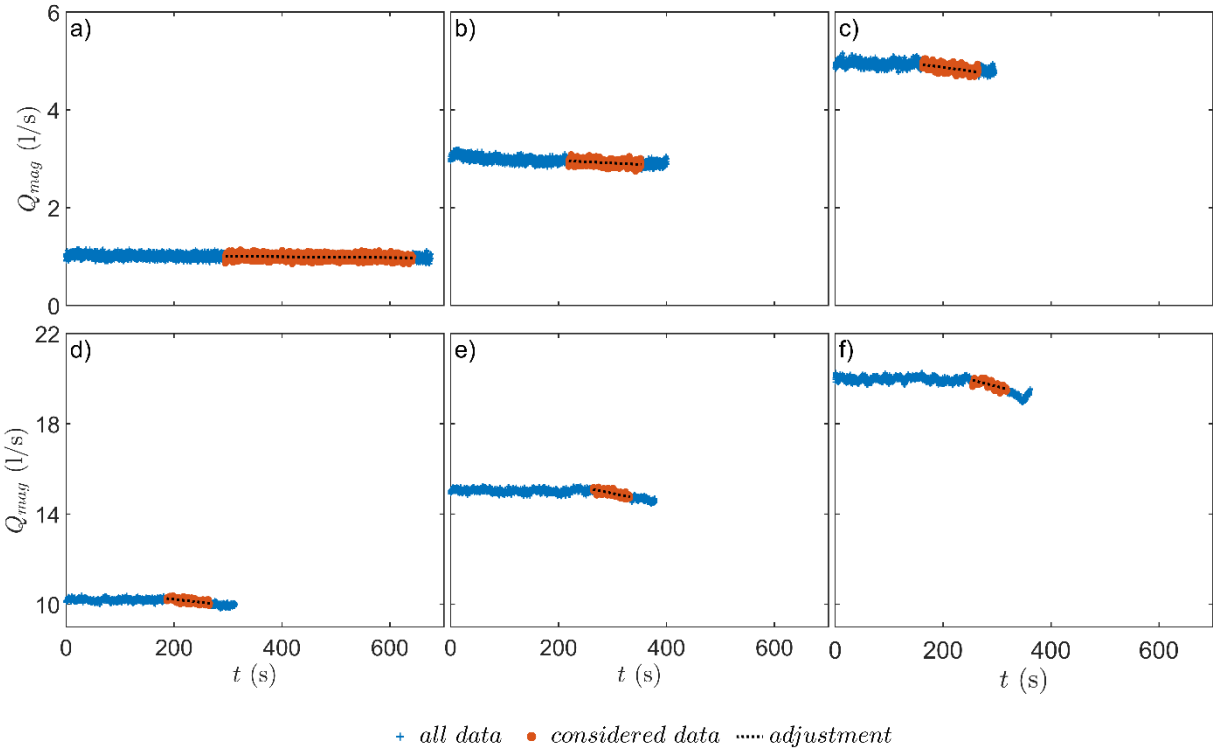

Figure A. 15. Discharge measured by the magnetic flowmeters, with the data considered in each calibration point. (a) for point A, (b) for point B, (c) for point C, (d) for point D, (e) for point E, and (f) for point F.

Table A. 9. Magnetic flowmeter data; volumetric discharge (Q_{weir}), discharge from weir formulation (Q_{weir}), and discharge from the magnetic flow meters (Q_{mag}).

Point	Q_{vol}	Q_{weir} (l/s)	Q_{mag}
A	1.02	1.06	0.99
B	2.89	2.88	2.92
C	4.74	4.77	4.85
D	10.03	10.27	10.15
E	15.19	15.24	14.93
F	19.67	20.10	19.74

A.3.2.d. Experimental calibration of discharge under experimental conditions

With the validation of the calibration of the magnetic flowmeters and the formulation of the rectangular weir on the flume, a new experimental calibration of the weir is conducted. In this case the calibration is focused on the discharges used in the experiments. The pumps are set to continuously fill the black tank to maintain a constant water height and ensure a constant discharge throughout the flume. The same methodology as defined in section A.3.2.c. Calibration of the magnetic flowmeters is followed, but the discharges are compared to those recorded by the magnetic flowmeters instead of the volumetric measurements. The results of this calibration are presented in Table A. 10 and Figure A. 16-a, and the performance curve in Figure A. 16-b.

Table A. 10. Rectangular-weir discharge data; water height on the piezometer (h_{piez}), water height on the weir (h_{weir}), effective head of the weir ($h_e = h_1 + k_h$), effective coefficient of discharge (C_e), computed discharge (Q_{weir}), and (Q_{mag}).

Point	h_{piez} (m)	h_{weir} (m)	h_e	C_e	Q_{weir} (l/s)	Q_{mag} (l/s)
A	0.0000	0.0011	0.0021	0.593	0.06	0.00
B	0.0560	0.0280	0.0290	0.594	3.20	3.00
C	0.1790	0.0870	0.0880	0.595	16.95	16.50
D	0.1980	0.0961	0.0971	0.595	19.66	19.00
E	0.2030	0.0985	0.0995	0.595	20.39	20.00
F	0.1840	0.0894	0.0904	0.595	17.65	17.50
G	0.1360	0.0663	0.0673	0.594	11.35	11.00
H	0.0880	0.0433	0.0443	0.594	6.05	6.00
I	0.0390	0.0198	0.0208	0.593	1.95	2.00
J	0.0260	0.0136	0.0146	0.593	1.14	1.00

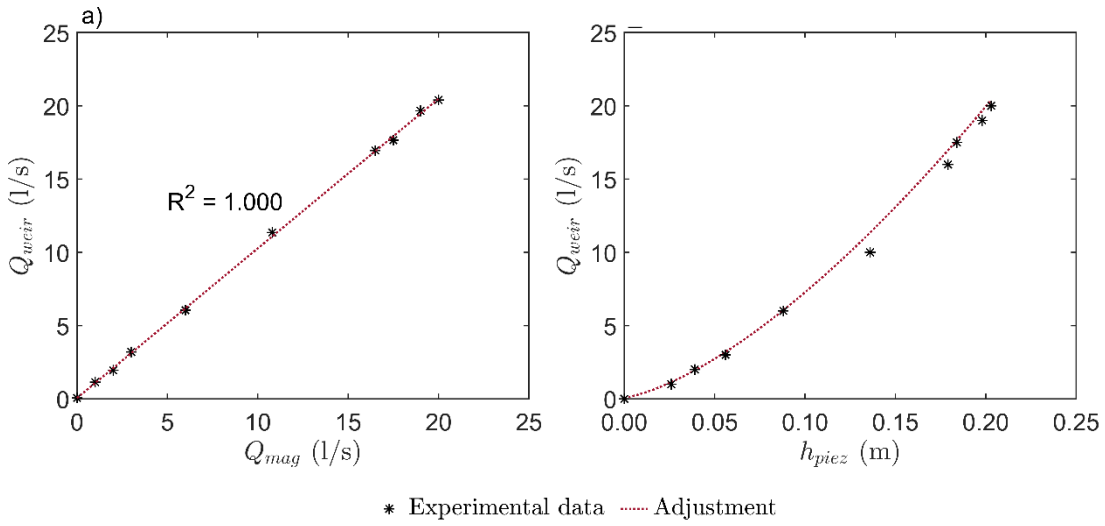

Figure A. 16. (a) Validation of the discharge calibration between magnetic flowmeters and rectangular weir formulation, and (b) performance curve of the Kindsvater and Carter's (1957) formulation on the flume as a function of the piezometer water height.

A.4. Wide-open Channel Conditions

This section assesses whether wide-open channel conditions can be applied in the experimental flume. The local mean velocity measured by the ADV/PTV gives us information about the instantaneous velocity at the centre of the channel, where the devices were located. Therefore, the velocity profile obtained corresponded to the velocity distribution along a vertical at this exact point (Fernández 2019). Velocity in rectangular channels under wide-open channels can be considered constant along the transversal area (Chow 1959). Therefore, integrating the velocity profile over the flow cross-section will give us the actual flow.

The main problem resides in the definition of the wide-open channel conditions; following Chow's (1959) definition, a rectangular channel whose width (B) is greater than 10 times the depth of flow (d) ($B/d > 10$) can be considered a wide-open channel. Under these conditions, the sides of the channel have practically no influence on the velocity distribution in the central region, and the flow in the central region can therefore be regarded as two-dimensional in hydraulic analyses. Furthermore, the hydraulic radius can be simplified as the hydraulic depth ($R_h \sim d$).

In the experiments carried out in this thesis, most of the experiments are under wide-open channel conditions ($B/d > 10$) since shallow waters are analyzed. Moreover, considering the difference in roughness between the bed surface and the sides of the glass channel, it is supposed that the sides of the channel have practically no influence in the central region.

A.5. References

Bos, M. G. (1978). *Discharge measurement structures*. Ilri.

Chow, V. Te. (1959). *Open-channel hydraulics*. *McGraw Hill Book Company*, McGraw-Hill Book Company, New York.

Fernández, C. (2019). "Experimental characterization of turbulence in steep rough streams." Universitat Politècnica de Catalunya.

Kindsvater, C. E., and Carter, R. W. C. (1957). "Discharge characteristics of rectangular thin-plate weirs." *Journal of the Hydraulics Division*, 83(6), 1–36.

Sotelo Avila, G. (1994). *Hidráulica general; fundamentos*. Limusa.

Appendix B: Supplemental Figures and Tables

Table of Contents

B.1. Introduction

The appendix contained herein presents a comprehensive collection of all the measurements obtained during the experiments, optimization results, and additional figures derived from the analysis conducted in the main body of the dissertation. This supplementary data provides a detailed and thorough understanding of the research conducted, offering an in-depth exploration of the experimental and analytical methods employed.

The tables included in this appendix present the quantitative measurements obtained from the experiments, enabling readers to fully comprehend the empirical results. Finally, the additional figures included provide visual aids that complement the analysis conducted in the dissertation's main body. Together, this appendix offers a comprehensive and detailed look into the research conducted, providing valuable insights for interested parties.

B.2. Experimental Hydraulic Conditions

The experimental hydraulic conditions are a critical aspect of any hydraulic or fluid dynamics experiment. This section presents a detailed description of the hydraulic conditions present during each experiment, with two subsections dedicated to the experimental conditions and the adjusted conditions following the methodology outlined in Chapter 4.

Table B. 1 provides an overview of the main hydraulic characteristics derived directly from flume measurements in laboratory conditions (i.e. the datum is assumed at the crests of the bed particles), with all variables having the super index $^{+}$, denoting that they are measured or directly derived from these measurements.

In contrast, Table B. 2 presents the main hydraulic characteristics following the velocity adjustment procedure, where the datum is determined by the objective functions defined in Chapter 4. By presenting both sets of data, researchers can gain a comprehensive understanding of the hydraulic conditions and the influence of velocity profile adjustment. These tables offer valuable insights into the experimental hydraulic conditions, including the channel slope (α), experiment number (i), profile number (j), measured interstitial velocity ($U_{\inf}^{+}$), measured total discharge (Q_{tot}^{+}), superficial discharge ($Q_{\sup}$), interstitial discharge ($Q_{\inf}$), depth-averaged velocity (U), water depth (d), hydraulic radius ($R_h = Bd/(2d+B)$ where B is the channel width), relative submergence (R_h/D_{50}), Froude number ($Fr = U/\sqrt{gd\cos\alpha}$), and Reynolds number ($\mathrm{Re} = 4R_hU/\nu$). The depth-averaged velocity is determined using continuity as $U = Q_{\sup}/A_{\sup}$ (where $A_{\sup} = dB$).

Table B. 1. Hydraulic characteristics of the experiments.

α (%)	i	j	D_{50} (m)	Q^+_{tot} (l/s)	$Q^+_{\inf}$ (l/s)	$Q^+_{\sup}$ (l/s)	U^+ (m/s)	$U^+_{\inf}$ (m/s)	d^+ (m)	R^+_h (m)	R^+_h/D_{50} (-)	Fr^+ (-)	Re^+ (-)
2	1	1	0.0145	2.06	0.66	1.39	0.381	0.03	0.009	0.009	0.6	1.27	11700
	1	2	0.0145	5.48	0.69	4.79	0.603	0.03	0.020	0.018	1.2	1.37	38214
	1	3	0.0145	8.96	0.66	8.30	0.709	0.03	0.029	0.026	1.8	1.32	63505
	1	4	0.0145	13.16	0.74	12.42	0.793	0.03	0.039	0.033	2.3	1.28	91122
	1	5	0.0145	17.01	0.70	16.32	0.881	0.03	0.046	0.038	2.6	1.31	116240
	1	6	0.0145	21.13	0.76	20.36	0.948	0.03	0.054	0.042	2.9	1.31	140811
	1	7	0.0145	25.10	0.74	24.36	0.996	0.03	0.061	0.047	3.2	1.29	163664
	1	8	0.0145	29.35	0.74	28.61	1.070	0.03	0.067	0.050	3.5	1.32	188117
	2	2	0.0145	6.40	0.63	5.77	0.584	0.02	0.025	0.022	1.5	1.19	45060
	2	3	0.0145	10.52	0.65	9.87	0.729	0.03	0.034	0.029	2.0	1.26	74024
	2	4	0.0145	14.11	0.71	13.40	0.790	0.03	0.042	0.035	2.4	1.22	97001
	2	5	0.0145	17.96	0.61	17.35	0.844	0.02	0.051	0.041	2.8	1.19	121091
	2	6	0.0145	21.93	0.68	21.25	0.896	0.03	0.059	0.046	3.2	1.18	143773
	2	7	0.0145	26.80	0.68	26.12	0.975	0.03	0.067	0.050	3.5	1.20	171608
	2	8	0.0145	29.75	0.72	29.04	1.043	0.03	0.070	0.052	3.6	1.26	188967
	3	1	0.0145	2.91	0.65	2.25	0.395	0.03	0.014	0.013	0.9	1.05	18458
	3	2	0.0145	6.00	0.65	5.35	0.557	0.03	0.024	0.021	1.5	1.15	41865
	3	3	0.0145	13.04	0.66	12.39	0.753	0.03	0.041	0.034	2.4	1.18	90109
	3	4	0.0145	18.13	0.65	17.48	0.857	0.03	0.051	0.041	2.8	1.21	122146
	3	5	0.0145	23.74	0.65	23.08	0.942	0.03	0.061	0.047	3.2	1.21	155000
	3	6	0.0145	27.82	0.65	27.17	1.007	0.03	0.067	0.050	3.5	1.24	178236
	3	7	0.0145	28.31	0.69	27.62	1.003	0.03	0.069	0.051	3.5	1.22	180248
	4	1	0.0145	16.15	0.69	15.45	0.815	0.03	0.047	0.038	2.6	1.19	109578
	5	1	0.0145	16.15	0.69	15.45	0.815	0.03	0.047	0.038	2.6	1.19	109578
3	6	2	0.0145	6.49	0.70	5.79	0.718	0.03	0.020	0.018	1.3	1.62	46105
	6	3	0.0145	7.88	0.72	7.15	0.787	0.03	0.023	0.020	1.4	1.67	56334
	6	4	0.0145	13.94	0.71	13.23	0.894	0.03	0.037	0.031	2.2	1.48	97946
	6	5	0.0145	20.24	0.72	19.51	1.032	0.03	0.047	0.038	2.6	1.52	138438
	7	2	0.0145	6.27	0.78	5.49	0.653	0.03	0.021	0.019	1.3	1.44	43551
	7	3	0.0145	10.09	0.73	9.36	0.758	0.03	0.031	0.027	1.8	1.38	71144
	7	4	0.0145	14.67	0.73	13.94	0.868	0.03	0.040	0.033	2.3	1.38	101846
	7	5	0.0145	19.95	0.75	19.20	0.960	0.03	0.050	0.040	2.8	1.37	134725
	8	1	0.0145	16.27	0.79	15.48	0.934	0.03	0.041	0.034	2.4	1.47	112464
	9	1	0.0145	16.27	0.79	15.48	0.934	0.03	0.041	0.034	2.4	1.47	112464
4	10	3	0.0145	6.04	0.77	5.26	0.725	0.03	0.018	0.017	1.1	1.72	42327
	10	4	0.0145	6.04	0.81	5.23	0.715	0.03	0.018	0.017	1.2	1.69	42037
	10	5	0.0145	8.74	0.79	7.95	0.854	0.03	0.023	0.021	1.4	1.79	62488
	10	6	0.0145	12.10	0.76	11.34	0.928	0.03	0.031	0.027	1.8	1.69	86300
	10	7	0.0145	12.82	0.83	11.99	0.954	0.03	0.031	0.027	1.9	1.72	90880
	10	8	0.0145	14.44	0.78	13.66	0.984	0.03	0.035	0.030	2.0	1.69	102104
	10	9	0.0145	16.63	0.77	15.86	1.013	0.03	0.039	0.033	2.3	1.63	116322
	11	2	0.0145	4.29	0.99	3.30	0.664	0.04	0.012	0.012	0.8	1.90	27280
	11	3	0.0145	5.93	0.99	4.95	0.716	0.04	0.017	0.016	1.1	1.74	39956
	11	4	0.0145	8.03	0.98	7.06	0.834	0.04	0.021	0.019	1.3	1.83	55973

α (%)	i	j	D_{50} (m)	Q^+_{tot} (l/s)	$Q^+_{\inf}$ (l/s)	$Q^+_{\sup}$ (l/s)	U^+ (m/s)	$U^+_{\inf}$ (m/s)	d^+ (m)	R^+_h (m)	R^+_h/D_{50} (-)	Fr^+ (-)	Re^+ (-)
	11	5	0.0145	9.90	0.97	8.93	0.903	0.04	0.025	0.022	1.5	1.83	69693
	11	6	0.0145	11.82	0.97	10.85	0.959	0.04	0.028	0.025	1.7	1.82	83381
	11	7	0.0145	14.23	1.00	13.23	1.057	0.04	0.031	0.027	1.9	1.91	100355
	11	8	0.0145	16.03	1.01	15.02	1.081	0.04	0.035	0.030	2.0	1.85	112244
	12	3	0.0145	7.44	1.01	6.44	0.782	0.04	0.021	0.019	1.3	1.74	51193
	12	4	0.0145	8.92	1.07	7.84	0.863	0.04	0.023	0.020	1.4	1.83	61783
	12	5	0.0145	11.02	1.03	9.99	0.888	0.04	0.028	0.025	1.7	1.69	76836
	12	6	0.0145	13.04	1.07	11.97	0.970	0.04	0.031	0.027	1.8	1.76	90970
	12	7	0.0145	15.00	1.07	13.93	1.037	0.04	0.034	0.029	2.0	1.81	104640
	14	1	0.0145	16.40	0.88	15.52	1.048	0.03	0.037	0.031	2.2	1.74	114859
	15	3	0.0145	6.46	1.23	5.23	0.803	0.05	0.016	0.015	1.0	2.01	42448
	15	4	0.0145	8.21	1.05	7.16	0.942	0.04	0.019	0.017	1.2	2.18	57341
	15	5	0.0145	8.93	1.08	7.85	0.989	0.04	0.020	0.018	1.2	2.24	62665
	15	6	0.0145	10.17	1.06	9.11	1.049	0.04	0.022	0.020	1.4	2.27	72096
	16	1	0.0145	3.54	1.08	2.46	0.672	0.04	0.009	0.009	0.6	2.25	20619
	16	2	0.0145	4.57	1.08	3.49	0.737	0.04	0.012	0.011	0.8	2.16	28939
	16	3	0.0145	6.04	1.08	4.96	0.811	0.04	0.015	0.014	1.0	2.10	40400
	16	4	0.0145	7.93	1.08	6.85	0.856	0.04	0.020	0.018	1.3	1.93	54616
6	16	6	0.0145	11.16	1.08	10.09	1.070	0.04	0.024	0.021	1.5	2.23	79141
	17	5	0.0145	7.93	0.99	6.95	0.928	0.04	0.019	0.017	1.2	2.17	55719
	17	7	0.0145	10.04	1.02	9.02	1.038	0.04	0.022	0.020	1.4	2.25	71367
	18	2	0.0145	3.49	1.16	2.32	0.581	0.05	0.010	0.010	0.7	1.86	19405
	18	3	0.0145	4.62	1.18	3.44	0.684	0.05	0.013	0.012	0.8	1.95	28379
	18	4	0.0145	5.63	1.14	4.49	0.741	0.05	0.015	0.014	1.0	1.92	36594
	18	5	0.0145	6.51	1.12	5.39	0.793	0.04	0.017	0.016	1.1	1.94	43584
	18	6	0.0145	8.14	1.17	6.97	0.865	0.05	0.020	0.018	1.3	1.95	55553
	18	7	0.0145	10.07	1.16	8.91	0.974	0.05	0.023	0.021	1.4	2.06	70122
	18	8	0.0145	11.52	1.14	10.37	1.055	0.05	0.025	0.022	1.5	2.15	81024
	19	2	0.0145	3.55	1.18	2.37	0.610	0.05	0.010	0.009	0.6	1.98	19833
	19	3	0.0145	4.30	1.21	3.09	0.676	0.05	0.011	0.011	0.7	2.02	25633
	19	4	0.0145	4.99	1.21	3.78	0.697	0.05	0.014	0.013	0.9	1.91	31086
	19	5	0.0145	5.86	1.28	4.58	0.756	0.05	0.015	0.014	1.0	1.96	37346
	19	6	0.0145	6.51	1.14	5.37	0.810	0.05	0.017	0.015	1.1	2.01	43484
	19	7	0.0145	7.27	1.07	6.20	0.847	0.04	0.018	0.017	1.2	2.00	49802
7	20	1	0.0145	3.25	1.28	1.98	0.524	0.05	0.009	0.009	0.6	1.73	16560
	20	3	0.0145	4.53	1.12	3.41	0.709	0.04	0.012	0.011	0.8	2.07	28182
	20	4	0.0145	5.08	1.08	4.00	0.722	0.04	0.014	0.013	0.9	1.96	32831
	20	5	0.0145	5.67	1.01	4.66	0.776	0.04	0.015	0.014	1.0	2.03	38012
	20	6	0.0145	6.04	1.11	4.94	0.771	0.04	0.016	0.015	1.0	1.95	40087
	20	7	0.0145	6.46	1.09	5.36	0.788	0.04	0.017	0.016	1.1	1.93	43347
	20	8	0.0145	6.82	1.08	5.74	0.803	0.04	0.018	0.016	1.1	1.92	46198
	21	3	0.0145	4.75	1.29	3.46	0.797	0.05	0.011	0.010	0.7	2.45	28802
	21	4	0.0145	5.22	1.27	3.95	0.864	0.05	0.011	0.011	0.7	2.58	32756
8	21	5	0.0145	6.00	1.27	4.73	0.891	0.05	0.013	0.012	0.9	2.47	38946
	22	4	0.0145	5.19	1.37	3.82	0.806	0.05	0.012	0.011	0.8	2.37	31651
	22	5	0.0145	5.97	1.41	4.55	0.805	0.06	0.014	0.013	0.9	2.16	37307

α (%)	i	j	D_{50} (m)	Q^+_{tot} (l/s)	$Q^+_{\inf}$ (l/s)	$Q^+_{\sup}$ (l/s)	U^+ (m/s)	$U^+_{\inf}$ (m/s)	d^+ (m)	R^+_h (m)	R^+_h/D_{50} (-)	Fr^+ (-)	Re^+ (-)
	22	6	0.0145	6.53	1.40	5.13	0.871	0.06	0.015	0.014	0.9	2.30	41887
	23	3	0.0145	4.69	1.38	3.32	0.744	0.05	0.011	0.011	0.7	2.25	27562
	23	4	0.0145	5.19	1.40	3.79	0.780	0.06	0.012	0.011	0.8	2.26	31348
	23	5	0.0145	6.15	1.33	4.82	0.870	0.05	0.014	0.013	0.9	2.36	39557
	23	6	0.0145	6.63	1.30	5.33	0.942	0.05	0.014	0.013	0.9	2.53	43673
	24	1	0.0145	4.13	1.27	2.86	0.668	0.05	0.011	0.010	0.7	2.06	23847
	24	2	0.0145	4.94	1.27	3.67	0.755	0.05	0.012	0.011	0.8	2.19	30314
	24	3	0.0145	5.49	1.27	4.22	0.849	0.05	0.012	0.012	0.8	2.44	34865
	24	4	0.0145	6.07	1.27	4.80	0.865	0.05	0.014	0.013	0.9	2.35	39346
	24	5	0.0145	6.46	1.27	5.19	0.849	0.05	0.015	0.014	1.0	2.20	42325
	25	1	0.0145	3.08	1.33	1.75	0.538	0.05	0.008	0.008	0.5	1.91	14758
	25	4	0.0145	4.44	1.35	3.10	0.694	0.05	0.011	0.011	0.7	2.11	25719
	25	5	0.0145	4.73	1.51	3.22	0.687	0.06	0.012	0.011	0.8	2.03	26668
	26	3	0.0145	4.04	1.46	2.58	0.655	0.06	0.010	0.009	0.6	2.11	21587
	26	4	0.0145	4.56	1.37	3.19	0.755	0.05	0.011	0.010	0.7	2.35	26605
	26	5	0.0145	5.04	1.37	3.67	0.774	0.05	0.012	0.011	0.8	2.27	30398
	27	1	0.0145	4.41	1.46	2.95	0.845	0.06	0.009	0.008	0.6	2.90	24772
	27	2	0.0145	5.06	1.46	3.59	0.796	0.06	0.011	0.011	0.7	2.40	29833
	27	3	0.0145	5.60	1.46	4.13	0.872	0.06	0.012	0.011	0.8	2.56	34238
10	28	1	0.0145	4.49	1.46	3.03	0.758	0.06	0.010	0.010	0.7	2.43	25323
	28	2	0.0145	5.65	1.46	4.19	0.940	0.06	0.011	0.011	0.7	2.85	34798
	29	2	0.0145	3.53	1.46	2.06	0.708	0.06	0.007	0.007	0.5	2.65	17463
	29	3	0.0145	5.20	1.46	3.73	0.883	0.06	0.011	0.010	0.7	2.75	31110
	30	1	0.0145	3.09	1.46	1.62	0.605	0.06	0.007	0.006	0.4	2.36	13788
	30	2	0.0145	3.51	1.46	2.05	0.597	0.06	0.009	0.008	0.6	2.06	17213
	30	3	0.0145	3.99	1.46	2.53	0.691	0.06	0.009	0.009	0.6	2.31	21200
	30	4	0.0145	4.46	1.46	3.00	0.739	0.06	0.010	0.010	0.7	2.35	25032
	30	5	0.0145	5.04	1.46	3.58	0.835	0.06	0.011	0.010	0.7	2.58	29779
	30	6	0.0145	5.62	1.46	4.15	0.898	0.06	0.012	0.011	0.8	2.67	34451

Table B. 2. Hydraulic characteristics of the experiments after the velocity profile adjustment.

α (%)	i	j	Q_{tot} (l/s)	Q_{sup} (l/s)	Q_{inf} (l/s)	U (m/s)	d (m)	R_h (m)	R_h/D_{50} (-)	Fr (-)	Re (-)
2	1	1	1.39	1.39	0.66	0.288	0.012	0.011	0.8	0.84	11521
	1	2	4.78	4.78	0.70	0.516	0.023	0.021	1.4	1.08	37587
	1	3	8.30	8.30	0.66	0.663	0.031	0.027	1.9	1.20	62954
	1	4	12.43	12.43	0.73	0.761	0.041	0.034	2.3	1.20	90533
	1	5	16.33	16.33	0.68	0.821	0.050	0.040	2.7	1.18	114709
	1	6	20.38	20.38	0.75	0.906	0.056	0.044	3.0	1.22	139511
	1	7	24.37	24.37	0.73	0.951	0.064	0.049	3.3	1.20	161889
	1	8	28.63	28.63	0.72	1.004	0.071	0.053	3.6	1.20	185147
	2	2	5.78	5.78	0.62	0.503	0.029	0.025	1.7	0.95	44314
	2	3	9.88	9.88	0.64	0.675	0.037	0.031	2.1	1.13	73235
	2	4	13.41	13.41	0.70	0.782	0.043	0.035	2.4	1.21	96873
	2	5	17.35	17.35	0.61	0.846	0.051	0.041	2.8	1.19	121172
	2	6	21.25	21.25	0.68	0.908	0.058	0.045	3.1	1.20	144199
	2	7	26.12	26.12	0.68	0.954	0.068	0.051	3.5	1.16	170662
	2	8	29.05	29.05	0.70	0.987	0.074	0.054	3.7	1.16	186307
	3	1	2.25	2.25	0.66	0.350	0.016	0.015	1.0	0.88	18244
	3	2	5.35	5.35	0.65	0.526	0.025	0.023	1.6	1.05	41665
	3	3	12.40	12.40	0.64	0.687	0.045	0.037	2.5	1.03	88760
	3	4	17.50	17.50	0.63	0.797	0.055	0.043	3.0	1.09	120440
	3	5	23.10	23.10	0.64	0.893	0.065	0.049	3.4	1.12	153128
	3	6	27.19	27.19	0.64	0.959	0.071	0.052	3.6	1.15	176093
	3	7	27.62	27.62	0.70	1.012	0.068	0.051	3.5	1.24	180627
	4	1	15.45	15.45	0.69	0.797	0.048	0.039	2.7	1.16	109114
	5	1	15.46	15.46	0.69	0.785	0.049	0.039	2.7	1.13	108817
3	6	2	5.78	5.78	0.71	0.661	0.022	0.020	1.4	1.43	45712
	6	3	7.15	7.15	0.73	0.666	0.027	0.024	1.6	1.30	55268
	6	4	13.24	13.24	0.71	0.885	0.037	0.031	2.2	1.46	97814
	6	5	19.51	19.51	0.73	1.036	0.047	0.038	2.6	1.52	138502
	7	2	5.50	5.50	0.77	0.616	0.022	0.020	1.4	1.32	43377
	7	3	9.37	9.37	0.72	0.766	0.031	0.027	1.8	1.40	71299
	7	4	13.94	13.94	0.73	0.897	0.039	0.033	2.2	1.45	102416
	7	5	19.19	19.19	0.76	0.992	0.048	0.039	2.7	1.44	135576
	8	1	15.47	15.47	0.79	0.921	0.042	0.035	2.4	1.44	112175
	9	1	15.47	15.47	0.80	0.919	0.042	0.035	2.4	1.43	112104
4	10	3	5.27	5.27	0.77	0.611	0.022	0.019	1.3	1.33	41704
	10	4	5.24	5.24	0.80	0.609	0.022	0.019	1.3	1.33	41487
	10	5	7.97	7.97	0.77	0.748	0.027	0.024	1.6	1.46	61699
	10	6	11.35	11.35	0.75	0.873	0.033	0.028	1.9	1.55	85662
	10	7	12.00	12.00	0.81	0.924	0.032	0.028	1.9	1.64	90587
	10	8	13.66	13.66	0.78	0.991	0.034	0.029	2.0	1.70	102221
	10	9	15.86	15.86	0.77	1.005	0.039	0.033	2.3	1.62	116207
	11	2	3.29	3.29	1.00	0.528	0.016	0.014	1.0	1.35	26796
	11	3	4.95	4.95	0.98	0.653	0.019	0.017	1.2	1.51	39660
	11	4	7.08	7.08	0.95	0.703	0.025	0.022	1.5	1.41	55156

α (%)	i	j	Q_{tot} (l/s)	Q_{sup} (l/s)	Q_{inf} (l/s)	U (m/s)	d (m)	R_h (m)	R_h/D_{50} (-)	Fr (-)	Re (-)
	11	5	8.94	8.94	0.96	0.782	0.029	0.025	1.7	1.48	68608
	11	6	10.88	10.88	0.94	0.832	0.033	0.028	1.9	1.47	82028
	11	7	13.26	13.26	0.97	0.908	0.036	0.031	2.1	1.52	98380
	11	8	15.03	15.03	1.00	0.979	0.038	0.032	2.2	1.60	110595
	12	3	6.45	6.45	0.99	0.703	0.023	0.021	1.4	1.48	50788
	12	4	7.85	7.85	1.06	0.783	0.025	0.022	1.5	1.58	61200
	12	5	10.01	10.01	1.02	0.824	0.030	0.026	1.8	1.51	76207
	12	6	11.97	11.97	1.07	0.915	0.033	0.028	1.9	1.62	90233
	12	7	13.95	13.95	1.05	0.915	0.038	0.032	2.2	1.50	102773
	14	1	15.51	15.51	0.89	1.035	0.037	0.032	2.2	1.71	114581
	15	3	5.26	5.26	1.20	0.642	0.020	0.019	1.3	1.43	41883
	15	4	7.17	7.17	1.04	0.800	0.022	0.020	1.4	1.71	56525
	15	5	7.89	7.89	1.04	0.808	0.024	0.022	1.5	1.65	61686
	15	6	9.15	9.15	1.02	0.967	0.024	0.021	1.5	2.01	71765
	16	1	2.49	2.49	1.05	0.457	0.014	0.013	0.9	1.25	20418
	16	2	3.52	3.52	1.06	0.560	0.016	0.015	1.0	1.43	28634
	16	3	4.99	4.99	1.05	0.594	0.021	0.019	1.3	1.31	39619
	16	4	6.88	6.88	1.05	0.694	0.025	0.022	1.5	1.41	53685
6	16	6	10.11	10.11	1.06	0.878	0.029	0.025	1.7	1.65	77529
	17	5	6.81	6.81	0.97	0.793	0.021	0.019	1.3	1.73	53925
	17	7	9.05	9.05	1.00	0.949	0.024	0.021	1.5	1.97	70903
	18	2	2.33	2.33	1.16	0.420	0.014	0.013	0.9	1.14	19100
	18	3	3.47	3.47	1.15	0.524	0.017	0.015	1.1	1.30	28114
	18	4	4.50	4.50	1.13	0.648	0.017	0.016	1.1	1.57	36319
	18	5	5.41	5.41	1.10	0.676	0.020	0.018	1.3	1.53	43172
	18	6	7.02	7.02	1.13	0.745	0.024	0.021	1.5	1.55	55080
	18	7	8.94	8.94	1.13	0.922	0.024	0.022	1.5	1.89	69930
	18	8	10.41	10.41	1.10	0.898	0.029	0.025	1.7	1.69	79784
	19	2	2.38	2.38	1.17	0.438	0.014	0.013	0.9	1.20	19568
	19	3	3.09	3.09	1.21	0.530	0.015	0.014	0.9	1.40	25264
	19	4	3.77	3.77	1.22	0.566	0.017	0.015	1.1	1.40	30558
	19	5	4.57	4.57	1.29	0.662	0.017	0.016	1.1	1.61	36874
	19	6	5.35	5.35	1.15	0.725	0.018	0.017	1.2	1.71	42981
	19	7	6.22	6.22	1.05	0.652	0.024	0.021	1.5	1.35	48725
7	20	1	1.96	1.96	1.29	0.422	0.012	0.011	0.8	1.25	16277
	20	3	3.40	3.40	1.13	0.581	0.015	0.014	0.9	1.54	27761
	20	4	3.99	3.99	1.08	0.571	0.017	0.016	1.1	1.38	32226
	20	5	4.67	4.67	1.00	0.657	0.018	0.016	1.1	1.58	37608
	20	6	4.94	4.94	1.10	0.695	0.018	0.016	1.1	1.67	39817
	20	7	5.35	5.35	1.10	0.710	0.019	0.017	1.2	1.65	42872
	20	8	5.72	5.72	1.08	0.675	0.021	0.019	1.3	1.48	45388
	21	3	3.50	3.50	1.25	0.686	0.013	0.012	0.8	1.94	28840
	21	4	3.97	3.97	1.25	0.645	0.015	0.014	1.0	1.66	32374
8	21	5	4.72	4.72	1.28	0.734	0.016	0.015	1.0	1.85	38339
	22	4	3.88	3.88	1.31	0.651	0.015	0.014	1.0	1.70	31697
	22	5	4.62	4.62	1.35	0.652	0.018	0.016	1.1	1.57	37235

α (%)	i	j	Q_{tot} (l/s)	Q_{sup} (l/s)	Q_{inf} (l/s)	U (m/s)	d (m)	R_h (m)	R_h/D_{50} (-)	Fr (-)	Re (-)
	22	6	5.15	5.15	1.38	0.830	0.016	0.014	1.0	2.13	41900
	23	3	3.37	3.37	1.32	0.534	0.016	0.015	1.0	1.36	27439
	23	4	3.85	3.85	1.34	0.635	0.015	0.014	1.0	1.65	31421
	23	5	4.86	4.86	1.29	0.679	0.018	0.016	1.1	1.62	39107
	23	6	5.37	5.37	1.26	0.735	0.018	0.017	1.2	1.74	43175
	24	1	2.90	2.90	1.24	0.474	0.015	0.014	1.0	1.23	23632
	24	2	3.70	3.70	1.24	0.574	0.016	0.015	1.0	1.45	30030
	24	3	4.25	4.25	1.24	0.608	0.017	0.016	1.1	1.47	34303
	24	4	4.83	4.83	1.23	0.630	0.019	0.017	1.2	1.46	38678
	24	5	5.23	5.23	1.24	0.635	0.021	0.019	1.3	1.42	41572
	25	1	1.75	1.75	1.33	0.397	0.011	0.010	0.7	1.21	14548
	25	4	3.11	3.11	1.33	0.570	0.014	0.013	0.9	1.56	25526
	25	5	3.25	3.25	1.48	0.593	0.014	0.013	0.9	1.62	26662
	26	3	2.59	2.59	1.45	0.482	0.013	0.013	0.9	1.33	21278
	26	4	3.18	3.18	1.38	0.734	0.011	0.010	0.7	2.25	26476
	26	5	3.68	3.68	1.36	0.593	0.016	0.014	1.0	1.52	29928
	27	1	3.01	3.01	1.40	0.538	0.014	0.013	0.9	1.46	24676
	27	2	3.64	3.64	1.41	0.600	0.015	0.014	1.0	1.56	29711
	27	3	4.18	4.18	1.42	0.668	0.016	0.015	1.0	1.71	34014
10	28	1	3.07	3.07	1.42	0.526	0.015	0.014	0.9	1.39	25074
	28	2	4.22	4.22	1.43	0.661	0.016	0.015	1.0	1.67	34245
	29	2	2.11	2.11	1.41	0.388	0.014	0.013	0.9	1.07	17347
	29	3	3.81	3.81	1.43	0.739	0.013	0.012	0.8	2.08	31424
	30	1	1.66	1.66	1.43	0.372	0.011	0.011	0.7	1.13	13778
	30	2	2.09	2.09	1.42	0.399	0.013	0.012	0.8	1.12	17180
	30	3	2.58	2.58	1.41	0.439	0.015	0.014	0.9	1.16	21054
	30	4	3.03	3.03	1.43	0.539	0.014	0.013	0.9	1.45	24839
	30	5	3.61	3.61	1.43	0.591	0.015	0.014	1.0	1.53	29435
	30	6	4.19	4.19	1.43	0.669	0.016	0.015	1.0	1.71	34053

B.3. Experimental Measurements

The table below presents a comprehensive summary of the experimental measurements conducted as part of a research study. The data provided encompasses a wide range of variables and parameters, including the channel slope (α), experiment number (i), profile number (j), median diameter of bed particle (D_{50}), total discharge (Q_{tot}^{+}), interstitial velocity ($U_{\inf}^{+}$), superficial velocity ($U_{\sup}^{+}$), water surface level (Z_{w}^{+}), and level of 'L' plates (Z_{L}^{+}). In addition, the table also indicates which velocity measurement technique was used in each profile, whether it was the Acoustic Doppler Velocimeter (ADV) or Particle Tracking Velocimetry (PTV), as well as the number of velocity measurements taken at each profile. The table has been carefully curated to exclude any derived variables, such as water depths, superficial discharge, or Reynolds number, in order to provide a clear and concise overview of the raw data.

Table B. 3. Experimental measurements.

α (%)	i	j	D_{50} (m)	Q_{tot}^{+} (l/s)	$U_{\inf}^{+}$ (m/s)	$U_{\sup}^{+}$ (m/s)	Z_{w}^{+} (m)	Z_{L}^{+} (m)	Type	# velocity measurements
2	1	1	0.0145	2.06	0.03	0.39	0.163	0.154	ADV	3
	1	2	0.0145	5.48	0.03	0.68	0.174	0.154	ADV	7
	1	3	0.0145	8.96	0.03	0.86	0.184	0.154	ADV	7
	1	4	0.0145	13.16	0.03	0.98	0.193	0.154	ADV	7
	1	5	0.0145	17.01	0.03	1.04	0.201	0.154	ADV	7
	1	6	0.0145	21.13	0.03	1.13	0.208	0.154	ADV	7
	1	7	0.0145	25.10	0.03	1.18	0.215	0.154	ADV	7
	1	8	0.0145	29.35	0.03	1.29	0.221	0.154	ADV	7
	2	2	0.0145	6.40	0.02	0.67	0.180	0.155	ADV	7
	2	3	0.0145	10.52	0.03	0.87	0.189	0.155	ADV	7
	2	4	0.0145	14.11	0.03	1.00	0.197	0.155	ADV	7
	2	5	0.0145	17.96	0.02	1.09	0.206	0.155	ADV	7
	2	6	0.0145	21.93	0.03	1.15	0.214	0.155	ADV	7
	2	7	0.0145	26.80	0.03	1.19	0.222	0.155	ADV	7
	2	8	0.0145	29.75	0.03	1.24	0.225	0.155	ADV	7
	3	1	0.0145	2.91	0.03	0.48	0.169	0.155	ADV	7
	3	2	0.0145	6.00	0.03	0.69	0.179	0.155	ADV	7
	3	3	0.0145	13.04	0.03	0.93	0.196	0.155	ADV	7
	3	4	0.0145	18.13	0.03	1.05	0.206	0.155	ADV	7
	3	5	0.0145	23.74	0.03	1.16	0.216	0.155	ADV	7
	3	6	0.0145	27.82	0.03	1.25	0.222	0.155	ADV	7
	3	7	0.0145	28.31	0.03	1.31	0.224	0.155	ADV	7
	4	1	0.0145	16.15	0.03	1.04	0.202	0.155	PTV	12265
	5	1	0.0145	16.15	0.03	1.04	0.202	0.155	ADV	5
3	6	2	0.0145	6.49	0.03	0.85	0.175	0.155	ADV	5
	6	3	0.0145	7.88	0.03	0.91	0.178	0.155	ADV	6
	6	4	0.0145	13.94	0.03	1.14	0.192	0.155	ADV	7
	6	5	0.0145	20.24	0.03	1.32	0.202	0.155	ADV	7

α (%)	i	j	D_{50} (m)	Q_{tot}^{+} (l/s)	$U_{\inf}^{+}$ (m/s)	$U_{\sup}^{+}$ (m/s)	Z_{w}^{+} (m)	Z_{L}^{+} (m)	Type	# velocity measurements
	7	2	0.0145	6.27	0.03	0.80	0.176	0.155	ADV	6
	7	3	0.0145	10.09	0.03	0.98	0.185	0.155	ADV	7
	7	4	0.0145	14.67	0.03	1.16	0.195	0.155	ADV	7
	7	5	0.0145	19.95	0.03	1.28	0.205	0.155	ADV	7
	8	1	0.0145	16.27	0.03	1.20	0.196	0.155	PTV	17359
	9	1	0.0145	16.27	0.03	1.20	0.196	0.155	ADV	4
4	10	3	0.0145	6.04	0.03	0.82	0.173	0.155	ADV	7
	10	4	0.0145	6.04	0.03	0.82	0.173	0.155	ADV	3
	10	5	0.0145	8.74	0.03	0.99	0.178	0.155	ADV	7
	10	6	0.0145	12.10	0.03	1.13	0.186	0.155	ADV	7
	10	7	0.0145	12.82	0.03	1.15	0.186	0.155	ADV	7
	10	8	0.0145	14.44	0.03	1.27	0.190	0.155	ADV	7
	10	9	0.0145	16.63	0.03	1.30	0.194	0.155	ADV	7
	11	2	0.0145	4.29	0.04	0.69	0.167	0.155	ADV	7
	11	3	0.0145	5.93	0.04	0.85	0.172	0.155	ADV	7
	11	4	0.0145	8.03	0.04	0.93	0.176	0.155	ADV	7
	11	5	0.0145	9.90	0.04	1.02	0.180	0.155	ADV	7
	11	6	0.0145	11.82	0.04	1.07	0.183	0.155	ADV	7
	11	7	0.0145	14.23	0.04	1.15	0.186	0.155	ADV	7
	11	8	0.0145	16.03	0.04	1.24	0.190	0.155	ADV	7
	12	3	0.0145	7.44	0.04	0.92	0.175	0.155	ADV	7
	12	4	0.0145	8.92	0.04	1.02	0.177	0.155	ADV	7
	12	5	0.0145	11.02	0.04	1.07	0.183	0.155	ADV	7
	12	6	0.0145	13.04	0.04	1.18	0.186	0.155	ADV	7
	12	7	0.0145	15.00	0.04	1.21	0.188	0.155	ADV	7
	14	1	0.0145	16.40	0.03	1.33	0.192	0.155	ADV	4
6	15	3	0.0145	6.46	0.05	0.88	0.172	0.156	ADV	7
	15	4	0.0145	8.21	0.04	1.06	0.175	0.156	ADV	7
	15	5	0.0145	8.93	0.04	1.08	0.176	0.156	ADV	7
	15	6	0.0145	10.17	0.04	1.24	0.178	0.156	ADV	7
	16	1	0.0145	3.54	0.04	0.64	0.164	0.155	PTV	4071
	16	2	0.0145	4.57	0.04	0.79	0.167	0.155	PTV	11113
	16	3	0.0145	6.04	0.04	0.87	0.170	0.155	PTV	19293
	16	4	0.0145	7.93	0.04	0.99	0.175	0.155	PTV	14150
	16	6	0.0145	11.16	0.04	1.26	0.179	0.155	PTV	20561
	17	5	0.0145	7.93	0.04	1.05	0.173	0.154	ADV	7
	17	7	0.0145	10.04	0.04	1.22	0.176	0.154	ADV	7
	18	2	0.0145	3.49	0.05	0.62	0.164	0.154	ADV	4
	18	3	0.0145	4.62	0.05	0.70	0.166	0.154	ADV	7
	18	4	0.0145	5.63	0.05	0.88	0.169	0.154	ADV	7
	18	5	0.0145	6.51	0.04	0.92	0.171	0.154	ADV	7
	18	6	0.0145	8.14	0.05	0.99	0.174	0.154	ADV	7
	18	7	0.0145	10.07	0.05	1.18	0.176	0.154	ADV	7
	18	8	0.0145	11.52	0.05	1.18	0.178	0.154	ADV	3
7	19	2	0.0145	3.55	0.05	0.65	0.164	0.155	ADV	7
	19	3	0.0145	4.30	0.05	0.75	0.166	0.155	ADV	7

α (%)	i	j	D_{50} (m)	Q^{+}_{tot} (l/s)	$U^{+}_{\inf}$ (m/s)	$U^{+}_{\sup}$ (m/s)	Z^{+}_{w} (m)	Z^{+}_{L} (m)	Type	# velocity measurements
	19	4	0.0145	4.99	0.05	0.81	0.168	0.155	ADV	7
	19	5	0.0145	5.86	0.05	0.93	0.170	0.155	ADV	7
	19	6	0.0145	6.51	0.05	0.98	0.171	0.155	ADV	7
	19	7	0.0145	7.27	0.04	0.93	0.173	0.155	ADV	7
	20	1	0.0145	3.25	0.05	0.62	0.164	0.155	ADV	3
	20	3	0.0145	4.53	0.04	0.75	0.167	0.155	ADV	7
	20	4	0.0145	5.08	0.04	0.80	0.169	0.155	ADV	7
	20	5	0.0145	5.67	0.04	0.90	0.170	0.155	ADV	7
	20	6	0.0145	6.04	0.04	0.95	0.171	0.155	ADV	7
	20	7	0.0145	6.46	0.04	0.97	0.172	0.155	ADV	7
	20	8	0.0145	6.82	0.04	0.94	0.173	0.155	ADV	7
	21	3	0.0145	4.75	0.05	0.91	0.166	0.155	ADV	7
	21	4	0.0145	5.22	0.05	0.89	0.166	0.155	ADV	7
	21	5	0.0145	6.00	0.05	1.03	0.168	0.155	ADV	7
	22	4	0.0145	5.19	0.05	0.89	0.167	0.155	ADV	7
	22	5	0.0145	5.97	0.06	0.89	0.169	0.155	ADV	7
	22	6	0.0145	6.53	0.06	1.10	0.170	0.155	ADV	7
	23	3	0.0145	4.69	0.05	0.77	0.166	0.155	ADV	7
8	23	4	0.0145	5.19	0.06	0.86	0.167	0.155	ADV	7
	23	5	0.0145	6.15	0.05	0.94	0.169	0.155	ADV	7
	23	6	0.0145	6.63	0.05	1.00	0.169	0.155	ADV	7
	24	1	0.0145	4.13	0.05	0.73	0.166	0.155	PTV	7775
	24	2	0.0145	4.94	0.05	0.84	0.167	0.155	PTV	12076
	24	3	0.0145	5.49	0.05	0.87	0.167	0.155	PTV	5788
	24	4	0.0145	6.07	0.05	0.90	0.169	0.155	PTV	10499
	24	5	0.0145	6.46	0.05	0.95	0.170	0.155	PTV	18623
	25	1	0.0145	3.08	0.05	0.63	0.163	0.155	ADV	3
	25	4	0.0145	4.44	0.05	0.86	0.166	0.155	ADV	7
	25	5	0.0145	4.73	0.06	0.86	0.167	0.155	ADV	7
	26	3	0.0145	4.04	0.06	0.73	0.165	0.155	ADV	7
	26	4	0.0145	4.56	0.05	0.91	0.166	0.155	ADV	7
	26	5	0.0145	5.04	0.05	0.86	0.167	0.155	ADV	7
	27	1	0.0145	4.41	0.06	0.78	0.164	0.155	PTV	5542
	27	2	0.0145	5.06	0.06	0.87	0.166	0.155	PTV	10850
	27	3	0.0145	5.60	0.06	0.95	0.167	0.155	PTV	8700
10	28	1	0.0145	4.49	0.06	0.77	0.165	0.155	PTV	9371
	28	2	0.0145	5.65	0.06	0.92	0.166	0.155	PTV	10008
	29	2	0.0145	3.53	0.06	0.60	0.162	0.155	PTV	5531
	29	3	0.0145	5.20	0.06	0.86	0.166	0.155	PTV	15505
	30	1	0.0145	3.09	0.06	0.58	0.162	0.155	PTV	5129
	30	2	0.0145	3.51	0.06	0.63	0.164	0.155	PTV	5680
	30	3	0.0145	3.99	0.06	0.68	0.164	0.155	PTV	7528
	30	4	0.0145	4.46	0.06	0.81	0.165	0.155	PTV	8682
	30	5	0.0145	5.04	0.06	0.88	0.166	0.155	PTV	14485
	30	6	0.0145	5.62	0.06	0.95	0.167	0.155	PTV	8939

B.4. Velocity Profile Distribution Adjustment Results

This section provides the necessary data and figures for conducting an in-depth analysis of the velocity profile adjustment conducted in this thesis. The purpose of this section is to provide a detailed overview of the data analysis used due to the number of profiles; it was impossible to include this level of detail in the main body of the thesis.

The section is divided into three parts, including a summary of the variables and parameters discussed in the profile distribution adjustment of Chapter 4, dimensionless log profiles grouped by flume slopes, and individual analysis for each profile.

The summary of the velocity profile adjustments offers a thorough examination of each profile, including the measurement techniques used, data adjustments made, and results obtained. This analysis is essential for understanding the behaviour of the flow in the channel and how it is affected by various variables.

By grouping all the profiles conducted under the same flume slope and organizing them by discharge, it is possible to identify or discard patterns and trends that were not observed in the figures provided in the main thesis.

Additionally, examining each profile individually enables the identification of patterns and trends and drawing conclusions about the overall behaviour of the flow in the channel. This appendix section offers a comprehensive analysis of the velocity profile adjustments and serves as a valuable resource for those interested in the methodology and data analysis used in the research study.

B. 1. 1. Summary of variables and parameters in velocity profile adjustment

The summary of variables outlines the various parameters and factors that were optimized or obtained through the velocity profile adjustment analysis. These variables include the channel slope, experiment number, profile number, including the channel slope (α), experiment number (i), profile number (j), superficial discharge ($Q_{\sup}$), interstitial discharge ($Q_{\inf}$), total discharge (Q_{tot}), water surface level ($Z_{w\delta}$), reference bed level (Z_T), origin of velocity profile level (Z_o), water depth (d), water depth from the reference level (d_{Z_T}), origin of the velocity profile height (z_o), reference level shifting distance (δ_{incr}), origin velocity profile shifting distance (δ_o), vibration of water surface shifting distance ($\delta_{\sup}$), PTV parameters (Δ, d_{ROI}), relative roughness height (k_s), shear velocity (u_*), and Von Karman constant (k). In addition, the table also indicates which velocity measurement technique was used in each profile, whether it was the Acoustic Doppler Velocimeter (ADV) or Particle Tracking Velocimetry (PTV).

Table B. 4. Variables and optimized parameters from the velocity profile adjustment.

α (%)	i	j	Type	Q_{sup} (l/s)	Q_{inf} (l/s)	Q_{tot} (l/s)	$Z_{w\delta}$ (m)	Z_T (m)	Z_o (m)	d (m)	d_{Z_T} (m)	z_o (m)	δ_{incr} (m)	δ_o (m)	δ_{sup} (m)	Δ (m)	d_{ROI} (m)	k_s (m)	u_* (m/s)	k (-)
2	1	1	ADV	1.39	0.66	2.06	0.166	0.154	0.154	0.012	0.012	0.000	0.000	0.000	0.003	NaN	NaN	0.008	0.041	0.403
	1	2	ADV	4.78	0.70	5.48	0.179	0.155	0.156	0.023	0.023	0.000	-0.001	-0.001	0.005	NaN	NaN	0.008	0.060	0.403
	1	3	ADV	8.30	0.66	8.96	0.186	0.154	0.154	0.031	0.032	0.000	0.000	0.000	0.002	NaN	NaN	0.008	0.071	0.403
	1	4	ADV	12.43	0.73	13.16	0.194	0.153	0.153	0.041	0.041	0.000	0.001	0.001	0.001	NaN	NaN	0.010	0.080	0.403
	1	5	ADV	16.33	0.68	17.01	0.202	0.151	0.152	0.050	0.050	0.000	0.003	0.002	0.001	NaN	NaN	0.012	0.086	0.403
	1	6	ADV	20.38	0.75	21.13	0.208	0.151	0.152	0.056	0.057	0.000	0.003	0.002	0.000	NaN	NaN	0.011	0.091	0.403
	1	7	ADV	24.37	0.73	25.10	0.217	0.152	0.153	0.064	0.065	0.000	0.002	0.002	0.001	NaN	NaN	0.013	0.096	0.403
	1	8	ADV	28.63	0.72	29.35	0.222	0.150	0.151	0.071	0.072	0.000	0.004	0.004	0.001	NaN	NaN	0.013	0.099	0.403
	2	2	ADV	5.78	0.62	6.40	0.182	0.153	0.153	0.029	0.029	0.001	0.002	0.002	0.002	NaN	NaN	0.014	0.066	0.403
	2	3	ADV	9.88	0.64	10.52	0.189	0.152	0.153	0.037	0.037	0.000	0.003	0.002	0.001	NaN	NaN	0.011	0.075	0.403
	2	4	ADV	13.41	0.70	14.11	0.197	0.154	0.154	0.043	0.043	0.000	0.001	0.001	0.000	NaN	NaN	0.010	0.083	0.403
	2	5	ADV	17.35	0.61	17.96	0.207	0.155	0.155	0.051	0.052	0.000	0.000	0.000	0.000	NaN	NaN	0.012	0.090	0.403
	2	6	ADV	21.25	0.68	21.93	0.214	0.155	0.156	0.058	0.059	0.001	0.000	-0.001	0.000	NaN	NaN	0.013	0.095	0.403
	2	7	ADV	26.12	0.68	26.79	0.223	0.154	0.155	0.068	0.069	0.001	0.001	0.000	0.001	NaN	NaN	0.016	0.099	0.403
	2	8	ADV	29.05	0.70	29.75	0.225	0.151	0.152	0.074	0.074	0.001	0.004	0.003	0.001	NaN	NaN	0.015	0.101	0.403
	3	1	ADV	2.25	0.66	2.90	0.172	0.155	0.156	0.016	0.017	0.000	0.000	-0.001	0.003	NaN	NaN	0.011	0.051	0.403
	3	2	ADV	5.35	0.65	6.00	0.178	0.153	0.153	0.025	0.026	0.000	0.002	0.002	0.000	NaN	NaN	0.011	0.065	0.403
	3	3	ADV	12.40	0.64	13.04	0.196	0.150	0.151	0.045	0.046	0.001	0.005	0.004	0.000	NaN	NaN	0.017	0.082	0.403
	3	4	ADV	17.50	0.63	18.13	0.205	0.149	0.150	0.055	0.056	0.001	0.006	0.005	-0.001	NaN	NaN	0.016	0.089	0.403
	3	5	ADV	23.10	0.64	23.74	0.216	0.150	0.151	0.065	0.065	0.001	0.005	0.004	-0.001	NaN	NaN	0.017	0.096	0.403
	3	6	ADV	27.19	0.64	27.82	0.222	0.150	0.151	0.071	0.071	0.001	0.005	0.004	-0.001	NaN	NaN	0.016	0.099	0.403
	3	7	ADV	27.62	0.70	28.31	0.225	0.156	0.156	0.068	0.069	0.000	-0.001	-0.001	0.001	NaN	NaN	0.013	0.100	0.403
	4	1	PTV	15.45	0.69	16.15	0.203	0.155	0.155	0.048	0.049	0.001	0.000	0.000	NaN	0.011	0.038	0.014	0.088	0.403
	5	1	ADV	15.46	0.69	16.15	0.203	0.154	0.154	0.049	0.050	0.001	0.001	0.001	0.001	NaN	NaN	0.014	0.087	0.403
3	6	2	ADV	5.78	0.71	6.49	0.178	0.156	0.156	0.022	0.022	0.000	-0.001	-0.001	0.003	NaN	NaN	0.006	0.073	0.403

α (%)	i	j	Type	$Q_{\sup}$ (l/s)	$Q_{\inf}$ (l/s)	Q_{tot} (l/s)	$Z_{w\delta}$ (m)	Z_T (m)	Z_o (m)	d (m)	d_{Z_T} (m)	z_o (m)	δ_{incr} (m)	δ_o (m)	$\delta_{\sup}$ (m)	Δ (m)	d_{ROI} (m)	k_s (m)	u_* (m/s)	k (-)
	6	3	ADV	7.15	0.73	7.87	0.182	0.155	0.156	0.027	0.027	0.000	0.000	-0.001	0.005	NaN	NaN	0.009	0.077	0.403
	6	4	ADV	13.24	0.71	13.94	0.192	0.154	0.154	0.037	0.038	0.000	0.001	0.001	0.000	NaN	NaN	0.010	0.096	0.403
	6	5	ADV	19.51	0.73	20.24	0.203	0.156	0.156	0.047	0.047	0.000	-0.001	-0.001	0.001	NaN	NaN	0.010	0.106	0.403
	7	2	ADV	5.50	0.77	6.27	0.175	0.152	0.153	0.022	0.023	0.000	0.002	0.002	-0.001	NaN	NaN	0.009	0.075	0.403
	7	3	ADV	9.37	0.72	10.10	0.183	0.152	0.153	0.031	0.031	0.000	0.002	0.002	-0.002	NaN	NaN	0.010	0.089	0.403
	7	4	ADV	13.94	0.73	14.67	0.193	0.154	0.154	0.039	0.039	0.000	0.001	0.000	-0.001	NaN	NaN	0.011	0.099	0.403
	7	5	ADV	19.19	0.76	19.95	0.204	0.155	0.156	0.048	0.049	0.000	-0.001	-0.001	0.000	NaN	NaN	0.013	0.108	0.403
	8	1	PTV	15.47	0.79	16.26	0.197	0.155	0.155	0.042	0.042	0.000	0.000	0.000	NaN	0.003	0.039	0.011	0.101	0.403
	9	1	ADV	15.47	0.80	16.26	0.199	0.156	0.156	0.042	0.043	0.000	-0.001	-0.001	0.002	NaN	NaN	0.012	0.100	0.403
4	10	3	ADV	5.27	0.77	6.03	0.176	0.154	0.154	0.022	0.022	0.000	0.001	0.001	0.002	NaN	NaN	0.011	0.081	0.403
	10	4	ADV	5.24	0.80	6.04	0.175	0.153	0.153	0.022	0.022	0.000	0.002	0.002	0.002	NaN	NaN	0.011	0.081	0.403
	10	5	ADV	7.97	0.77	8.74	0.178	0.151	0.152	0.027	0.027	0.000	0.004	0.003	0.000	NaN	NaN	0.010	0.090	0.403
	10	6	ADV	11.35	0.75	12.10	0.185	0.152	0.153	0.033	0.033	0.000	0.003	0.002	0.000	NaN	NaN	0.011	0.102	0.403
	10	7	ADV	12.00	0.81	12.82	0.185	0.152	0.152	0.032	0.033	0.000	0.003	0.003	-0.002	NaN	NaN	0.010	0.103	0.403
	10	8	ADV	13.66	0.78	14.44	0.189	0.155	0.155	0.034	0.035	0.000	0.000	0.000	0.000	NaN	NaN	0.009	0.107	0.403
	10	9	ADV	15.86	0.77	16.63	0.194	0.154	0.154	0.039	0.040	0.000	0.001	0.001	0.000	NaN	NaN	0.012	0.113	0.403
	11	2	ADV	3.29	1.00	4.29	0.172	0.156	0.156	0.016	0.016	0.000	-0.001	-0.001	0.004	NaN	NaN	0.007	0.068	0.403
	11	3	ADV	4.95	0.98	5.93	0.174	0.154	0.155	0.019	0.019	0.000	0.001	0.000	0.001	NaN	NaN	0.007	0.079	0.403
	11	4	ADV	7.08	0.95	8.03	0.176	0.151	0.151	0.025	0.026	0.000	0.004	0.004	0.000	NaN	NaN	0.010	0.086	0.403
	11	5	ADV	8.94	0.96	9.90	0.181	0.152	0.153	0.029	0.029	0.000	0.003	0.002	0.002	NaN	NaN	0.011	0.093	0.403
	11	6	ADV	10.88	0.94	11.82	0.183	0.150	0.150	0.033	0.033	0.000	0.005	0.005	0.000	NaN	NaN	0.012	0.098	0.403
	11	7	ADV	13.26	0.97	14.23	0.186	0.150	0.150	0.036	0.037	0.000	0.005	0.005	0.000	NaN	NaN	0.011	0.103	0.403
	11	8	ADV	15.03	1.00	16.03	0.191	0.153	0.153	0.038	0.039	0.000	0.002	0.002	0.002	NaN	NaN	0.011	0.108	0.403
	12	3	ADV	6.45	0.99	7.44	0.175	0.152	0.152	0.023	0.023	0.000	0.003	0.003	0.000	NaN	NaN	0.009	0.085	0.403
	12	4	ADV	7.85	1.06	8.92	0.179	0.153	0.153	0.025	0.025	0.000	0.002	0.001	0.001	NaN	NaN	0.008	0.089	0.403
	12	5	ADV	10.01	1.02	11.02	0.183	0.152	0.153	0.030	0.031	0.000	0.002	0.002	0.000	NaN	NaN	0.011	0.098	0.403
	12	6	ADV	11.97	1.07	13.04	0.188	0.154	0.155	0.033	0.033	0.000	0.000	0.000	0.002	NaN	NaN	0.010	0.102	0.403

α (%)	i	j	Type	$Q_{\sup}$ (l/s)	$Q_{\inf}$ (l/s)	Q_{tot} (l/s)	$Z_{w\delta}$ (m)	Z_T (m)	Z_o (m)	d (m)	d_{Z_T} (m)	z_o (m)	δ_{incr} (m)	δ_o (m)	$\delta_{\sup}$ (m)	Δ (m)	d_{ROI} (m)	k_s (m)	u_* (m/s)	k (-)
	12	7	ADV	13.95	1.05	15.00	0.190	0.152	0.152	0.038	0.039	0.001	0.003	0.003	0.002	NaN	NaN	0.013	0.106	0.403
	14	1	ADV	15.51	0.89	16.40	0.193	0.156	0.156	0.037	0.038	0.000	-0.001	-0.001	0.001	NaN	NaN	0.009	0.111	0.403
	15	3	ADV	5.26	1.20	6.46	0.172	0.151	0.152	0.020	0.021	0.001	0.005	0.004	0.000	NaN	NaN	0.014	0.094	0.403
	15	4	ADV	7.17	1.04	8.21	0.177	0.154	0.155	0.022	0.023	0.000	0.002	0.001	0.002	NaN	NaN	0.010	0.101	0.403
	15	5	ADV	7.89	1.04	8.93	0.175	0.150	0.151	0.024	0.025	0.000	0.006	0.005	-0.001	NaN	NaN	0.011	0.103	0.403
	15	6	ADV	9.15	1.02	10.17	0.174	0.151	0.151	0.024	0.024	0.000	0.005	0.005	-0.003	NaN	NaN	0.007	0.107	0.403
	16	1	PTV	2.49	1.05	3.54	0.165	0.151	0.151	0.014	0.013	0.000	0.004	0.004	NaN	0.003	0.008	0.011	0.072	0.403
	16	2	PTV	3.52	1.06	4.58	0.168	0.153	0.152	0.016	0.015	0.000	0.002	0.003	NaN	0.004	0.010	0.011	0.081	0.403
	16	3	PTV	4.99	1.05	6.04	0.172	0.151	0.151	0.021	0.020	0.001	0.004	0.004	NaN	0.005	0.013	0.017	0.091	0.403
	16	4	PTV	6.88	1.05	7.93	0.176	0.152	0.151	0.025	0.024	0.001	0.003	0.004	NaN	0.007	0.015	0.018	0.103	0.403
6	16	6	PTV	10.11	1.06	11.17	0.181	0.152	0.152	0.029	0.029	0.001	0.003	0.003	NaN	0.012	0.016	0.013	0.111	0.403
	17	5	ADV	6.81	0.97	7.78	0.174	0.152	0.152	0.021	0.022	0.000	0.002	0.002	0.001	NaN	NaN	0.010	0.100	0.403
	17	7	ADV	9.05	1.00	10.04	0.174	0.150	0.150	0.024	0.024	0.000	0.004	0.004	-0.002	NaN	NaN	0.007	0.107	0.403
	18	2	ADV	2.33	1.16	3.48	0.166	0.152	0.153	0.014	0.015	0.001	0.002	0.001	0.003	NaN	NaN	0.016	0.075	0.403
	18	3	ADV	3.47	1.15	4.62	0.166	0.149	0.149	0.017	0.017	0.001	0.005	0.004	0.000	NaN	NaN	0.014	0.083	0.403
	18	4	ADV	4.50	1.13	5.63	0.169	0.151	0.152	0.017	0.018	0.000	0.002	0.002	0.001	NaN	NaN	0.011	0.091	0.403
	18	5	ADV	5.41	1.10	6.51	0.170	0.150	0.150	0.020	0.021	0.001	0.004	0.003	0.000	NaN	NaN	0.013	0.096	0.403
	18	6	ADV	7.02	1.13	8.15	0.171	0.147	0.148	0.024	0.024	0.001	0.007	0.006	-0.003	NaN	NaN	0.014	0.104	0.403
	18	7	ADV	8.94	1.13	10.07	0.174	0.149	0.150	0.024	0.025	0.000	0.004	0.004	-0.002	NaN	NaN	0.009	0.110	0.403
	18	8	ADV	10.41	1.10	11.52	0.177	0.148	0.148	0.029	0.029	0.001	0.006	0.006	-0.001	NaN	NaN	0.013	0.113	0.403
	19	2	ADV	2.38	1.17	3.55	0.167	0.152	0.153	0.014	0.014	0.001	0.002	0.002	0.002	NaN	NaN	0.016	0.080	0.403
	19	3	ADV	3.09	1.21	4.30	0.169	0.154	0.154	0.015	0.015	0.001	0.001	0.000	0.003	NaN	NaN	0.013	0.086	0.403
	19	4	ADV	3.77	1.22	4.99	0.172	0.155	0.156	0.017	0.017	0.001	-0.001	-0.001	0.004	NaN	NaN	0.016	0.093	0.403
7	19	5	ADV	4.57	1.29	5.86	0.173	0.156	0.156	0.017	0.018	0.001	-0.001	-0.002	0.004	NaN	NaN	0.013	0.098	0.403
	19	6	ADV	5.35	1.15	6.50	0.174	0.155	0.156	0.018	0.019	0.000	-0.001	-0.001	0.003	NaN	NaN	0.012	0.102	0.403
	19	7	ADV	6.22	1.05	7.27	0.175	0.151	0.151	0.024	0.024	0.001	0.004	0.003	0.002	NaN	NaN	0.022	0.107	0.403
	20	1	ADV	1.96	1.29	3.25	0.168	0.156	0.156	0.012	0.012	0.001	-0.001	-0.001	0.004	NaN	NaN	0.015	0.078	0.403

α (%)	i	j	Type	$Q_{\sup}$ (l/s)	$Q_{\inf}$ (l/s)	Q_{tot} (l/s)	$Z_{w\delta}$ (m)	Z_T (m)	Z_o (m)	d (m)	d_{Z_T} (m)	z_o (m)	δ_{incr} (m)	δ_o (m)	$\delta_{\sup}$ (m)	Δ (m)	d_{ROI} (m)	k_s (m)	u_* (m/s)	k (-)
	20	3	ADV	3.40	1.13	4.52	0.171	0.156	0.156	0.015	0.015	0.000	-0.001	-0.001	0.004	NaN	NaN	0.011	0.088	0.403
	20	4	ADV	3.99	1.08	5.08	0.173	0.155	0.156	0.017	0.018	0.001	0.000	-0.001	0.004	NaN	NaN	0.017	0.094	0.403
	20	5	ADV	4.67	1.00	5.67	0.171	0.153	0.153	0.018	0.018	0.001	0.002	0.002	0.001	NaN	NaN	0.013	0.098	0.403
	20	6	ADV	4.94	1.10	6.04	0.172	0.153	0.154	0.018	0.018	0.000	0.002	0.001	0.001	NaN	NaN	0.012	0.101	0.403
	20	7	ADV	5.35	1.10	6.45	0.175	0.156	0.156	0.019	0.019	0.001	-0.001	-0.001	0.003	NaN	NaN	0.013	0.104	0.403
	20	8	ADV	5.72	1.08	6.80	0.177	0.155	0.155	0.021	0.022	0.001	0.000	0.000	0.004	NaN	NaN	0.018	0.106	0.403
	21	3	ADV	3.50	1.25	4.75	0.164	0.151	0.151	0.013	0.013	0.000	0.004	0.004	-0.002	NaN	NaN	0.006	0.090	0.403
	21	4	ADV	3.97	1.25	5.22	0.167	0.151	0.152	0.015	0.016	0.000	0.004	0.003	0.001	NaN	NaN	0.010	0.092	0.403
	21	5	ADV	4.72	1.28	6.00	0.172	0.156	0.156	0.016	0.016	0.000	-0.001	-0.001	0.004	NaN	NaN	0.009	0.099	0.403
	22	4	ADV	3.88	1.31	5.19	0.163	0.148	0.148	0.015	0.015	0.000	0.007	0.007	-0.004	NaN	NaN	0.010	0.094	0.403
	22	5	ADV	4.62	1.35	5.97	0.166	0.147	0.148	0.018	0.018	0.001	0.008	0.007	-0.004	NaN	NaN	0.015	0.102	0.403
	22	6	ADV	5.15	1.38	6.53	0.169	0.153	0.153	0.016	0.016	0.000	0.002	0.002	-0.001	NaN	NaN	0.007	0.104	0.403
	23	3	ADV	3.37	1.32	4.69	0.164	0.148	0.148	0.016	0.016	0.001	0.007	0.006	-0.002	NaN	NaN	0.016	0.091	0.403
8	23	4	ADV	3.85	1.34	5.19	0.163	0.147	0.148	0.015	0.016	0.000	0.007	0.007	-0.004	NaN	NaN	0.011	0.095	0.403
	23	5	ADV	4.86	1.29	6.15	0.169	0.150	0.151	0.018	0.018	0.001	0.005	0.004	0.000	NaN	NaN	0.013	0.101	0.403
	23	6	ADV	5.37	1.26	6.63	0.168	0.150	0.150	0.018	0.019	0.000	0.005	0.005	-0.001	NaN	NaN	0.011	0.102	0.403
	24	1	PTV	2.90	1.24	4.14	0.167	0.152	0.151	0.015	0.015	0.001	0.003	0.004	NaN	0.006	0.007	0.020	0.089	0.403
	24	2	PTV	3.70	1.24	4.94	0.167	0.150	0.151	0.016	0.017	0.001	0.005	0.004	NaN	0.004	0.008	0.015	0.095	0.403
	24	3	PTV	4.25	1.24	5.49	0.169	0.152	0.151	0.017	0.017	0.001	0.003	0.004	NaN	0.008	0.007	0.015	0.096	0.403
	24	4	PTV	4.83	1.23	6.07	0.170	0.151	0.151	0.019	0.019	0.001	0.004	0.004	NaN	0.006	0.010	0.017	0.101	0.403
	24	5	PTV	5.23	1.24	6.47	0.172	0.152	0.151	0.021	0.020	0.001	0.003	0.004	NaN	0.008	0.011	0.020	0.106	0.403
	25	1	ADV	1.75	1.33	3.08	0.166	0.154	0.155	0.011	0.012	0.001	0.001	0.000	0.003	NaN	NaN	0.019	0.087	0.403
	25	4	ADV	3.11	1.33	4.44	0.167	0.153	0.153	0.014	0.014	0.001	0.002	0.002	0.001	NaN	NaN	0.016	0.102	0.403
	25	5	ADV	3.25	1.48	4.72	0.166	0.151	0.152	0.014	0.014	0.001	0.004	0.003	-0.001	NaN	NaN	0.015	0.104	0.403
10	26	3	ADV	2.59	1.45	4.04	0.168	0.154	0.154	0.013	0.014	0.001	0.001	0.001	0.003	NaN	NaN	0.019	0.096	0.403
	26	4	ADV	3.18	1.38	4.56	0.167	0.156	0.156	0.011	0.011	0.000	-0.001	-0.001	0.001	NaN	NaN	0.006	0.099	0.403
	26	5	ADV	3.68	1.36	5.04	0.170	0.154	0.154	0.016	0.016	0.001	0.001	0.001	0.003	NaN	NaN	0.017	0.105	0.403

α (%)	i	j	Type	Q_{sup} (l/s)	Q_{inf} (l/s)	Q_{tot} (l/s)	$Z_{w\delta}$ (m)	Z_T (m)	Z_o (m)	d (m)	d_{Z_T} (m)	z_o (m)	δ_{incr} (m)	δ_o (m)	δ_{sup} (m)	Δ (m)	d_{ROI} (m)	k_s (m)	u_* (m/s)	k (-)
	27	1	PTV	3.01	1.40	4.41	0.162	0.149	0.148	0.014	0.014	0.001	0.006	0.007	NaN	0.002	0.004	0.014	0.090	0.403
	27	2	PTV	3.64	1.41	5.06	0.165	0.149	0.150	0.015	0.016	0.001	0.006	0.005	NaN	0.001	0.007	0.016	0.102	0.403
	27	3	PTV	4.18	1.42	5.60	0.166	0.150	0.150	0.016	0.016	0.001	0.005	0.005	NaN	0.003	0.007	0.013	0.105	0.403
	28	1	PTV	3.07	1.42	4.49	0.166	0.151	0.151	0.015	0.015	0.001	0.004	0.004	NaN	0.004	0.008	0.018	0.096	0.403
	28	2	PTV	4.22	1.43	5.65	0.168	0.152	0.152	0.016	0.016	0.001	0.002	0.003	NaN	0.004	0.011	0.013	0.102	0.403
	29	2	PTV	2.11	1.41	3.52	0.163	0.149	0.150	0.014	0.014	0.001	0.006	0.005	NaN	0.002	0.007	0.023	0.083	0.403
	29	3	PTV	3.81	1.43	5.24	0.164	0.152	0.151	0.013	0.012	0.000	0.003	0.004	NaN	0.001	0.011	0.007	0.099	0.403
	30	1	PTV	1.66	1.43	3.09	0.163	0.151	0.151	0.011	0.011	0.001	0.004	0.004	NaN	0.004	0.004	0.019	0.080	0.403
	30	2	PTV	2.09	1.42	3.51	0.164	0.151	0.151	0.013	0.013	0.001	0.004	0.004	NaN	0.004	0.004	0.024	0.090	0.403
	30	3	PTV	2.58	1.41	3.99	0.164	0.149	0.150	0.015	0.015	0.001	0.006	0.005	NaN	0.005	0.005	0.024	0.092	0.403
	30	4	PTV	3.03	1.43	4.46	0.166	0.152	0.152	0.014	0.014	0.001	0.003	0.003	NaN	0.005	0.006	0.016	0.097	0.403
	30	5	PTV	3.61	1.43	5.04	0.167	0.152	0.151	0.015	0.015	0.001	0.003	0.004	NaN	0.006	0.006	0.015	0.100	0.403
	30	6	PTV	4.19	1.43	5.62	0.168	0.152	0.152	0.016	0.015	0.001	0.003	0.003	NaN	0.008	0.006	0.013	0.103	0.403

B. 1. 2. Dimensionless log profiles grouped by flume slopes

In this section, the dimensionless log profiles are grouped by flume slopes, allowing for a better understanding of the flow behaviour in channels with different slopes. Dimensionless log profiles grouped by flume slopes offer a useful tool for analyzing the behaviour of fluid flow in channels with different slopes. This approach is based on the concept of dimensionless analysis, which reduces the number of variables affecting the flow behaviour, making it easier to identify patterns and trends. The analysis of the dimensionless log profiles has been previously conducted in Chapter 4 and Chapter 5 using all the profiles together.

By grouping the profiles by flume slope and organizing them by discharge, any patterns and trends not previously observed in the figures provided in the main thesis can be identified (or discarded). In this section each figure shows all the profiles adjusted for the same flume slope. And they are organized by discharge (i.e. water depth or relative submergence).

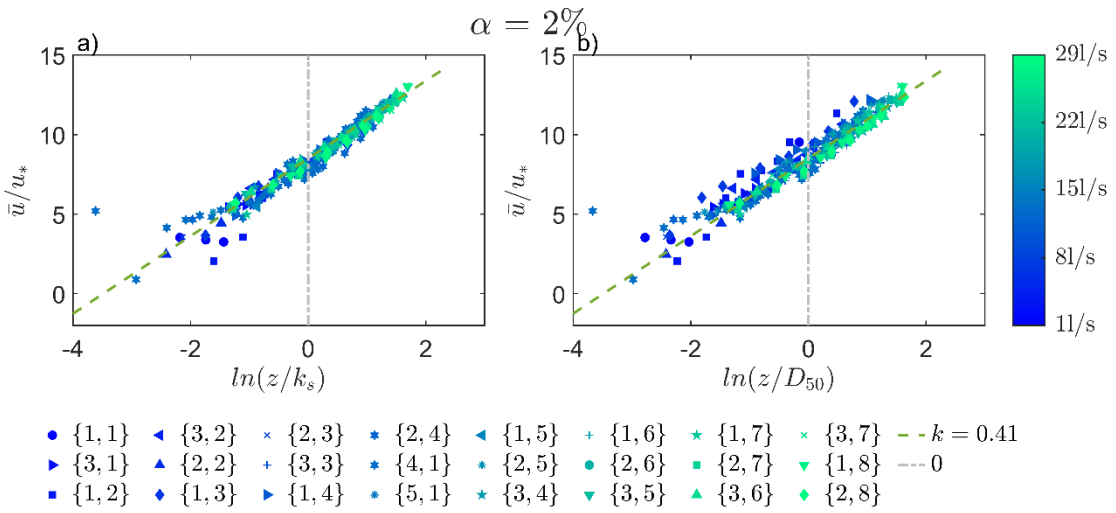

Figure B. 1. Dimensionless log profiles in the horizontal semi-log scale for the 2% flume slope.

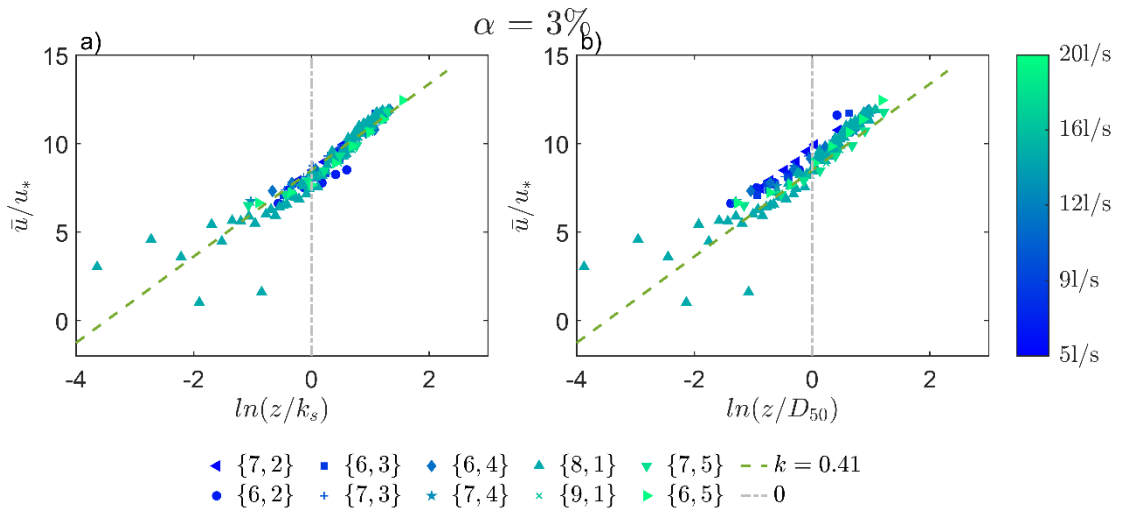

Figure B. 2. Dimensionless log profiles in the horizontal semi-log scale for the 3% flume slope.

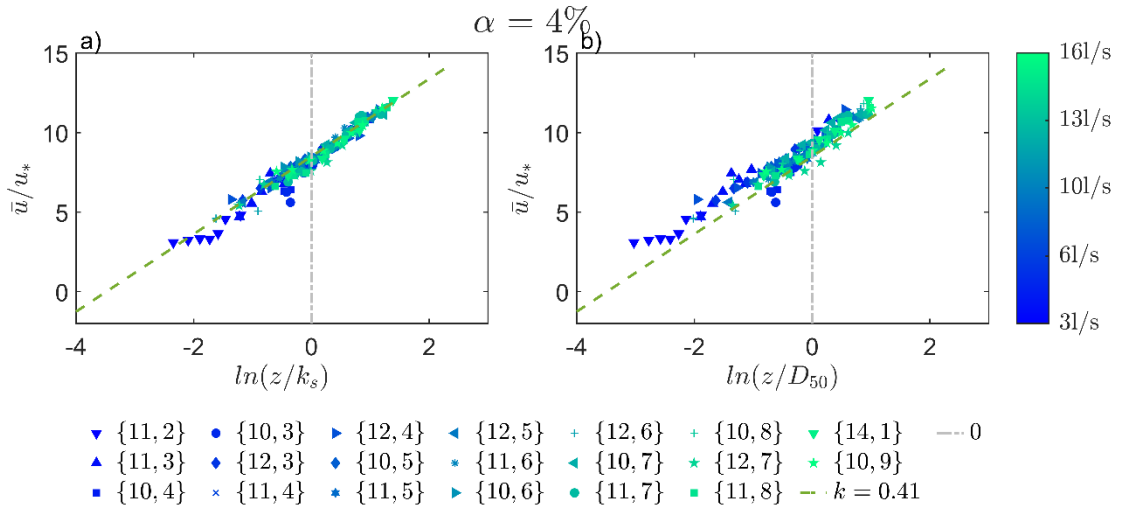

Figure B. 3. Dimensionless log profiles in the horizontal semi-log scale for the 4% flume slope.

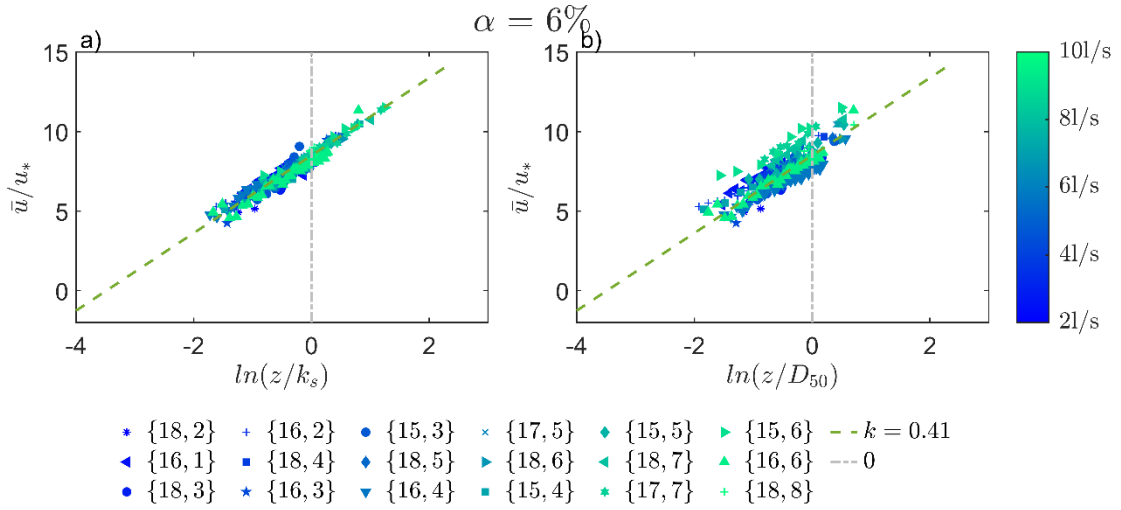

Figure B. 4. Dimensionless log profiles in the horizontal semi-log scale for the 6% flume slope.

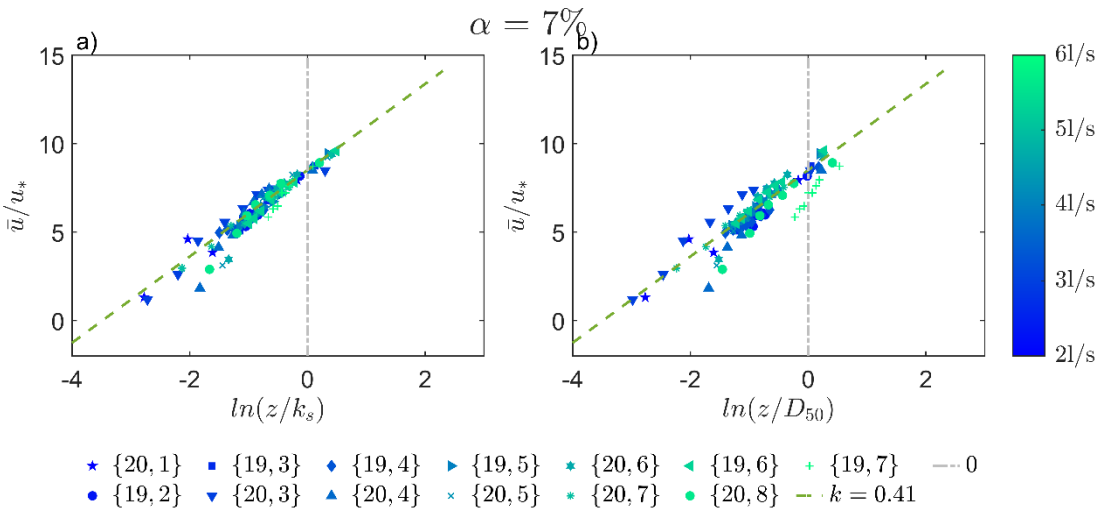

Figure B. 5. Dimensionless log profiles in the horizontal semi-log scale for the 7% flume slope.

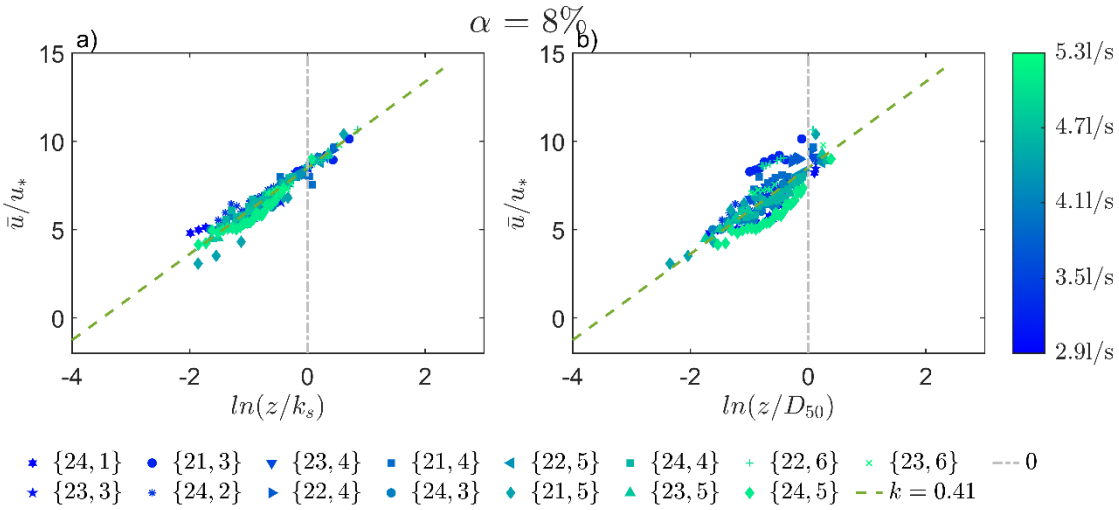

Figure B. 6. Dimensionless log profiles in the horizontal semi-log scale for the 8% flume slope.

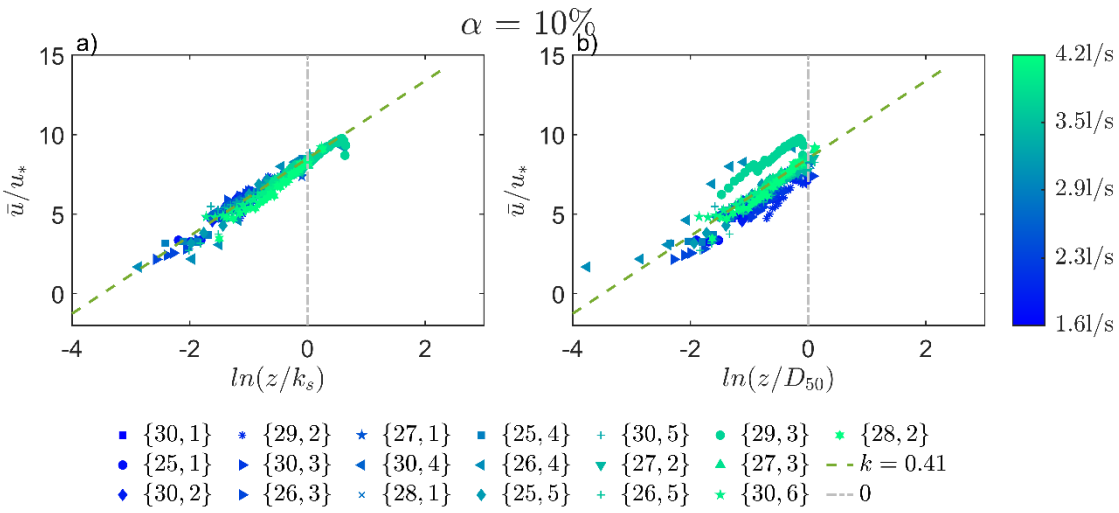

Figure B. 7. Dimensionless log profiles in the horizontal semi-log scale for the 10% flume slope.

B. 1. 3. Individual results per each profile analysis

By examining each profile individually, it is possible to identify patterns and trends that may not be visible when analyzing multiple profiles at the same time. This approach allows for a more in-depth analysis of each profile and provides valuable insights into the characteristics of fluid flow in the channel. This detailed analysis of each profile provides a comprehensive understanding of the behaviour of fluid flow in the channel and is an important resource for anyone interested in the methodology and data analysis used in the research study.

Each figure in this section consists of three parts. The first part displays the velocity profile as a function of levels and highlights the differences between the shifting distances and water surfaces. The second part shows the velocity profile as a function of water depths. Finally, the third part follows the dimensionless analysis conducted in the previous section, comparing the current profile with all the others. By presenting the data in this way, it is possible to gain a more comprehensive understanding of the flow behaviour for each individual profile. The figures provide detailed information on the velocity and its variations, allowing for a thorough analysis of the results.

The figures are ordered from milder slopes to stepper slopes (2 —10%), following experiments numbers (1 —30).

B.1.3.a. 2% flume slope

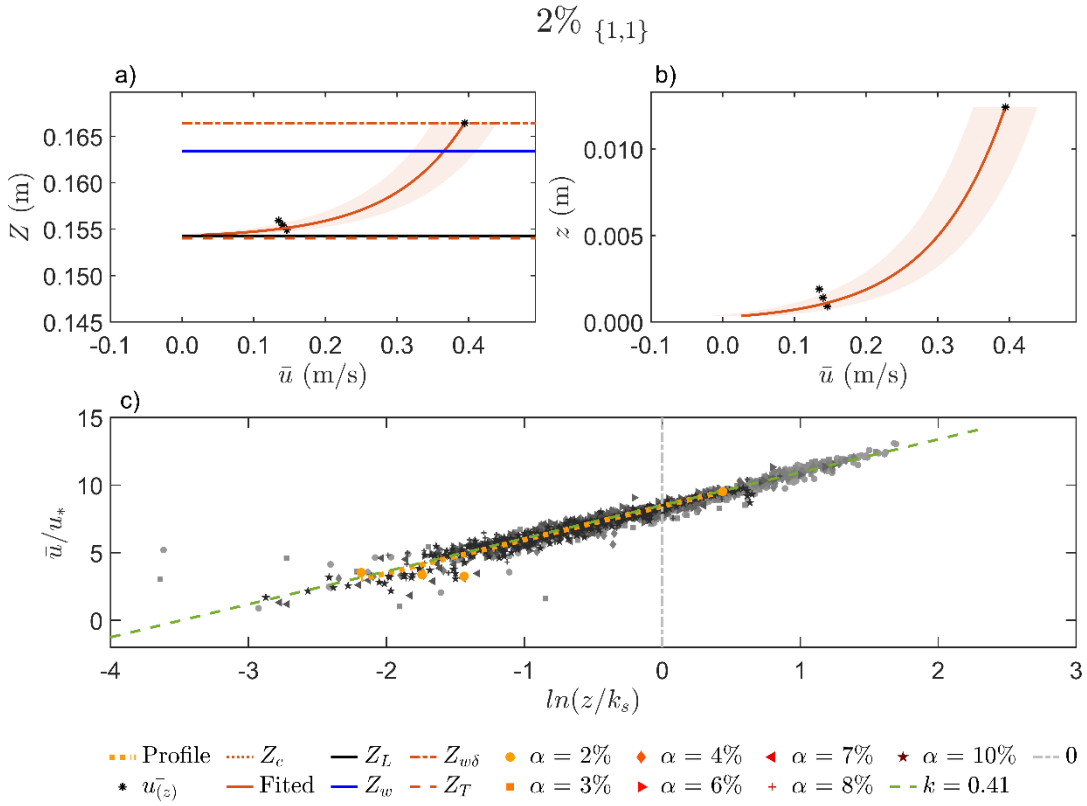

Figure B. 8. (a) Velocity profile as a function of water levels, (b) velocity profile as a function of water depths, and (c) dimensionless log profiles in the horizontal semi-log scale on a 2% flume slope.

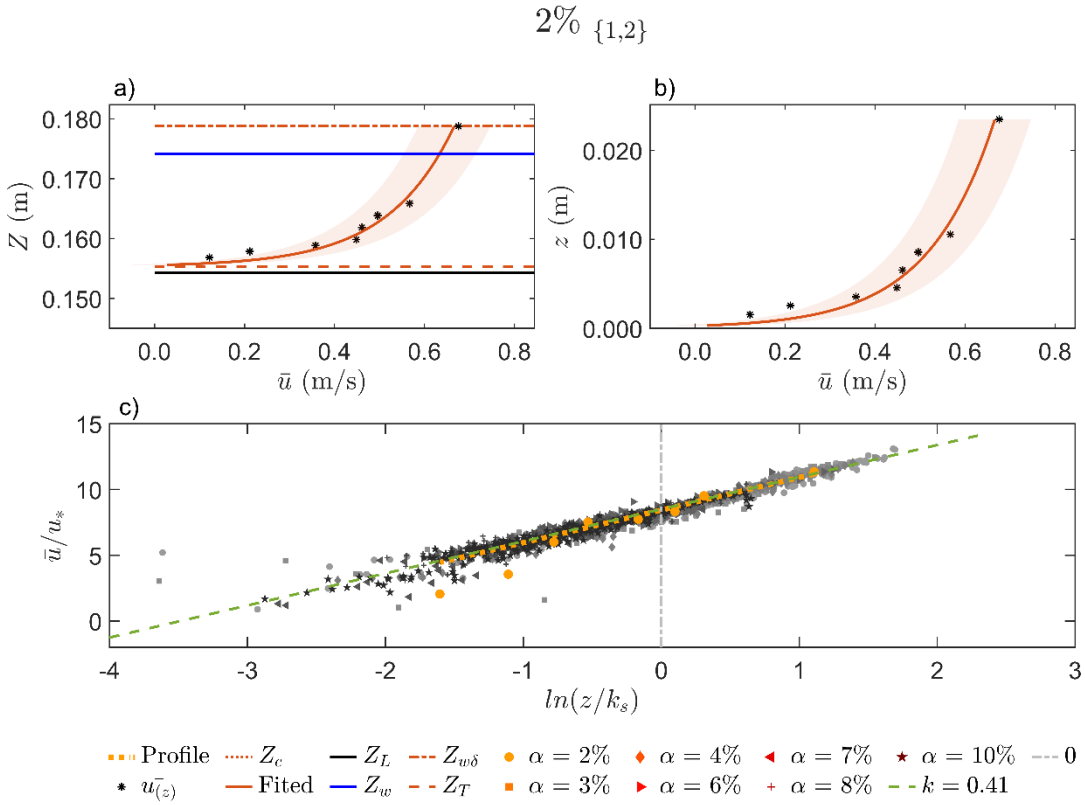

Figure B. 9. (a) Velocity profile as a function of water levels, (b) velocity profile as a function of water depths, and (c) dimensionless log profiles in the horizontal semi-log scale on a 2% flume slope.

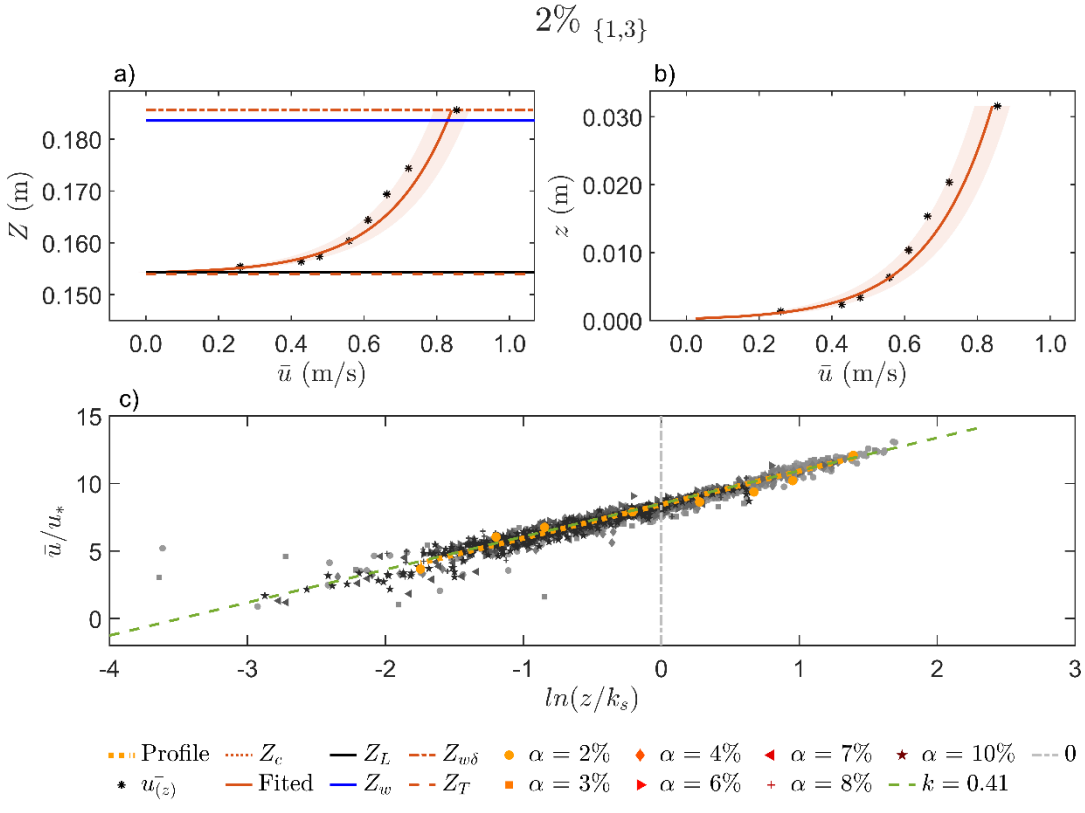

Figure B. 10. (a) Velocity profile as a function of water levels, (b) velocity profile as a function of water depths, and (c) dimensionless log profiles in the horizontal semi-log scale on a 2% flume slope.

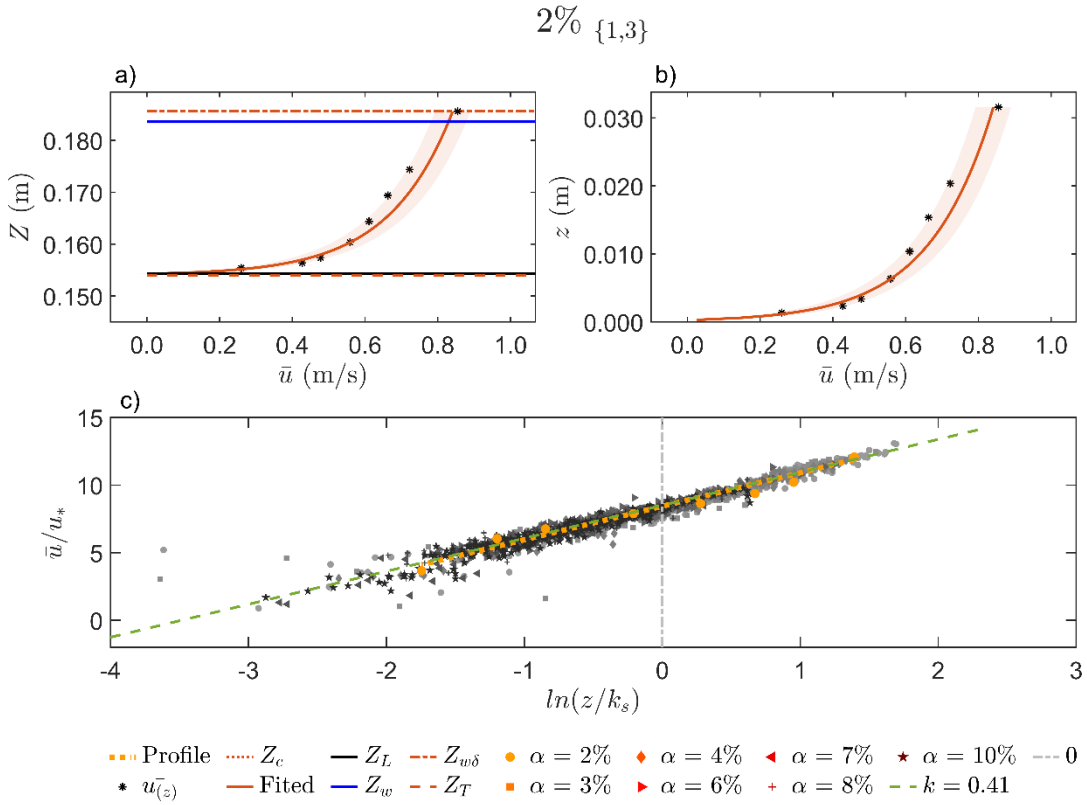

Figure B. 11. (a) Velocity profile as a function of water levels, (b) velocity profile as a function of water depths, and (c) dimensionless log profiles in the horizontal semi-log scale on a 2% flume slope.

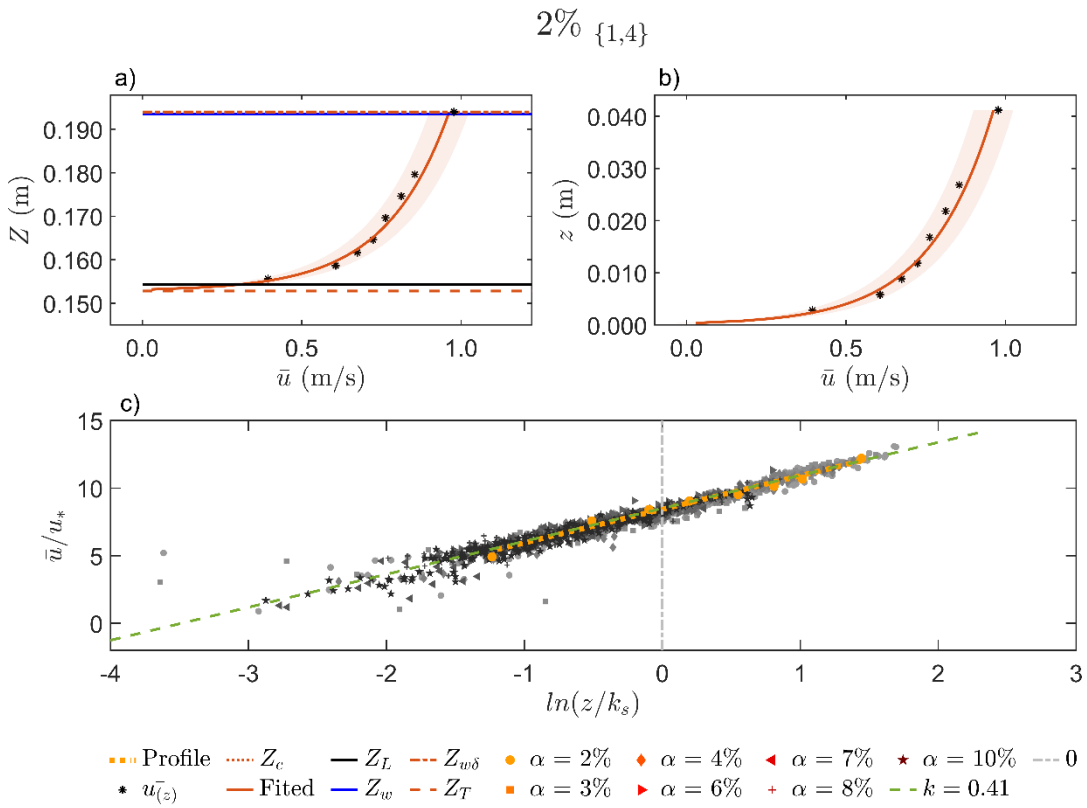

Figure B. 12. (a) Velocity profile as a function of water levels, (b) velocity profile as a function of water depths, and (c) dimensionless log profiles in the horizontal semi-log scale on a 2% flume slope.

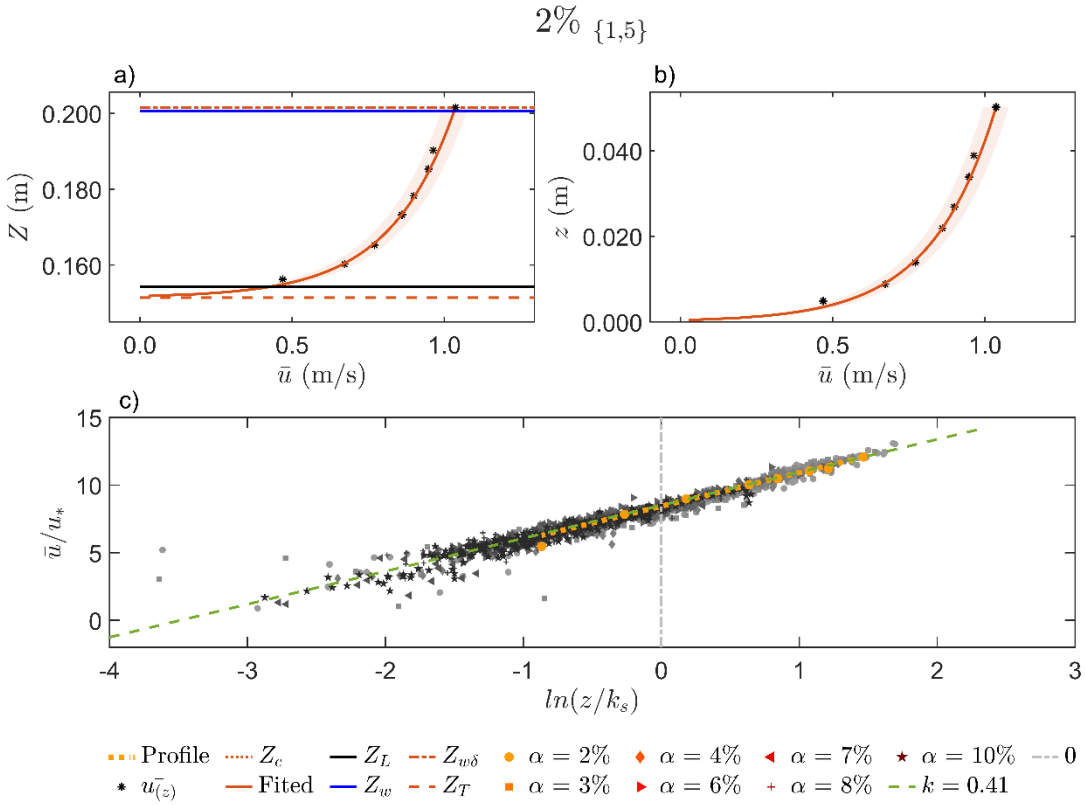

Figure B. 13. (a) Velocity profile as a function of water levels, (b) velocity profile as a function of water depths, and (c) dimensionless log profiles in the horizontal semi-log scale on a 2% flume slope.

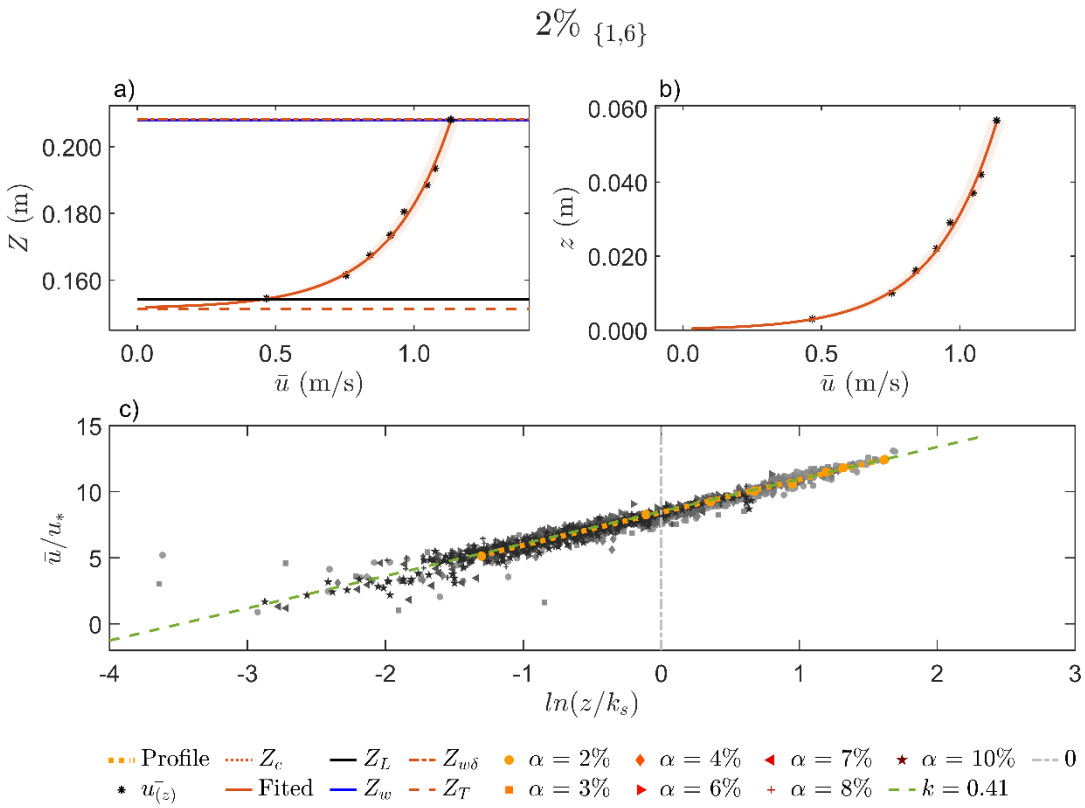

Figure B. 14. (a) Velocity profile as a function of water levels, (b) velocity profile as a function of water depths, and (c) dimensionless log profiles in the horizontal semi-log scale on a 2% flume slope.

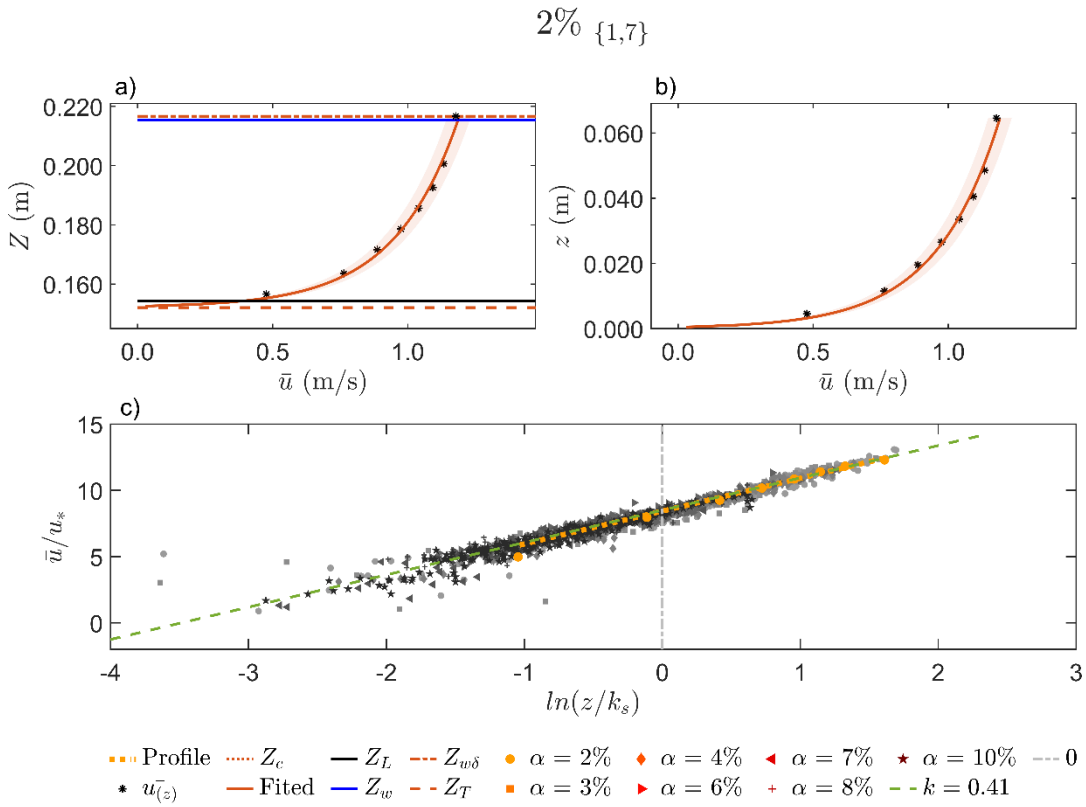

Figure B. 15. (a) Velocity profile as a function of water levels, (b) velocity profile as a function of water depths, and (c) dimensionless log profiles in the horizontal semi-log scale on a 2% flume slope.

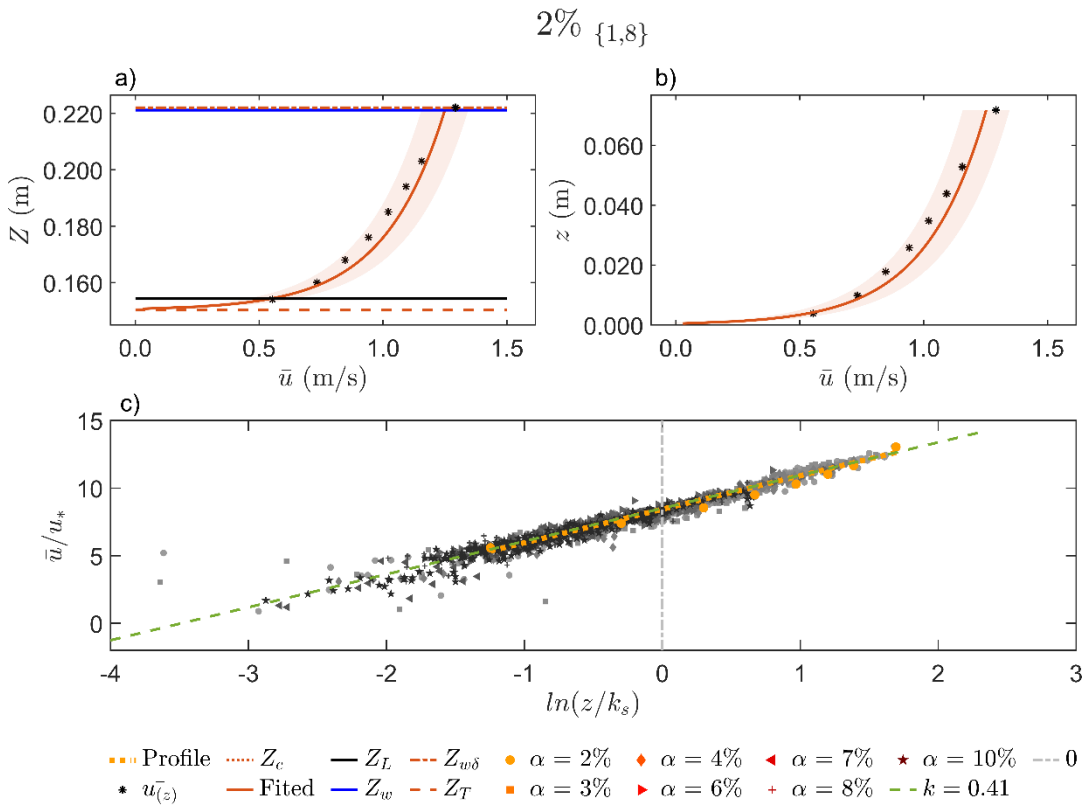

Figure B. 16. (a) Velocity profile as a function of water levels, (b) velocity profile as a function of water depths, and (c) dimensionless log profiles in the horizontal semi-log scale on a 2% flume slope.

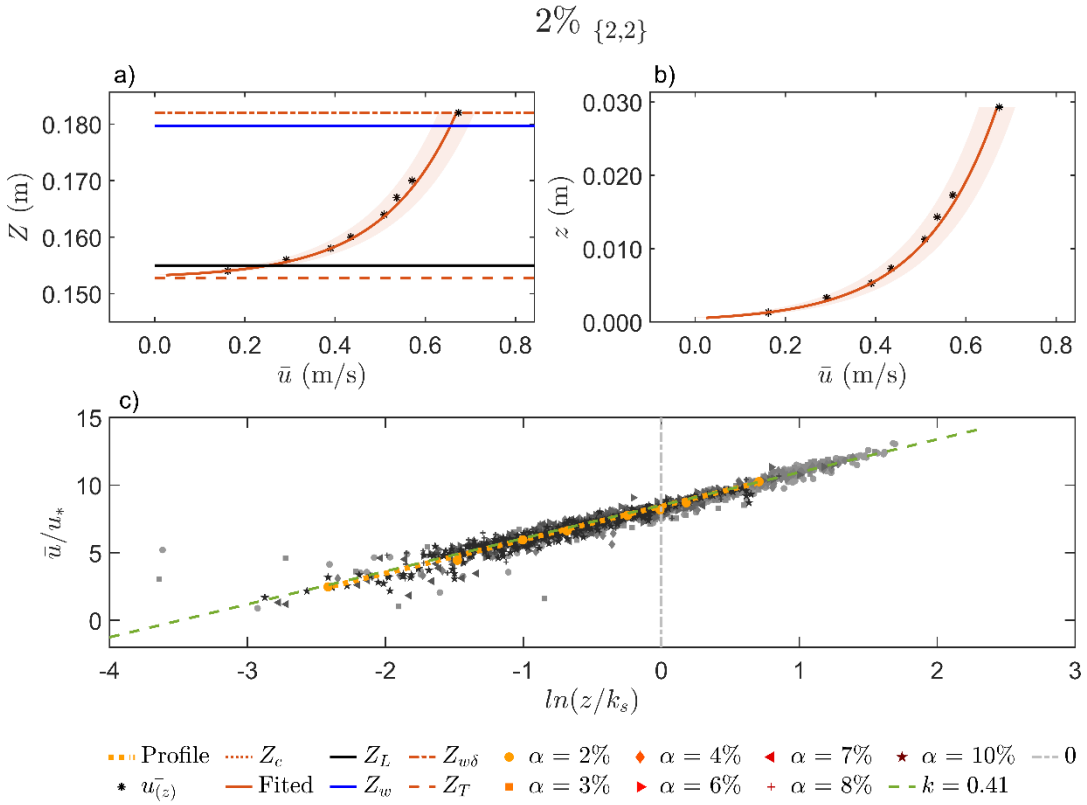

Figure B. 17. (a) Velocity profile as a function of water levels, (b) velocity profile as a function of water depths, and (c) dimensionless log profiles in the horizontal semi-log scale on a 2% flume slope.

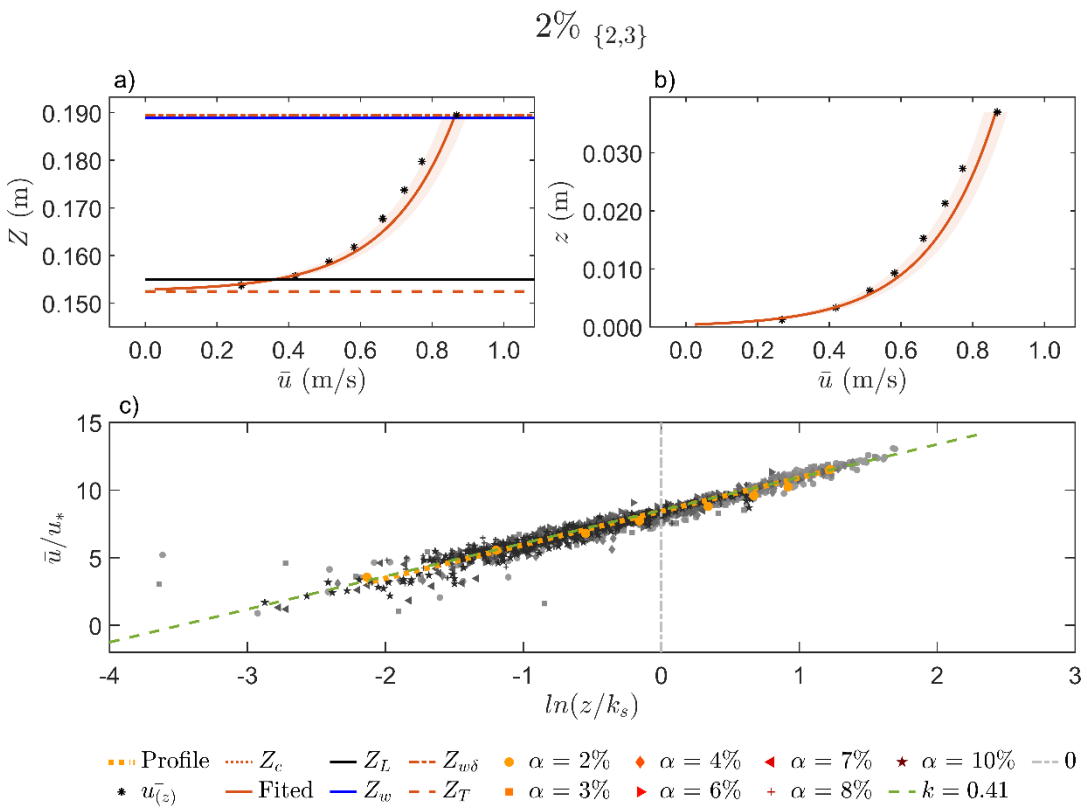

Figure B. 18. (a) Velocity profile as a function of water levels, (b) velocity profile as a function of water depths, and (c) dimensionless log profiles in the horizontal semi-log scale on a 2% flume slope.

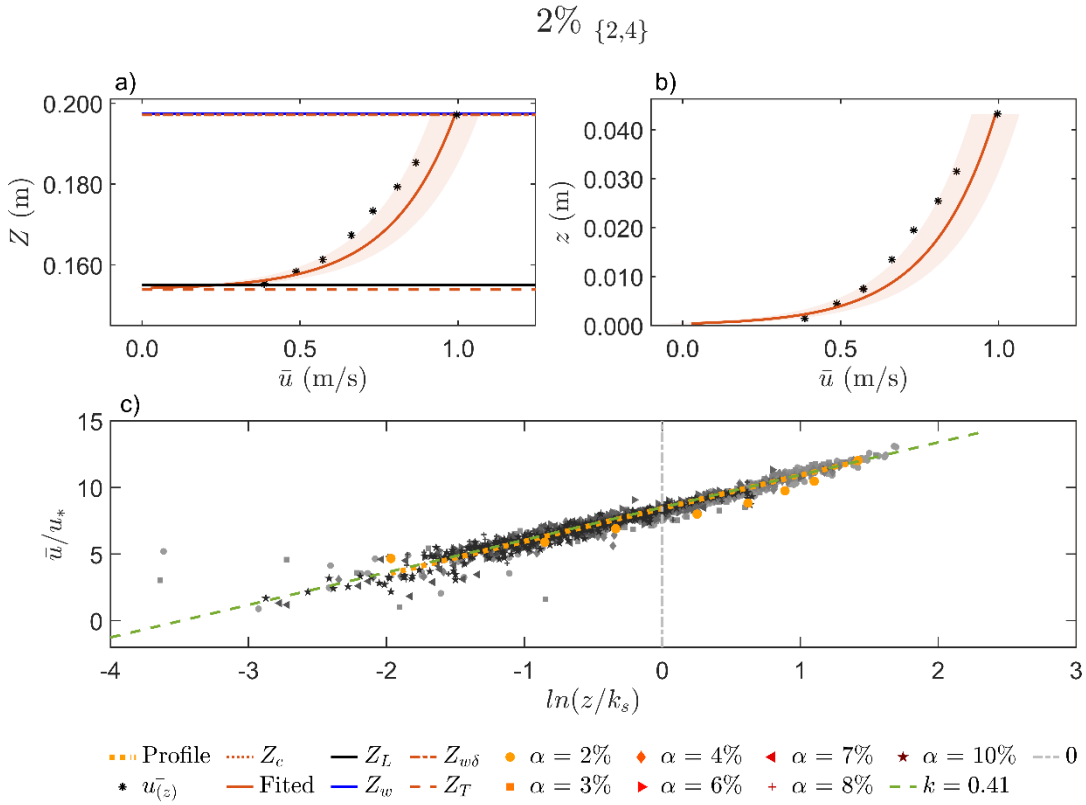

Figure B. 19. (a) Velocity profile as a function of water levels, (b) velocity profile as a function of water depths, and (c) dimensionless log profiles in the horizontal semi-log scale on a 2% flume slope.

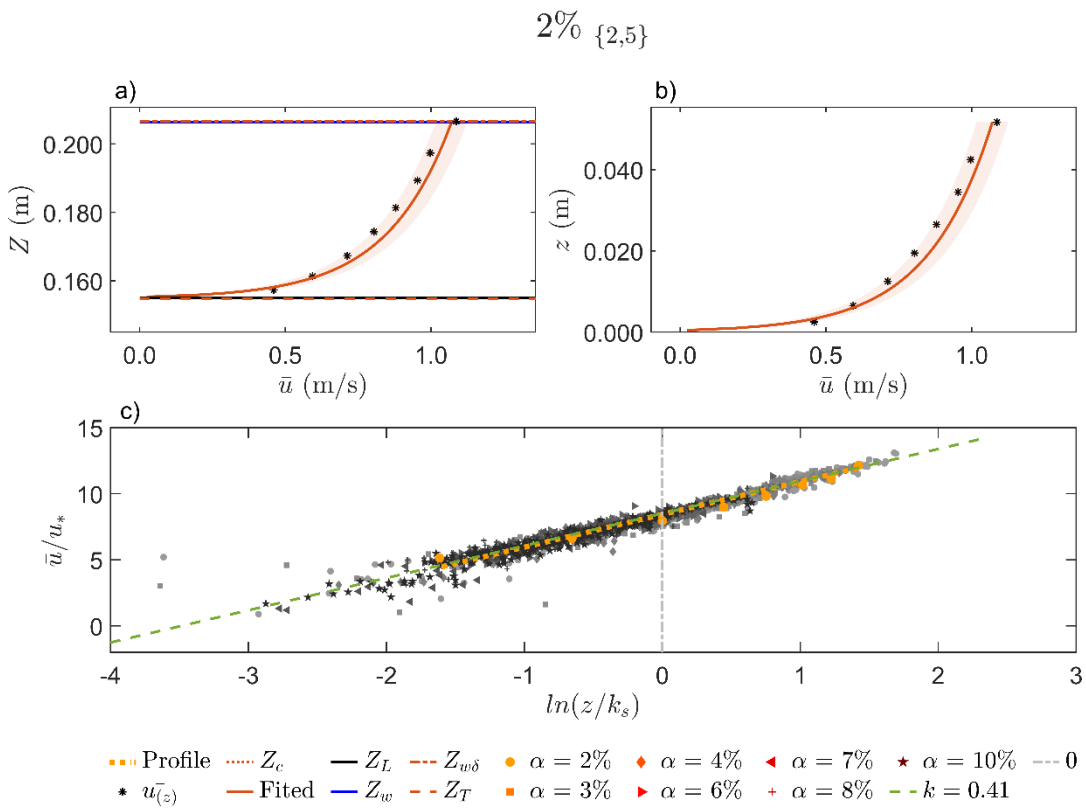

Figure B. 20. (a) Velocity profile as a function of water levels, (b) velocity profile as a function of water depths, and (c) dimensionless log profiles in the horizontal semi-log scale on a 2% flume slope.

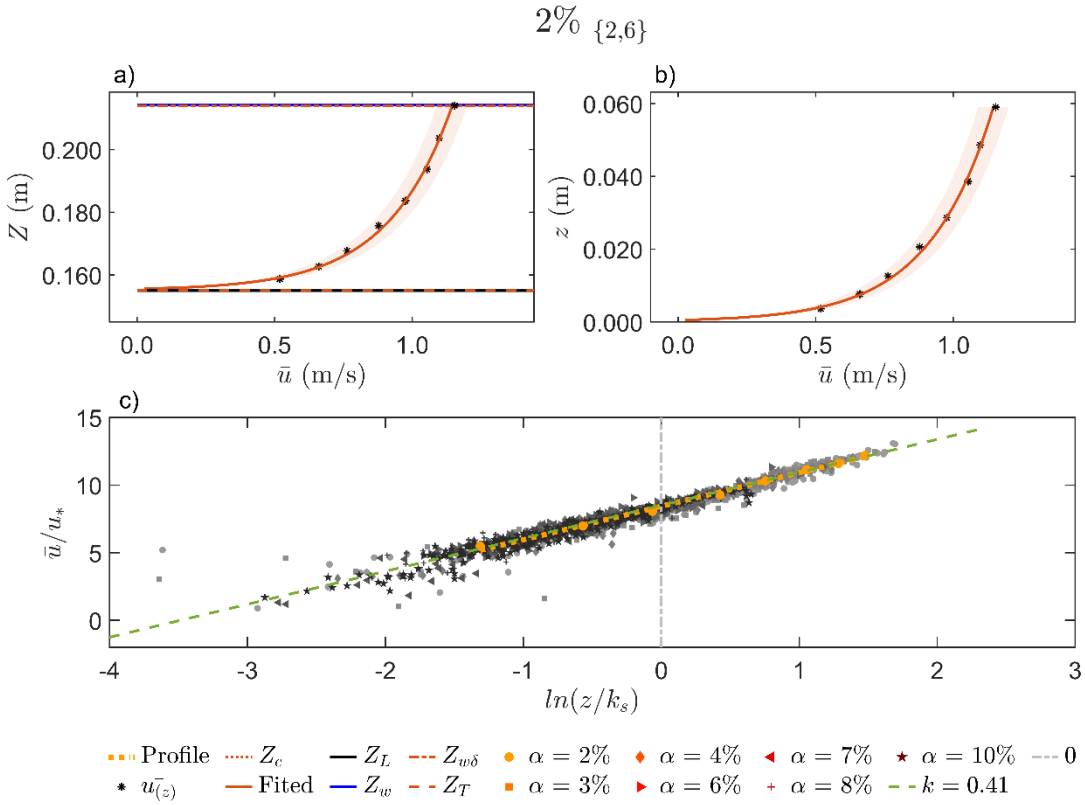

Figure B. 21. (a) Velocity profile as a function of water levels, (b) velocity profile as a function of water depths, and (c) dimensionless log profiles in the horizontal semi-log scale on a 2% flume slope.

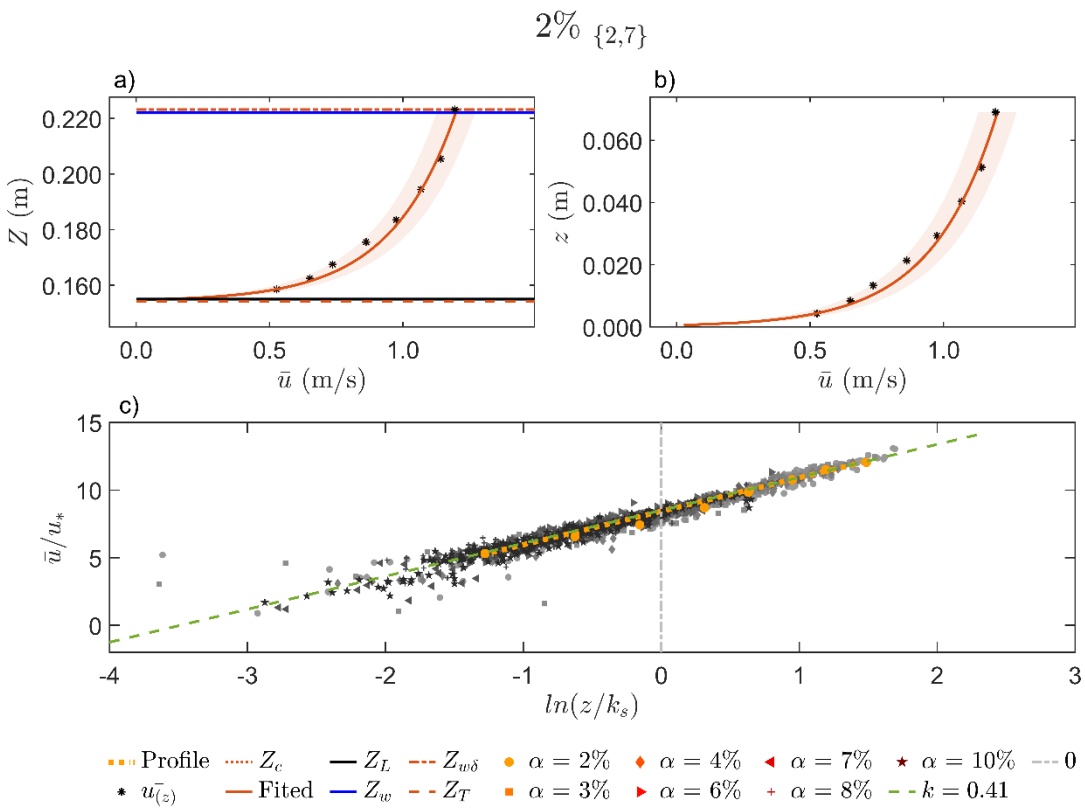

Figure B. 22. (a) Velocity profile as a function of water levels, (b) velocity profile as a function of water depths, and (c) dimensionless log profiles in the horizontal semi-log scale on a 2% flume slope.

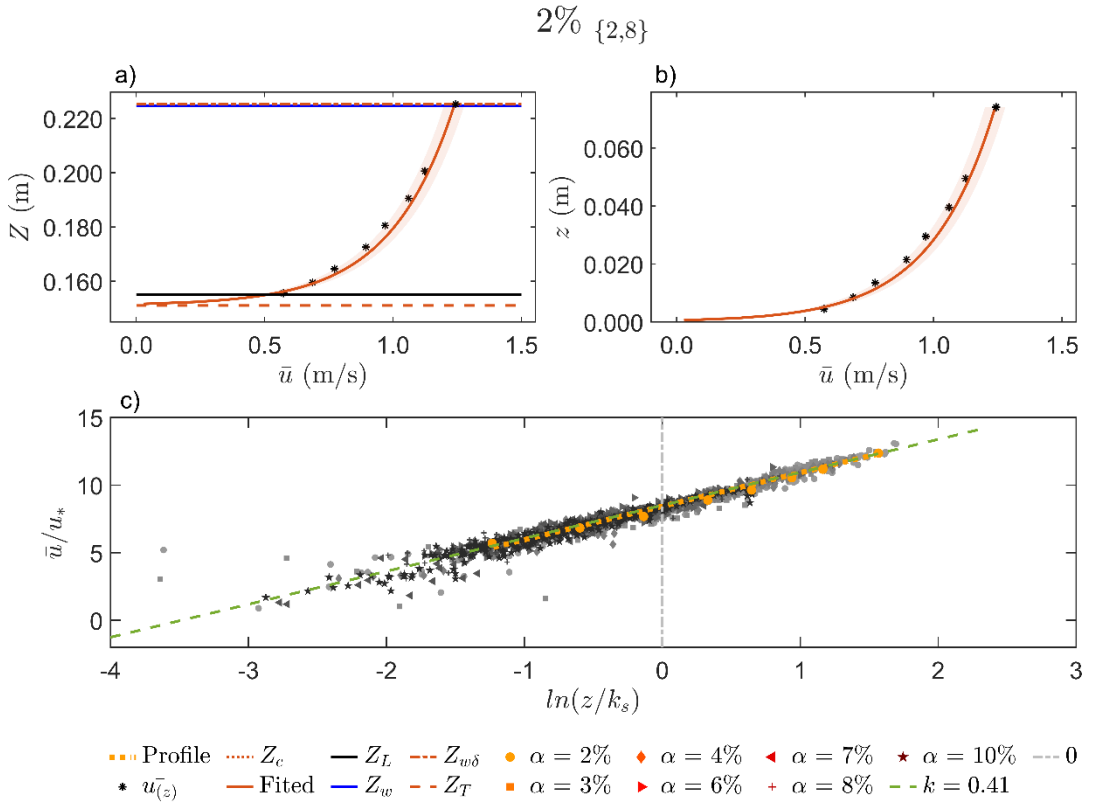

Figure B. 23. (a) Velocity profile as a function of water levels, (b) velocity profile as a function of water depths, and (c) dimensionless log profiles in the horizontal semi-log scale on a 2% flume slope.

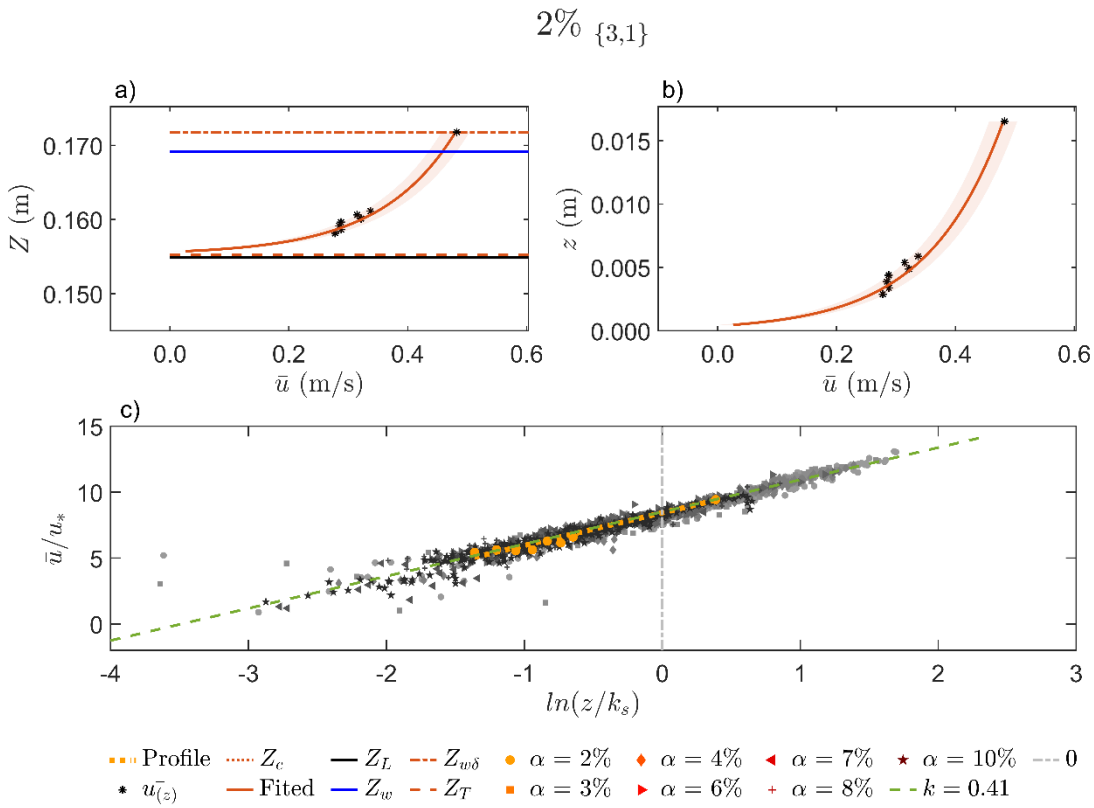

Figure B. 24. (a) Velocity profile as a function of water levels, (b) velocity profile as a function of water depths, and (c) dimensionless log profiles in the horizontal semi-log scale on a 2% flume slope.

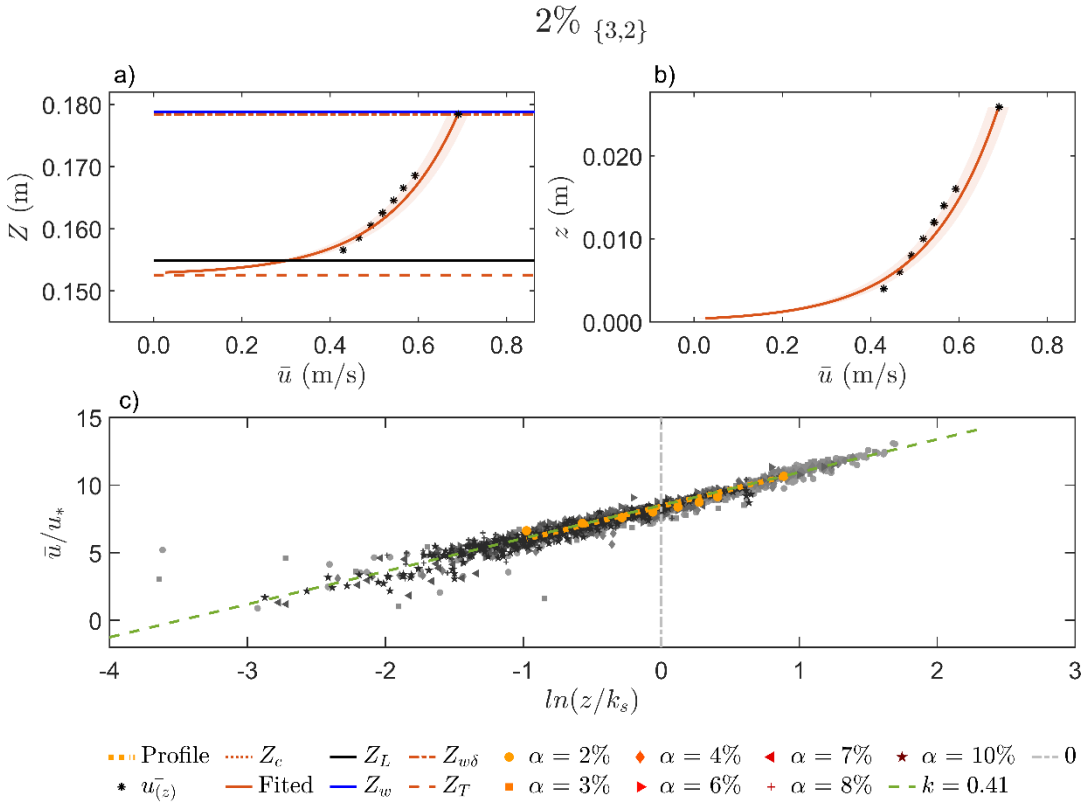

Figure B. 25. (a) Velocity profile as a function of water levels, (b) velocity profile as a function of water depths, and (c) dimensionless log profiles in the horizontal semi-log scale on a 2% flume slope.

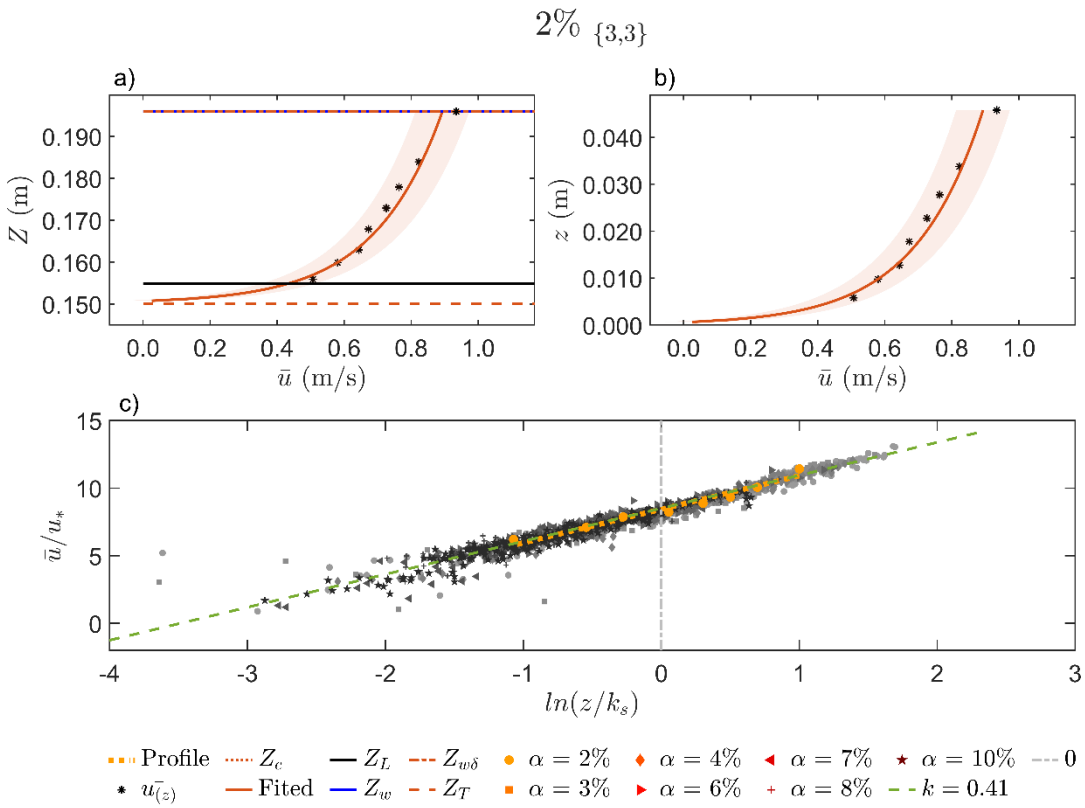

Figure B. 26. (a) Velocity profile as a function of water levels, (b) velocity profile as a function of water depths, and (c) dimensionless log profiles in the horizontal semi-log scale on a 2% flume slope.

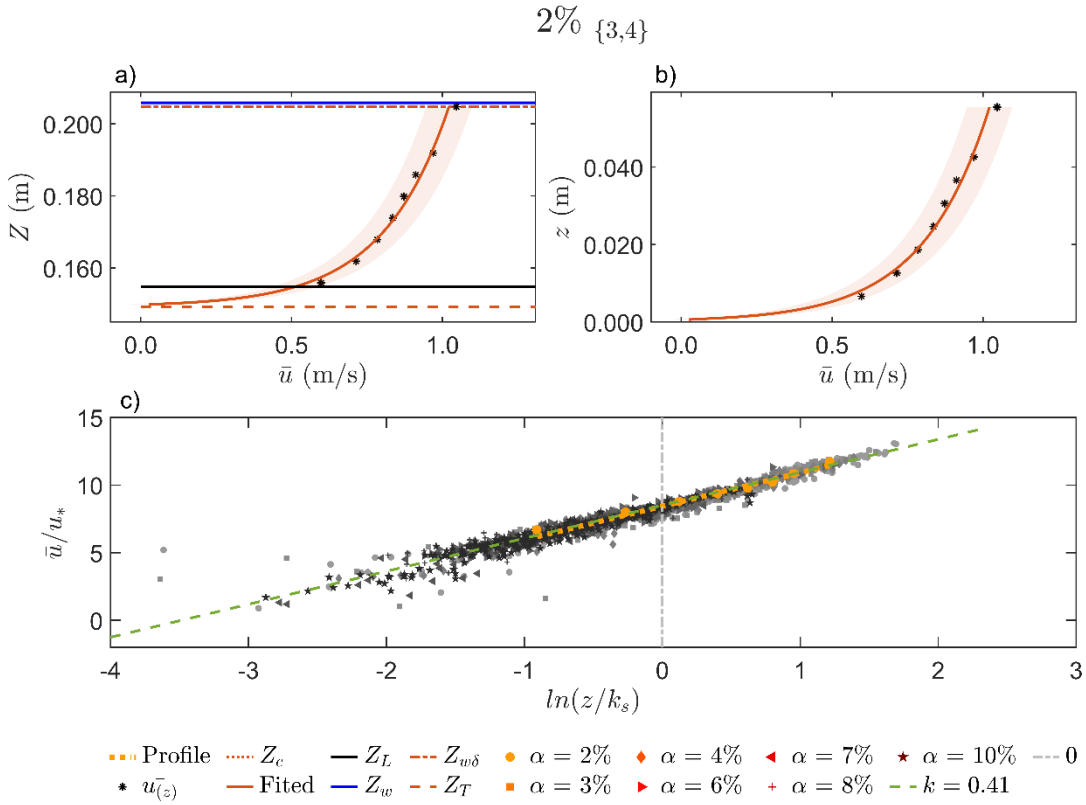

Figure B. 27. (a) Velocity profile as a function of water levels, (b) velocity profile as a function of water depths, and (c) dimensionless log profiles in the horizontal semi-log scale on a 2% flume slope.

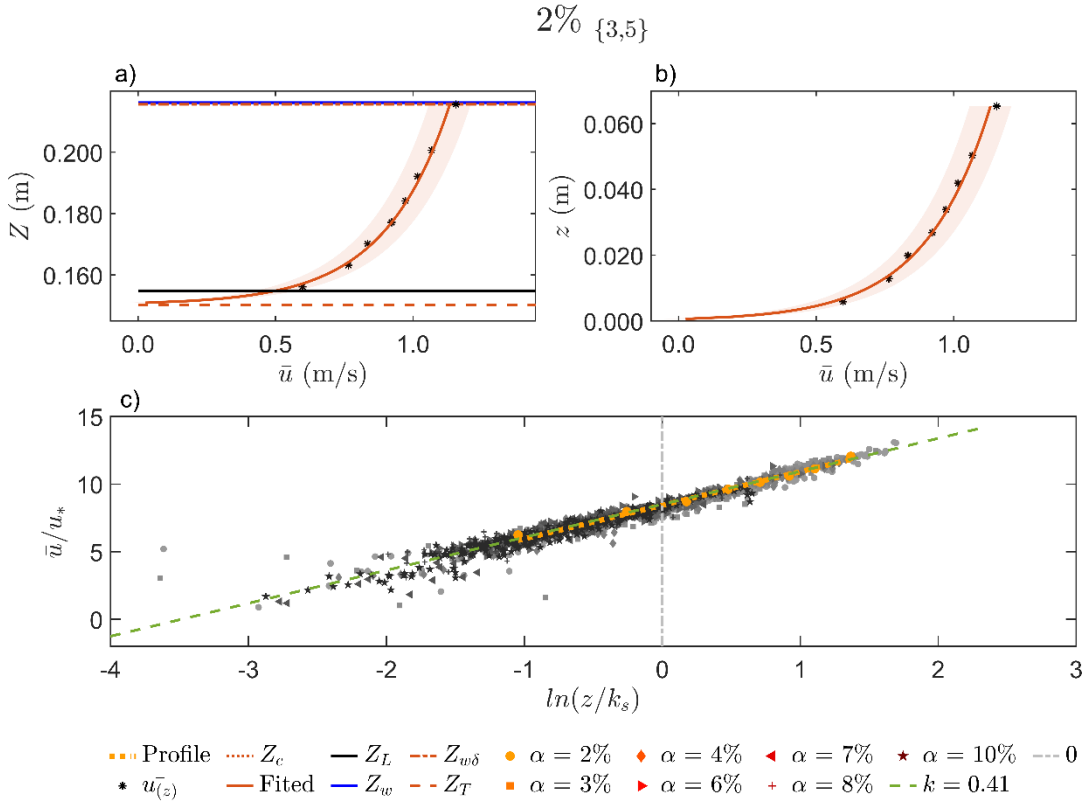

Figure B. 28. (a) Velocity profile as a function of water levels, (b) velocity profile as a function of water depths, and (c) dimensionless log profiles in the horizontal semi-log scale on a 2% flume slope.

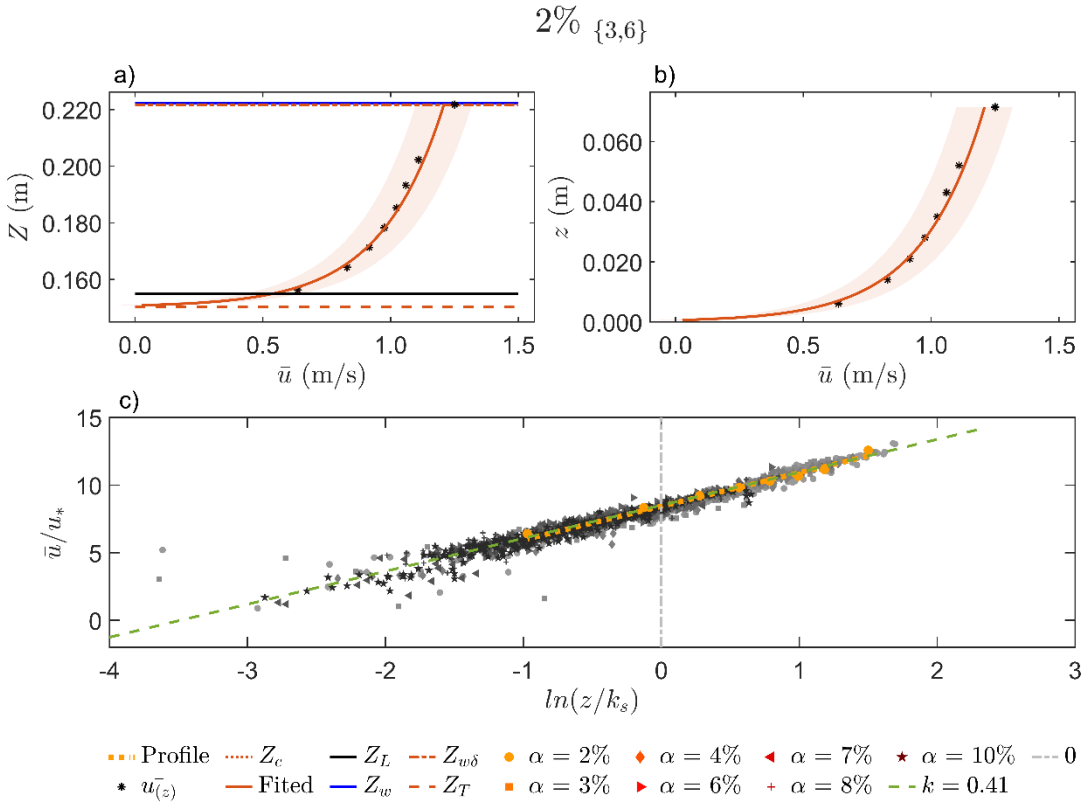

Figure B. 29. (a) Velocity profile as a function of water levels, (b) velocity profile as a function of water depths, and (c) dimensionless log profiles in the horizontal semi-log scale on a 2% flume slope.

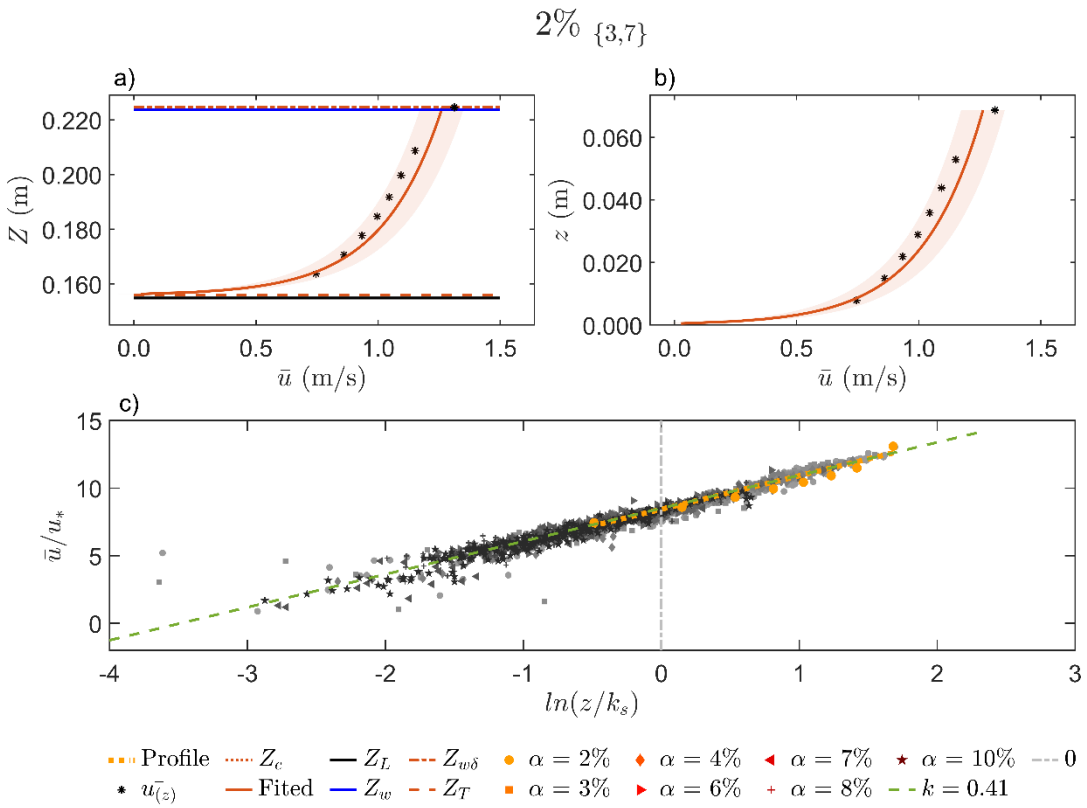

Figure B. 30. (a) Velocity profile as a function of water levels, (b) velocity profile as a function of water depths, and (c) dimensionless log profiles in the horizontal semi-log scale on a 2% flume slope.

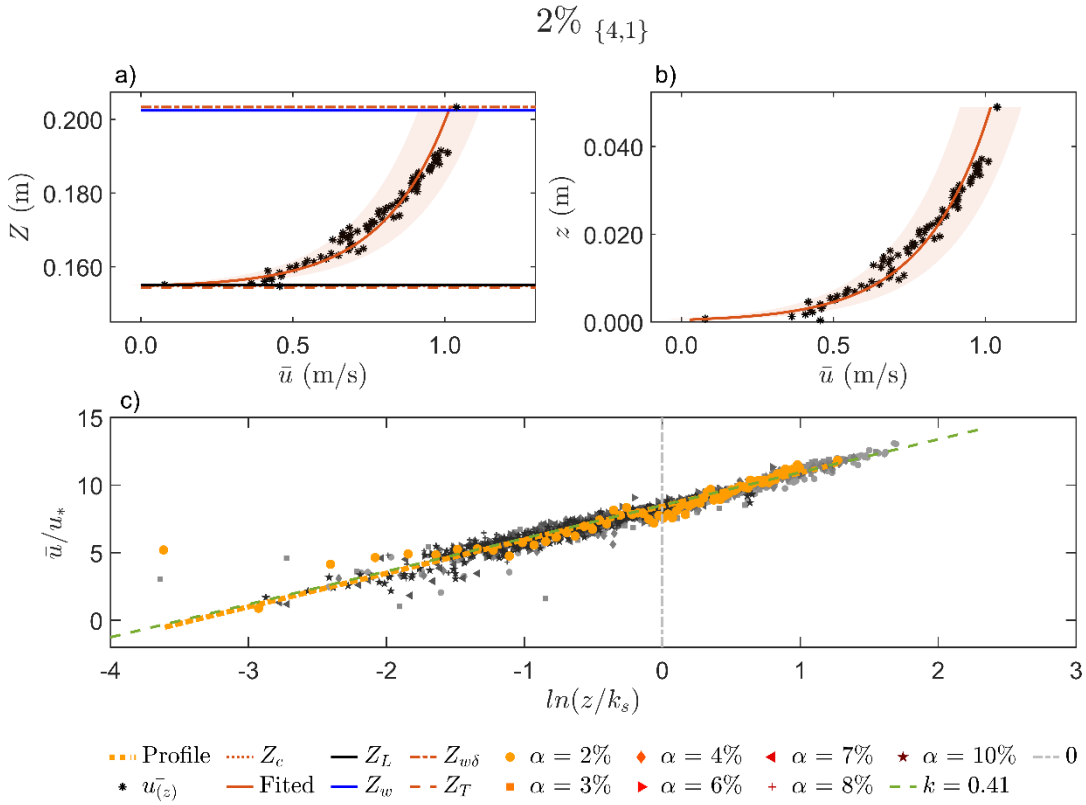

Figure B. 31. (a) Velocity profile as a function of water levels, (b) velocity profile as a function of water depths, and (c) dimensionless log profiles in the horizontal semi-log scale on a 2% flume slope.

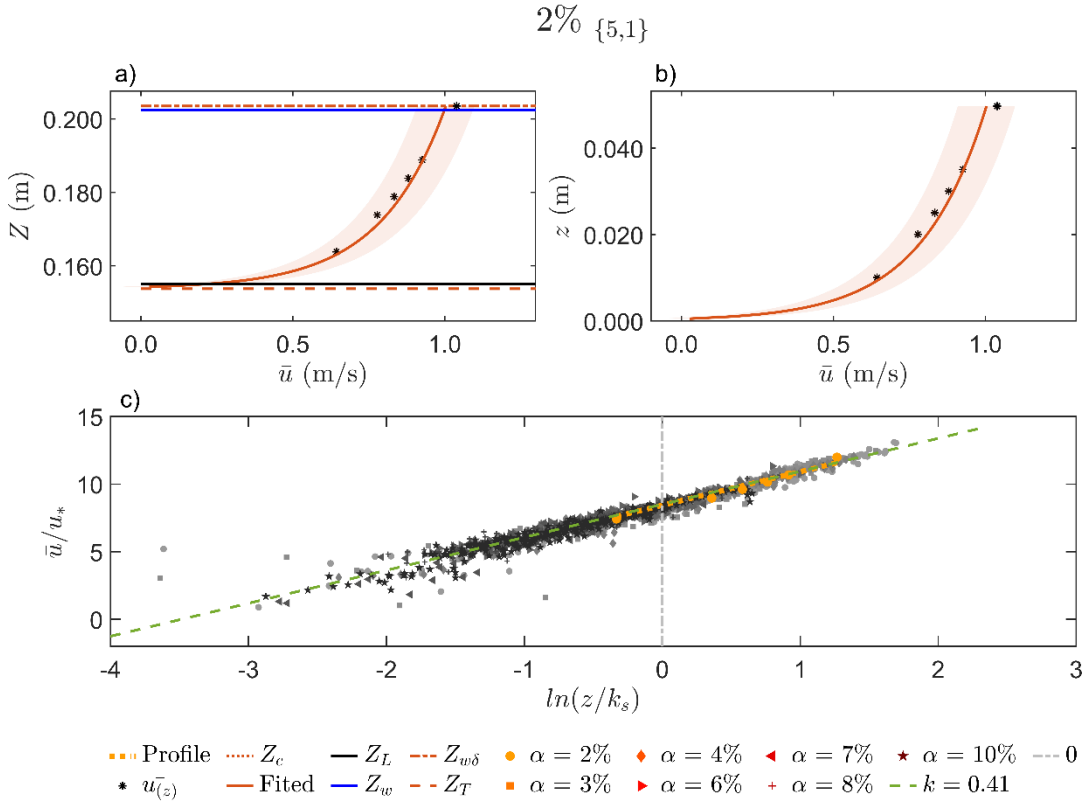

Figure B. 32. (a) Velocity profile as a function of water levels, (b) velocity profile as a function of water depths, and (c) dimensionless log profiles in the horizontal semi-log scale on a 2% flume slope.

B.1.3.b. 3% flume slope

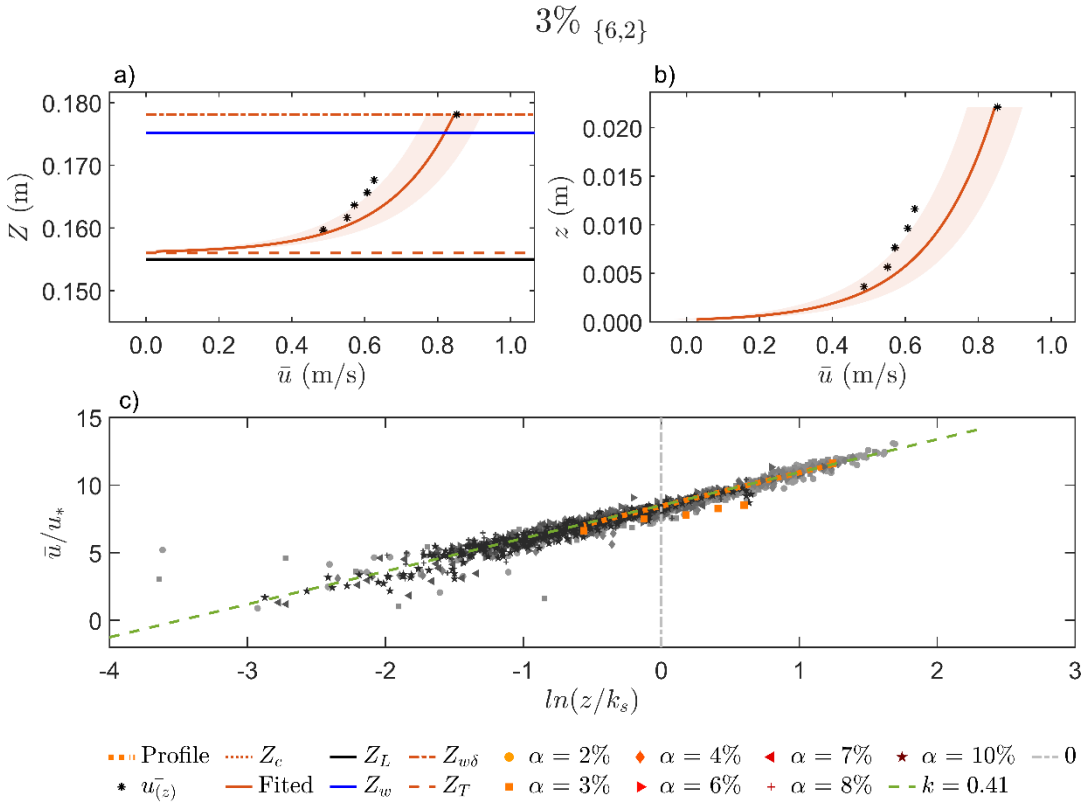

Figure B. 33. (a) Velocity profile as a function of water levels, (b) velocity profile as a function of water depths, and (c) dimensionless log profiles in the horizontal semi-log scale on a 3% flume slope.

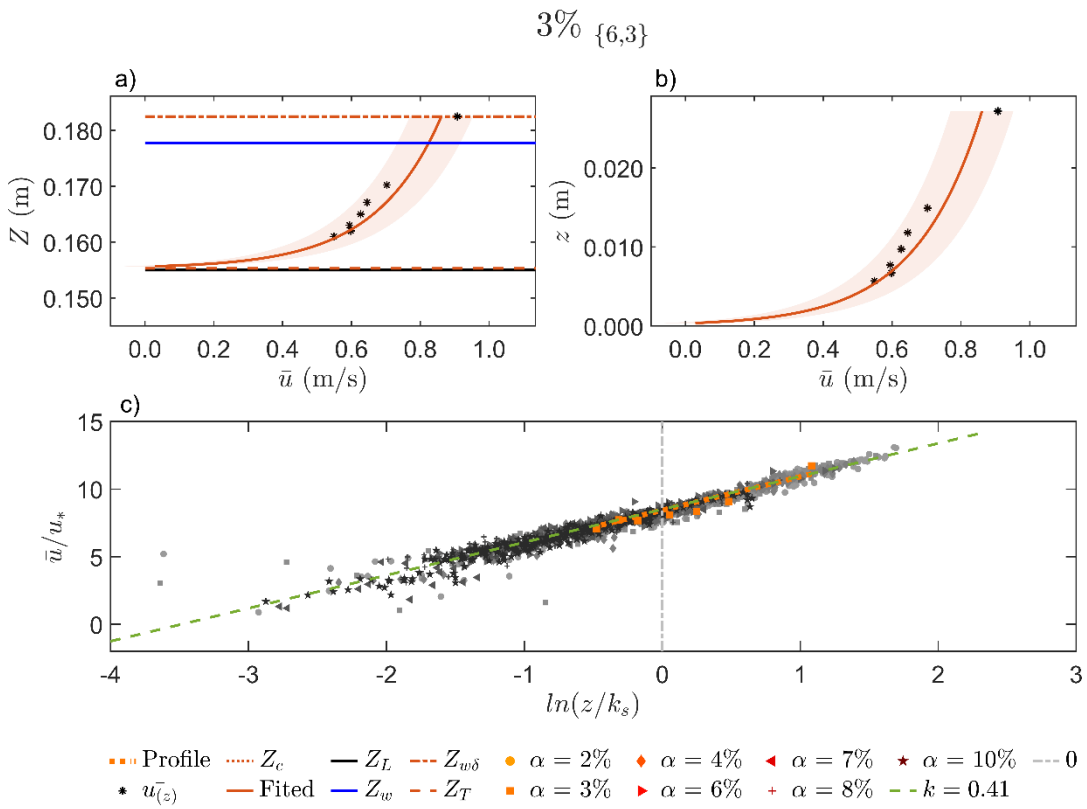

Figure B. 34. (a) Velocity profile as a function of water levels, (b) velocity profile as a function of water depths, and (c) dimensionless log profiles in the horizontal semi-log scale on a 3% flume slope.

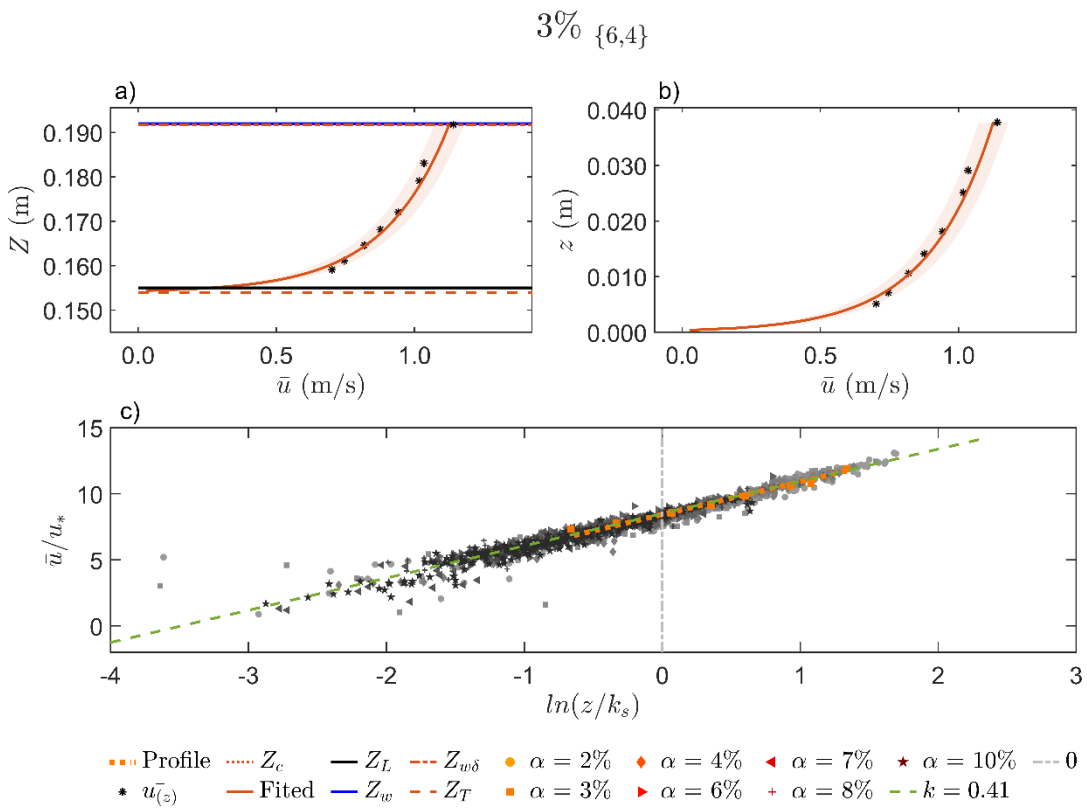

Figure B. 35. (a) Velocity profile as a function of water levels, (b) velocity profile as a function of water depths, and (c) dimensionless log profiles in the horizontal semi-log scale on a 3% flume slope.

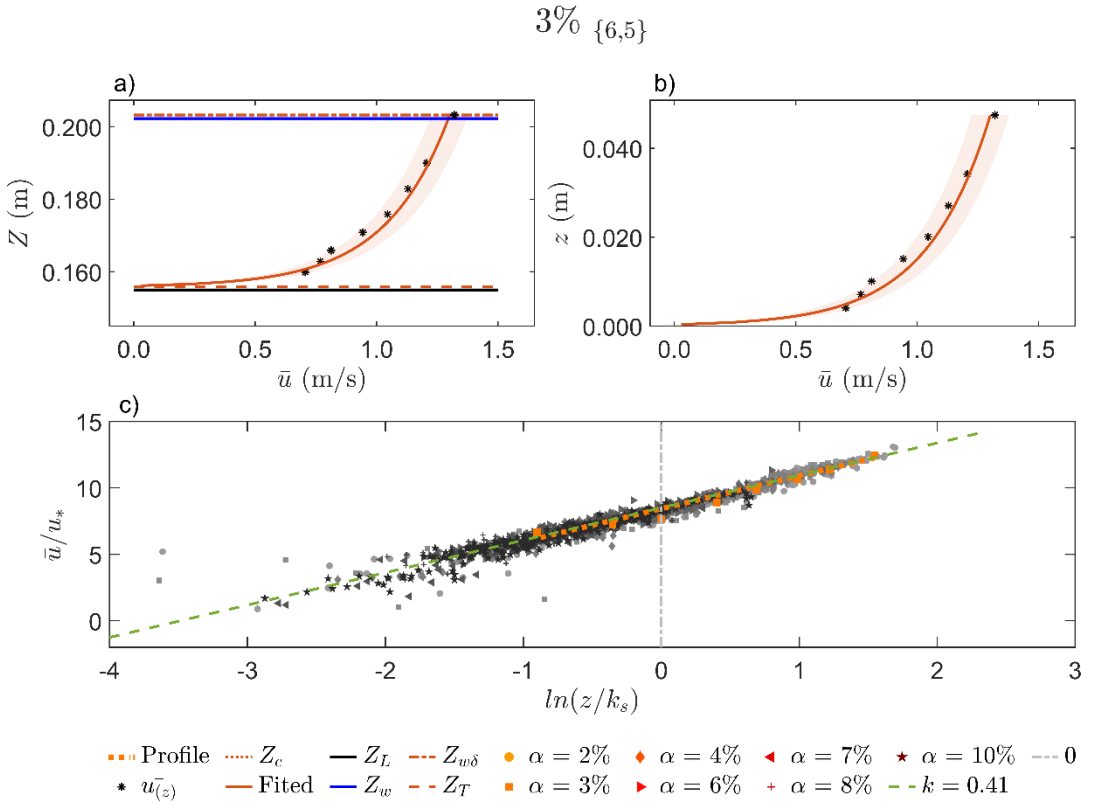

Figure B. 36. (a) Velocity profile as a function of water levels, (b) velocity profile as a function of water depths, and (c) dimensionless log profiles in the horizontal semi-log scale on a 3% flume slope.

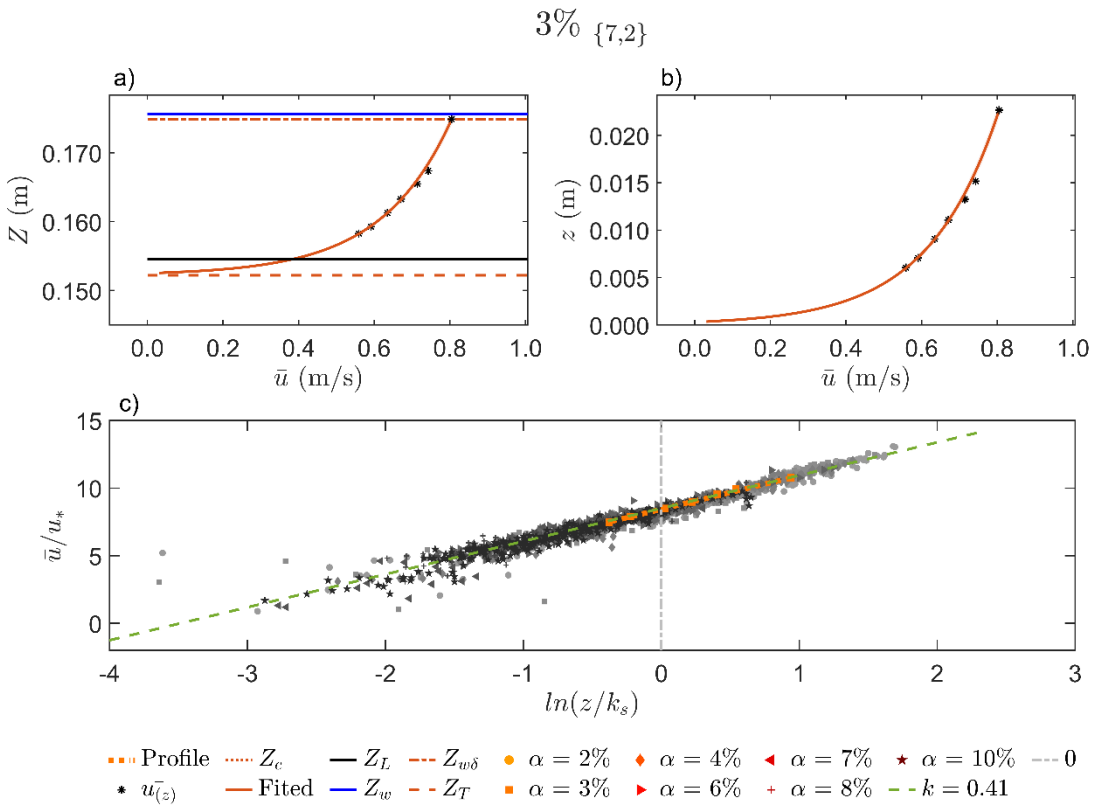

Figure B. 37. (a) Velocity profile as a function of water levels, (b) velocity profile as a function of water depths, and (c) dimensionless log profiles in the horizontal semi-log scale on a 3% flume slope.

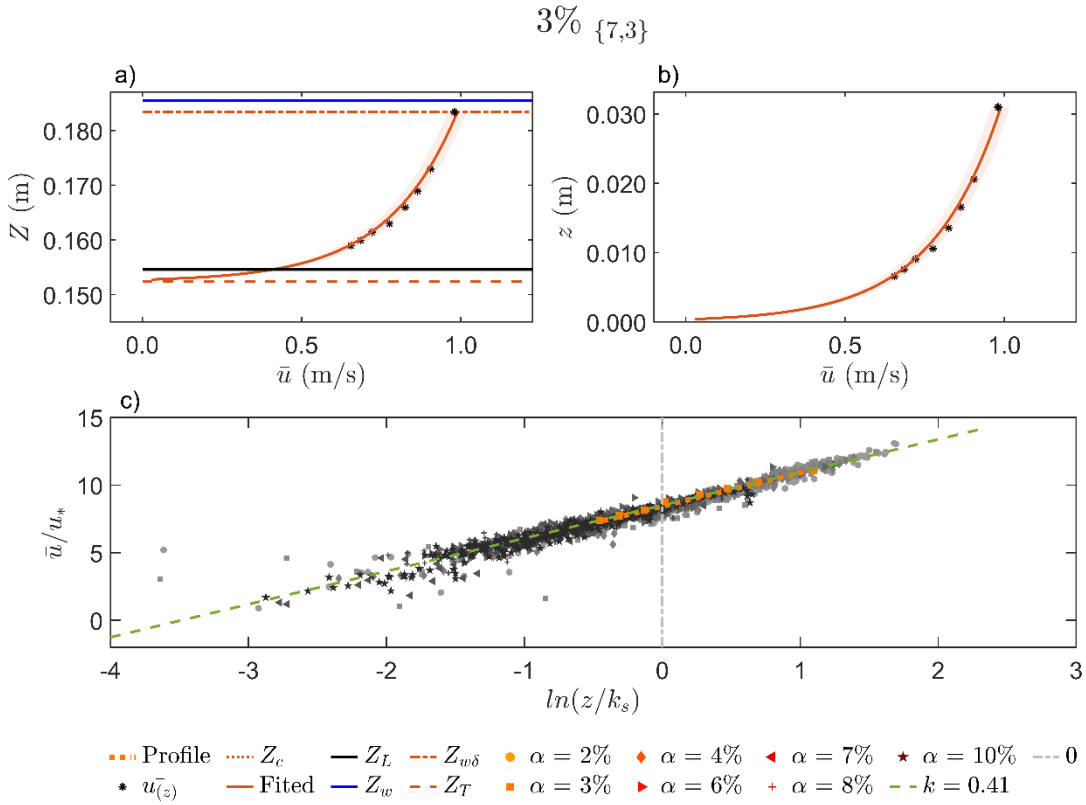

Figure B. 38. (a) Velocity profile as a function of water levels, (b) velocity profile as a function of water depths, and (c) dimensionless log profiles in the horizontal semi-log scale on a 3% flume slope.

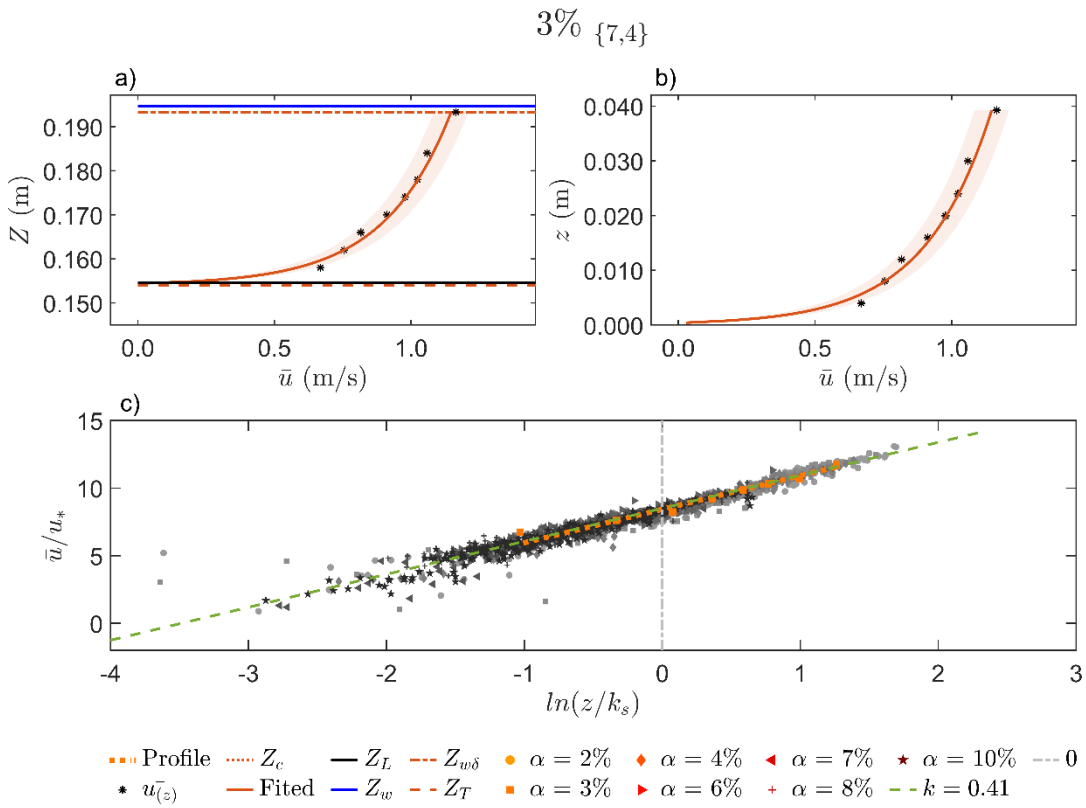

Figure B. 39. (a) Velocity profile as a function of water levels, (b) velocity profile as a function of water depths, and (c) dimensionless log profiles in the horizontal semi-log scale on a 3% flume slope.

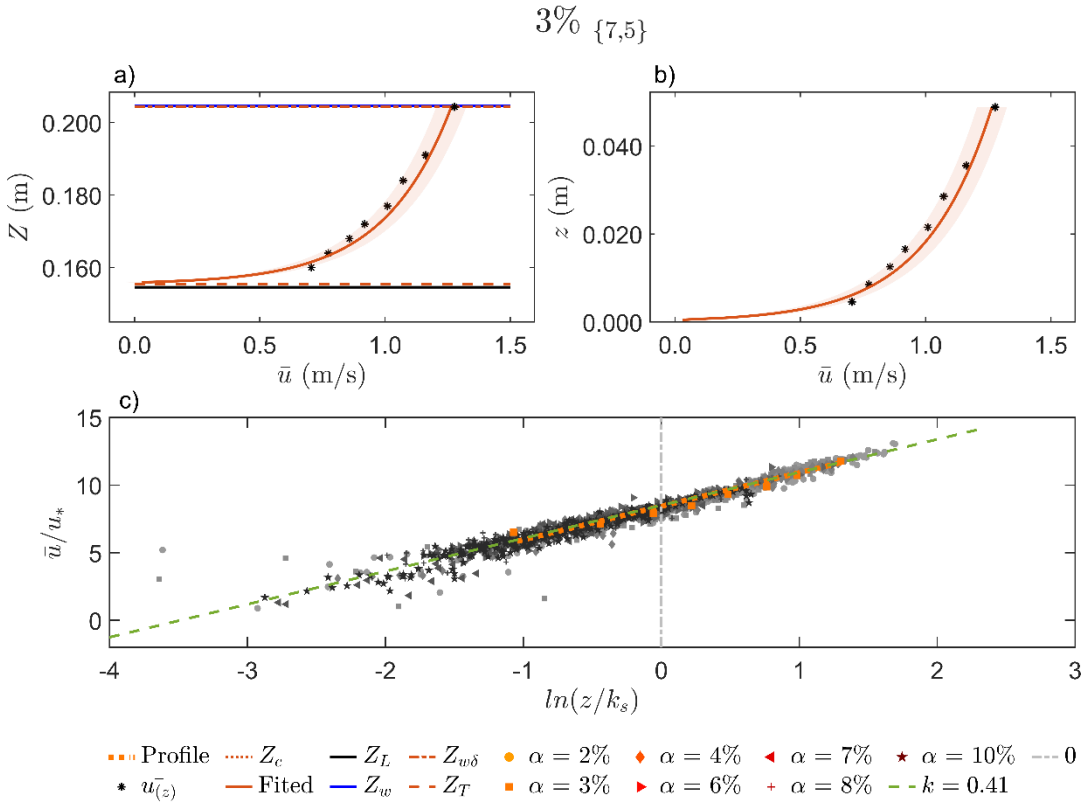

Figure B. 40. (a) Velocity profile as a function of water levels, (b) velocity profile as a function of water depths, and (c) dimensionless log profiles in the horizontal semi-log scale on a 3% flume slope.

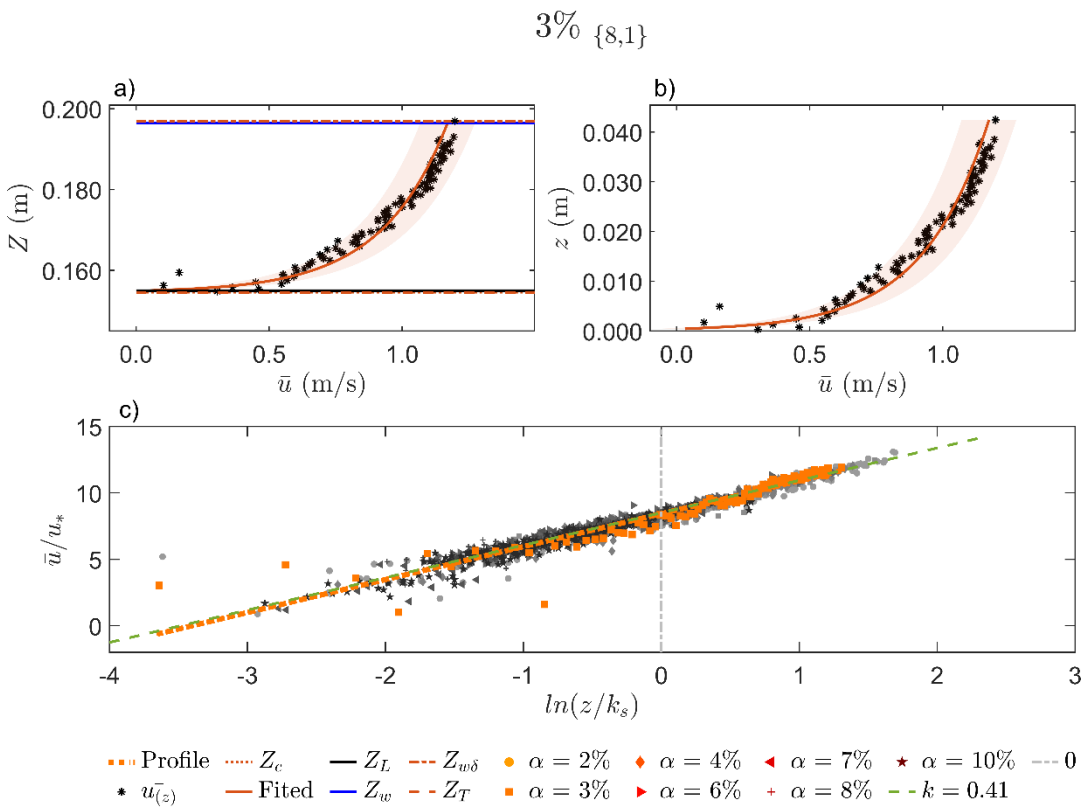

Figure B. 41. (a) Velocity profile as a function of water levels, (b) velocity profile as a function of water depths, and (c) dimensionless log profiles in the horizontal semi-log scale on a 3% flume slope.

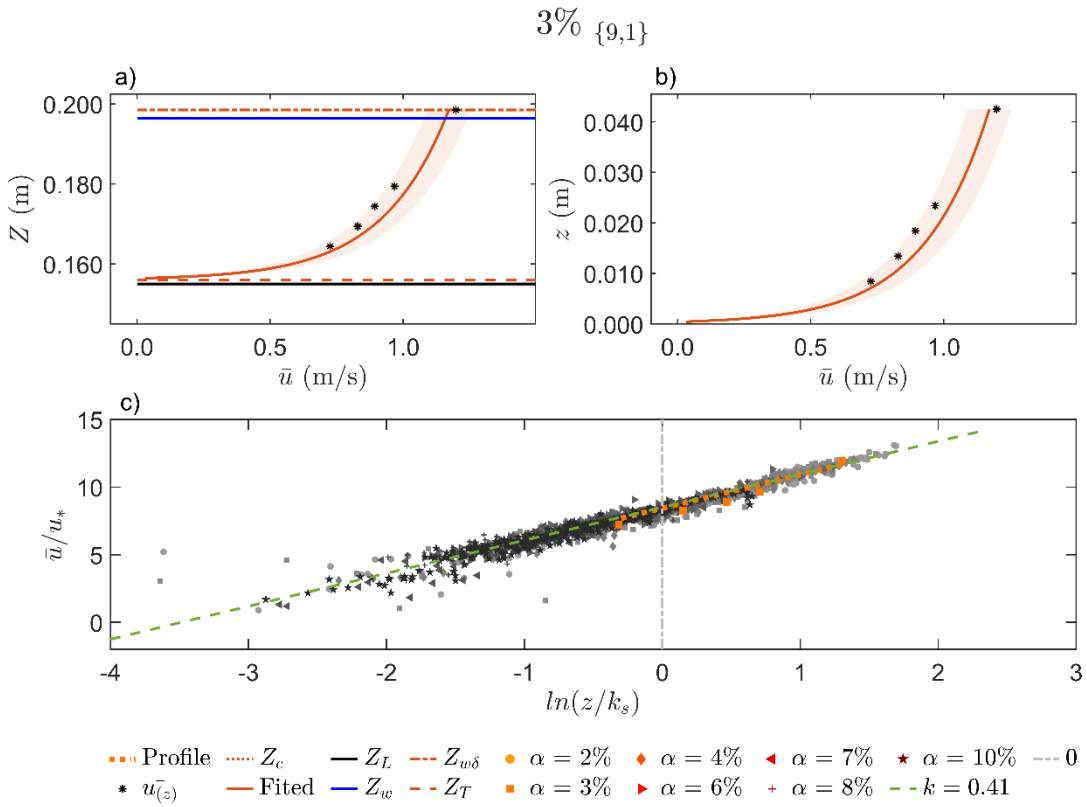

Figure B. 42. (a) Velocity profile as a function of water levels, (b) velocity profile as a function of water depths, and (c) dimensionless log profiles in the horizontal semi-log scale on a 3% flume slope.

B.1.3.c. 4% flume slope

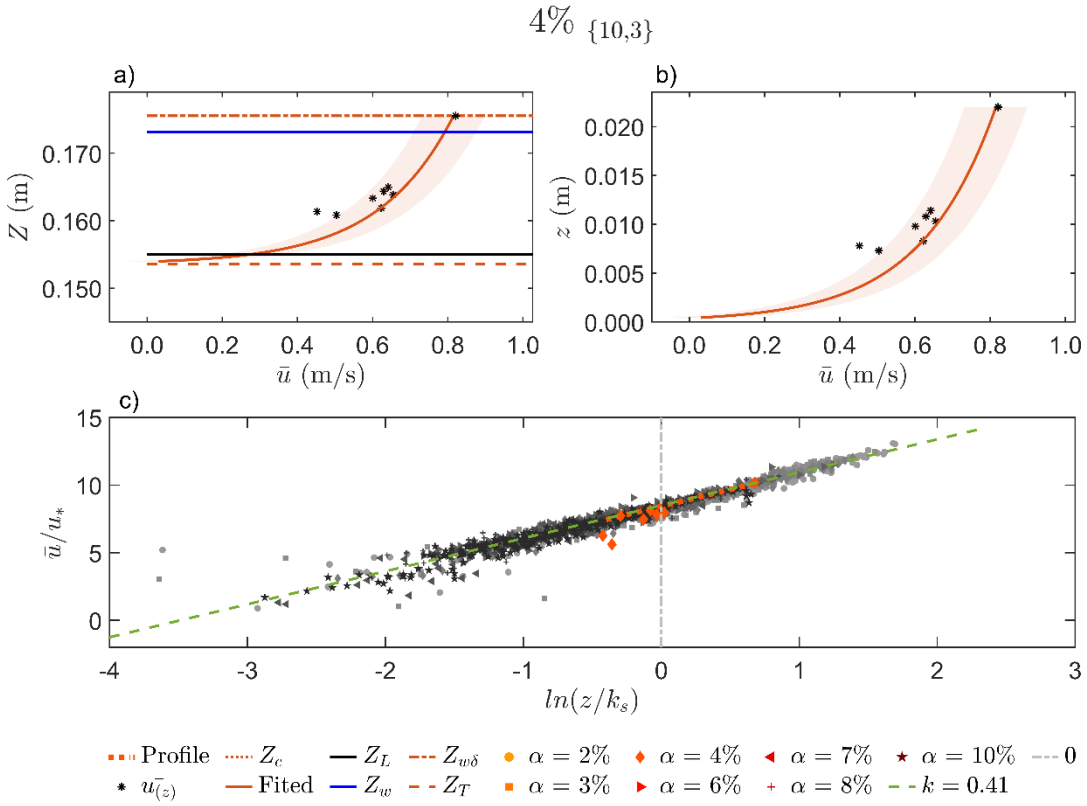

Figure B. 43. (a) Velocity profile as a function of water levels, (b) velocity profile as a function of water depths, and (c) dimensionless log profiles in the horizontal semi-log scale on a 4% flume slope.

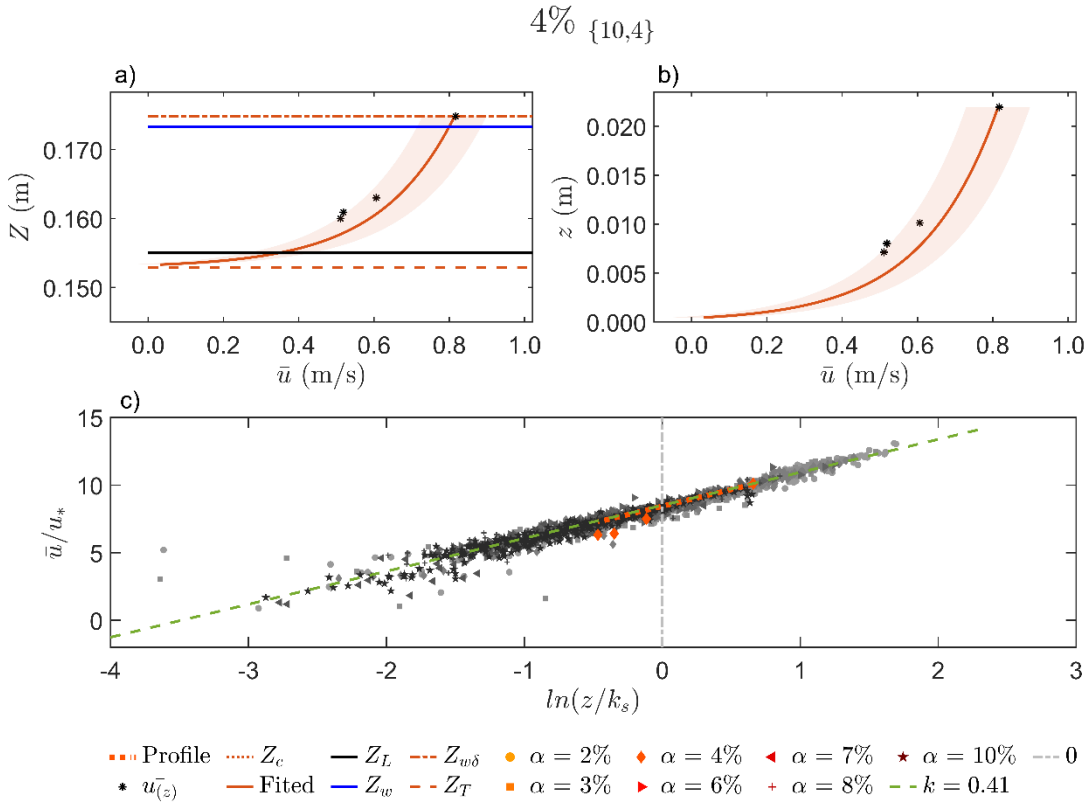

Figure B. 44. (a) Velocity profile as a function of water levels, (b) velocity profile as a function of water depths, and (c) dimensionless log profiles in the horizontal semi-log scale on a 4% flume slope.

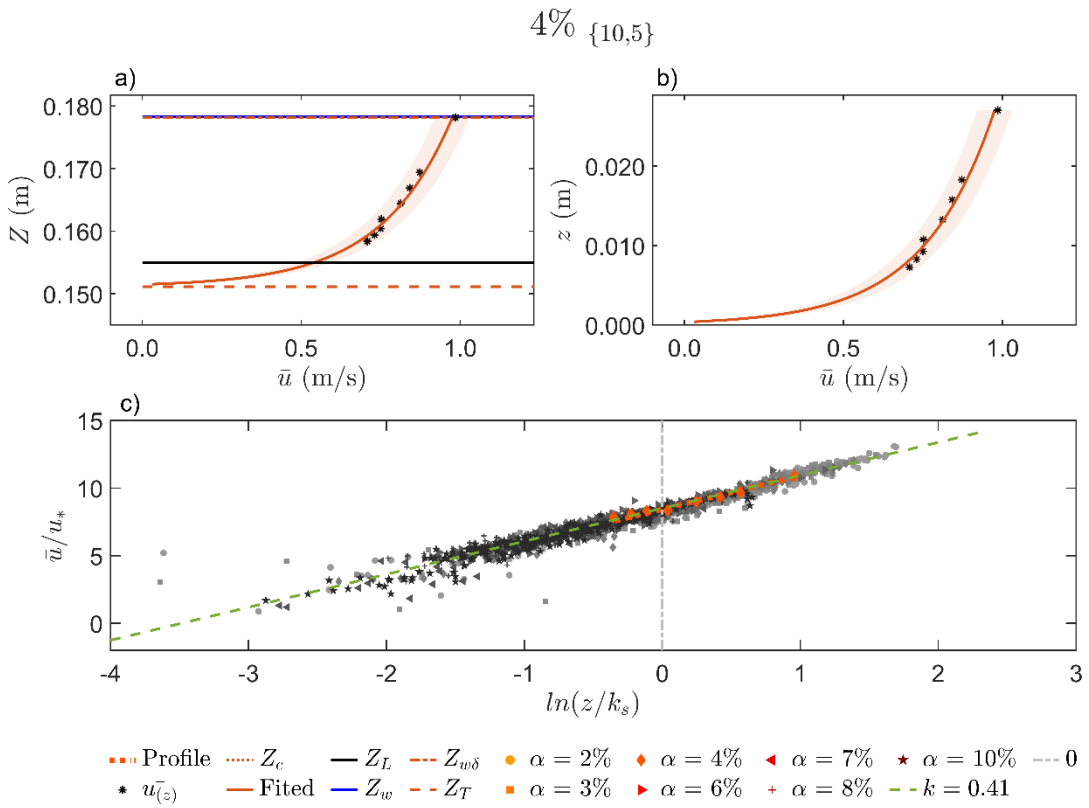

Figure B. 45. (a) Velocity profile as a function of water levels, (b) velocity profile as a function of water depths, and (c) dimensionless log profiles in the horizontal semi-log scale on a 4% flume slope.

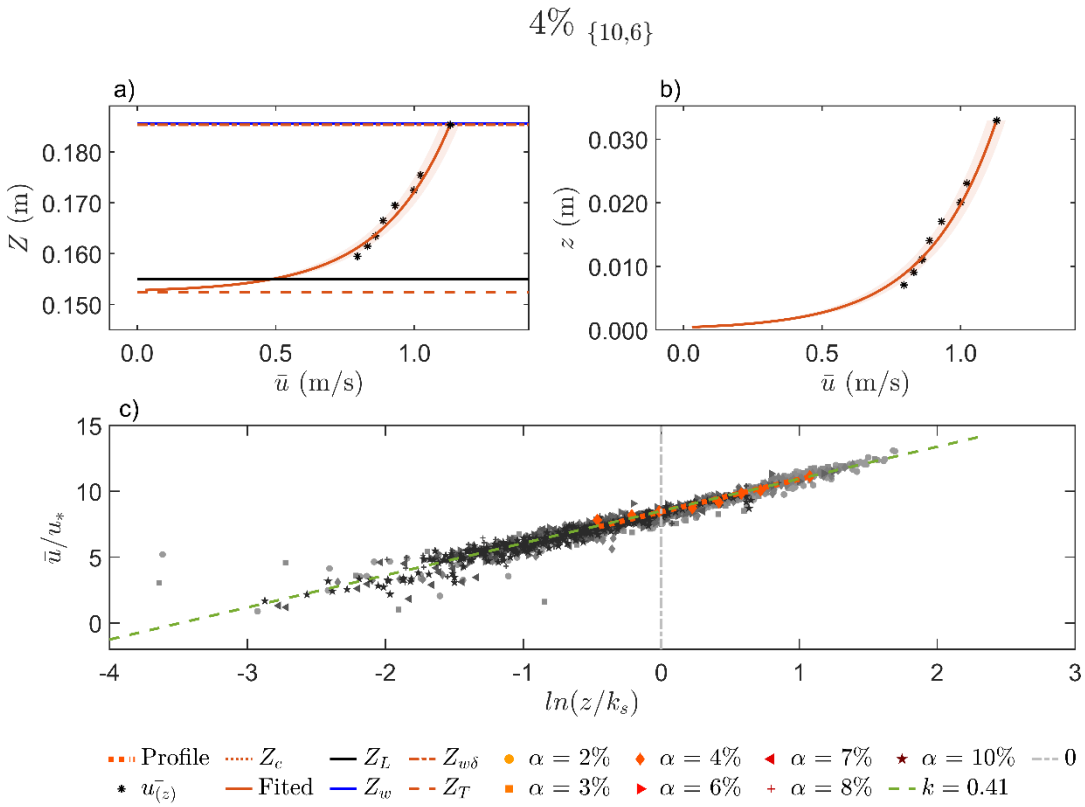

Figure B. 46. (a) Velocity profile as a function of water levels, (b) velocity profile as a function of water depths, and (c) dimensionless log profiles in the horizontal semi-log scale on a 4% flume slope.

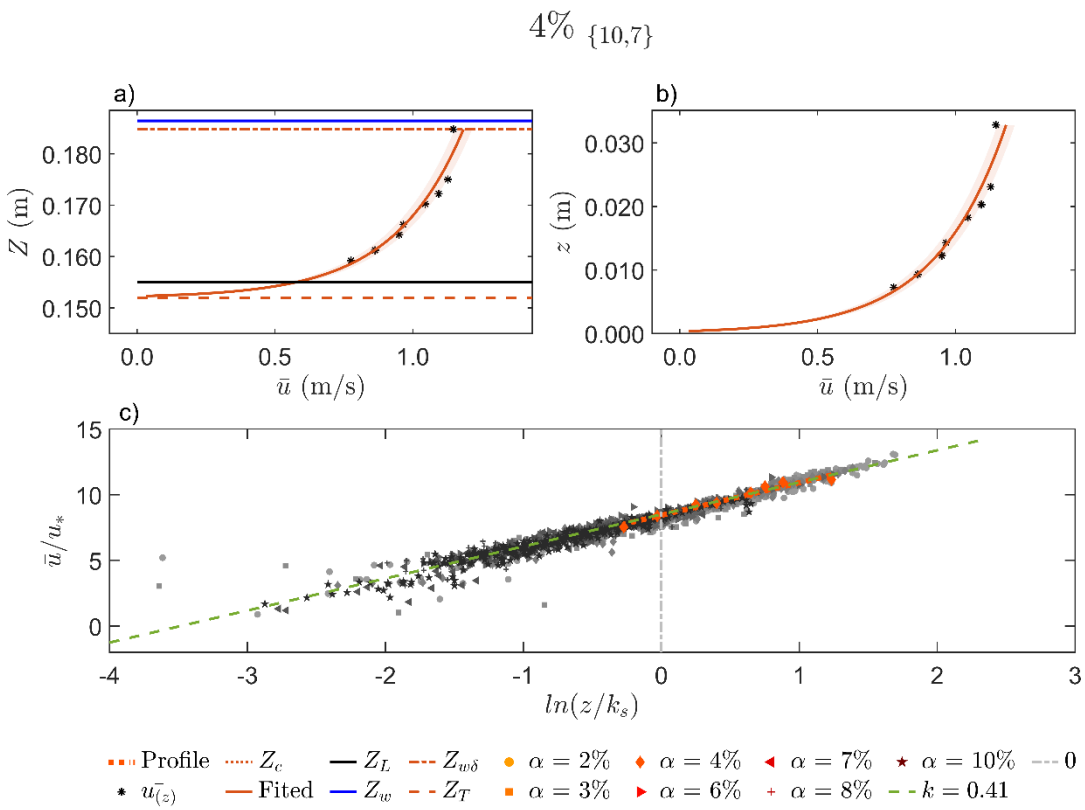

Figure B. 47. (a) Velocity profile as a function of water levels, (b) velocity profile as a function of water depths, and (c) dimensionless log profiles in the horizontal semi-log scale on a 4% flume slope.

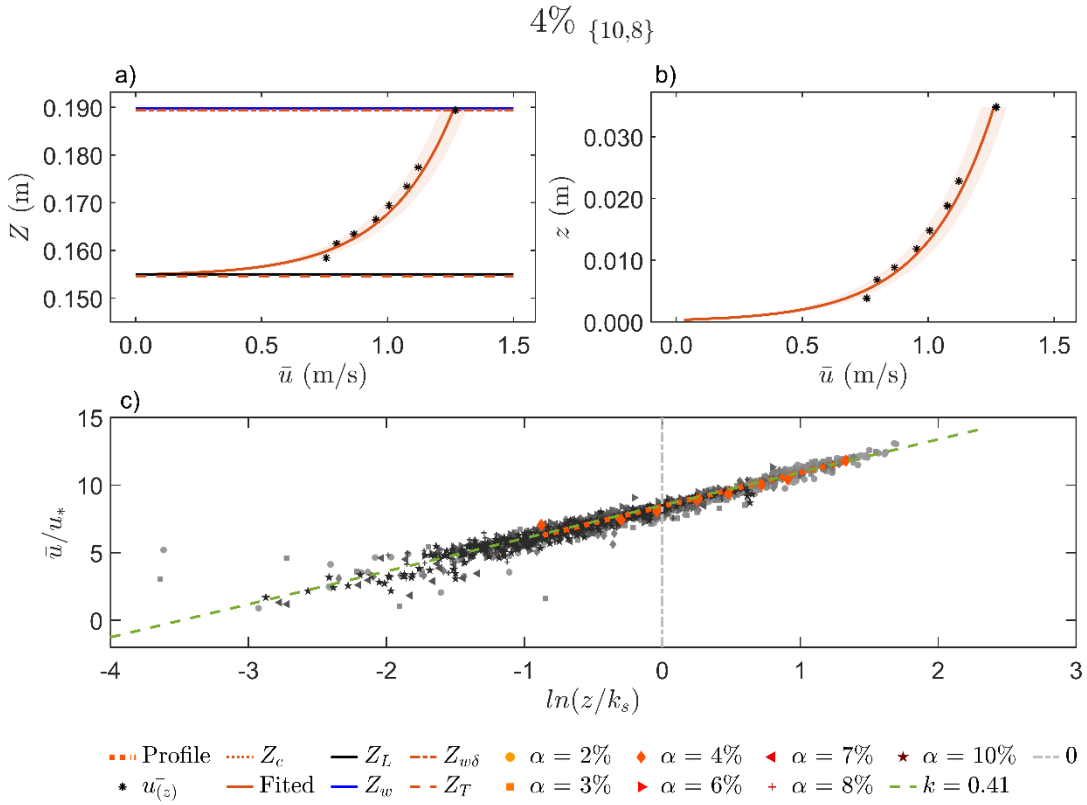

Figure B. 48. (a) Velocity profile as a function of water levels, (b) velocity profile as a function of water depths, and (c) dimensionless log profiles in the horizontal semi-log scale on a 4% flume slope.

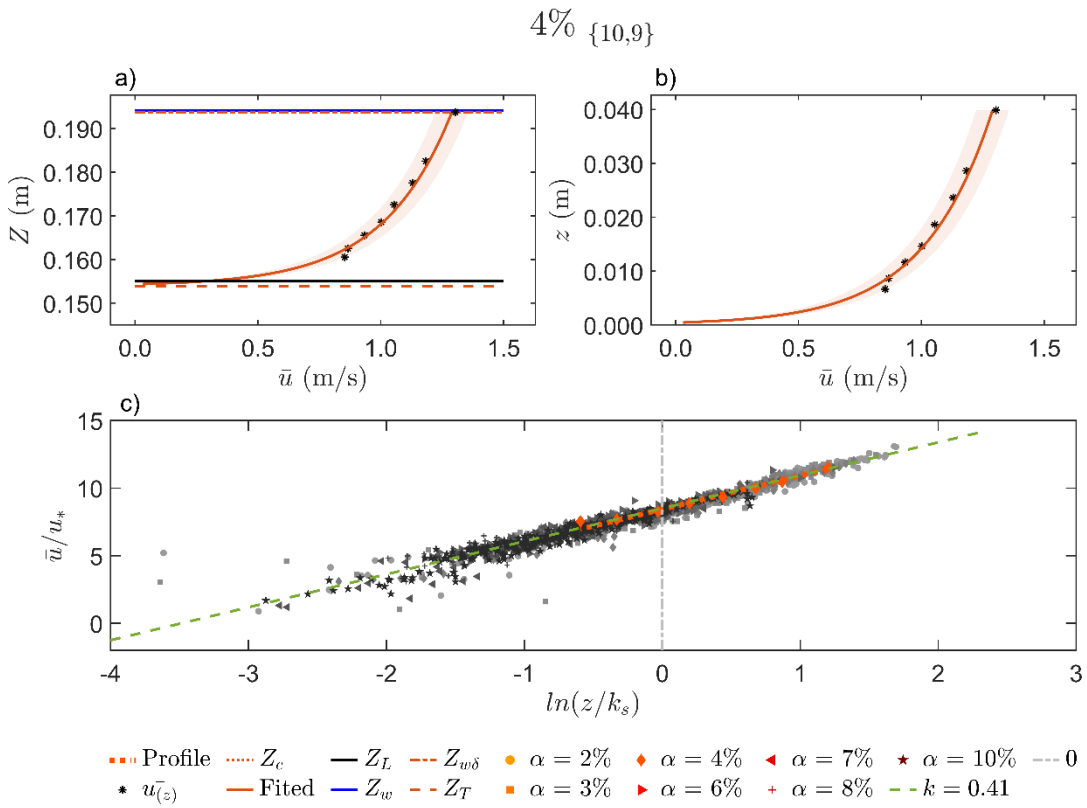

Figure B. 49. (a) Velocity profile as a function of water levels, (b) velocity profile as a function of water depths, and (c) dimensionless log profiles in the horizontal semi-log scale on a 4% flume slope.

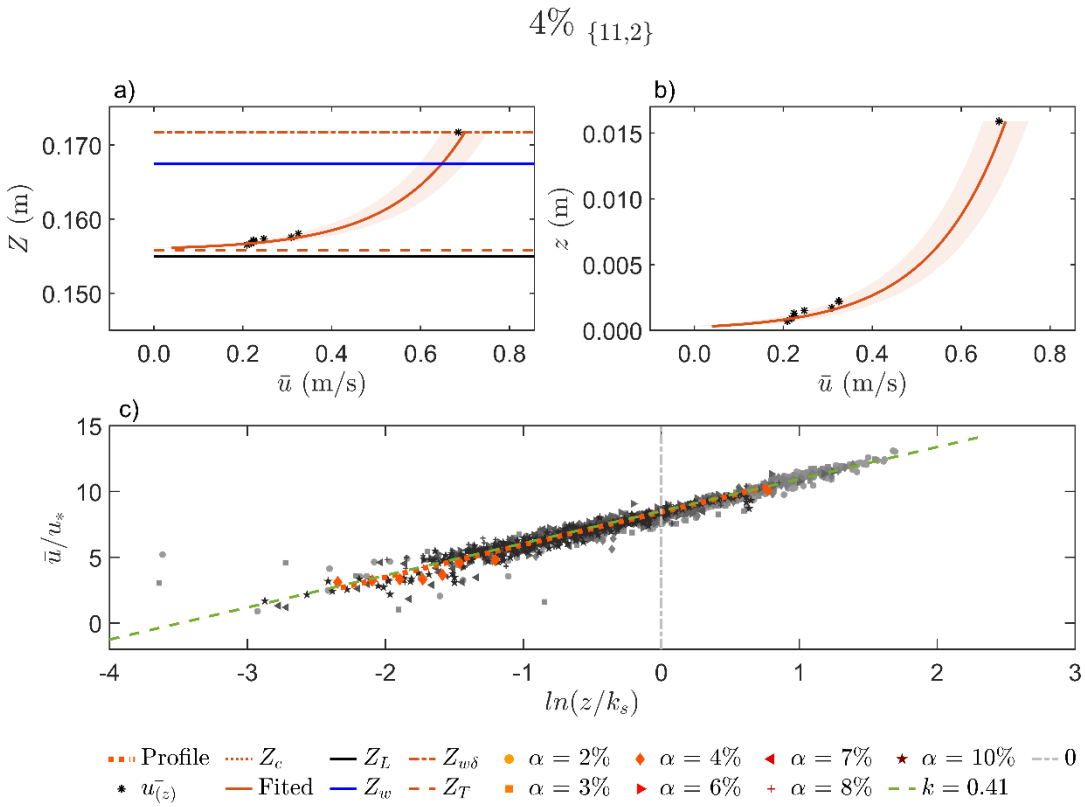

Figure B. 50. (a) Velocity profile as a function of water levels, (b) velocity profile as a function of water depths, and (c) dimensionless log profiles in the horizontal semi-log scale on a 4% flume slope.

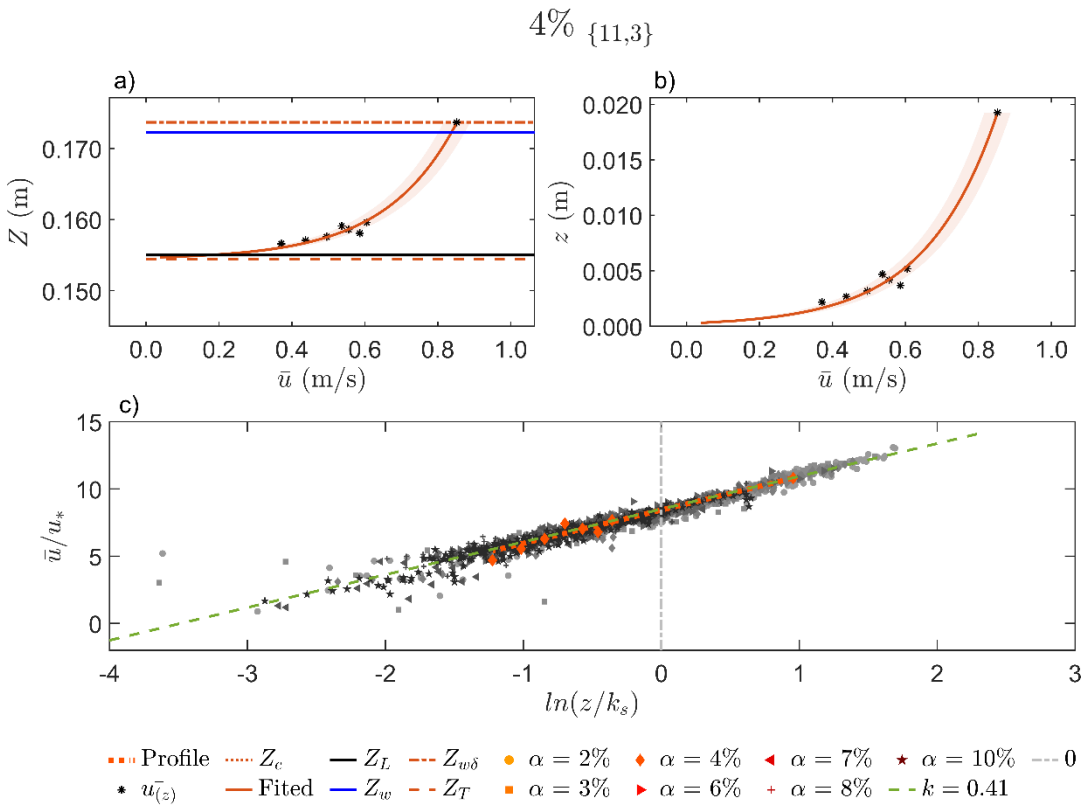

Figure B. 51. (a) Velocity profile as a function of water levels, (b) velocity profile as a function of water depths, and (c) dimensionless log profiles in the horizontal semi-log scale on a 4% flume slope.

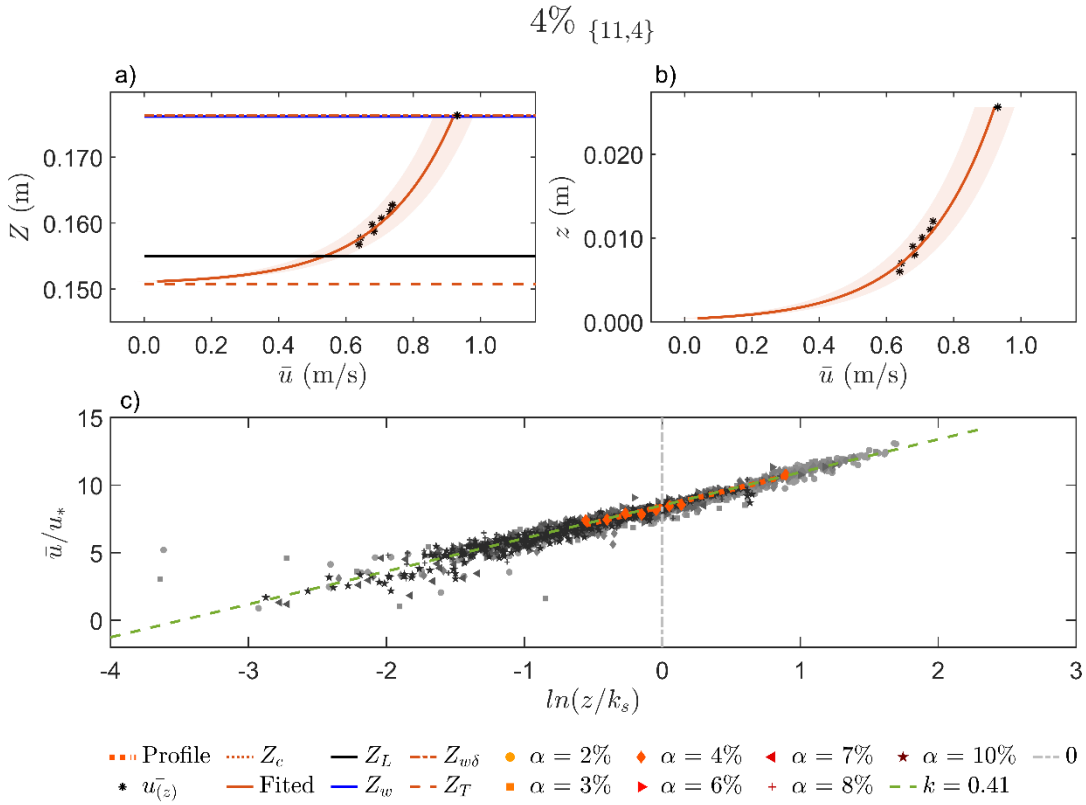

Figure B. 52. (a) Velocity profile as a function of water levels, (b) velocity profile as a function of water depths, and (c) dimensionless log profiles in the horizontal semi-log scale on a 4% flume slope.

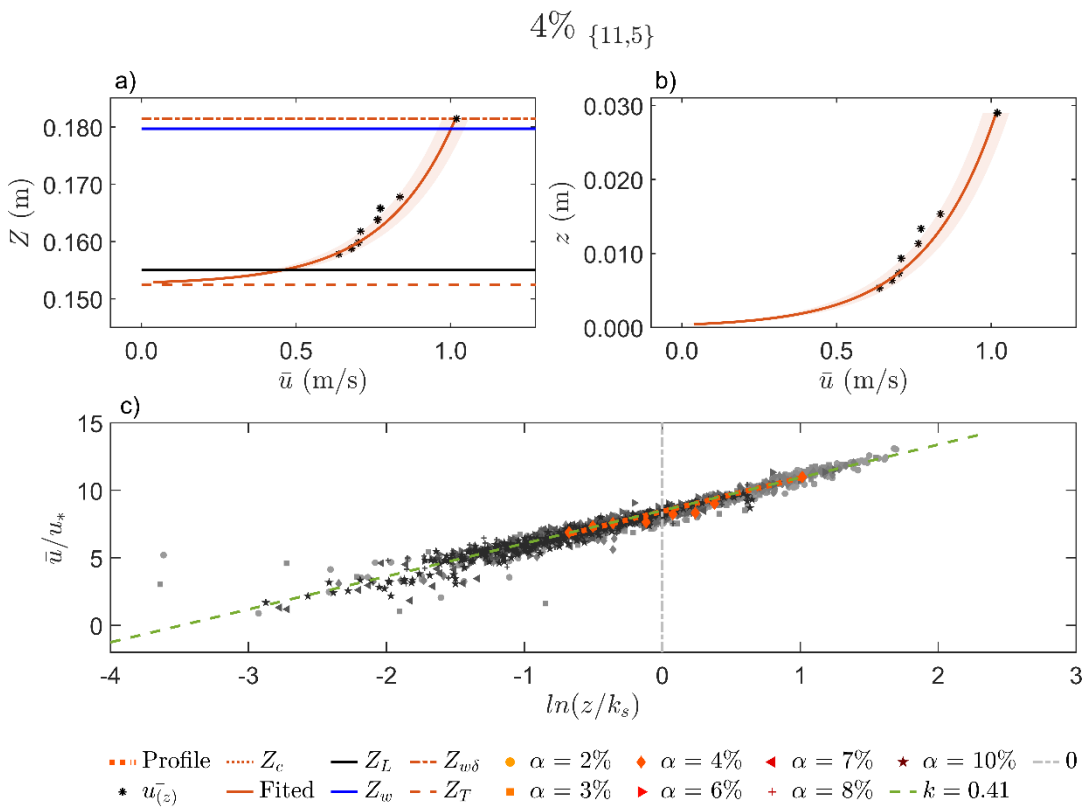

Figure B. 53. (a) Velocity profile as a function of water levels, (b) velocity profile as a function of water depths, and (c) dimensionless log profiles in the horizontal semi-log scale on a 4% flume slope.

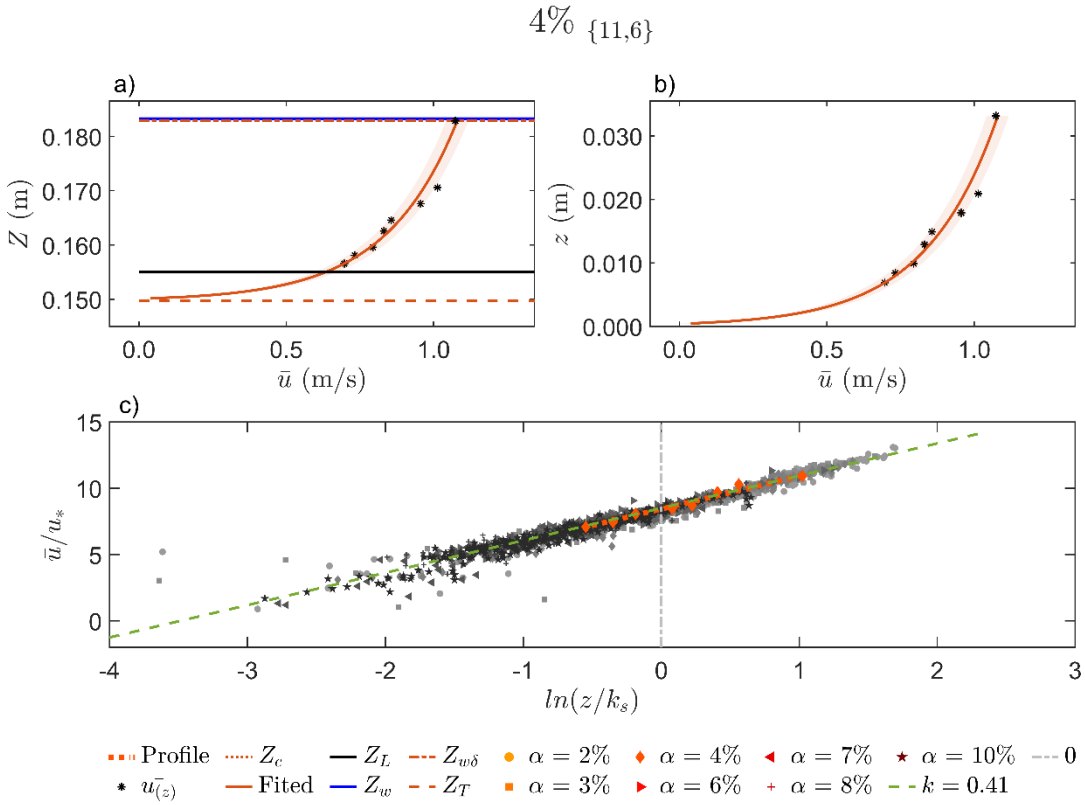

Figure B. 54. (a) Velocity profile as a function of water levels, (b) velocity profile as a function of water depths, and (c) dimensionless log profiles in the horizontal semi-log scale on a 4% flume slope.

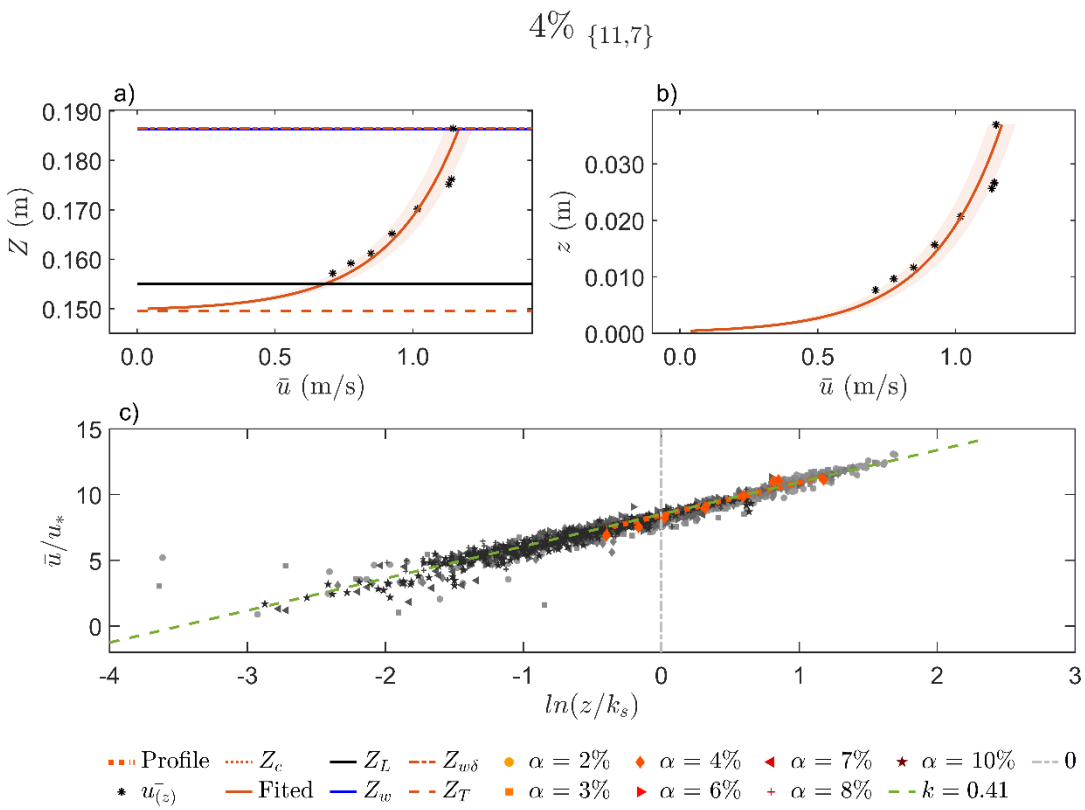

Figure B. 55. (a) Velocity profile as a function of water levels, (b) velocity profile as a function of water depths, and (c) dimensionless log profiles in the horizontal semi-log scale on a 4% flume slope.

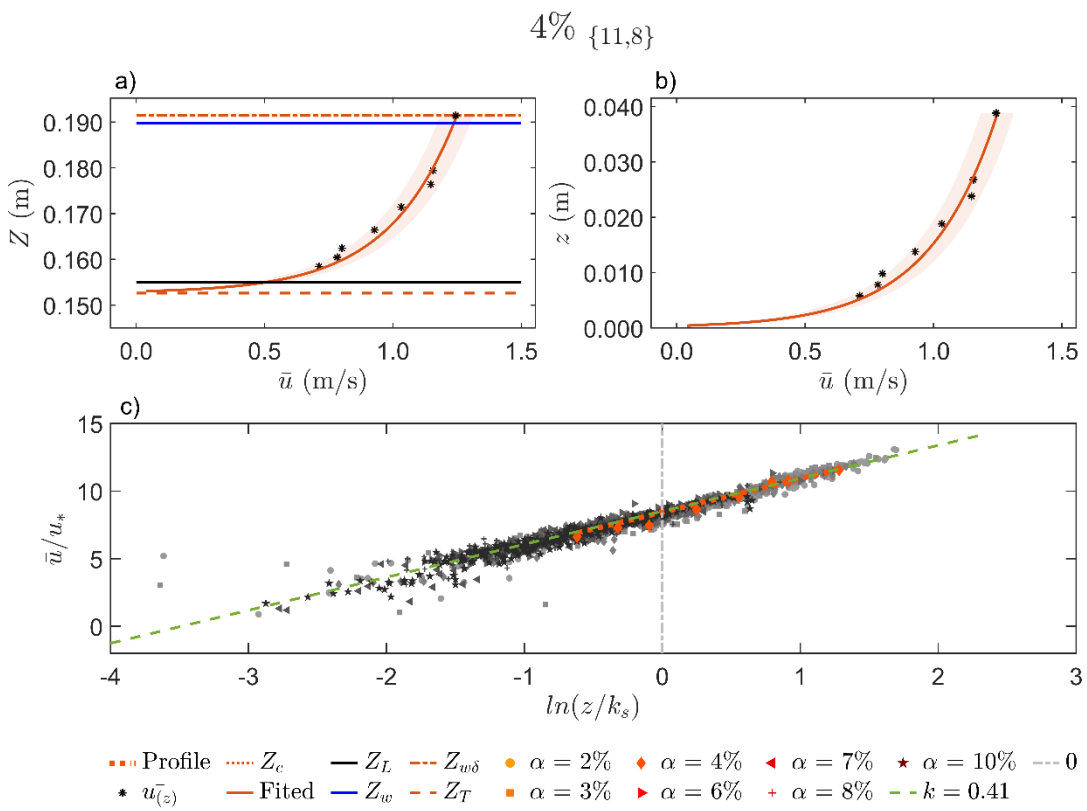

Figure B. 56. (a) Velocity profile as a function of water levels, (b) velocity profile as a function of water depths, and (c) dimensionless log profiles in the horizontal semi-log scale on a 4% flume slope.

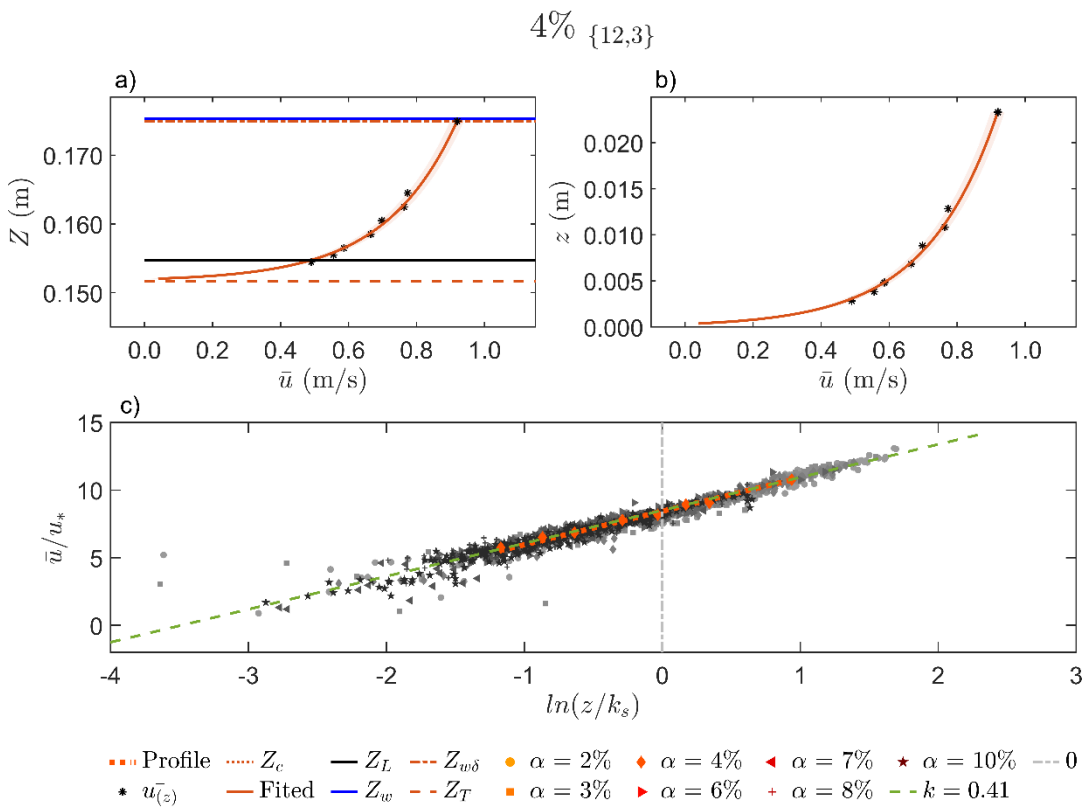

Figure B. 57. (a) Velocity profile as a function of water levels, (b) velocity profile as a function of water depths, and (c) dimensionless log profiles in the horizontal semi-log scale on a 4% flume slope.

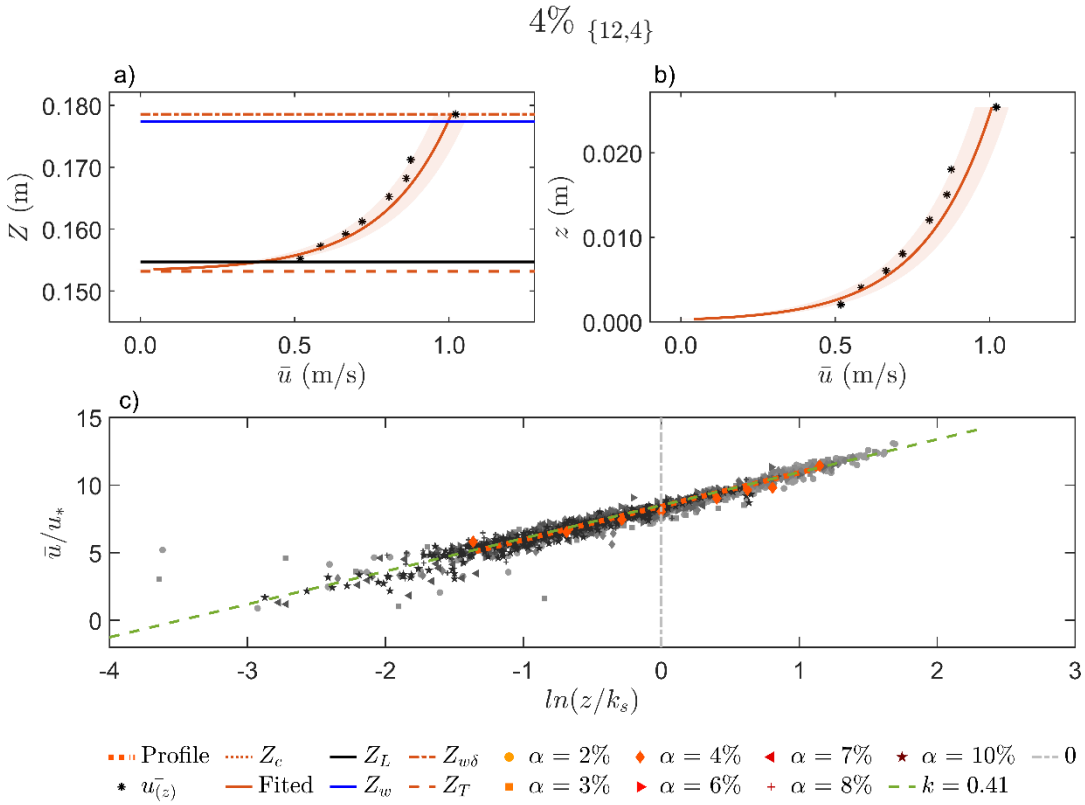

Figure B. 58. (a) Velocity profile as a function of water levels, (b) velocity profile as a function of water depths, and (c) dimensionless log profiles in the horizontal semi-log scale on a 4% flume slope.

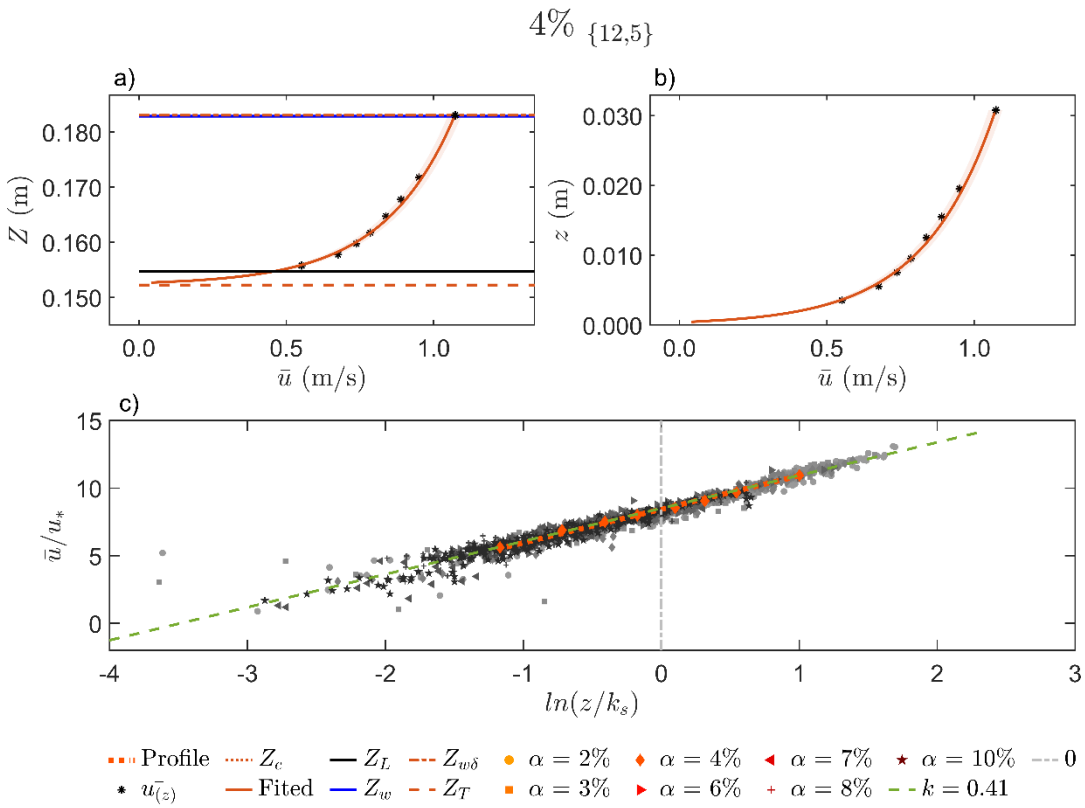

Figure B. 59. (a) Velocity profile as a function of water levels, (b) velocity profile as a function of water depths, and (c) dimensionless log profiles in the horizontal semi-log scale on a 4% flume slope.

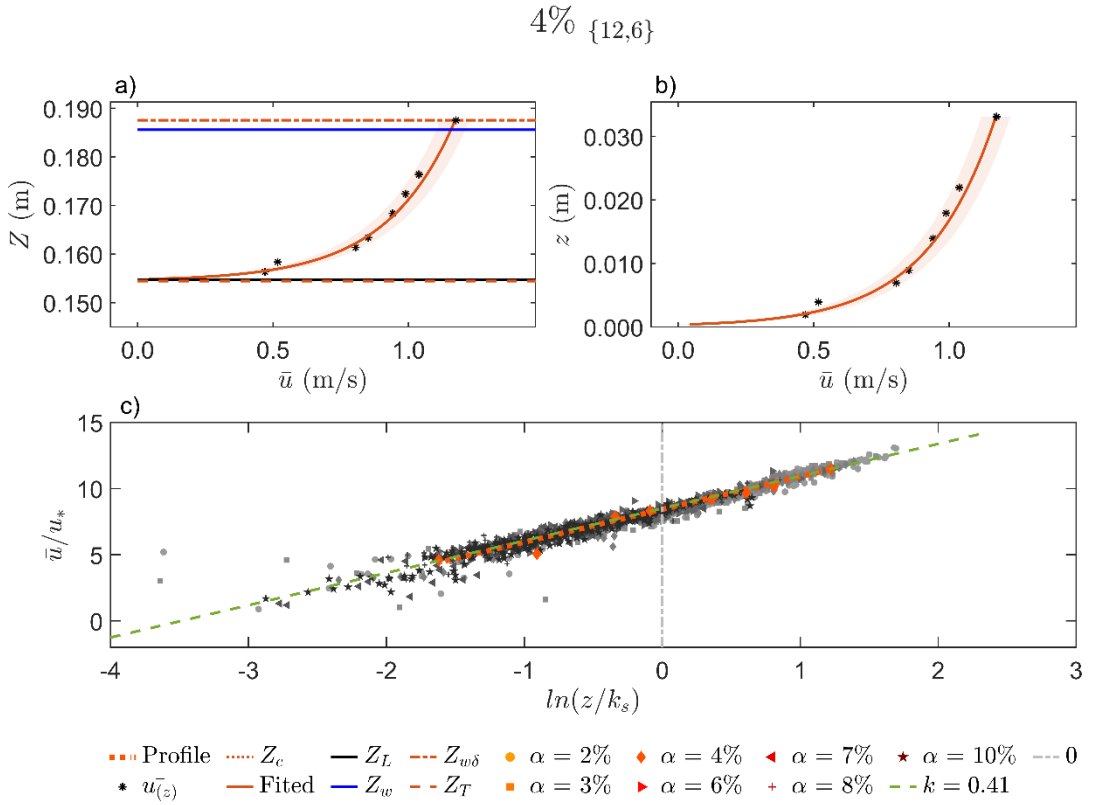

Figure B. 60. (a) Velocity profile as a function of water levels, (b) velocity profile as a function of water depths, and (c) dimensionless log profiles in the horizontal semi-log scale on a 4% flume slope.

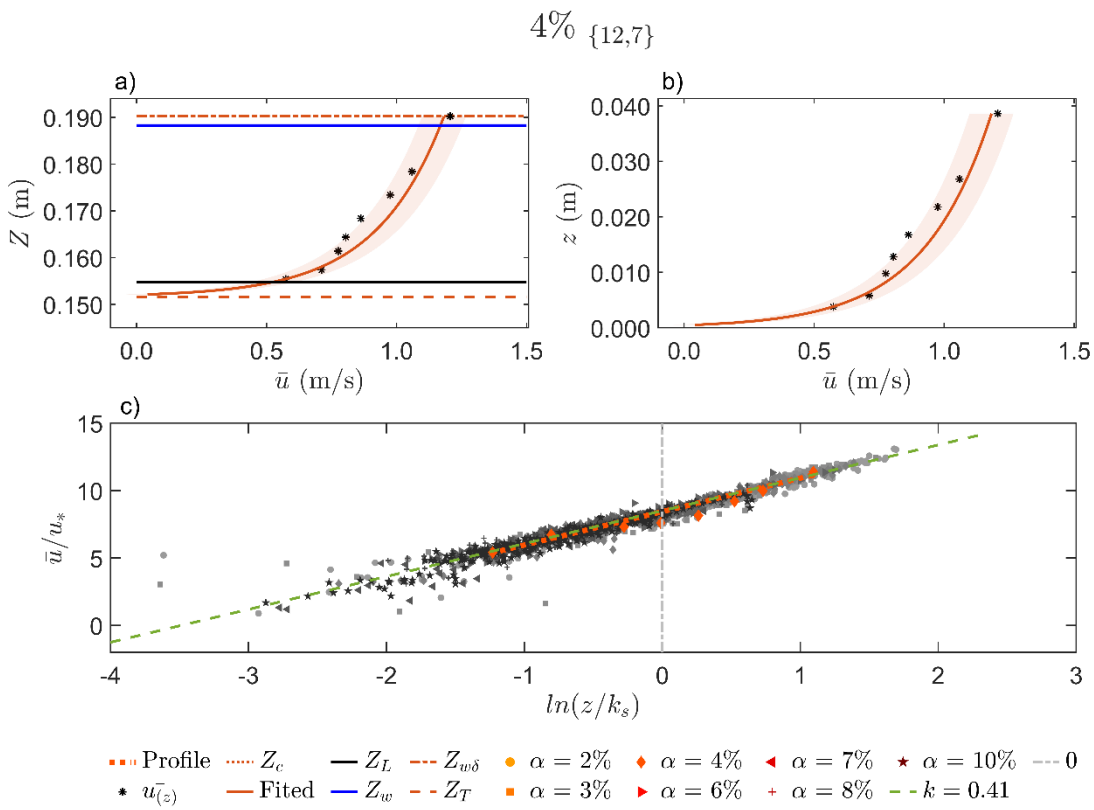

Figure B. 61. (a) Velocity profile as a function of water levels, (b) velocity profile as a function of water depths, and (c) dimensionless log profiles in the horizontal semi-log scale on a 4% flume slope.

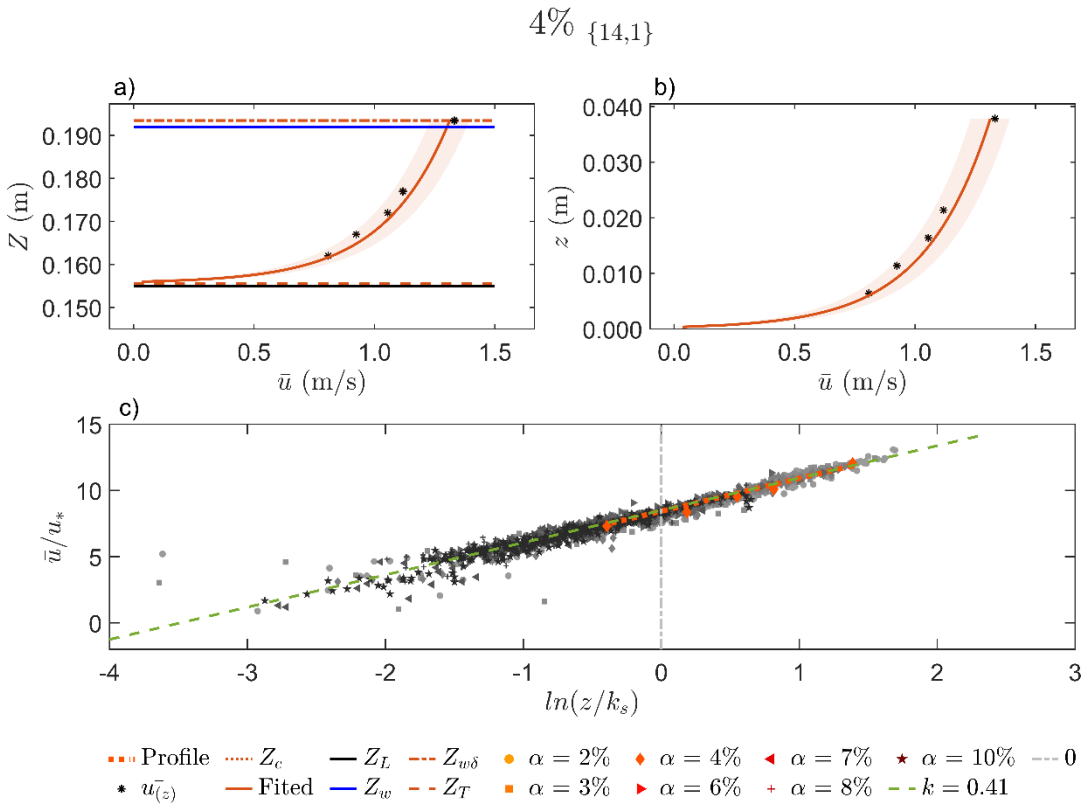

Figure B. 62. (a) Velocity profile as a function of water levels, (b) velocity profile as a function of water depths, and (c) dimensionless log profiles in the horizontal semi-log scale on a 4% flume slope.

B.1.3.d. 6% flume slope

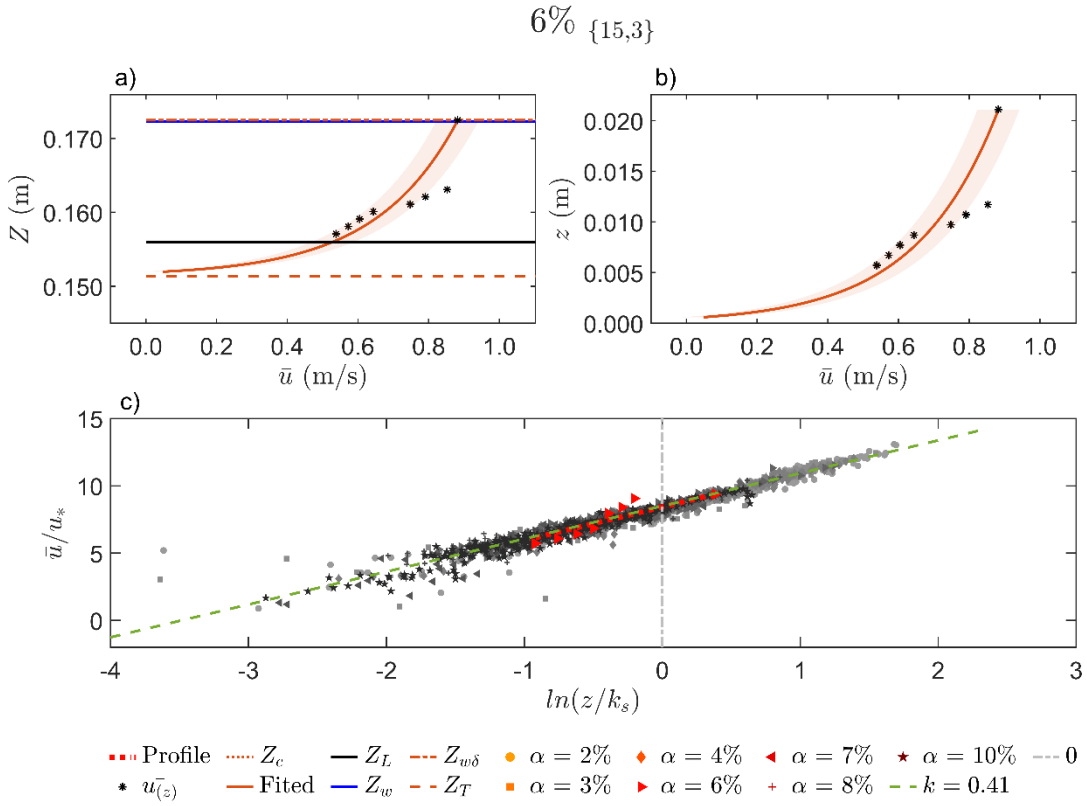

Figure B. 63. (a) Velocity profile as a function of water levels, (b) velocity profile as a function of water depths, and (c) dimensionless log profiles in the horizontal semi-log scale on a 6% flume slope.

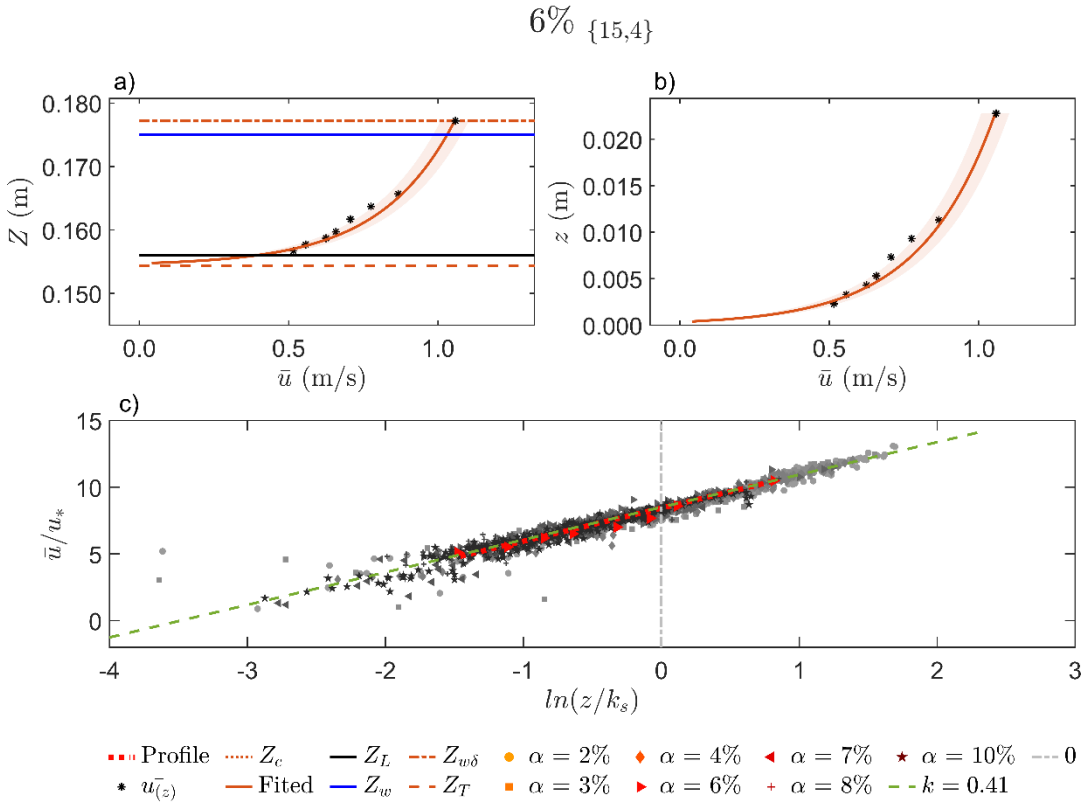

Figure B. 64. (a) Velocity profile as a function of water levels, (b) velocity profile as a function of water depths, and (c) dimensionless log profiles in the horizontal semi-log scale on a 6% flume slope.

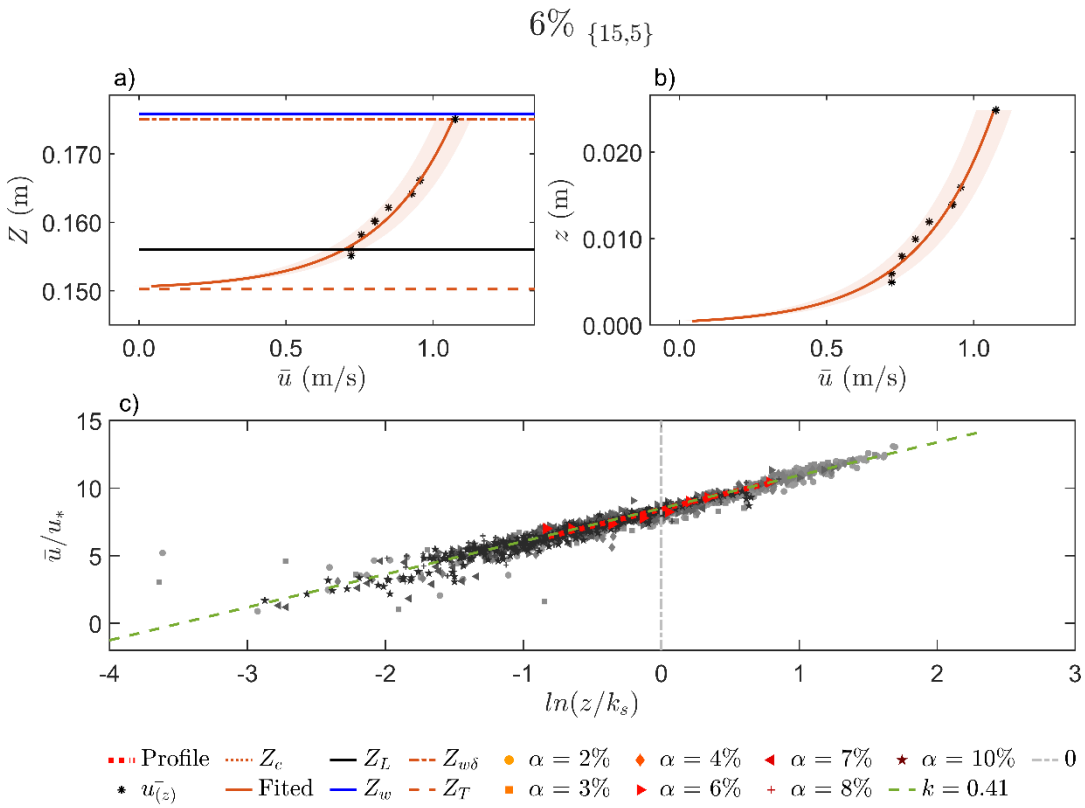

Figure B. 65. (a) Velocity profile as a function of water levels, (b) velocity profile as a function of water depths, and (c) dimensionless log profiles in the horizontal semi-log scale on a 6% flume slope.

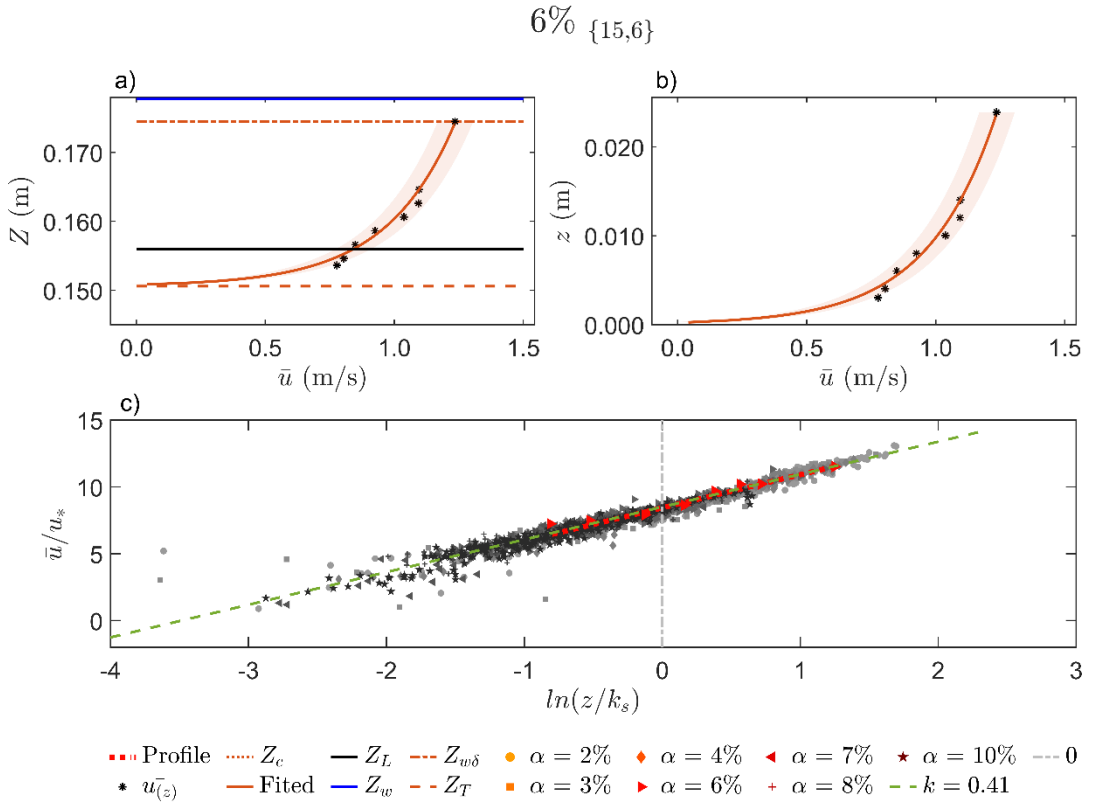

Figure B. 66. (a) Velocity profile as a function of water levels, (b) velocity profile as a function of water depths, and (c) dimensionless log profiles in the horizontal semi-log scale on a 6% flume slope.

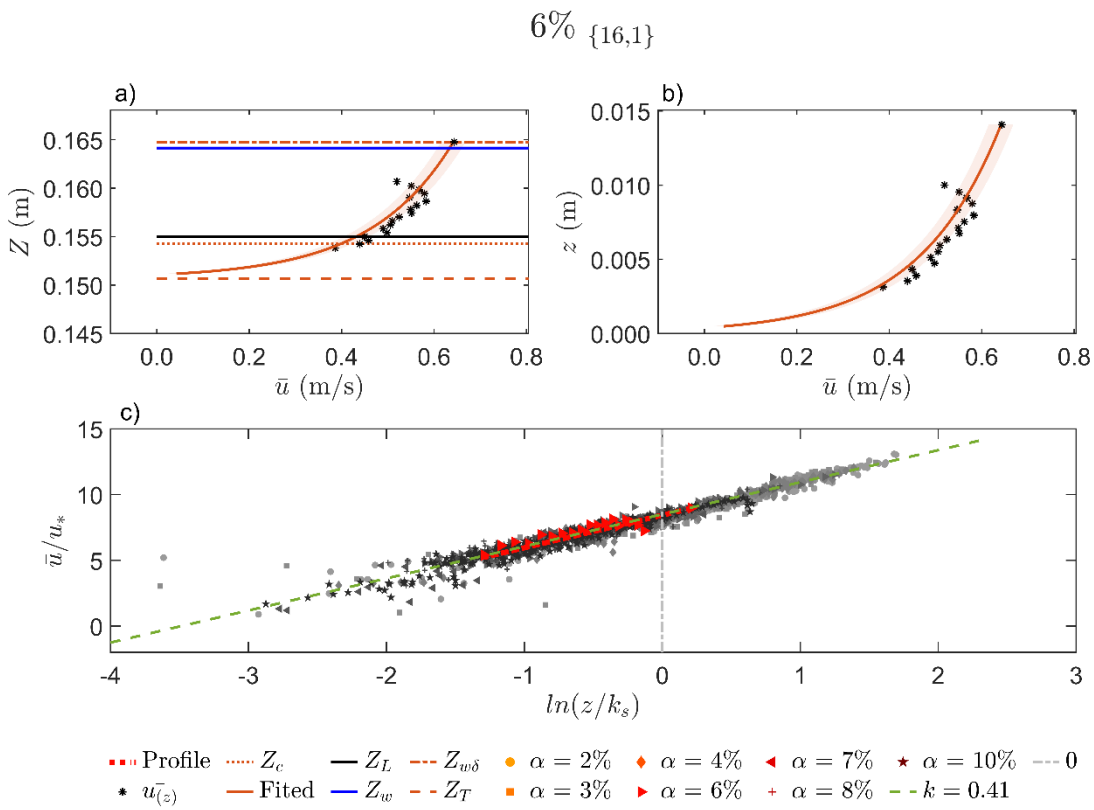

Figure B. 67. (a) Velocity profile as a function of water levels, (b) velocity profile as a function of water depths, and (c) dimensionless log profiles in the horizontal semi-log scale on a 6% flume slope.

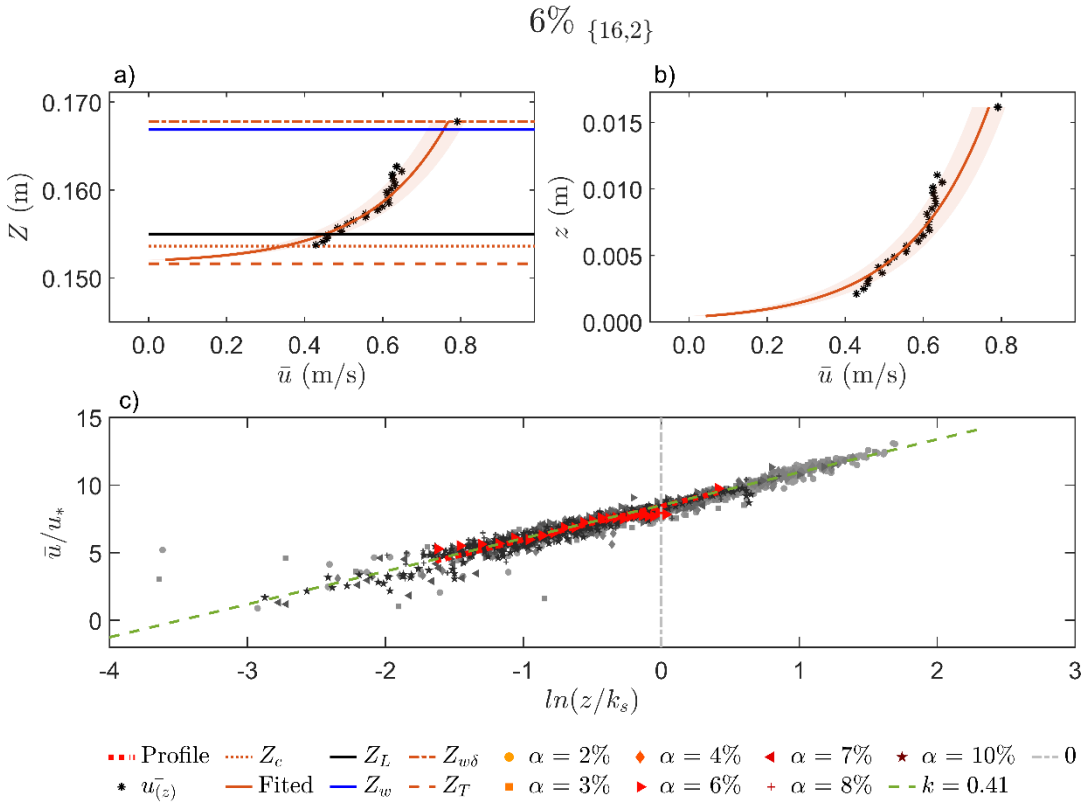

Figure B. 68. (a) Velocity profile as a function of water levels, (b) velocity profile as a function of water depths, and (c) dimensionless log profiles in the horizontal semi-log scale on a 6% flume slope.

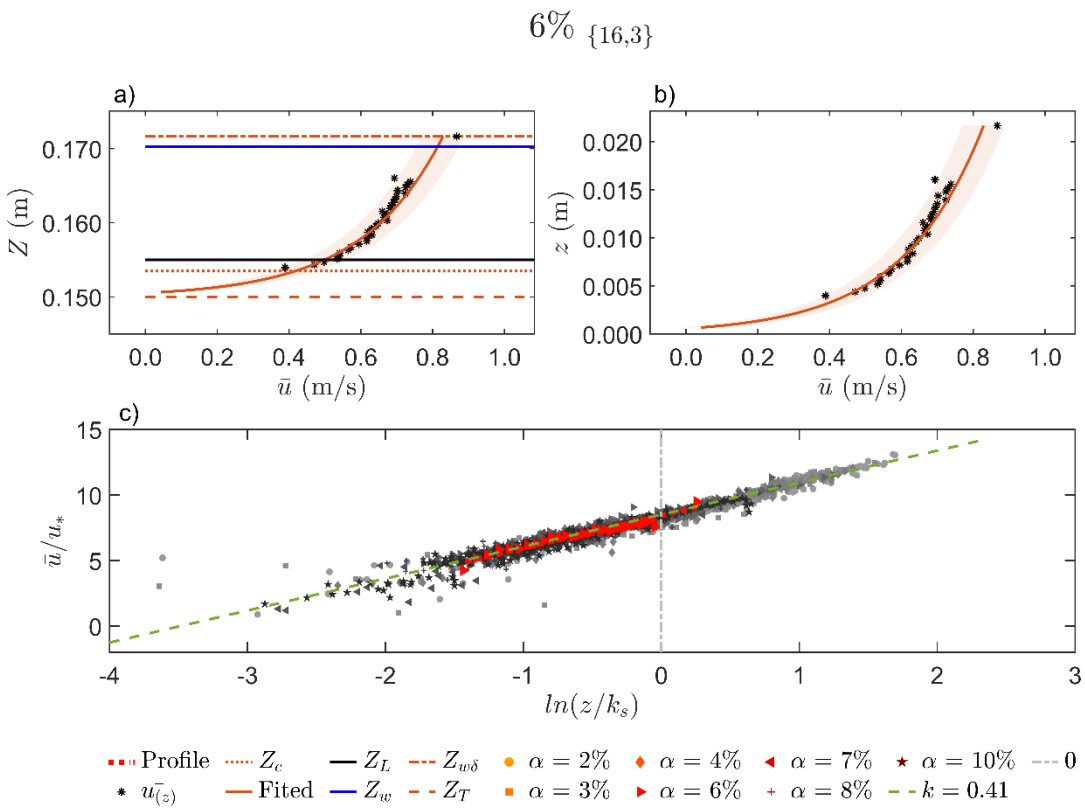

Figure B. 69. (a) Velocity profile as a function of water levels, (b) velocity profile as a function of water depths, and (c) dimensionless log profiles in the horizontal semi-log scale on a 6% flume slope.

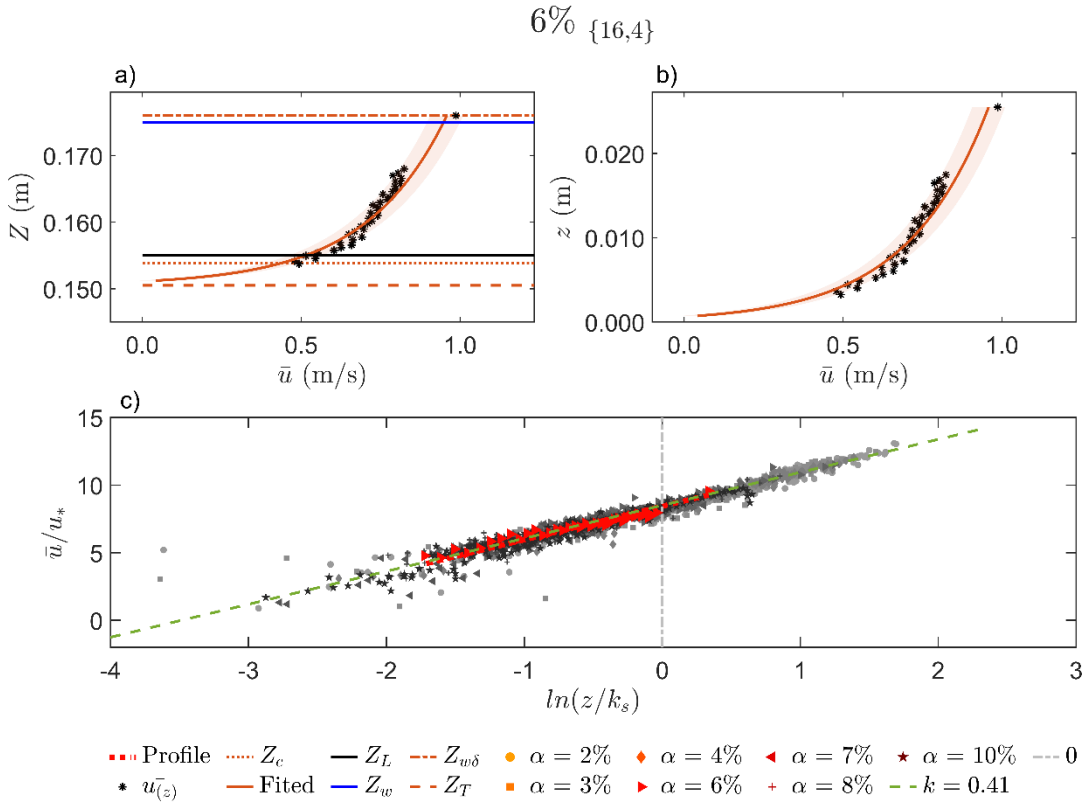

Figure B. 70. (a) Velocity profile as a function of water levels, (b) velocity profile as a function of water depths, and (c) dimensionless log profiles in the horizontal semi-log scale on a 6% flume slope.

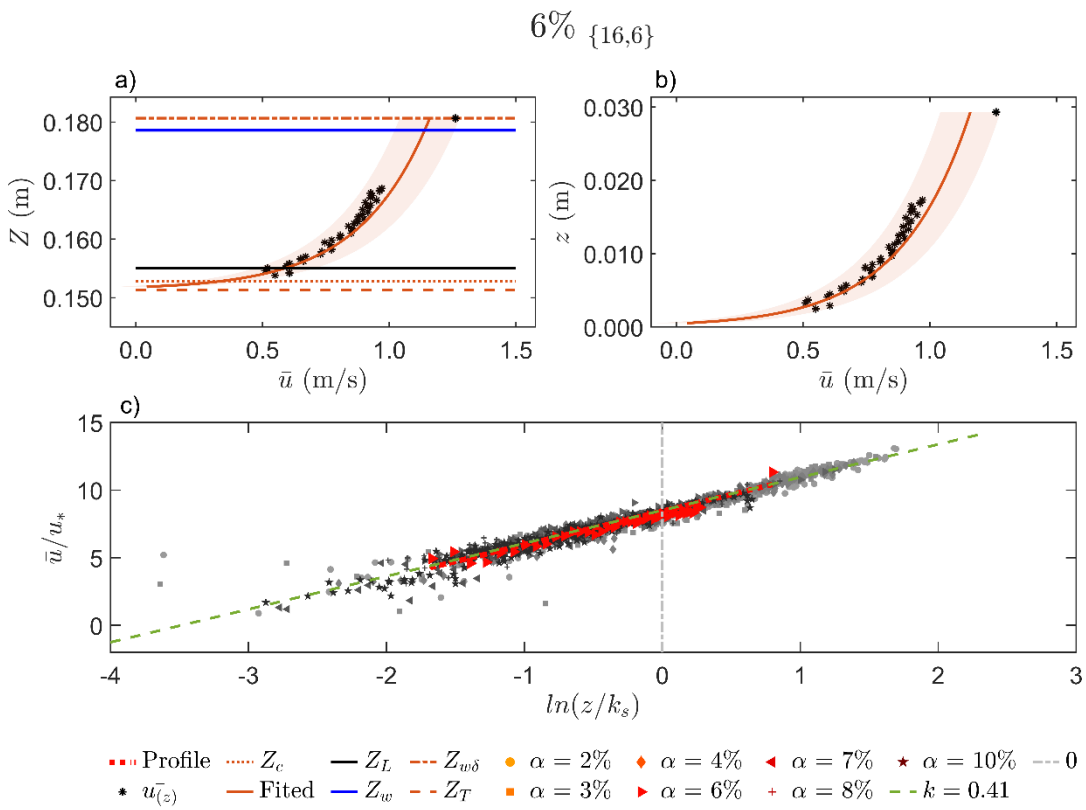

Figure B. 71. (a) Velocity profile as a function of water levels, (b) velocity profile as a function of water depths, and (c) dimensionless log profiles in the horizontal semi-log scale on a 6% flume slope.

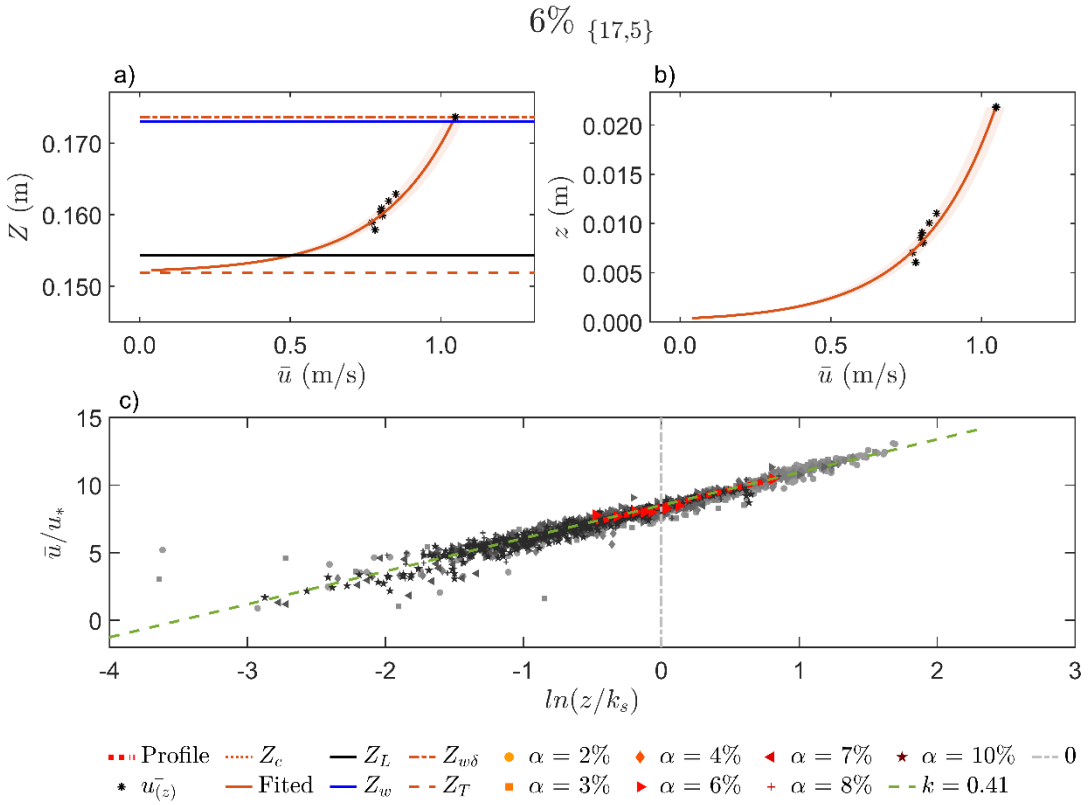

Figure B. 72. (a) Velocity profile as a function of water levels, (b) velocity profile as a function of water depths, and (c) dimensionless log profiles in the horizontal semi-log scale on a 6% flume slope.

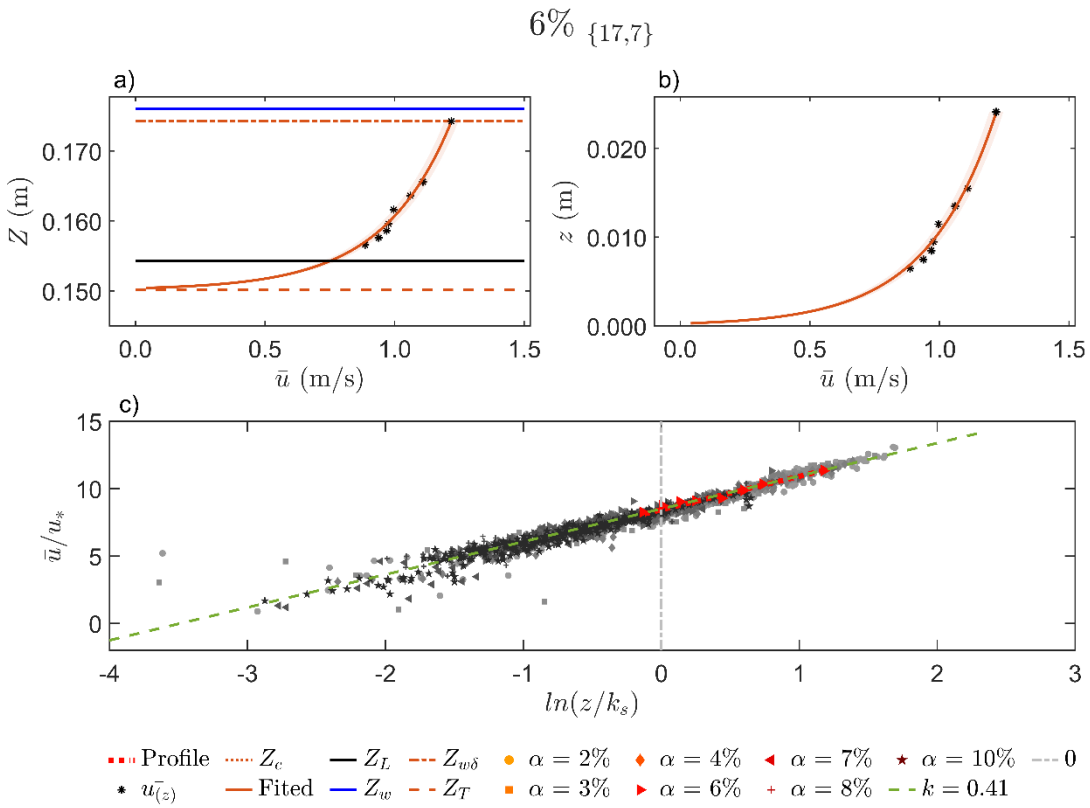

Figure B. 73. (a) Velocity profile as a function of water levels, (b) velocity profile as a function of water depths, and (c) dimensionless log profiles in the horizontal semi-log scale on a 6% flume slope.

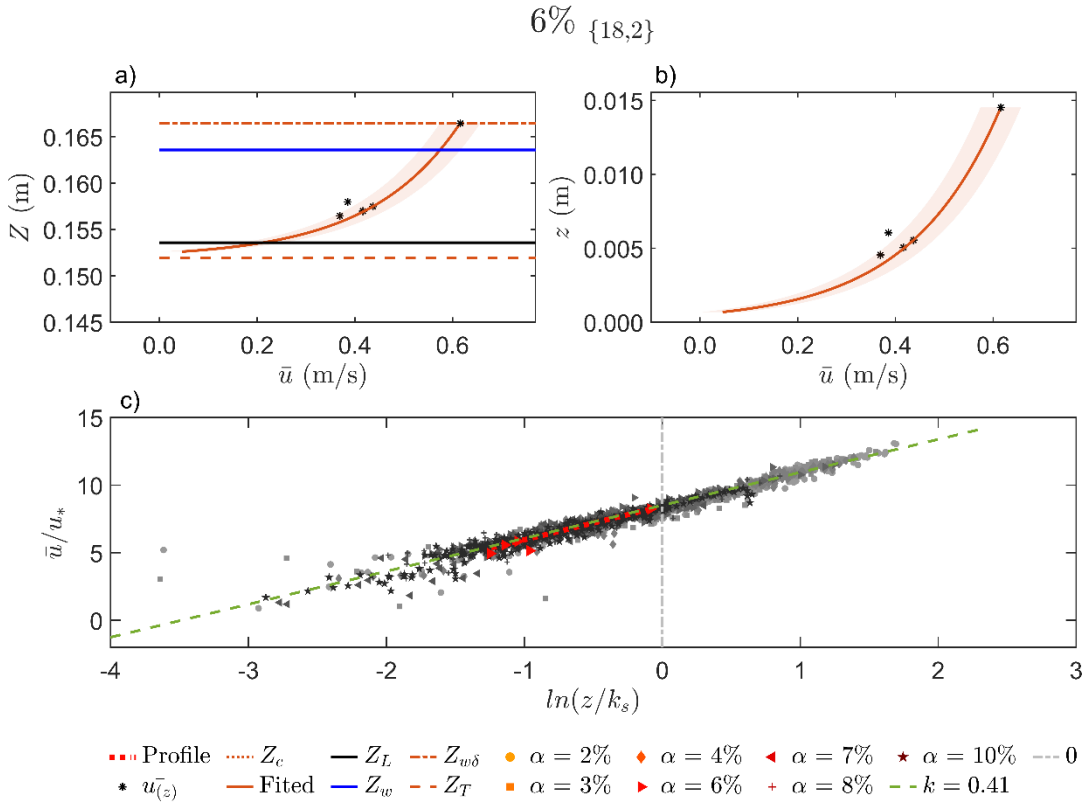

Figure B. 74. (a) Velocity profile as a function of water levels, (b) velocity profile as a function of water depths, and (c) dimensionless log profiles in the horizontal semi-log scale on a 6% flume slope.

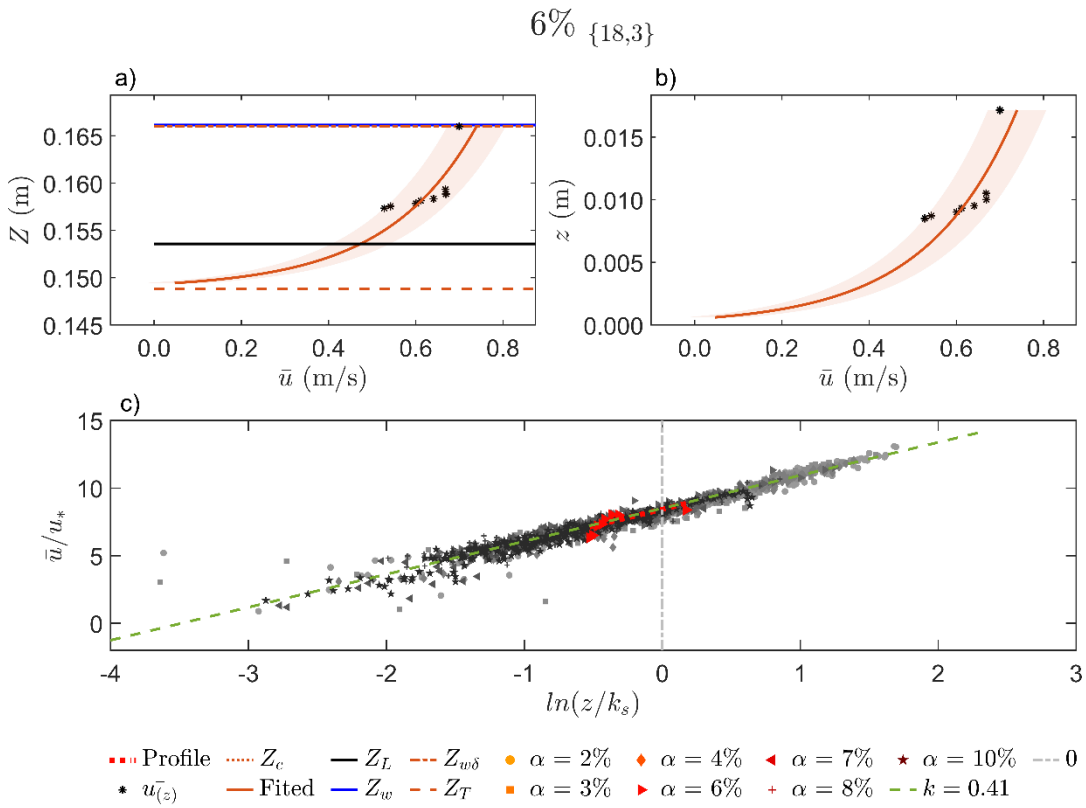

Figure B. 75. (a) Velocity profile as a function of water levels, (b) velocity profile as a function of water depths, and (c) dimensionless log profiles in the horizontal semi-log scale on a 6% flume slope.

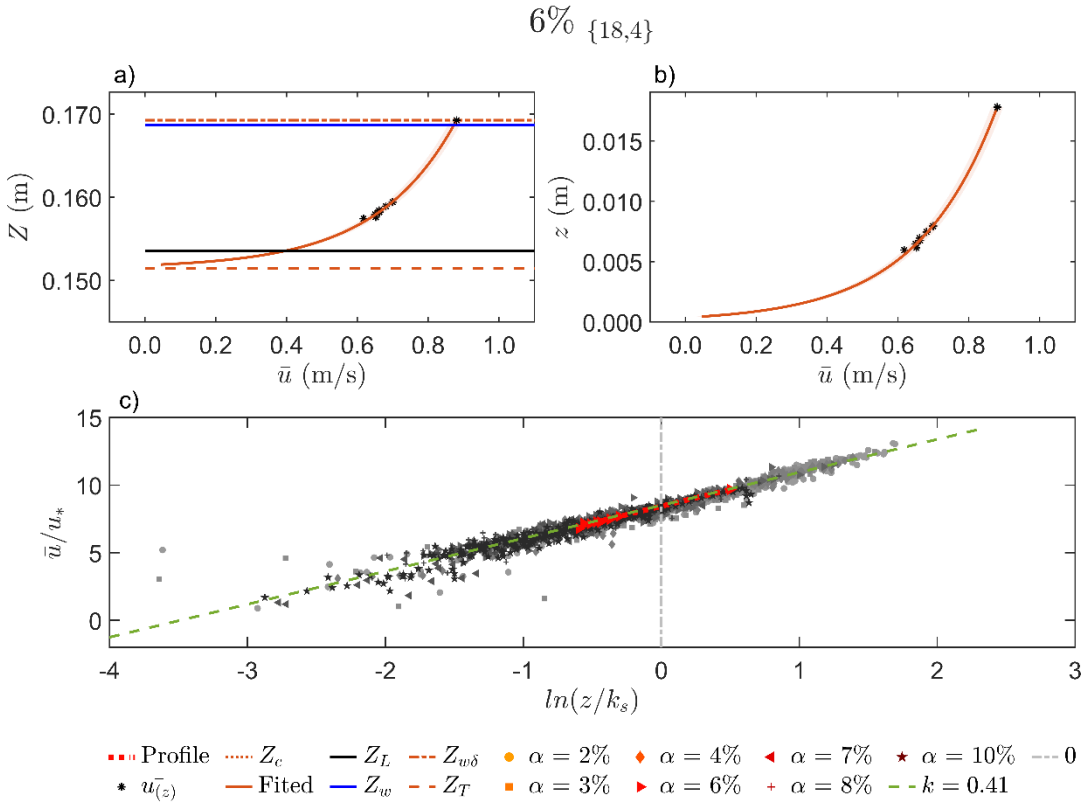

Figure B. 76. (a) Velocity profile as a function of water levels, (b) velocity profile as a function of water depths, and (c) dimensionless log profiles in the horizontal semi-log scale on a 6% flume slope.

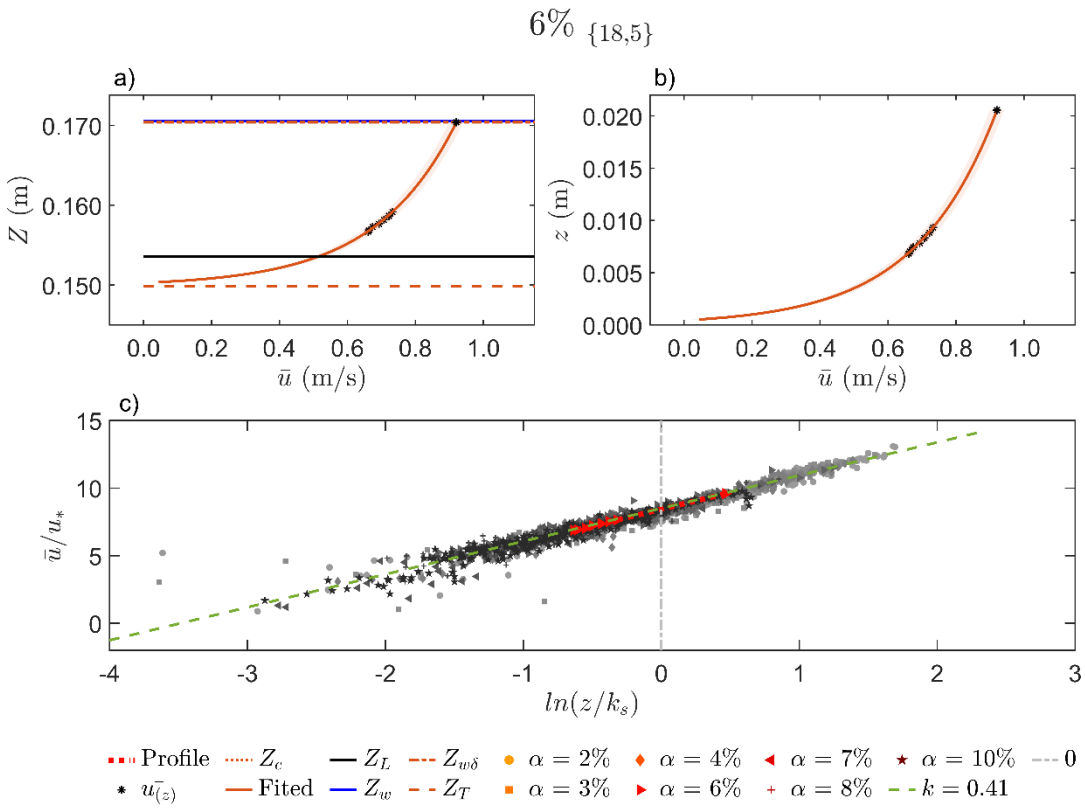

Figure B. 77. (a) Velocity profile as a function of water levels, (b) velocity profile as a function of water depths, and (c) dimensionless log profiles in the horizontal semi-log scale on a 6% flume slope.

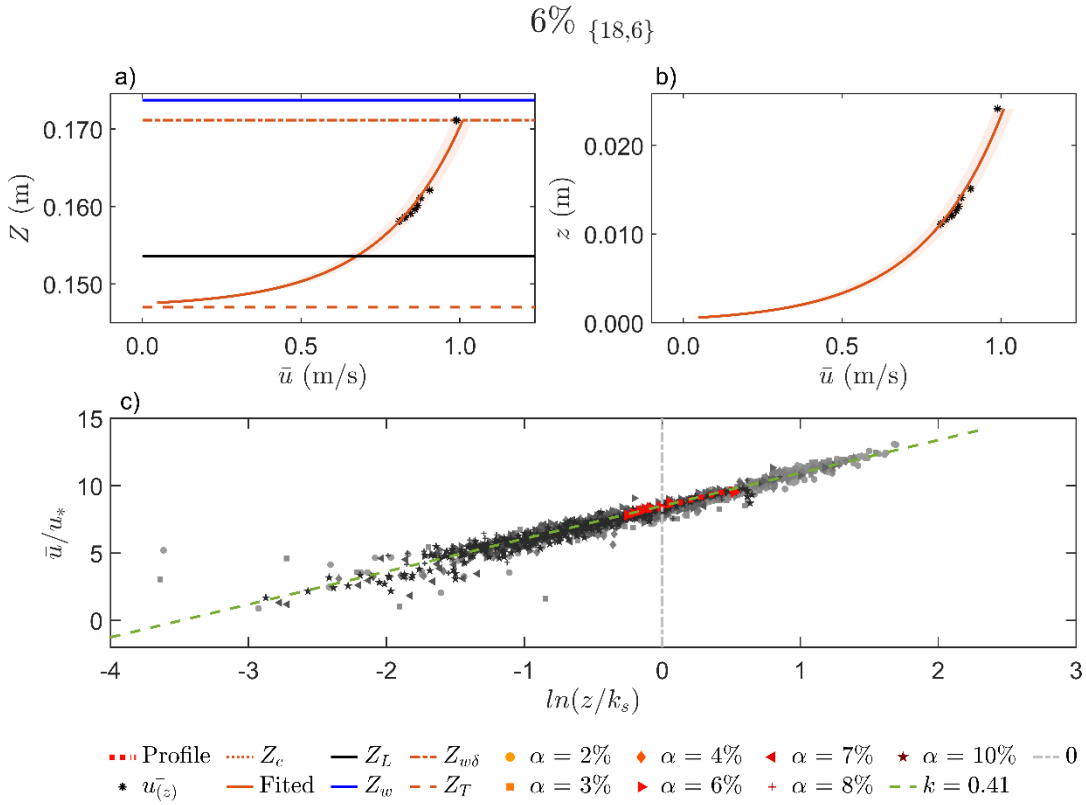

Figure B. 78. (a) Velocity profile as a function of water levels, (b) velocity profile as a function of water depths, and (c) dimensionless log profiles in the horizontal semi-log scale on a 6% flume slope.

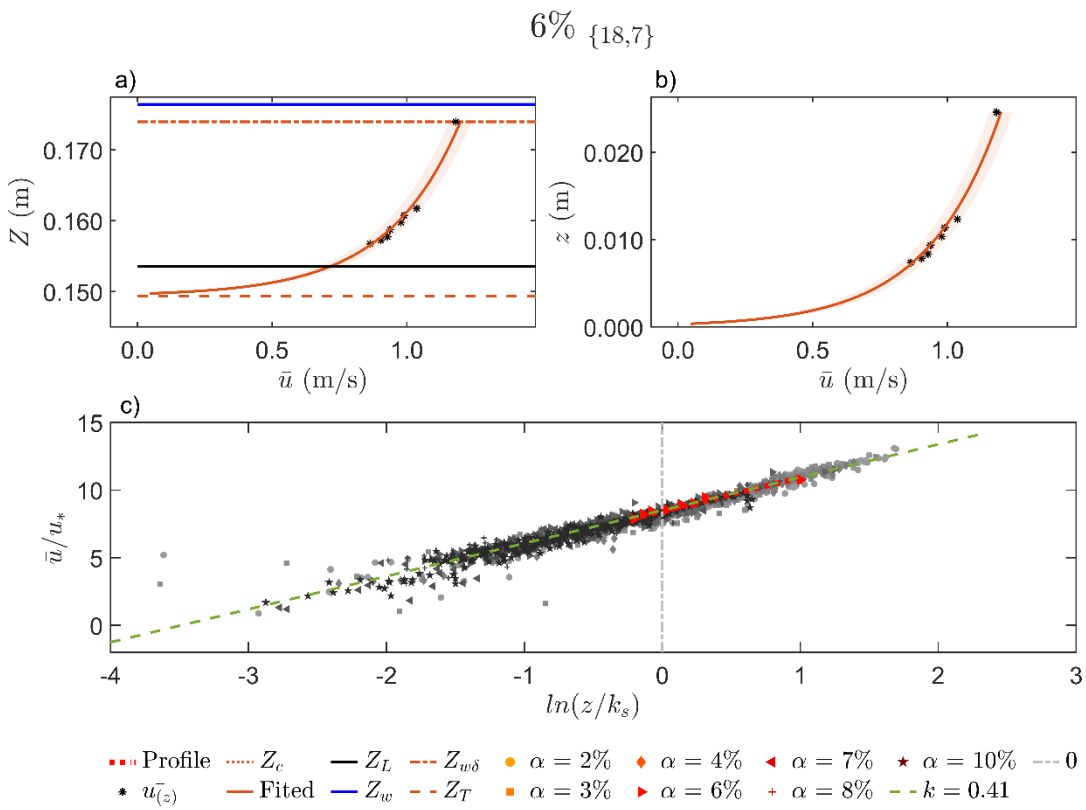

Figure B. 79. (a) Velocity profile as a function of water levels, (b) velocity profile as a function of water depths, and (c) dimensionless log profiles in the horizontal semi-log scale on a 6% flume slope.

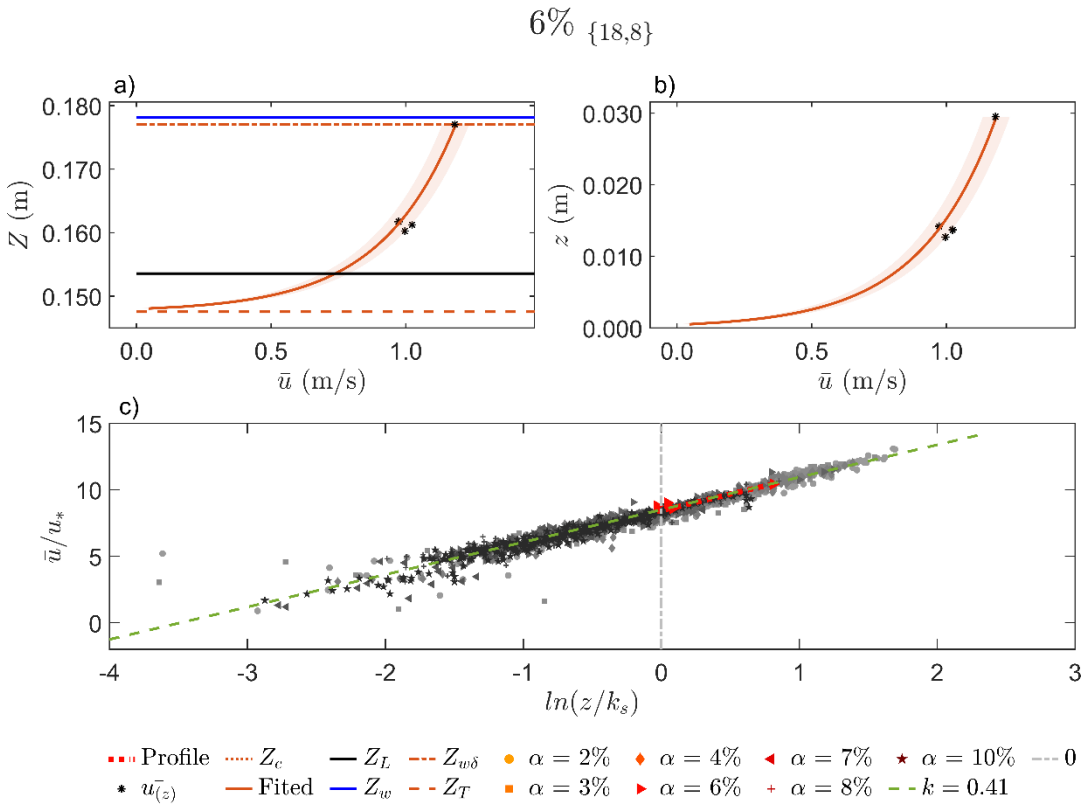

Figure B. 80. (a) Velocity profile as a function of water levels, (b) velocity profile as a function of water depths, and (c) dimensionless log profiles in the horizontal semi-log scale on a 6% flume slope.

B.1.3.e. 7% flume slope

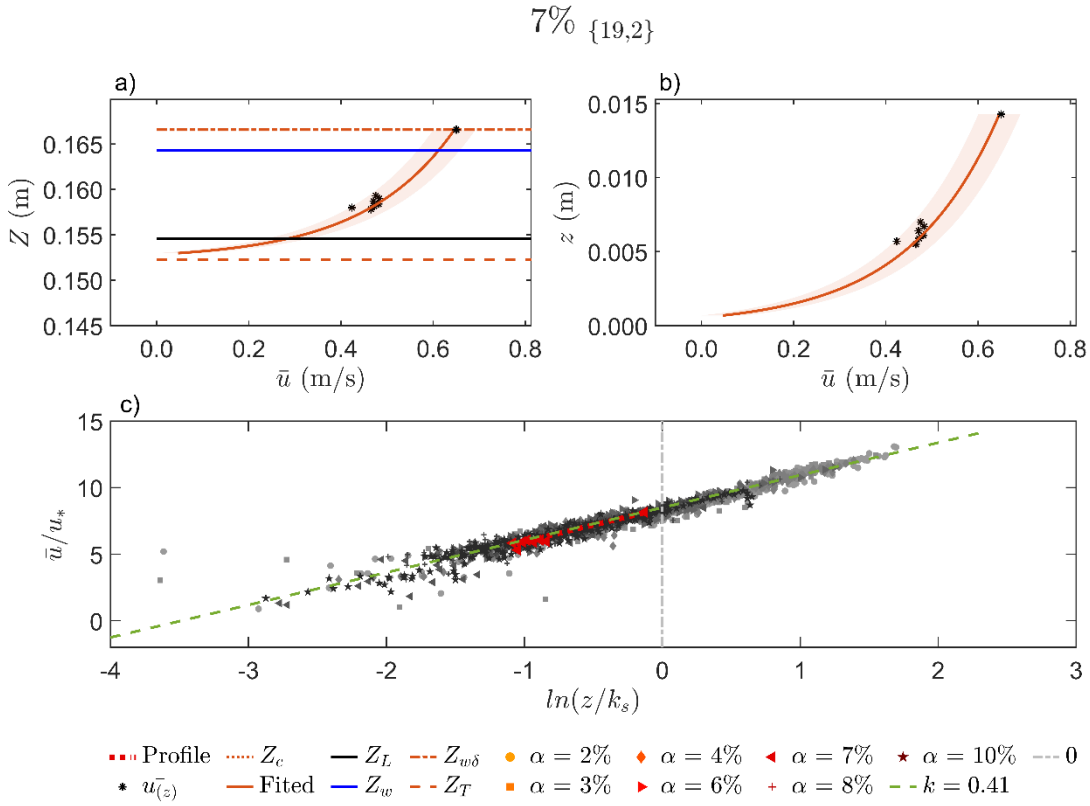

Figure B. 81. (a) Velocity profile as a function of water levels, (b) velocity profile as a function of water depths, and (c) dimensionless log profiles in the horizontal semi-log scale on a 7% flume slope.

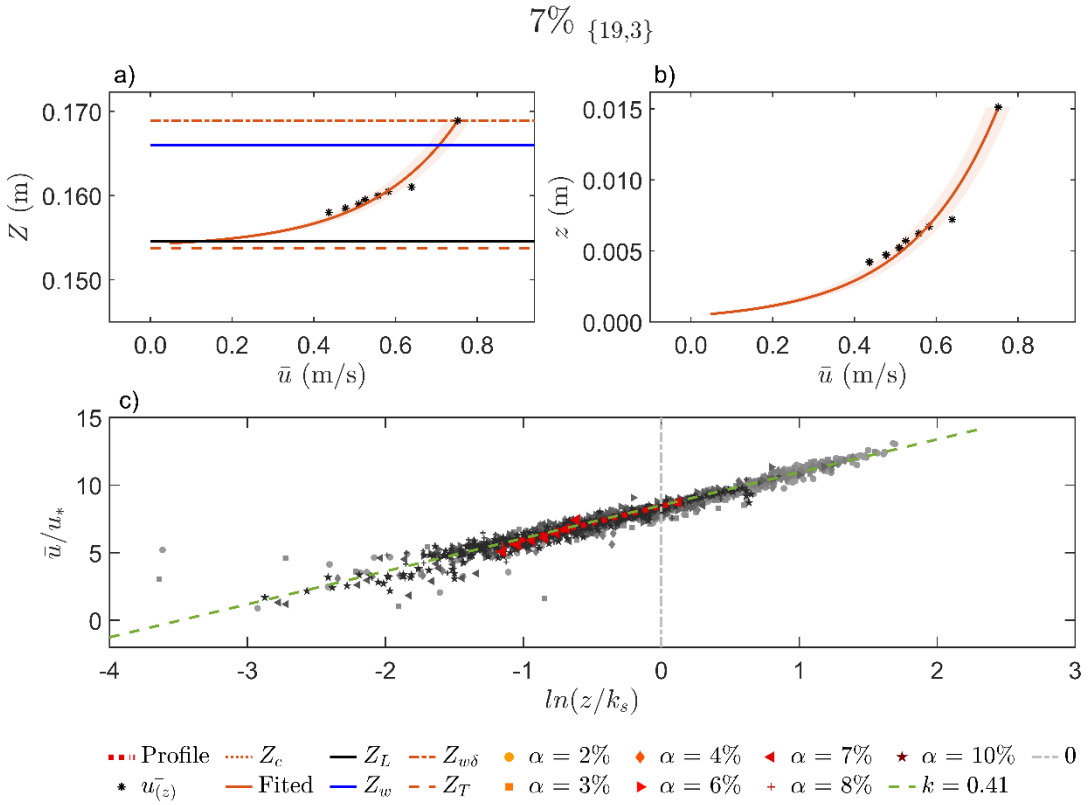

Figure B. 82. (a) Velocity profile as a function of water levels, (b) velocity profile as a function of water depths, and (c) dimensionless log profiles in the horizontal semi-log scale on a 7% flume slope.

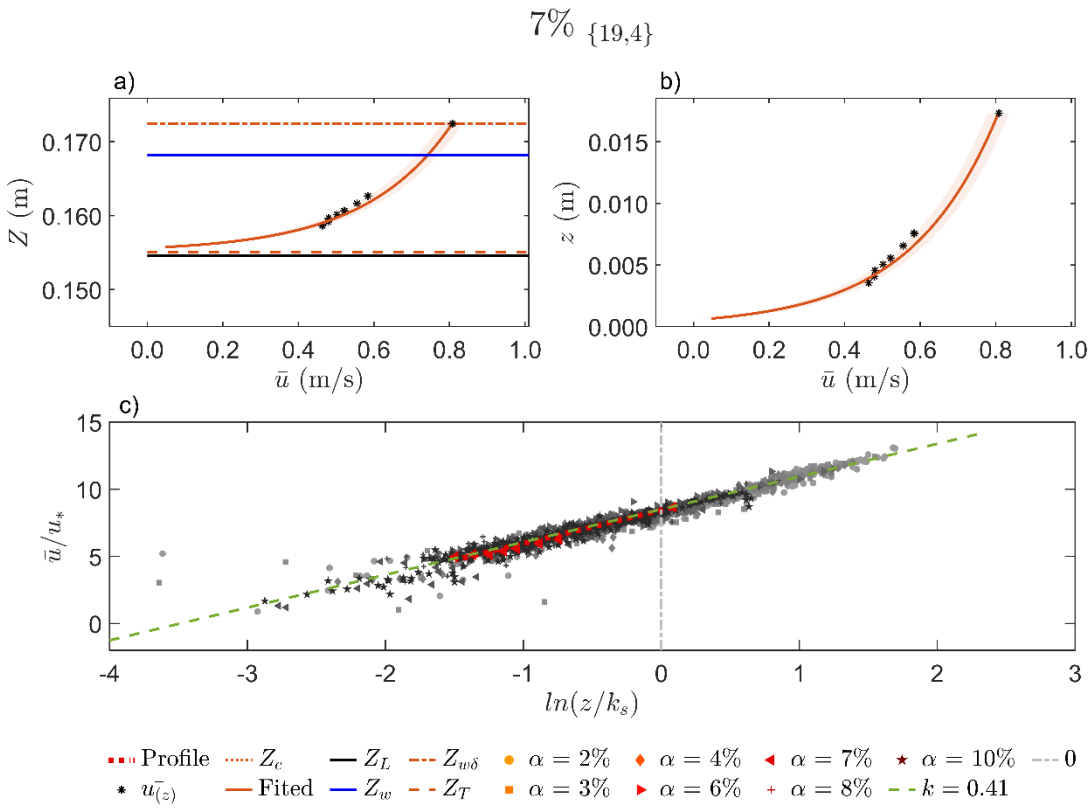

Figure B. 83. (a) Velocity profile as a function of water levels, (b) velocity profile as a function of water depths, and (c) dimensionless log profiles in the horizontal semi-log scale on a 7% flume slope.

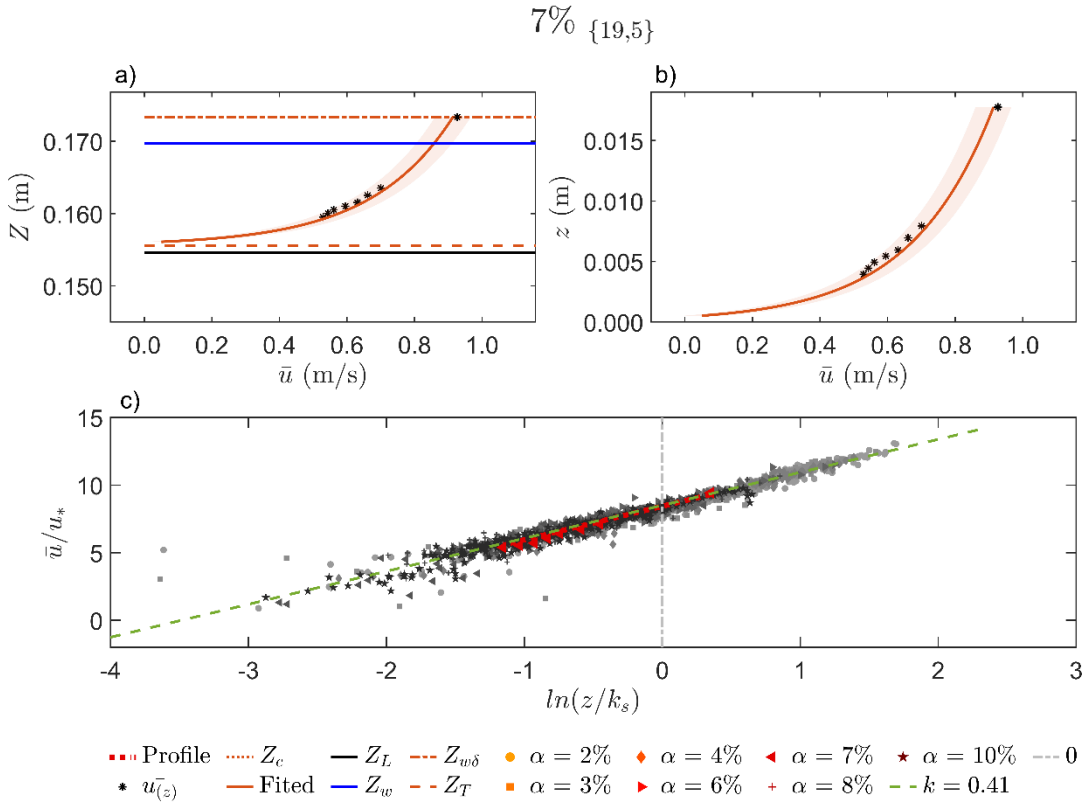

Figure B. 84. (a) Velocity profile as a function of water levels, (b) velocity profile as a function of water depths, and (c) dimensionless log profiles in the horizontal semi-log scale on a 7% flume slope.

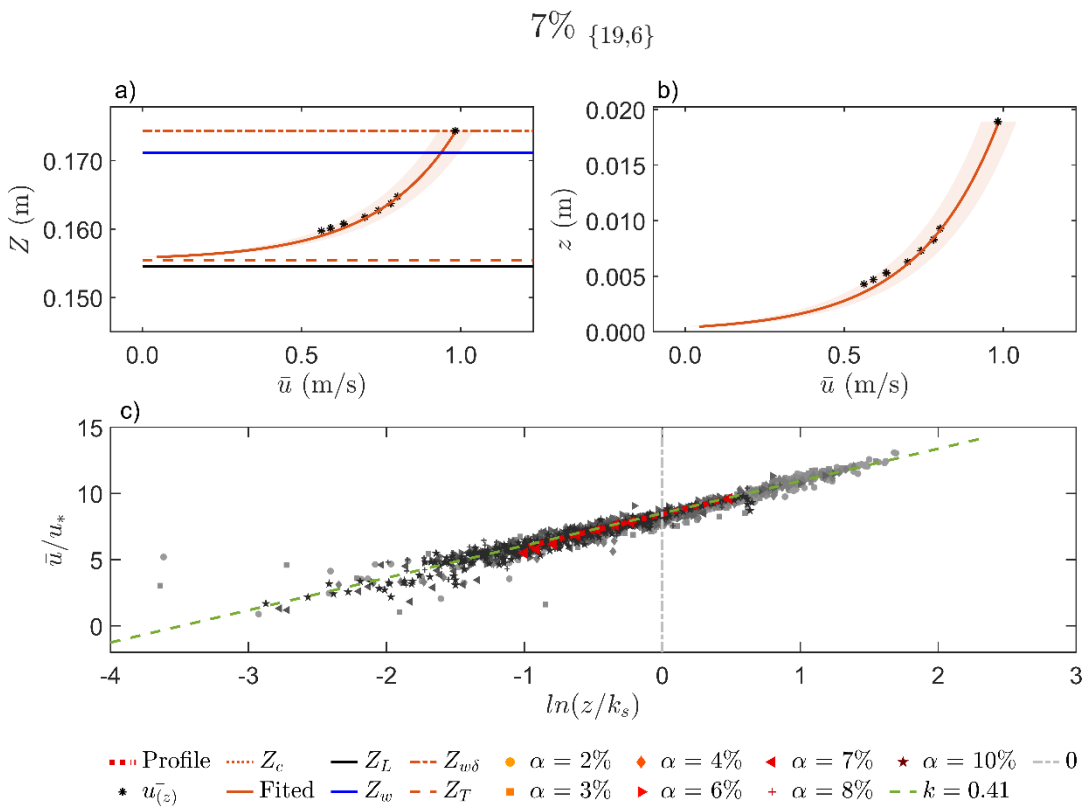

Figure B. 85. (a) Velocity profile as a function of water levels, (b) velocity profile as a function of water depths, and (c) dimensionless log profiles in the horizontal semi-log scale on a 7% flume slope.

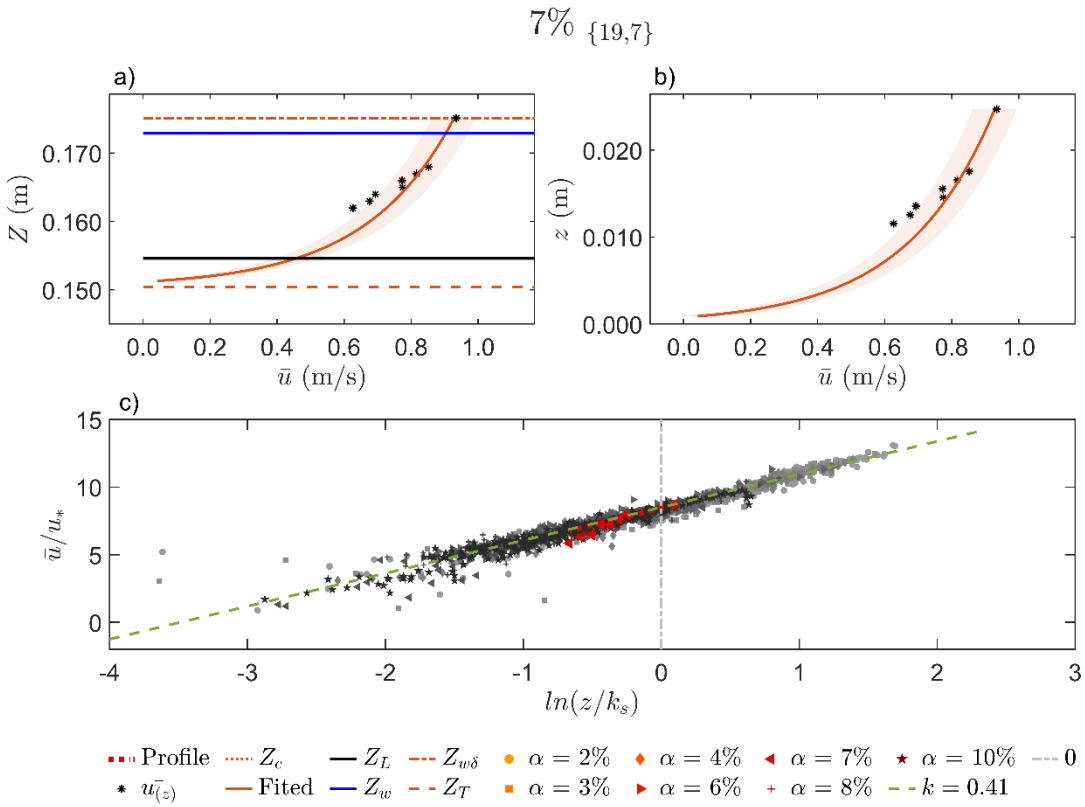

Figure B. 86. (a) Velocity profile as a function of water levels, (b) velocity profile as a function of water depths, and (c) dimensionless log profiles in the horizontal semi-log scale on a 7% flume slope.

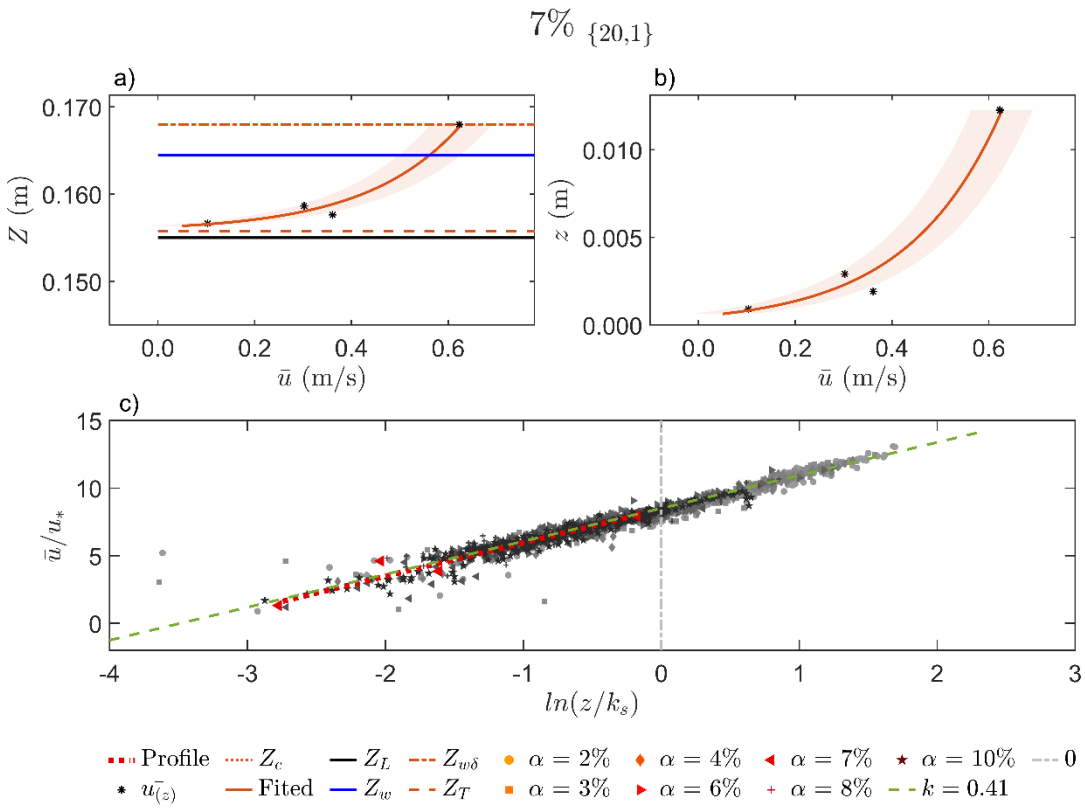

Figure B. 87. (a) Velocity profile as a function of water levels, (b) velocity profile as a function of water depths, and (c) dimensionless log profiles in the horizontal semi-log scale on a 7% flume slope.

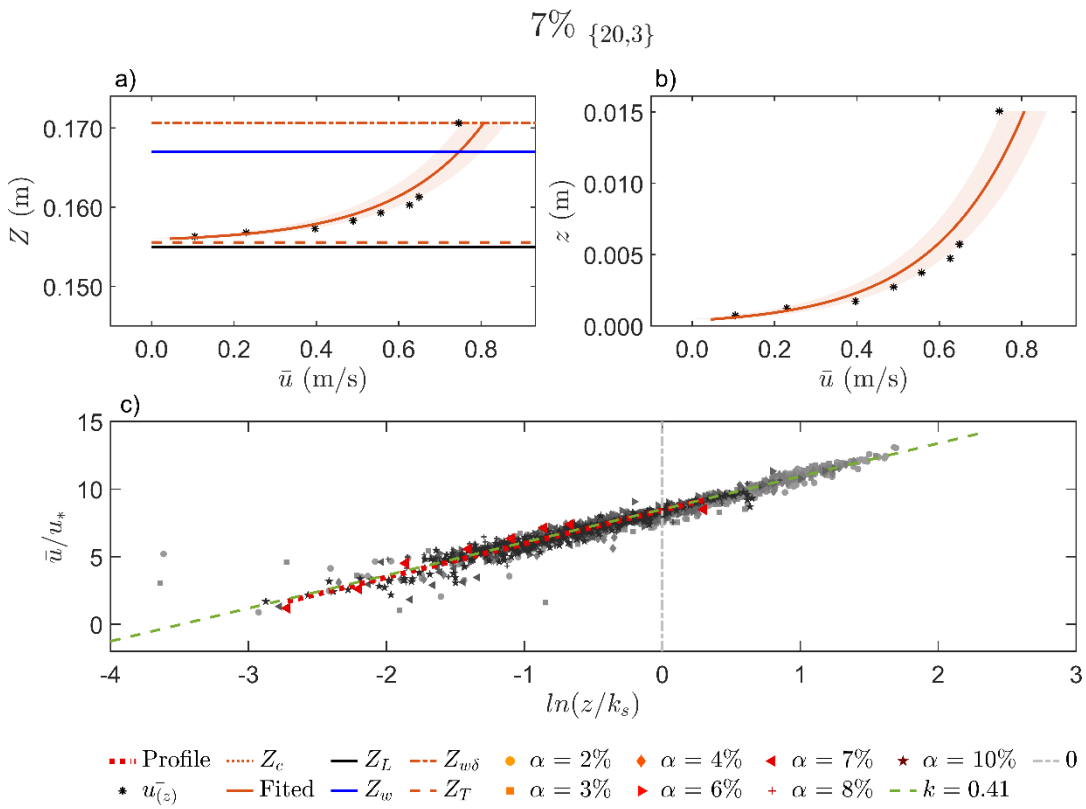

Figure B. 88. (a) Velocity profile as a function of water levels, (b) velocity profile as a function of water depths, and (c) dimensionless log profiles in the horizontal semi-log scale on a 7% flume slope.

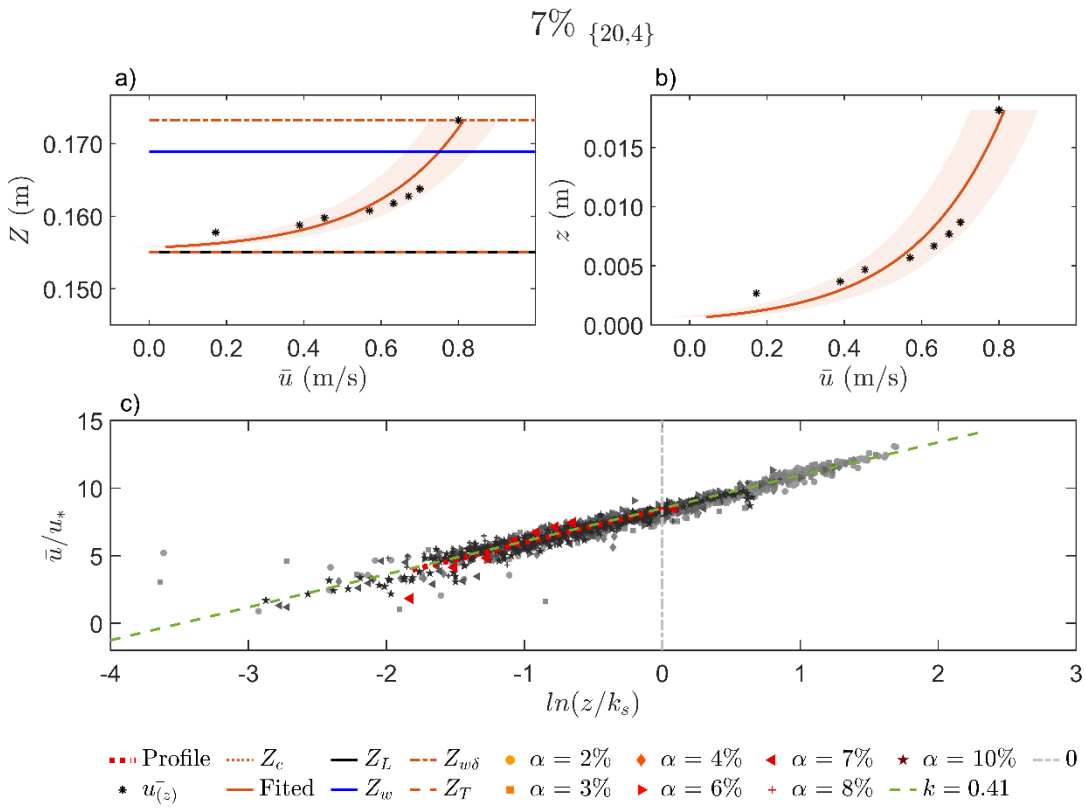

Figure B. 89. (a) Velocity profile as a function of water levels, (b) velocity profile as a function of water depths, and (c) dimensionless log profiles in the horizontal semi-log scale on a 7% flume slope.

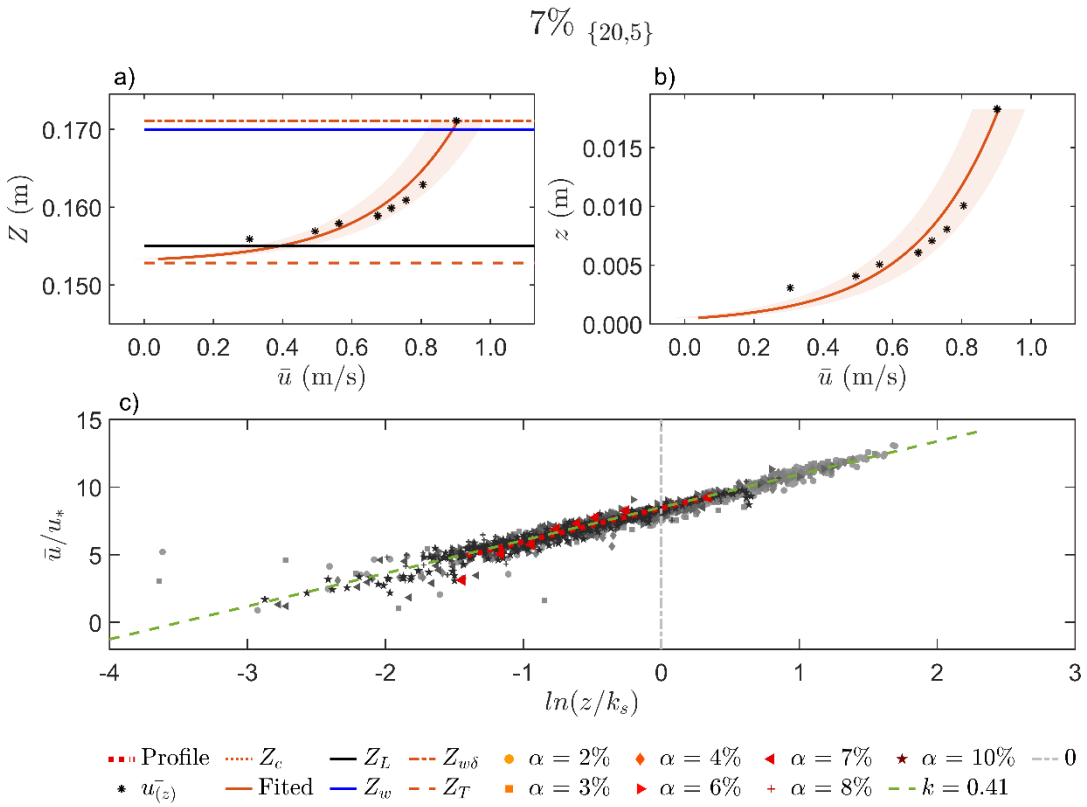

Figure B. 90. (a) Velocity profile as a function of water levels, (b) velocity profile as a function of water depths, and (c) dimensionless log profiles in the horizontal semi-log scale on a 7% flume slope.

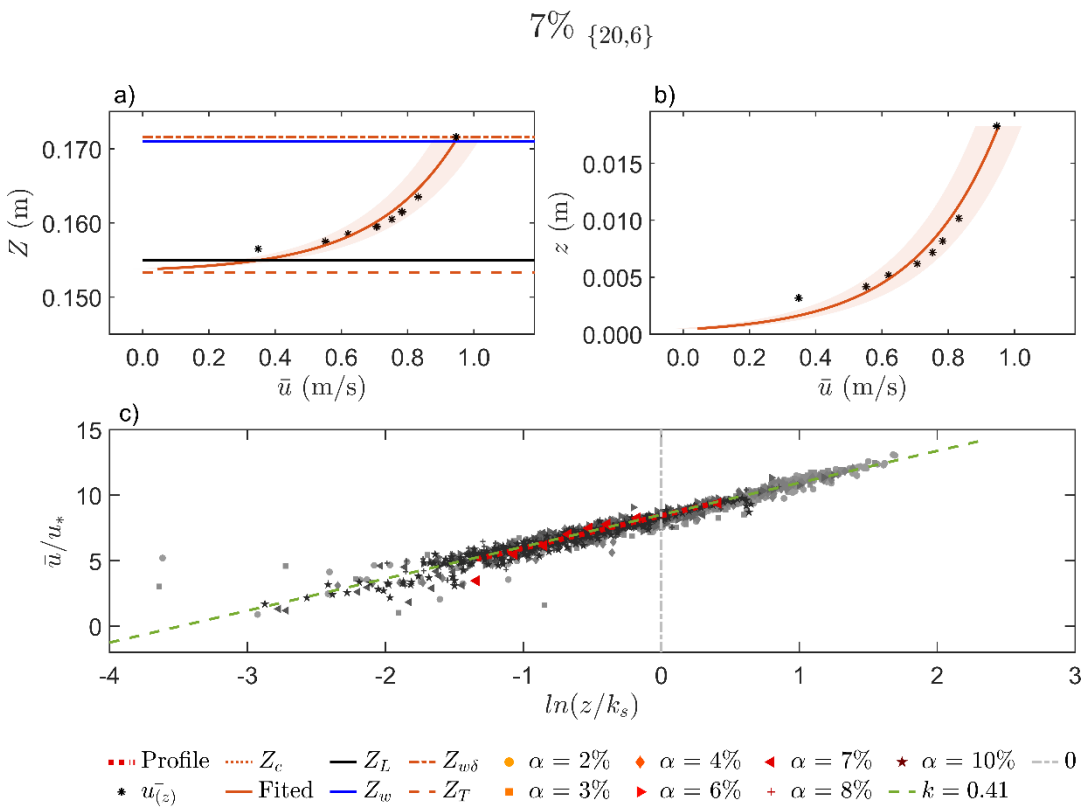

Figure B. 91. (a) Velocity profile as a function of water levels, (b) velocity profile as a function of water depths, and (c) dimensionless log profiles in the horizontal semi-log scale on a 7% flume slope.

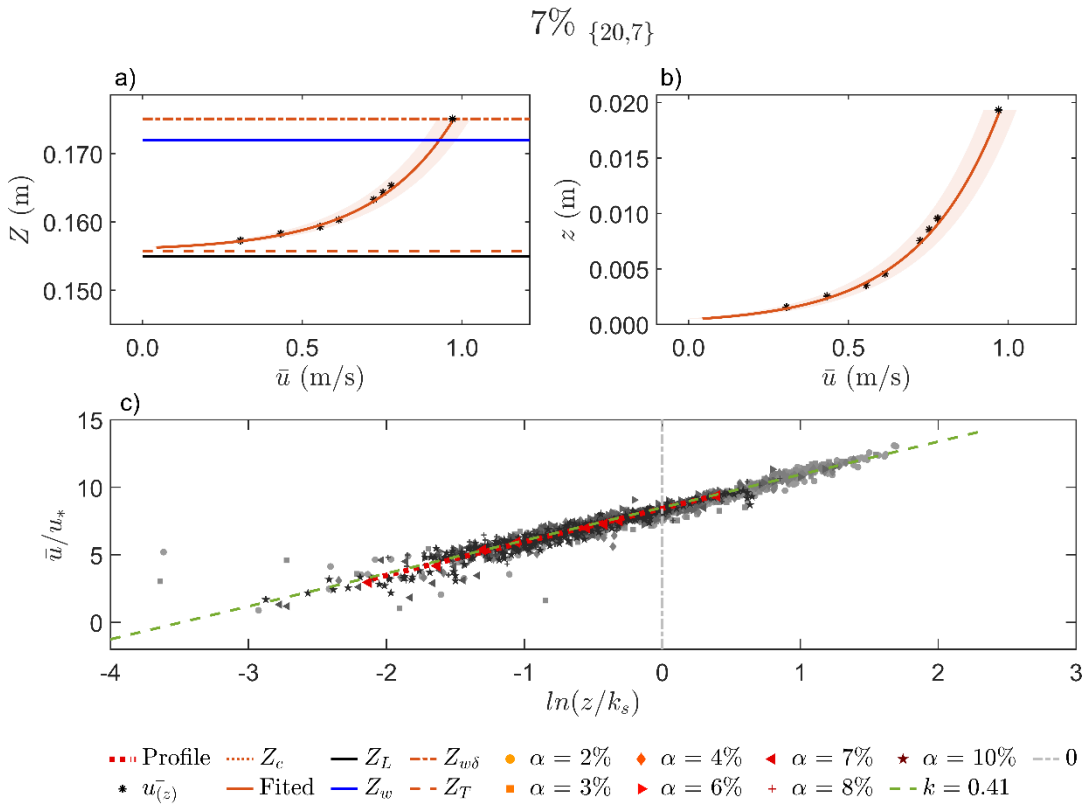

Figure B. 92. (a) Velocity profile as a function of water levels, (b) velocity profile as a function of water depths, and (c) dimensionless log profiles in the horizontal semi-log scale on a 7% flume slope.

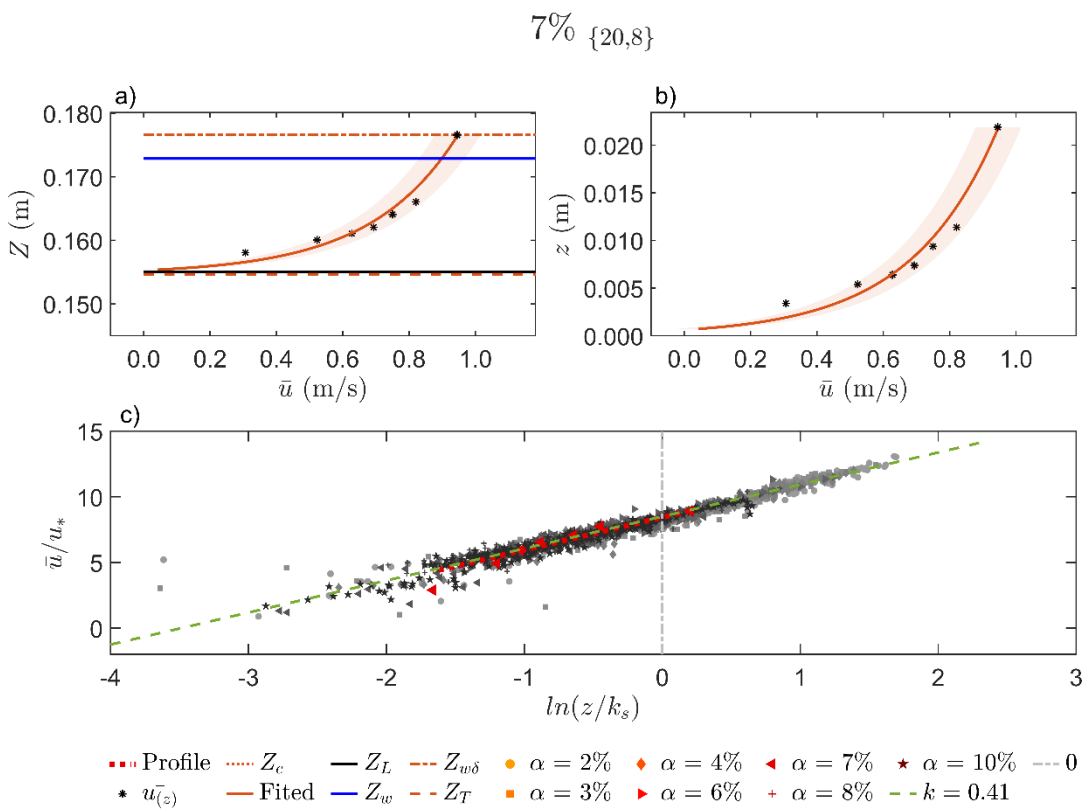

Figure B. 93. (a) Velocity profile as a function of water levels, (b) velocity profile as a function of water depths, and (c) dimensionless log profiles in the horizontal semi-log scale on a 7% flume slope.

B.1.3.f. 8% flume slope

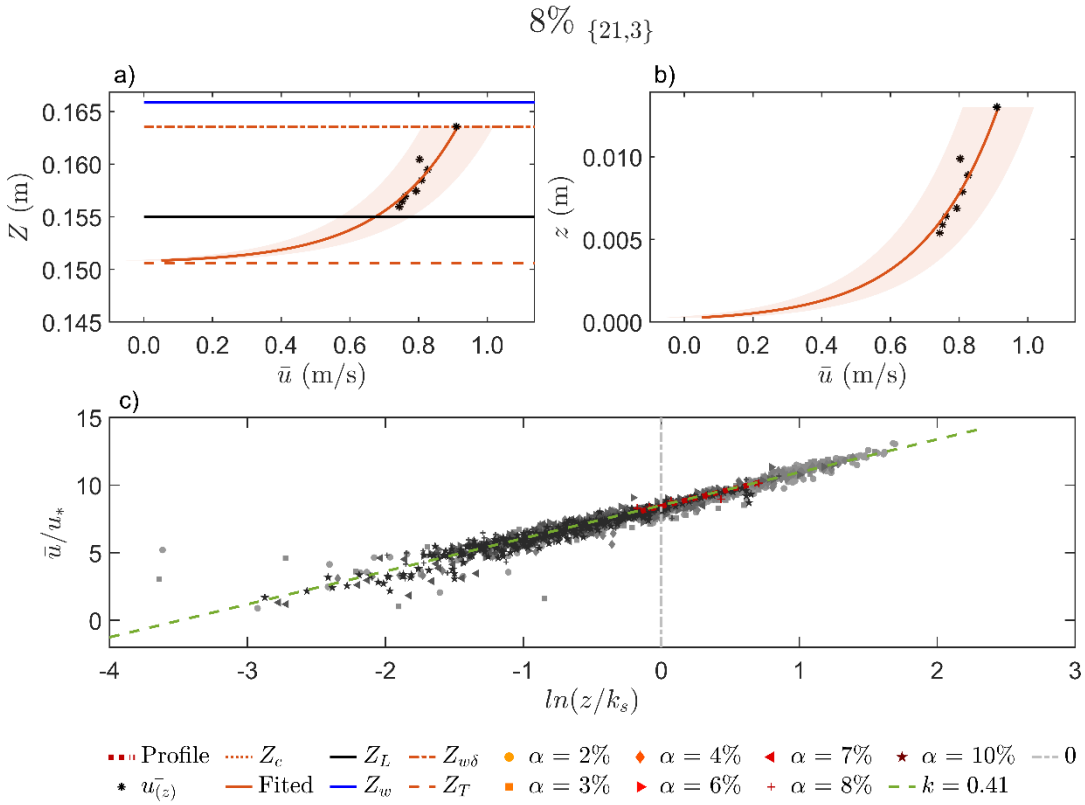

Figure B. 94. (a) Velocity profile as a function of water levels, (b) velocity profile as a function of water depths, and (c) dimensionless log profiles in the horizontal semi-log scale on a 8% flume slope.

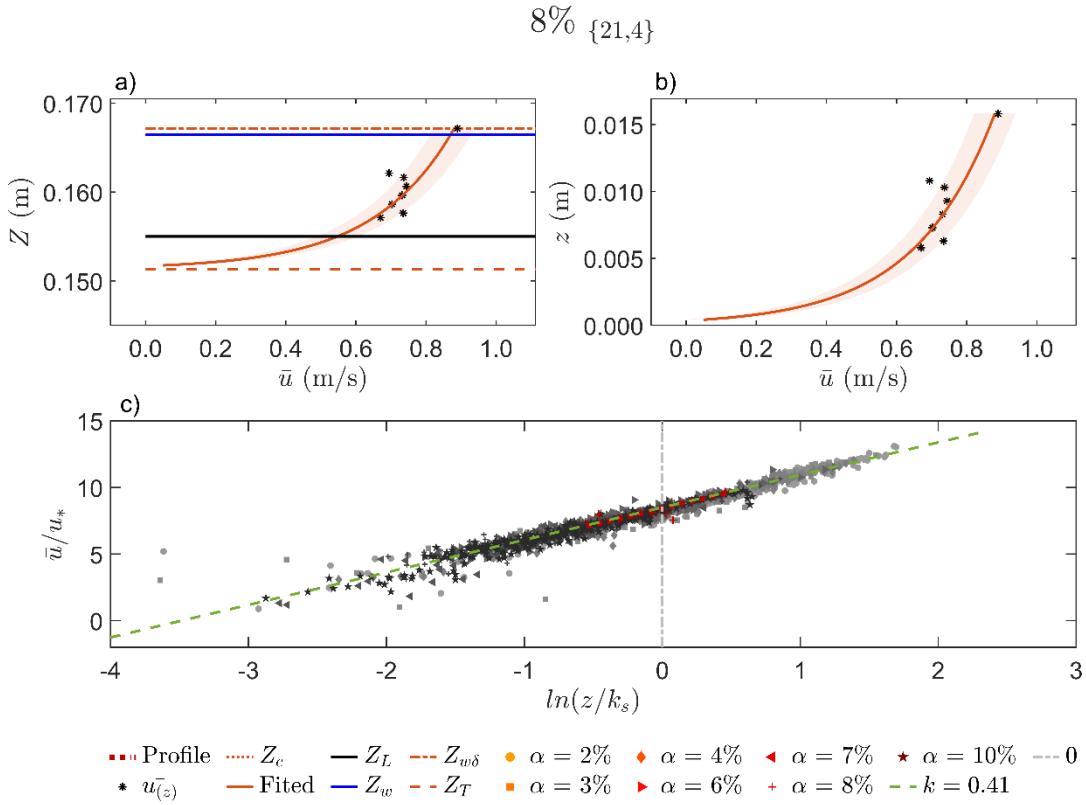

Figure B. 95. (a) Velocity profile as a function of water levels, (b) velocity profile as a function of water depths, and (c) dimensionless log profiles in the horizontal semi-log scale on a 8% flume slope.

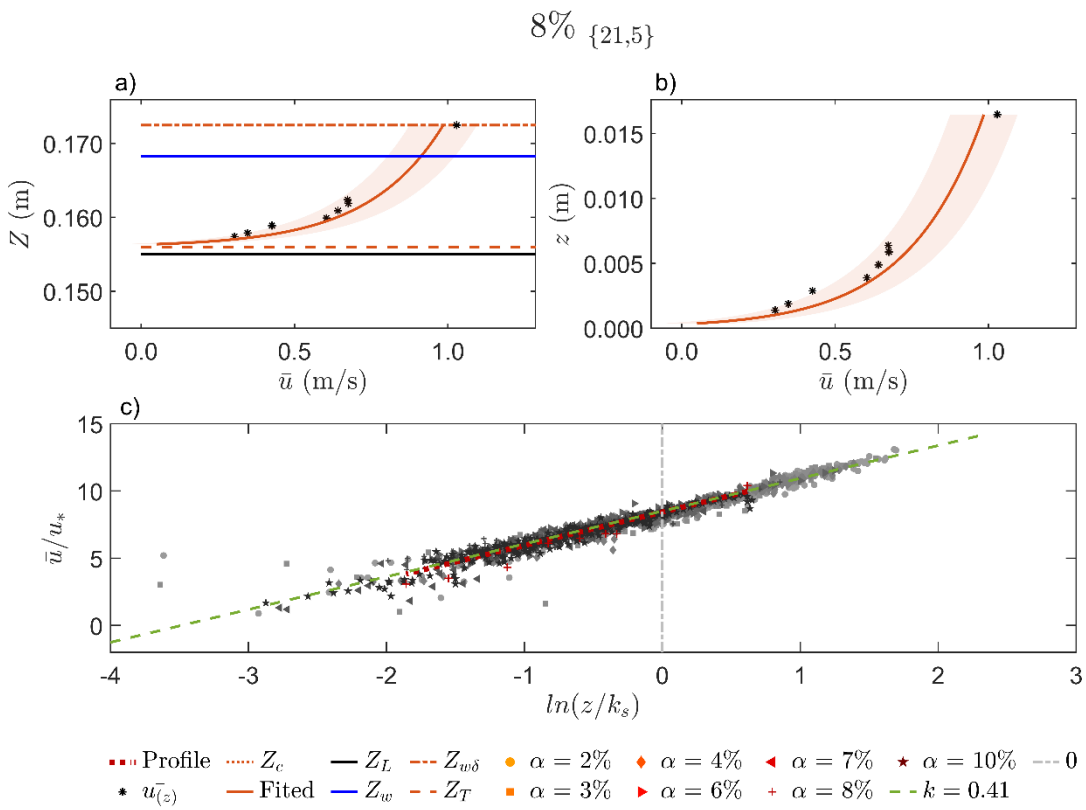

Figure B. 96. (a) Velocity profile as a function of water levels, (b) velocity profile as a function of water depths, and (c) dimensionless log profiles in the horizontal semi-log scale on a 8% flume slope.

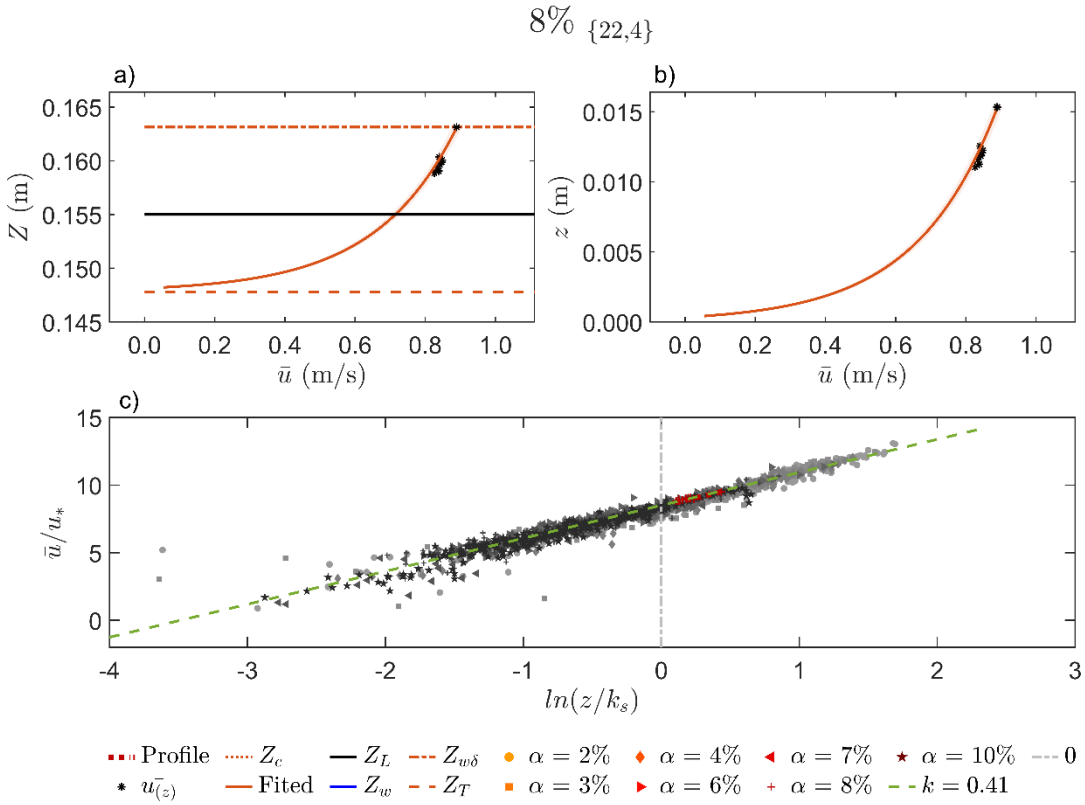

Figure B. 97. (a) Velocity profile as a function of water levels, (b) velocity profile as a function of water depths, and (c) dimensionless log profiles in the horizontal semi-log scale on a 8% flume slope.

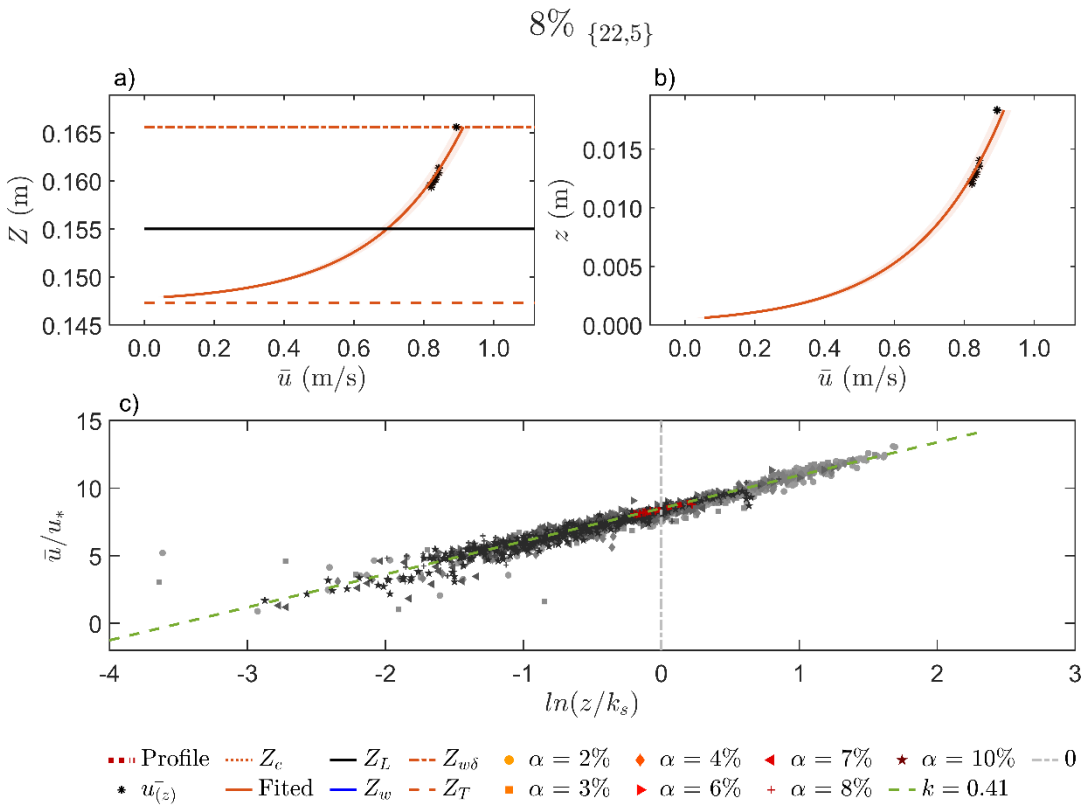

Figure B. 98. (a) Velocity profile as a function of water levels, (b) velocity profile as a function of water depths, and (c) dimensionless log profiles in the horizontal semi-log scale on a 8% flume slope.

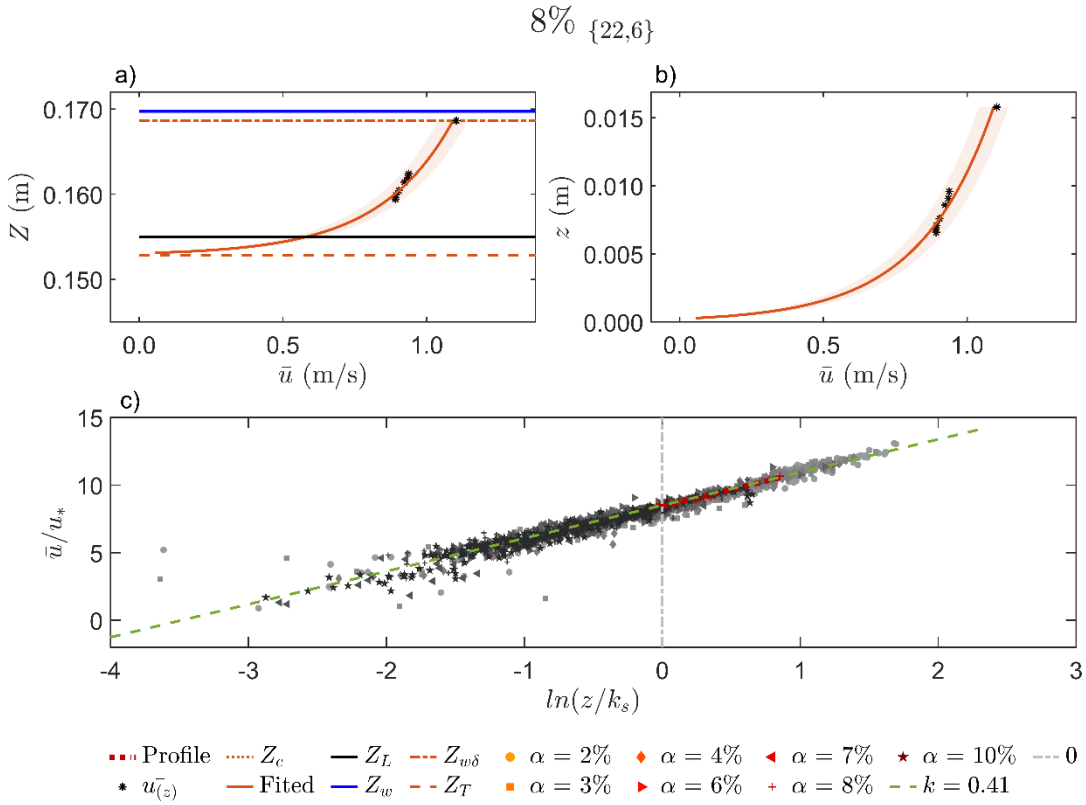

Figure B. 99. (a) Velocity profile as a function of water levels, (b) velocity profile as a function of water depths, and (c) dimensionless log profiles in the horizontal semi-log scale on a 8% flume slope.

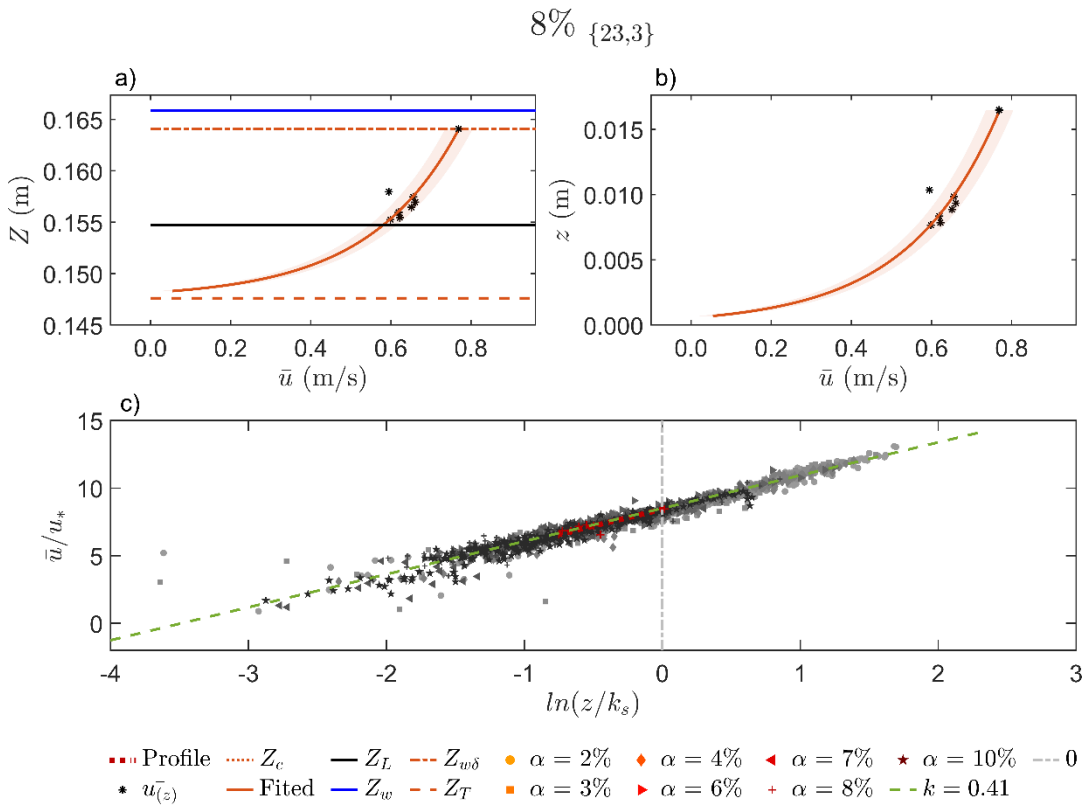

Figure B. 100. (a) Velocity profile as a function of water levels, (b) velocity profile as a function of water depths, and (c) dimensionless log profiles in the horizontal semi-log scale on a 8% flume slope.

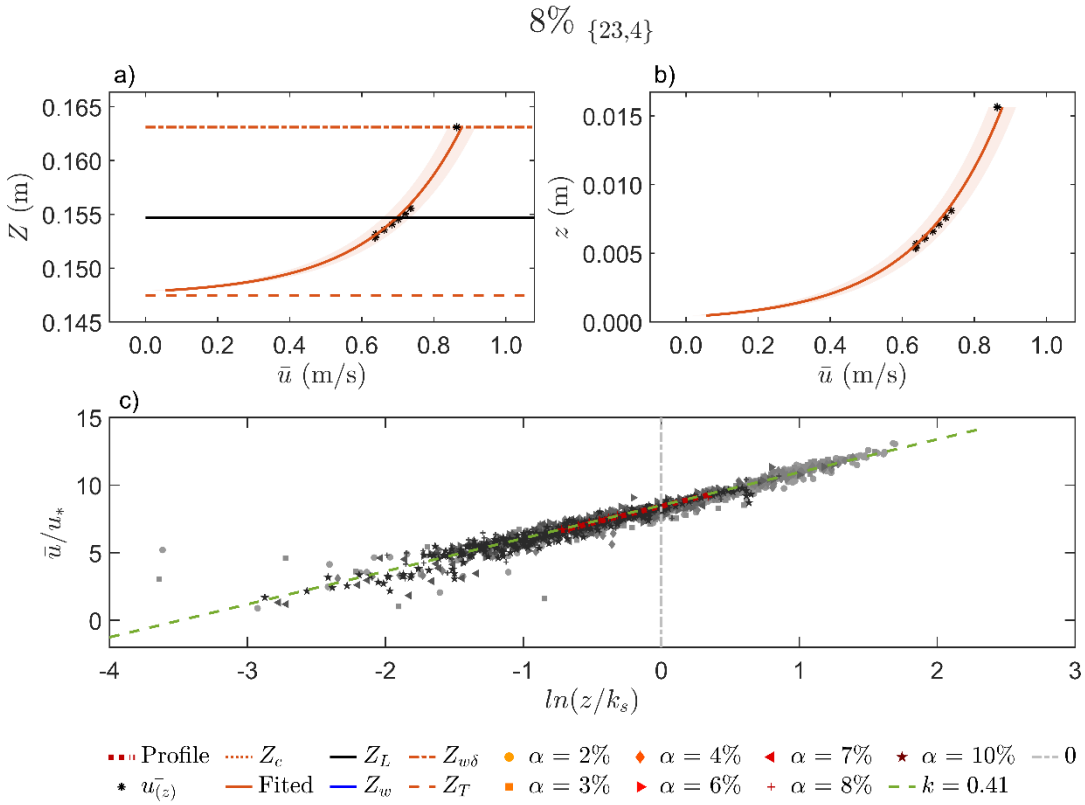

Figure B. 101. (a) Velocity profile as a function of water levels, (b) velocity profile as a function of water depths, and (c) dimensionless log profiles in the horizontal semi-log scale on a 8% flume slope.

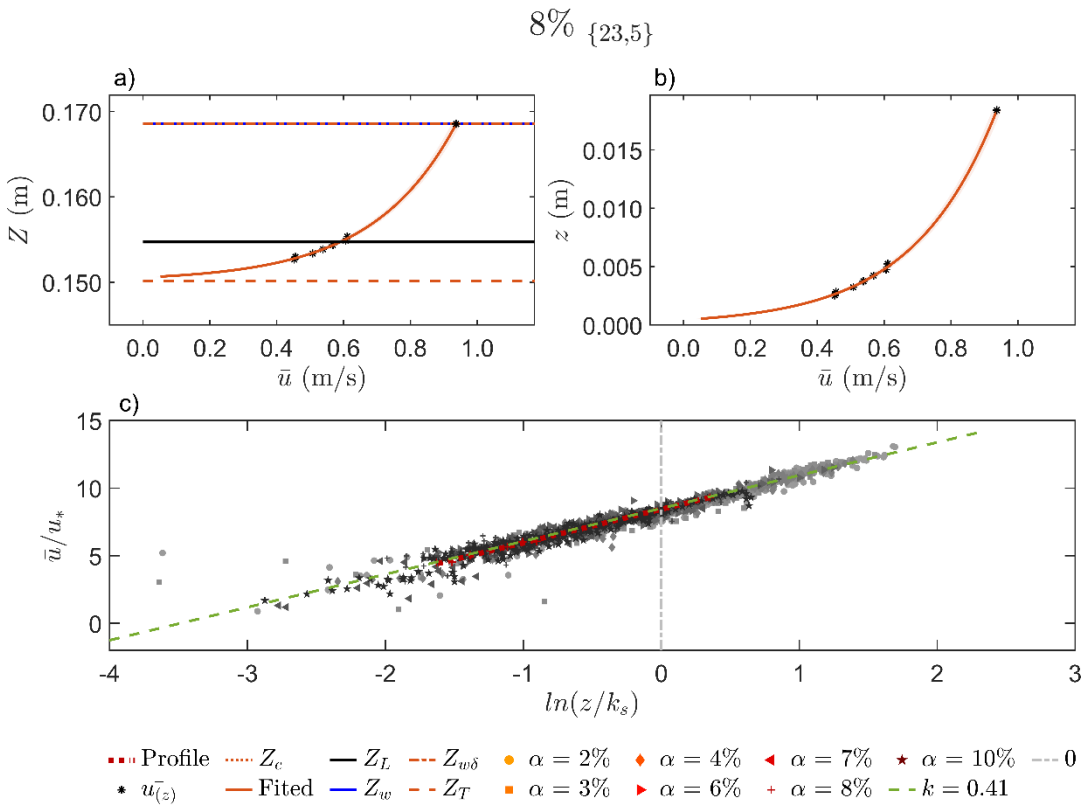

Figure B. 102. (a) Velocity profile as a function of water levels, (b) velocity profile as a function of water depths, and (c) dimensionless log profiles in the horizontal semi-log scale on a 8% flume slope.

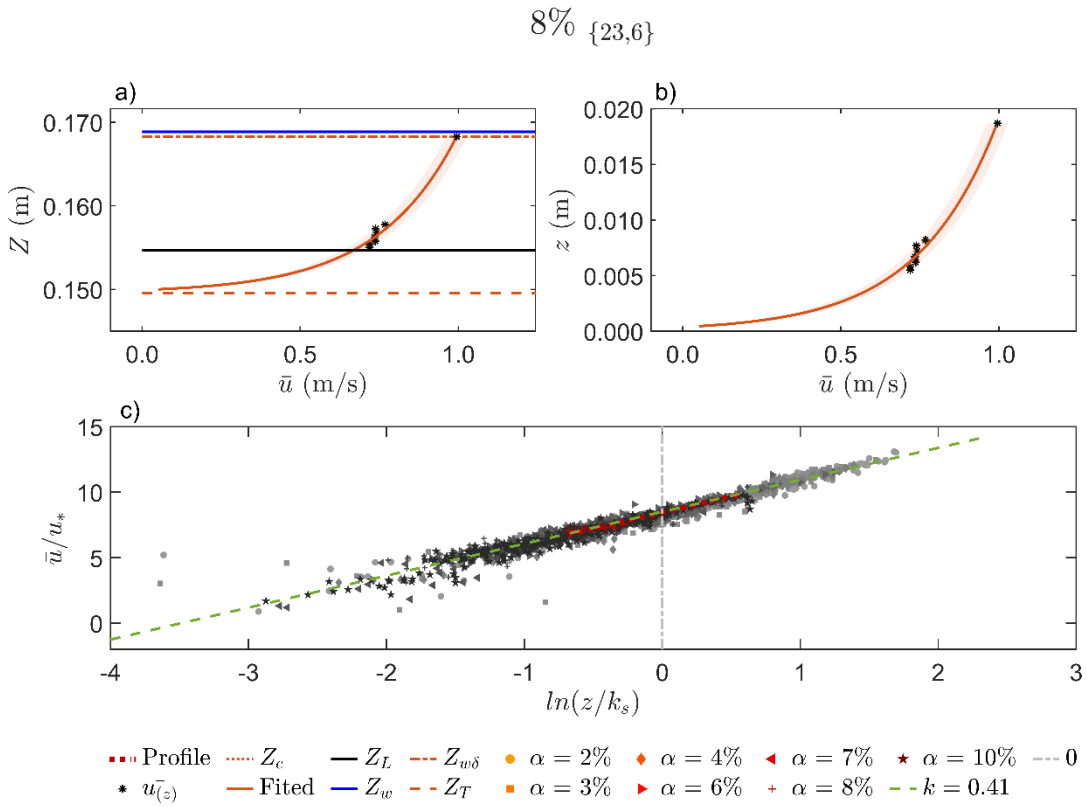

Figure B. 103. (a) Velocity profile as a function of water levels, (b) velocity profile as a function of water depths, and (c) dimensionless log profiles in the horizontal semi-log scale on a 8% flume slope.

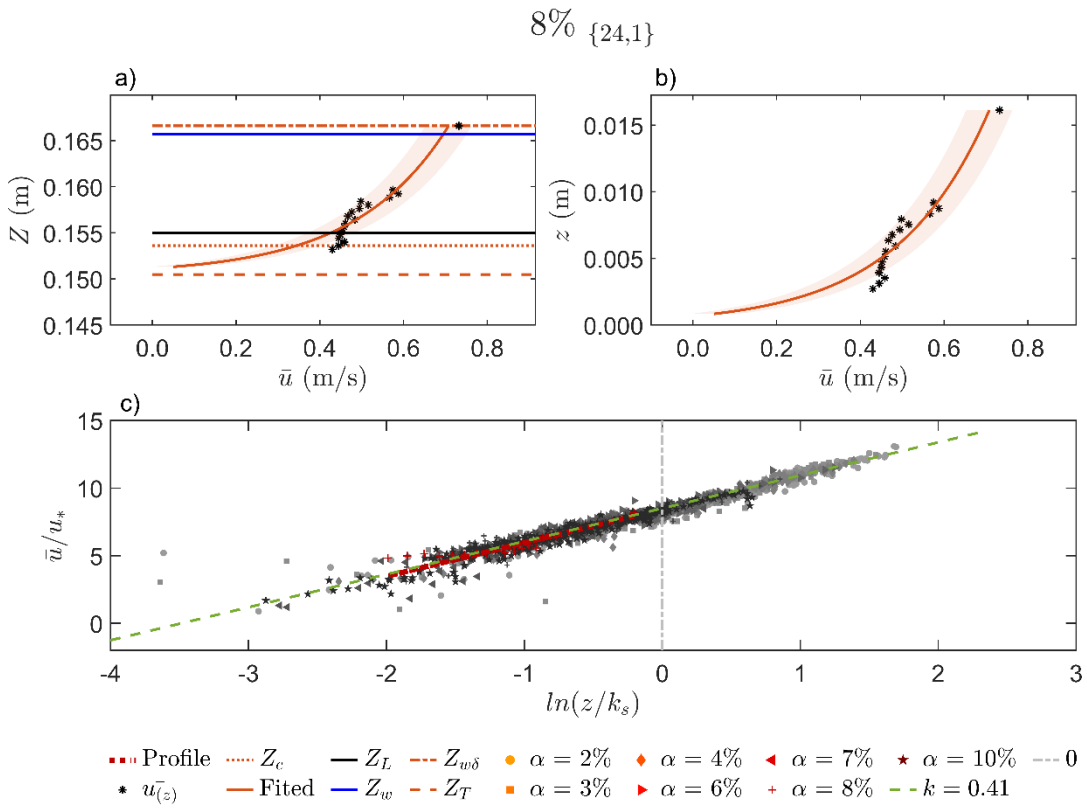

Figure B. 104. (a) Velocity profile as a function of water levels, (b) velocity profile as a function of water depths, and (c) dimensionless log profiles in the horizontal semi-log scale on a 8% flume slope.

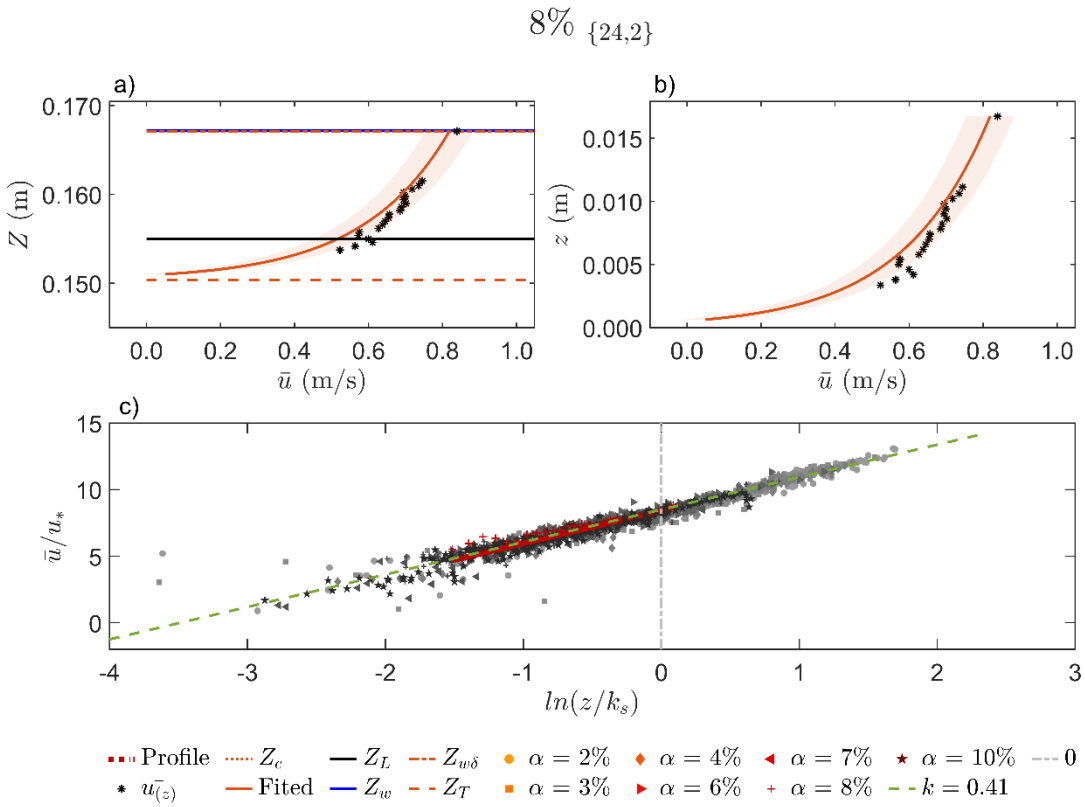

Figure B. 105. (a) Velocity profile as a function of water levels, (b) velocity profile as a function of water depths, and (c) dimensionless log profiles in the horizontal semi-log scale on a 8% flume slope.

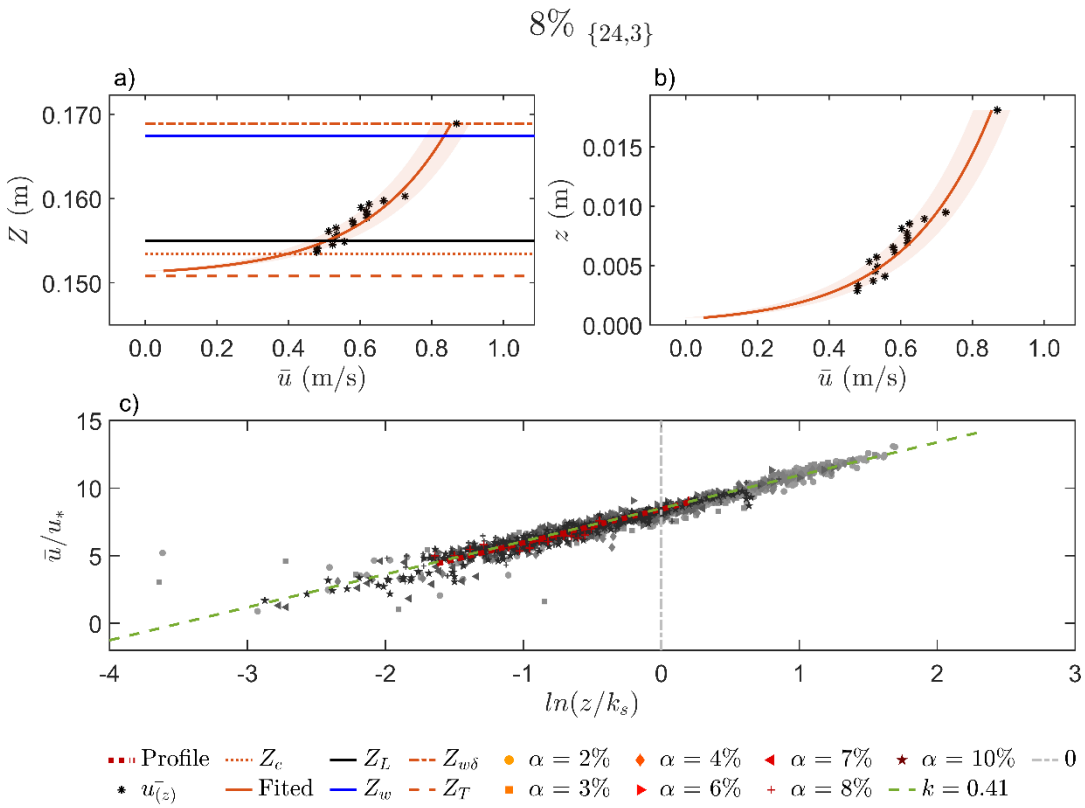

Figure B. 106. (a) Velocity profile as a function of water levels, (b) velocity profile as a function of water depths, and (c) dimensionless log profiles in the horizontal semi-log scale on a 8% flume slope.

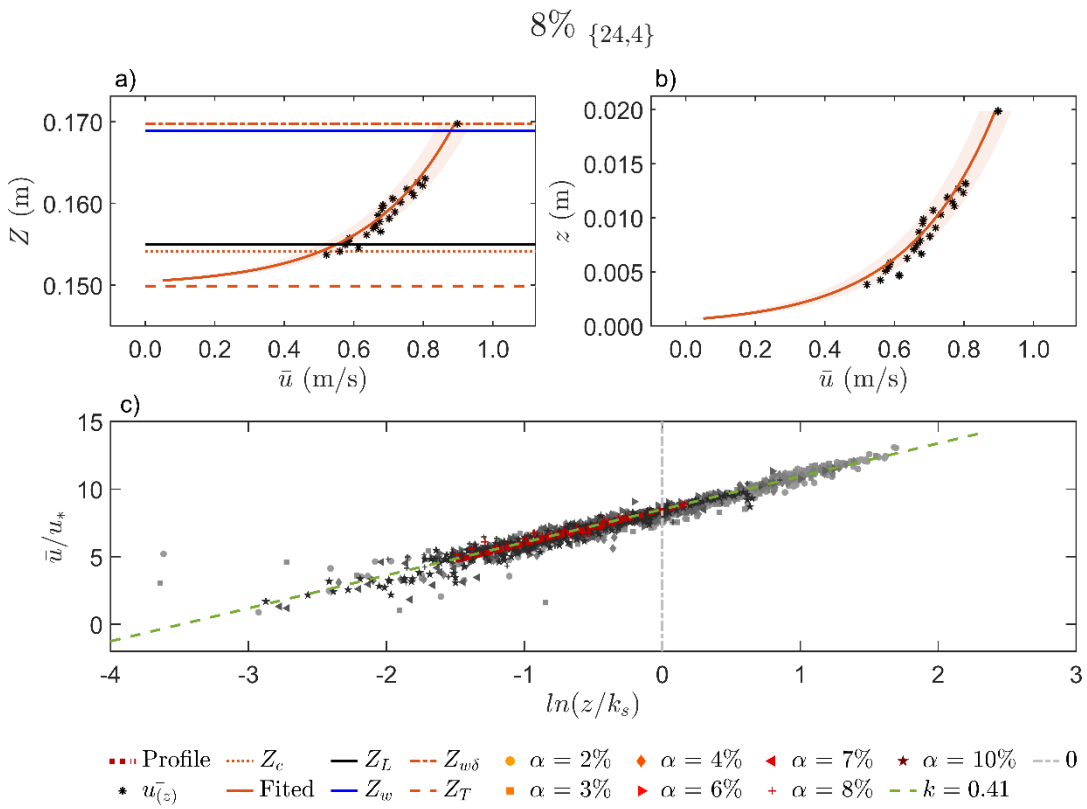

Figure B. 107. (a) Velocity profile as a function of water levels, (b) velocity profile as a function of water depths, and (c) dimensionless log profiles in the horizontal semi-log scale on a 8% flume slope.

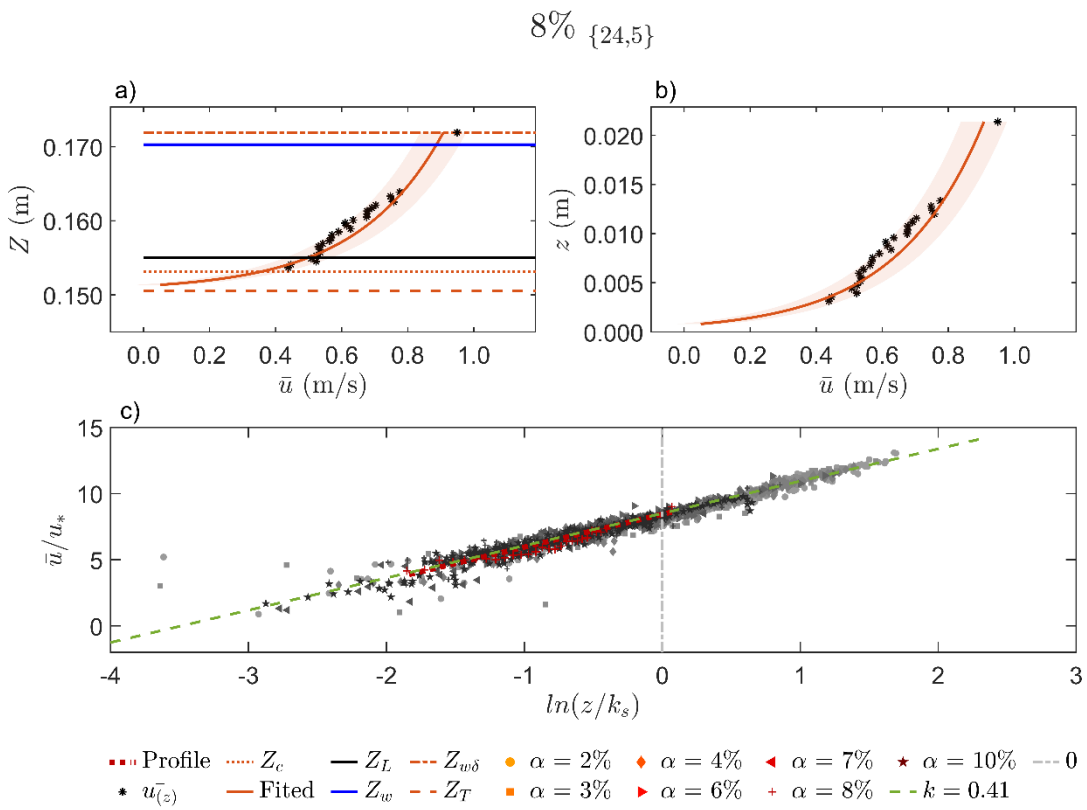

Figure B. 108. (a) Velocity profile as a function of water levels, (b) velocity profile as a function of water depths, and (c) dimensionless log profiles in the horizontal semi-log scale on a 8% flume slope.

B.1.3.g. 10% flume slope

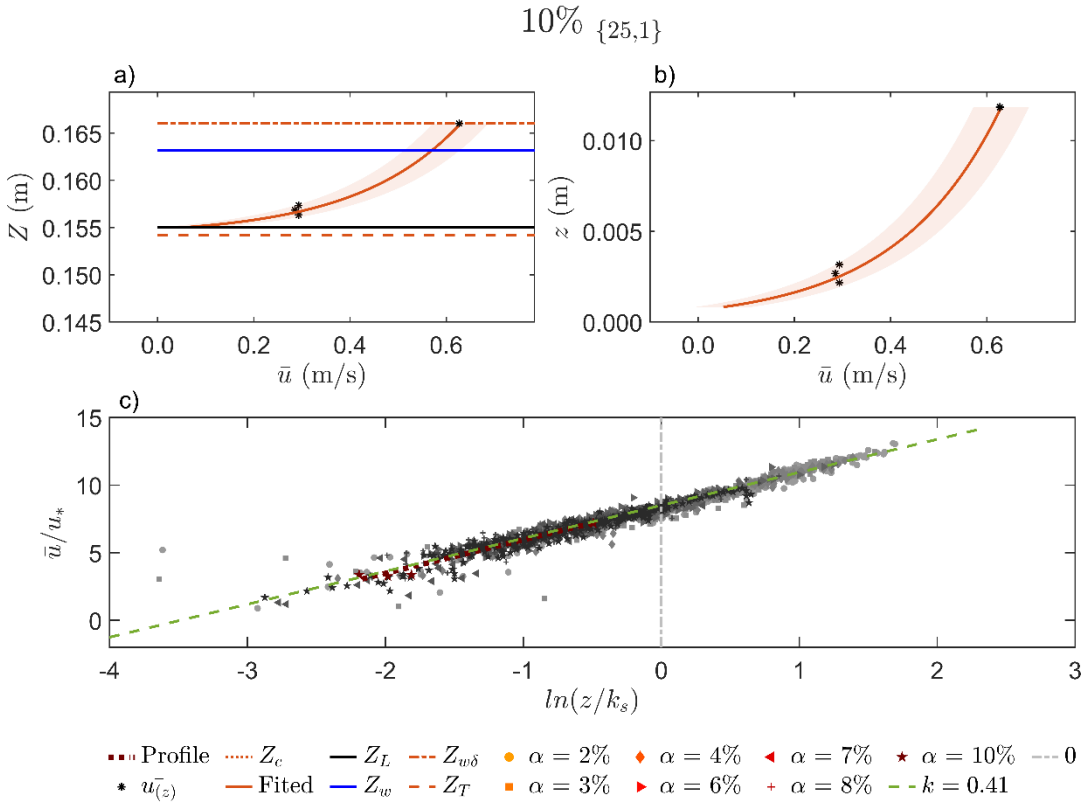

Figure B. 109. (a) Velocity profile as a function of water levels, (b) velocity profile as a function of water depths, and (c) dimensionless log profiles in the horizontal semi-log scale on a 10% flume slope.

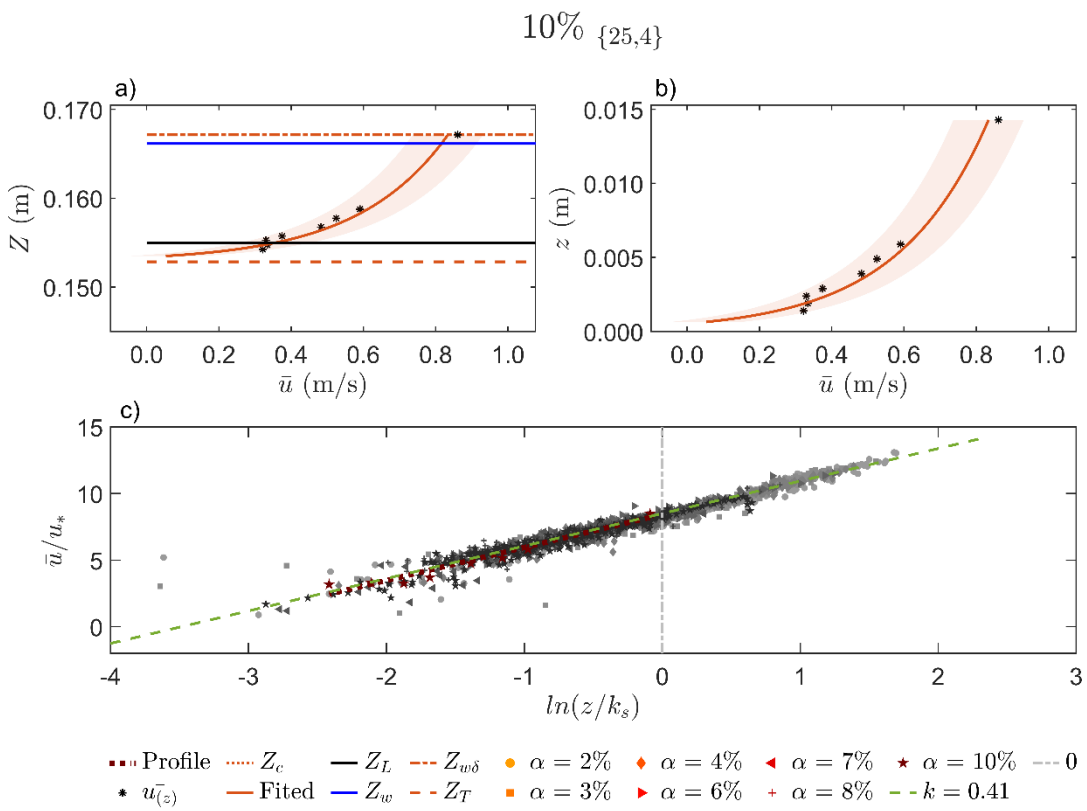

Figure B. 110. (a) Velocity profile as a function of water levels, (b) velocity profile as a function of water depths, and (c) dimensionless log profiles in the horizontal semi-log scale on a 10% flume slope.

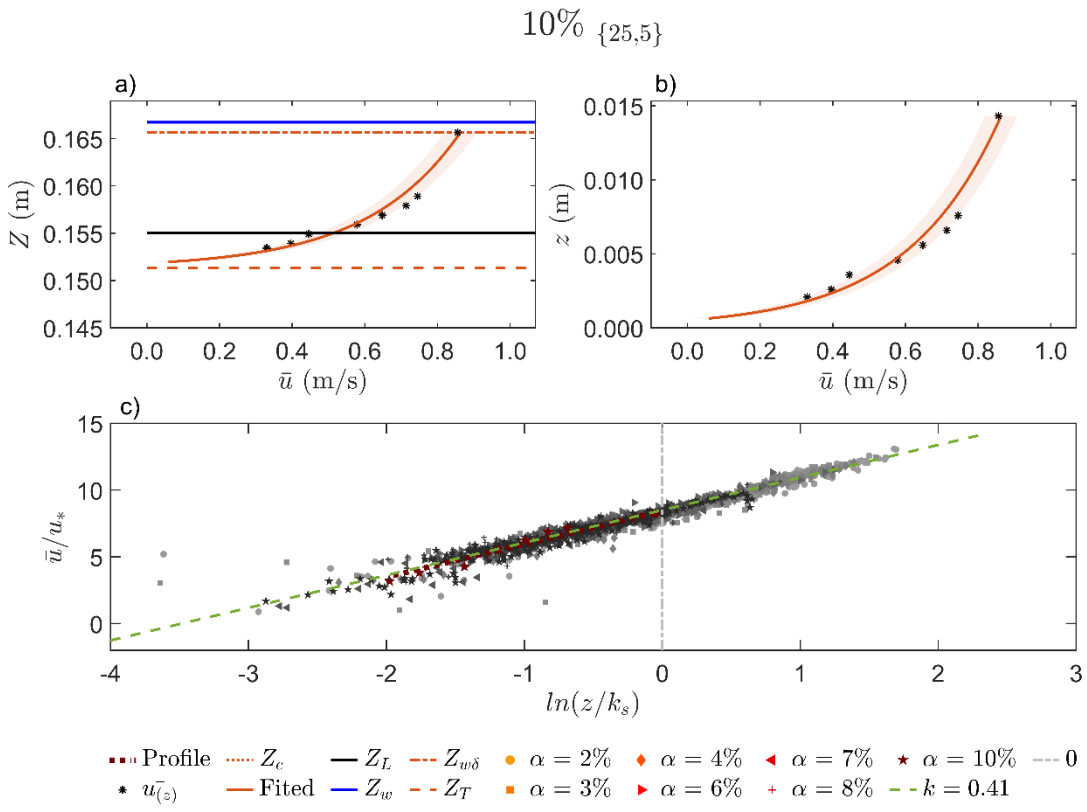

Figure B. 111. (a) Velocity profile as a function of water levels, (b) velocity profile as a function of water depths, and (c) dimensionless log profiles in the horizontal semi-log scale on a 10% flume slope.

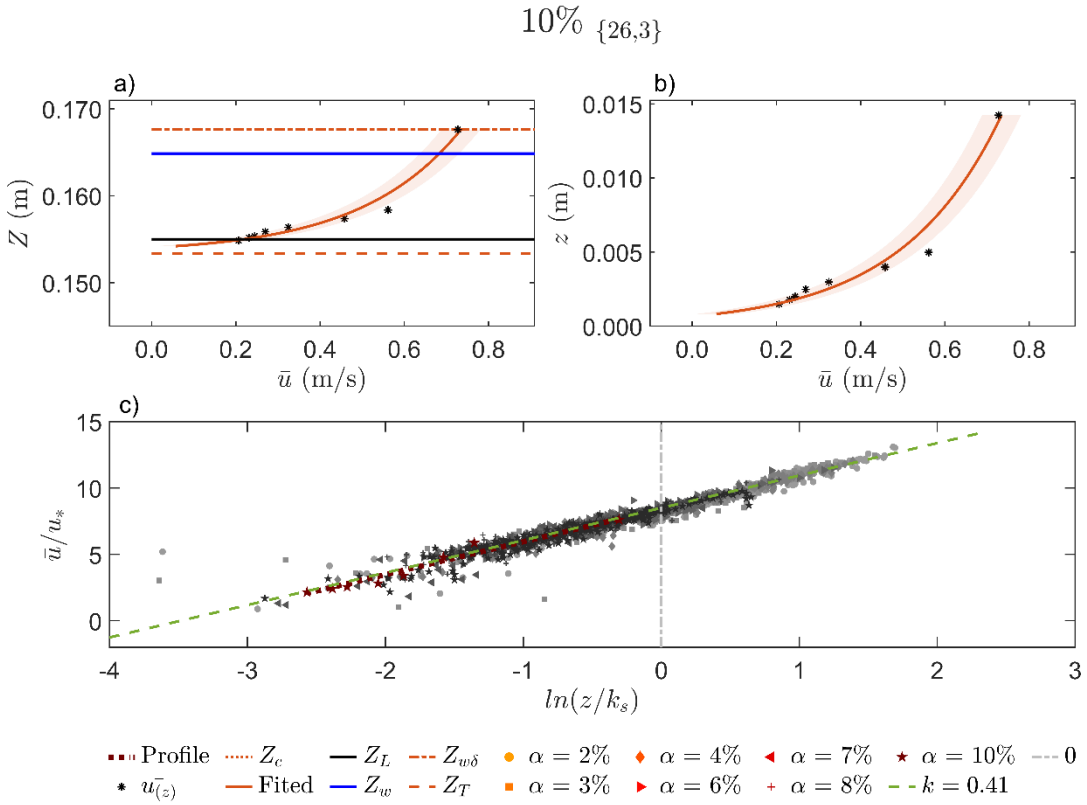

Figure B. 112. (a) Velocity profile as a function of water levels, (b) velocity profile as a function of water depths, and (c) dimensionless log profiles in the horizontal semi-log scale on a 10% flume slope.

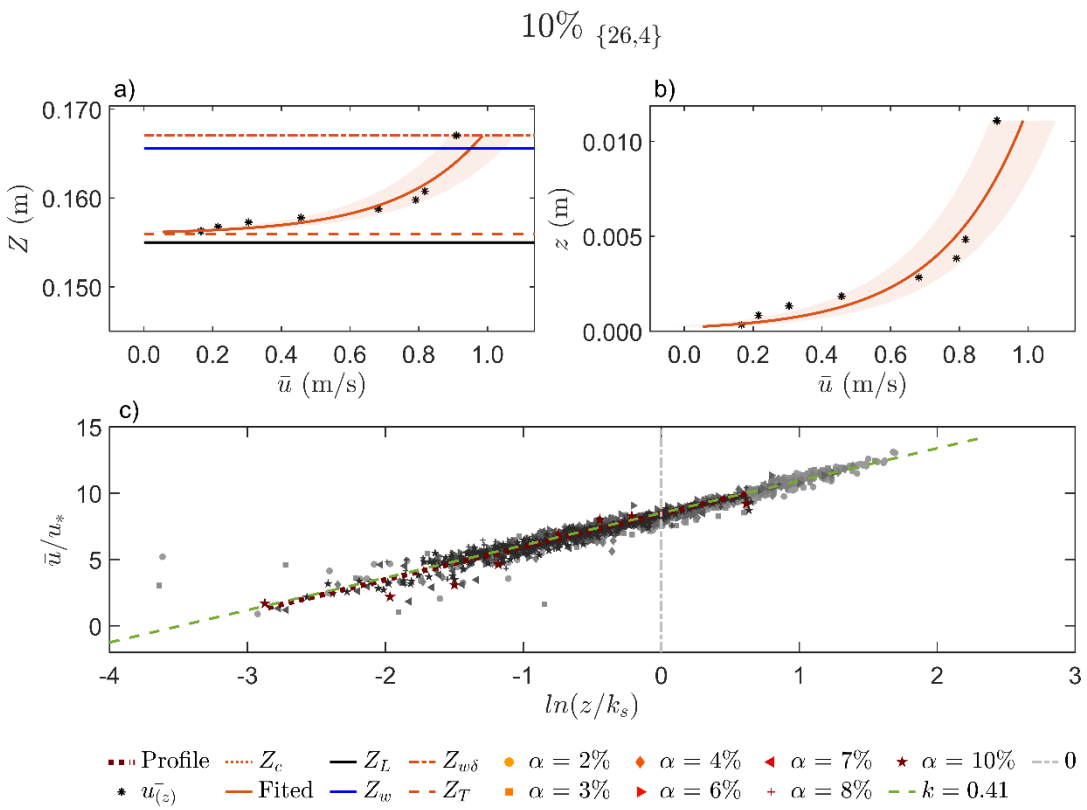

Figure B. 113. (a) Velocity profile as a function of water levels, (b) velocity profile as a function of water depths, and (c) dimensionless log profiles in the horizontal semi-log scale on a 10% flume slope.

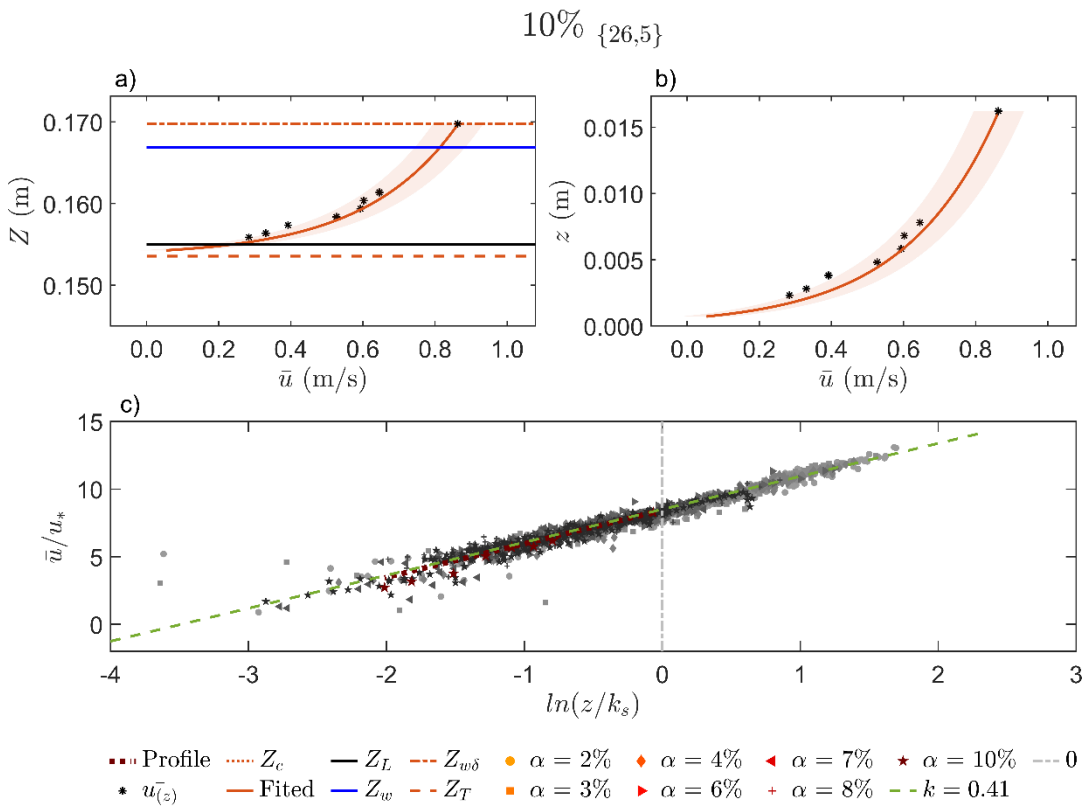

Figure B. 114. (a) Velocity profile as a function of water levels, (b) velocity profile as a function of water depths, and (c) dimensionless log profiles in the horizontal semi-log scale on a 10% flume slope.

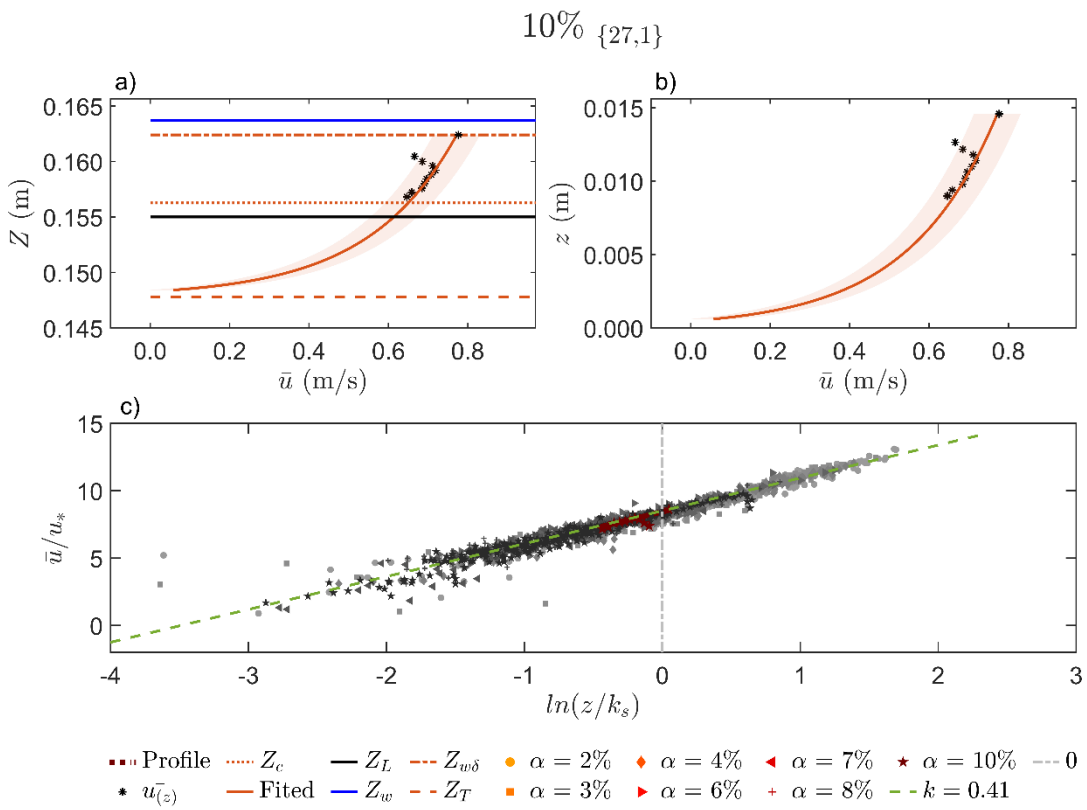

Figure B. 115. (a) Velocity profile as a function of water levels, (b) velocity profile as a function of water depths, and (c) dimensionless log profiles in the horizontal semi-log scale on a 10% flume slope.

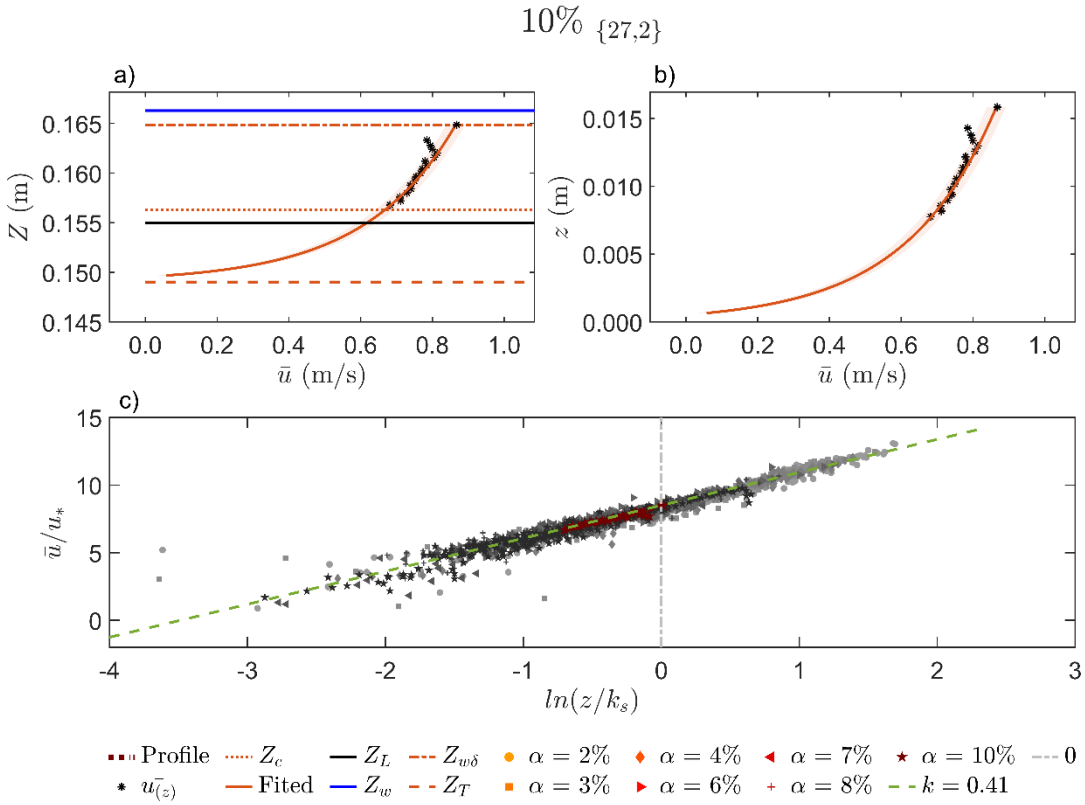

Figure B. 116. (a) Velocity profile as a function of water levels, (b) velocity profile as a function of water depths, and (c) dimensionless log profiles in the horizontal semi-log scale on a 10% flume slope.

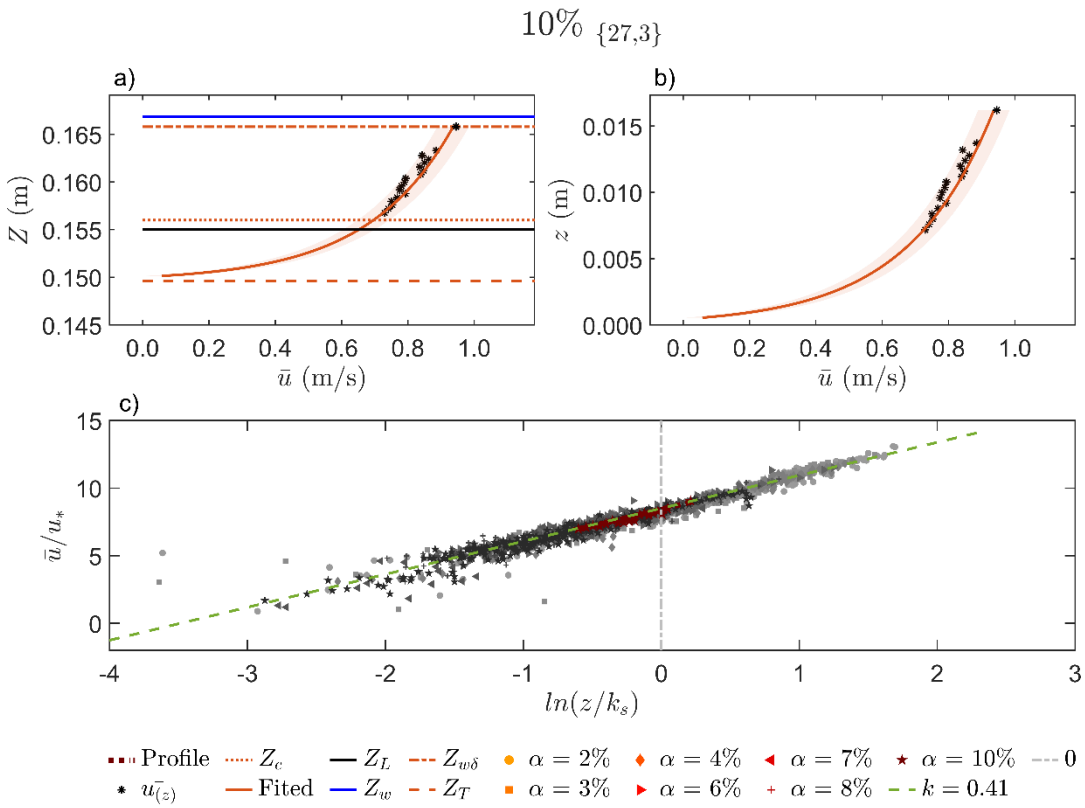

Figure B. 117. (a) Velocity profile as a function of water levels, (b) velocity profile as a function of water depths, and (c) dimensionless log profiles in the horizontal semi-log scale on a 10% flume slope.

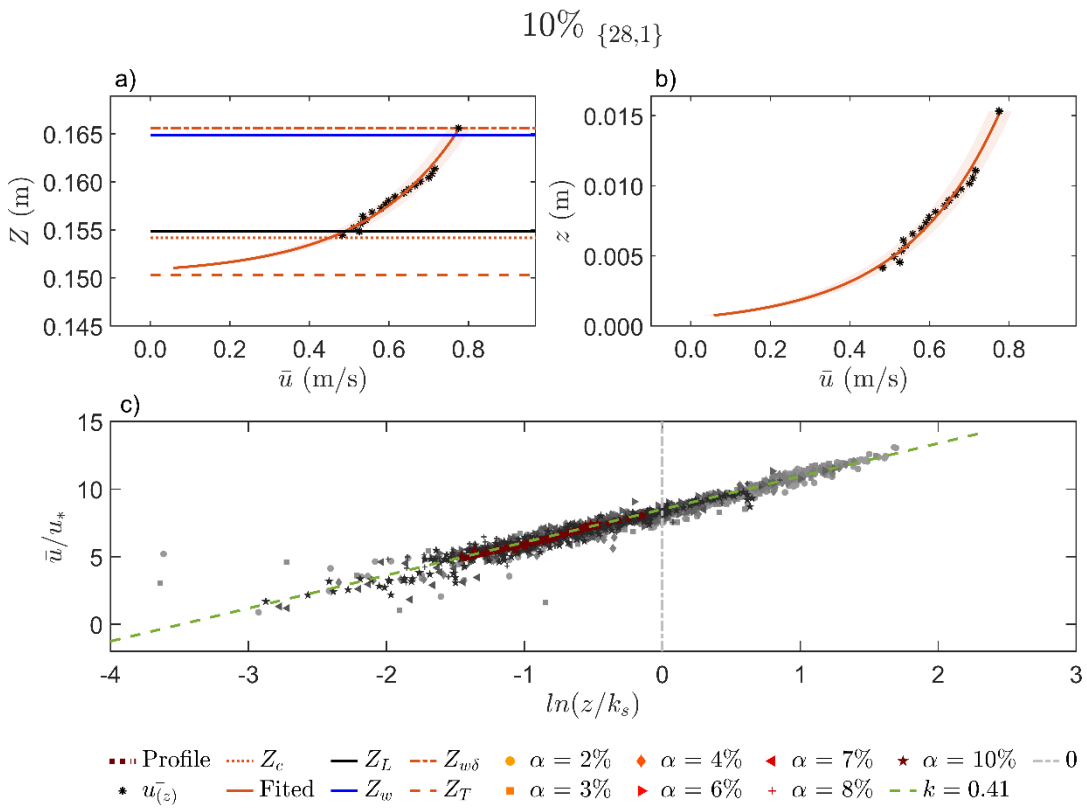

Figure B. 118. (a) Velocity profile as a function of water levels, (b) velocity profile as a function of water depths, and (c) dimensionless log profiles in the horizontal semi-log scale on a 10% flume slope.

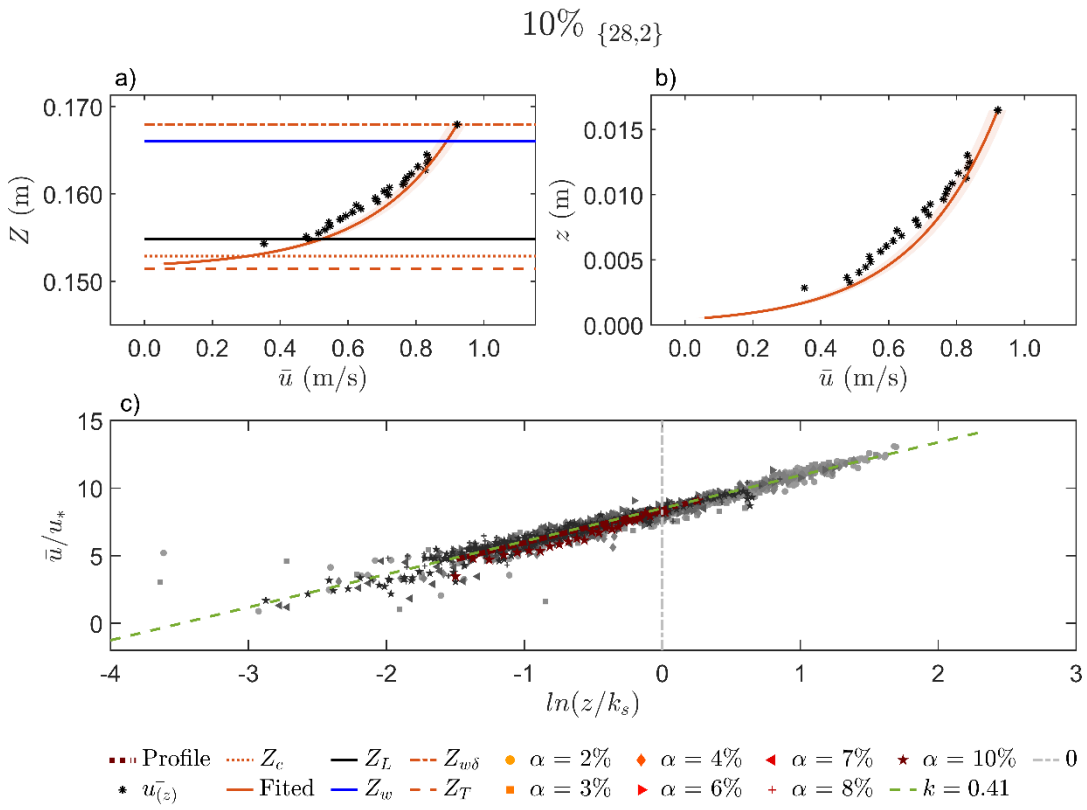

Figure B. 119. (a) Velocity profile as a function of water levels, (b) velocity profile as a function of water depths, and (c) dimensionless log profiles in the horizontal semi-log scale on a 10% flume slope.

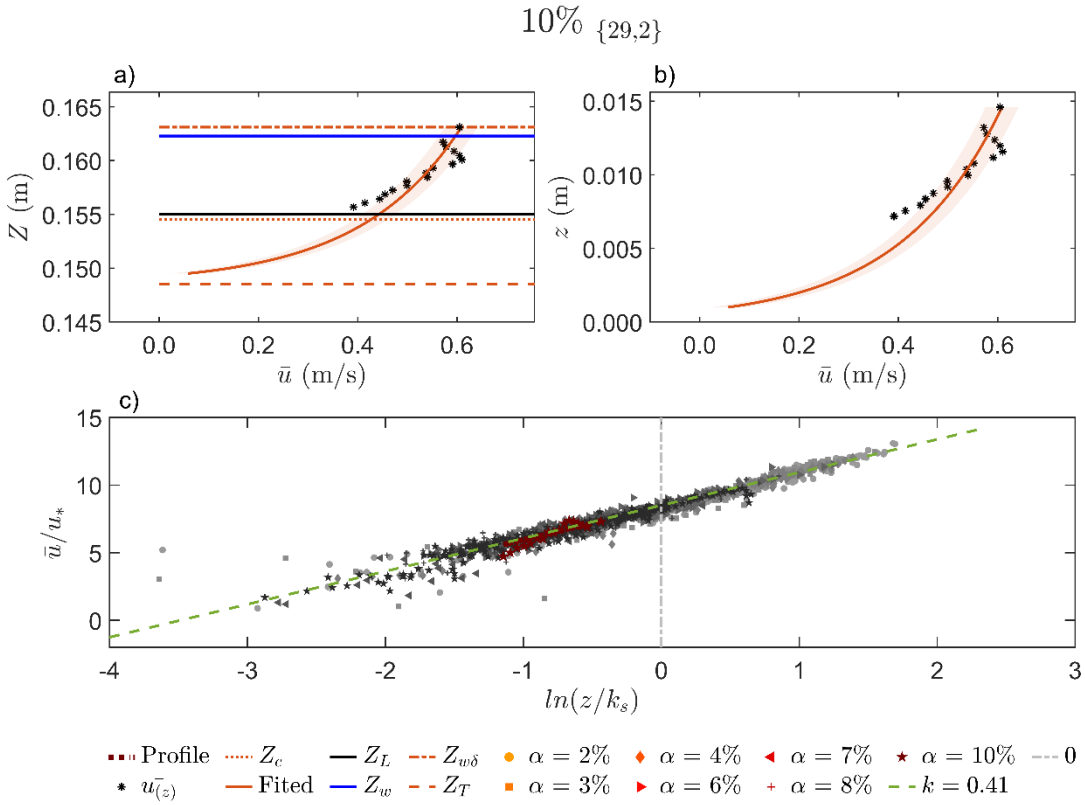

Figure B. 120. (a) Velocity profile as a function of water levels, (b) velocity profile as a function of water depths, and (c) dimensionless log profiles in the horizontal semi-log scale on a 10% flume slope.

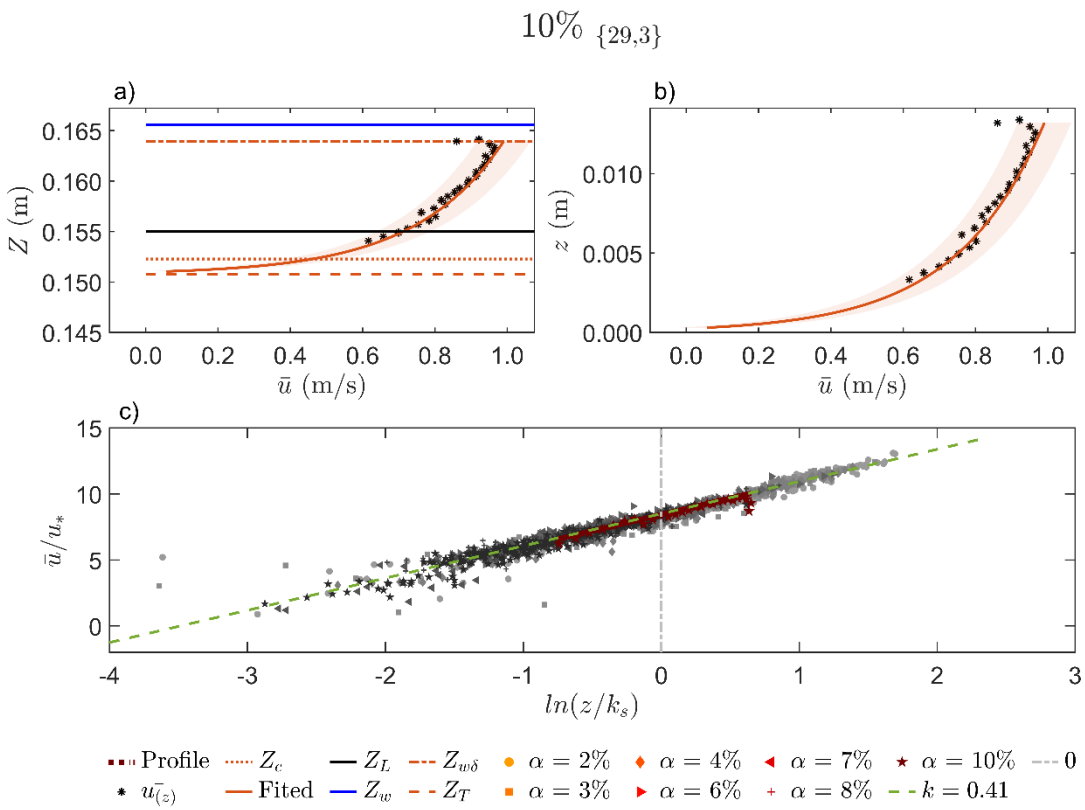

Figure B. 121. (a) Velocity profile as a function of water levels, (b) velocity profile as a function of water depths, and (c) dimensionless log profiles in the horizontal semi-log scale on a 10% flume slope.

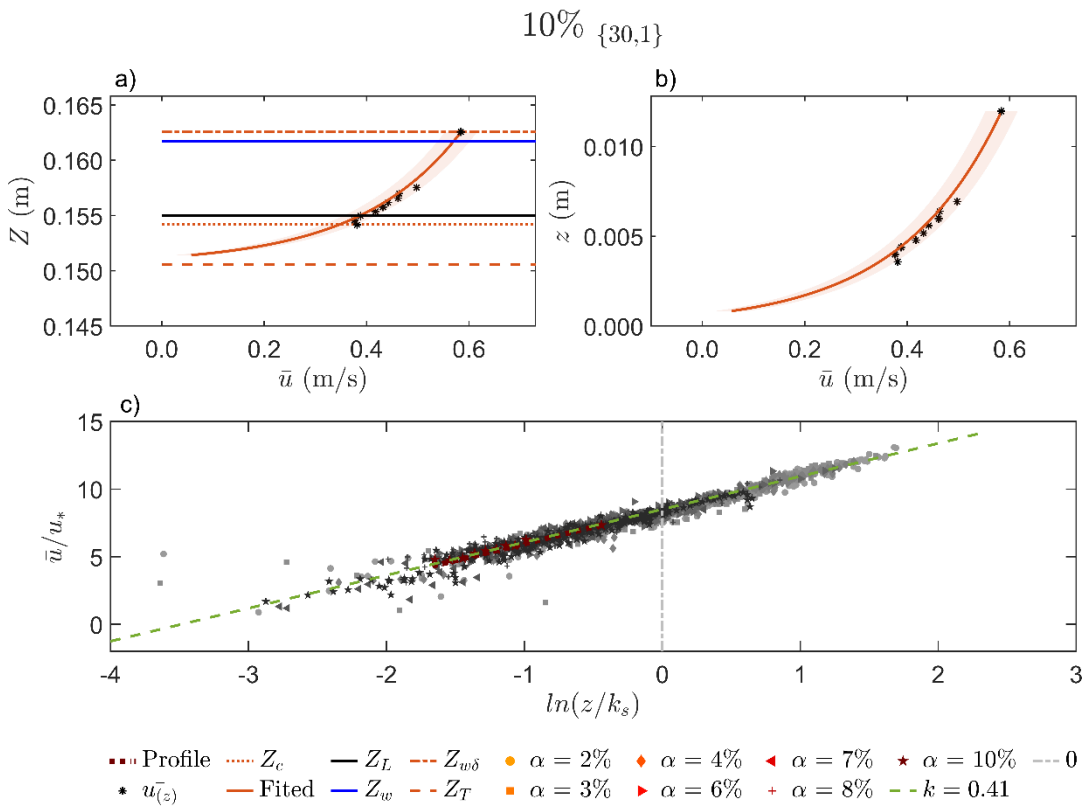

Figure B. 122. (a) Velocity profile as a function of water levels, (b) velocity profile as a function of water depths, and (c) dimensionless log profiles in the horizontal semi-log scale on a 10% flume slope.

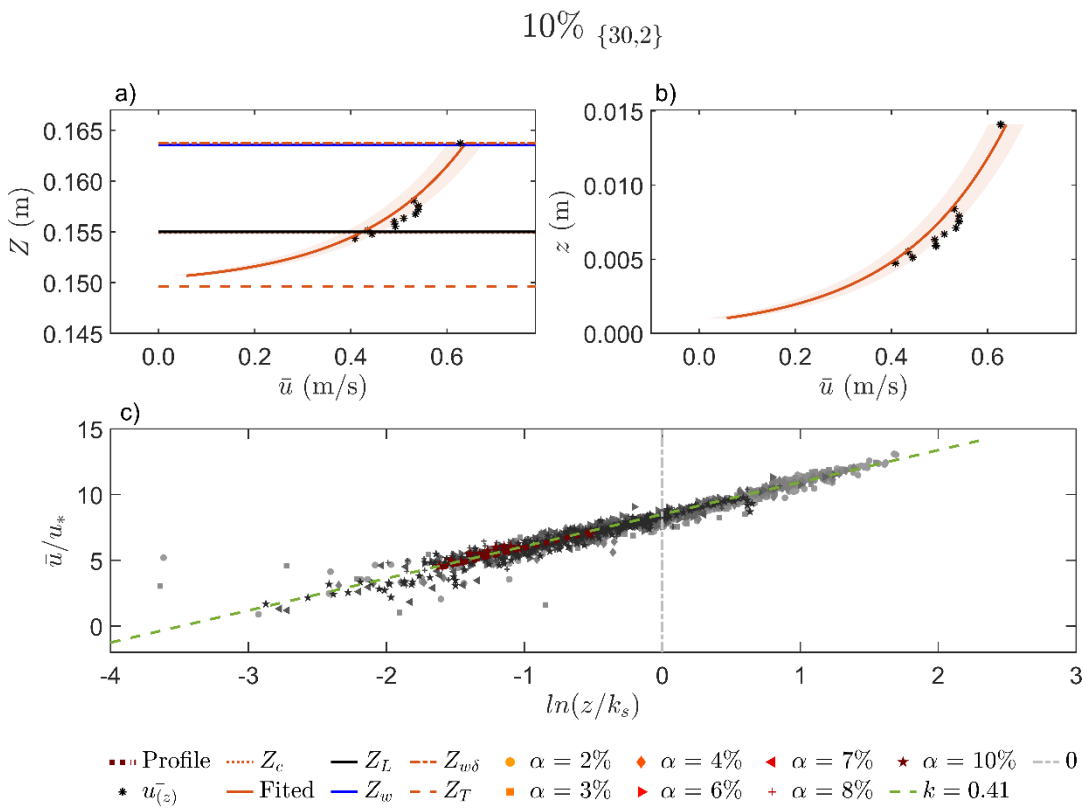

Figure B. 123. (a) Velocity profile as a function of water levels, (b) velocity profile as a function of water depths, and (c) dimensionless log profiles in the horizontal semi-log scale on a 10% flume slope.

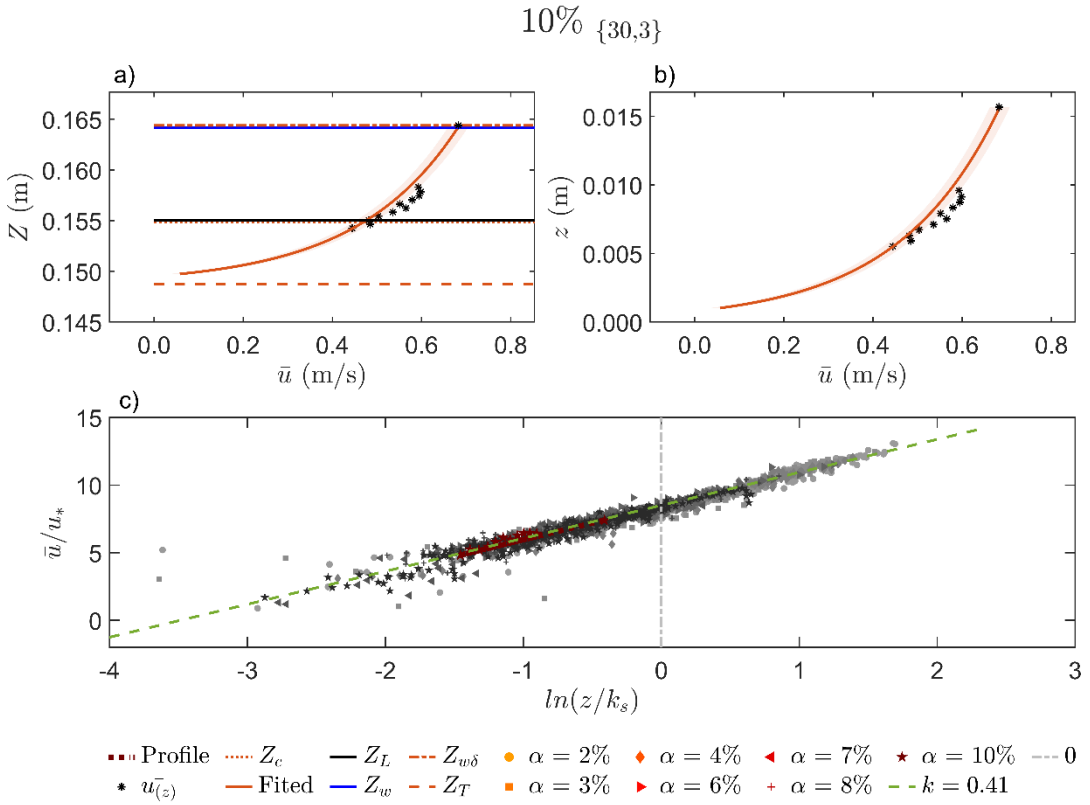

Figure B. 124. (a) Velocity profile as a function of water levels, (b) velocity profile as a function of water depths, and (c) dimensionless log profiles in the horizontal semi-log scale on a 10% flume slope.

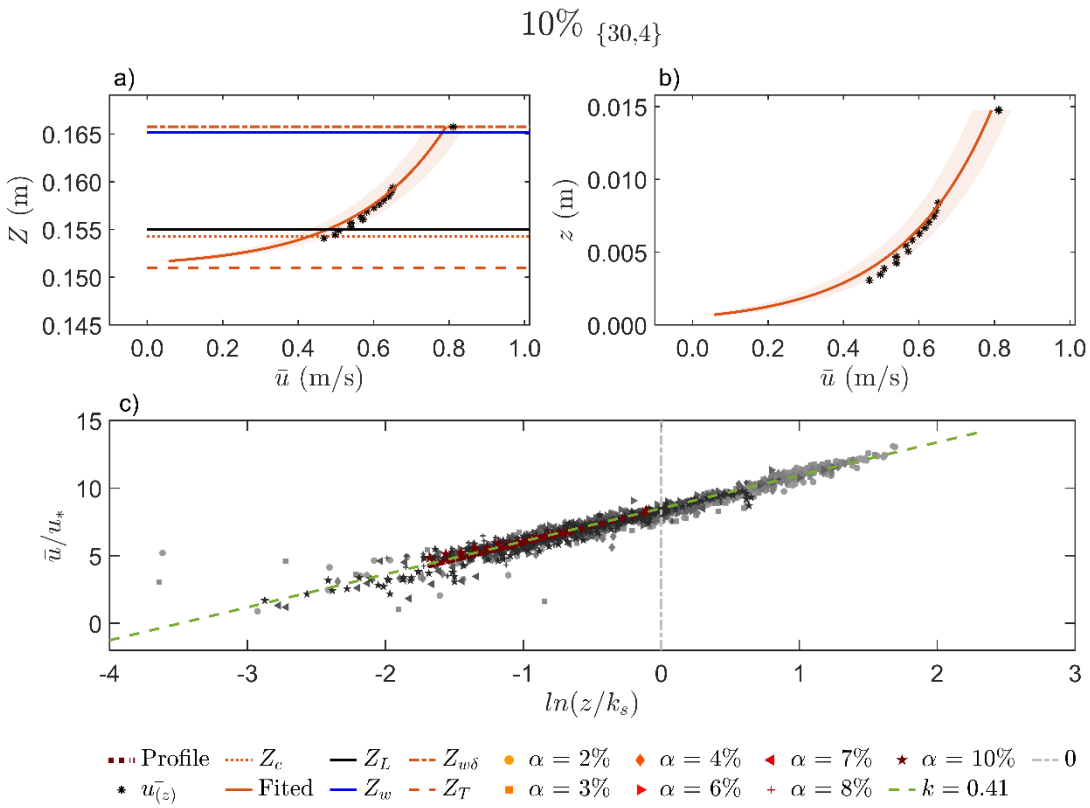

Figure B. 125. (a) Velocity profile as a function of water levels, (b) velocity profile as a function of water depths, and (c) dimensionless log profiles in the horizontal semi-log scale on a 10% flume slope.

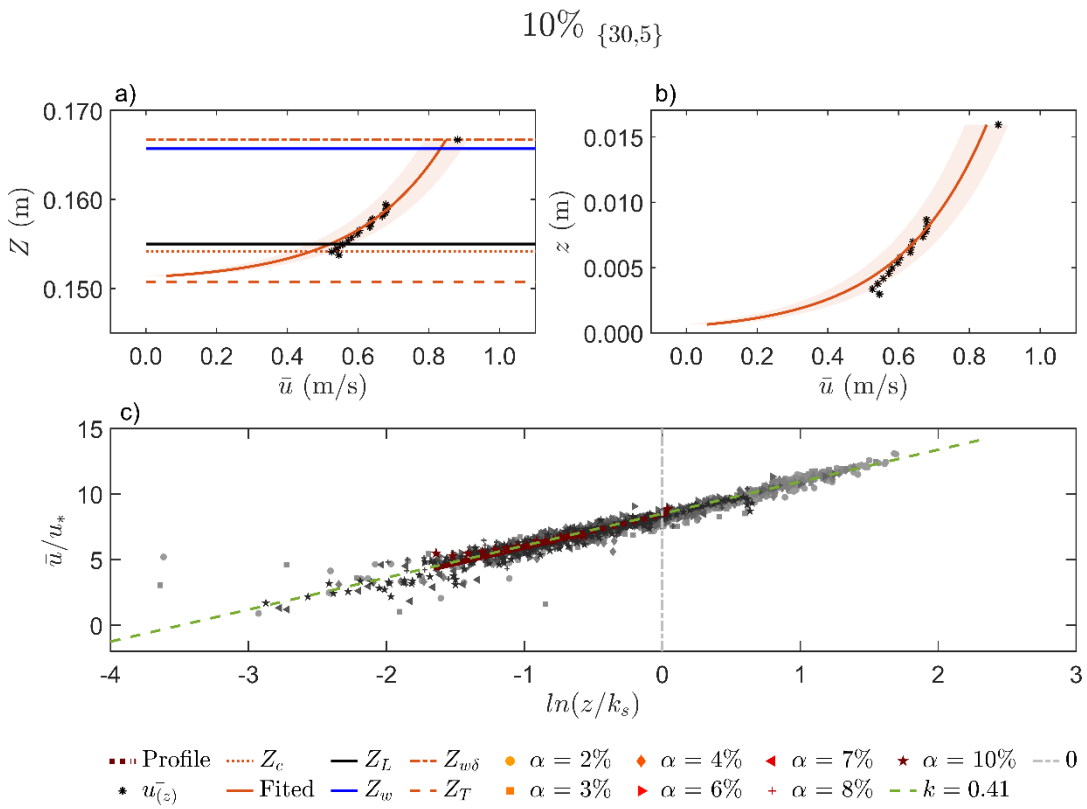

Figure B. 126. (a) Velocity profile as a function of water levels, (b) velocity profile as a function of water depths, and (c) dimensionless log profiles in the horizontal semi-log scale on a 10% flume slope.

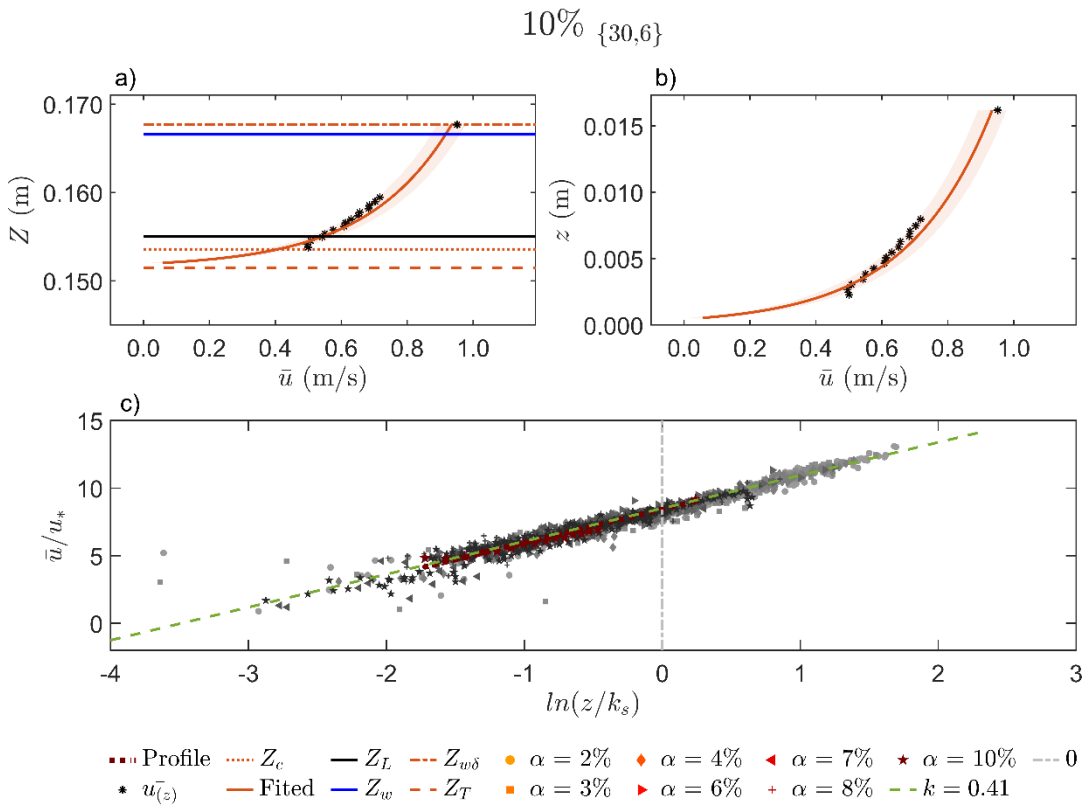

Figure B. 127. (a) Velocity profile as a function of water levels, (b) velocity profile as a function of water depths, and (c) dimensionless log profiles in the horizontal semi-log scale on a 10% flume slope.